OPTICALLY CONTROLLED MANIPULATION OF SINGLE NANO-OBJECTS BY THERMAL FIELDS

Von der Fakultät für Physik und Geowissenschaften

der Universität Leipzig

genehmigte

DISSERTATION

zur Erlangung des akademischen Grades

doctor rerum naturalium

Dr. rer. nat.

vorgelegt

von Dipl.-Phys. Marco Braun

geboren am 23.12.1984 in Karl-Marx-Stadt

Gutachter:
Prof. Dr. Dieter Braun, Ludwig-Maximilians-Universität München
Prof. Dr. Frank Cichos, Universität Leipzig

Tag der Verleihung: 20.06.2016

Bibliographic Description

Braun, Marco
Optically Controlled Manipulation of Single Nano-Objects by Thermal Fields
Universität Leipzig, Dissertation
157 pages, 192 references , 70 figures, 2 tables

Abstract

This dissertation presents and explores a technique to confine and manipulate single and multiple nano-objects in solution by exploiting the thermophoretic interactions with local temperature gradients. The method named thermophoretic trap uses an all-optically controlled heating via plasmonic absorption by a gold nano-structure designed for this purpose. The dissipation of absorbed laser light to thermal energy generates a localized temperature field. The spatial localization of the heat source thereby leads to strong temperature gradients that are used to drive a particle or molecule into a desired direction. The behavior of nano-objects confined by thermal inhomogeneities is explored experimentally as well as theoretically.

The monograph treats three major experimental stages of development, which essentially differ in the way the heating laser beam is shaped and controlled. In a first generation, a static heating of an appropriate gold structure is used to induce a steady temperature profile that exhibits a local minimum in which particles can be confined. This simple realization illustrates the working principle best. In a second step, the static heating is replaced. A focused laser beam is used to heat a smaller spatial region. In order to confine a particle, the beam is steered in circles along a circular gold structure. The trapping dynamics are studied in detail and reveal similarities to the well-established Paul trap. The largest part of the thesis is dedicated to the third generation of the trap. While the hardware is identical to the second generation, using the real-time information on the position of the trapped object to heat only particular sites of the gold structure strongly increases the efficiency of the trap compared to the earlier versions. Beyond that, the optical feedback control allows for an active shaping of the effective virtual trapping potential by applying modified feedback rules, including *e.g.* a double-well or a box-like potential. This transforms the formerly pure trapping device to a versatile technique for micro and nano-fluidic manipulation. The physical and technical contributions to the limits of the method are explored. Finally, the feasibility of trapping single macro-molecules is demonstrated by the confinement of λ-DNA for extended time periods over which the molecules center-of-mass motion as well as its conformational dynamics can be studied.

This work has been funded by
the European Union and the Free State of Saxony.

Gefördert aus Mitteln
der Europäischen Union

Europa fördert Sachsen.
ESF
Europäischer Sozialfonds

Freistaat
SACHSEN

Contents

Abbreviations

ABEL	anti-Brownian electrokinetic (trap)
AOD	acousto-optic deflector
Au	aurum – gold
CCD	charge-coupled device
COM	center of mass
cw	continuous wave
DNA	deoxyribonucleic acid
e.g.	exempli gratia – for example
et al.	et alia – and others
FB	feedback
FCS	fluorescence correlation spectroscopy
FEM	finite element method
FPE	Fokker-Planck equation
i.e.	id est – that is
MSD	mean squared displacement
NA	numerical aperture
NP	nano-particle
NSE	Navier-Stokes equation
PDF	probability distribution function
PS	polystyrene
PDF	position distribution function
PS	polystyrene
PSD	power spectral density
PSF	point spread function
PT	photothermal
rel.	relative
rms	root mean squared
RNA	ribonucleic acid
sdev	standard deviation
SMS	single molecule spectroscopy
SNR	signal to noise ratio
SPR	surface plasmon resonance
VFTH	Vogel-Fulcher-Tammann-Hesse (law)
WF	wide-field

Chapter 1

Introduction

Recent advances in biochemical, biophysical and life science as well as soft matter physics would have been unthinkable without the development of tools, which are nowadays standard in modern laboratories. The appearance of single molecule detection led to important developments in both microscopy and spectroscopy.[1–5] Since the first experimental realizations of single molecule detection directly by absorption[6] and later via fluorescence,[7] single molecule spectroscopy (SMS) has become a powerful toolbox as it allows to gather information from individual molecules. This enables to probe the local environment in which they are embedded on the nanometer scale, which is in direct contrast to ensemble measurements yielding averaged parameters for a large number of assumedly identical molecules.[8] Today, most SMS experiments are based on either wide-field detection techniques of epifluorescence and total internal reflection, or confocal and near-field optical scanning microscopy setups. Observation variables range from absorption and emission spectra of single molecules, orientation of molecules by probing their transition dipole moment to the excited state lifetime. Advanced techniques measure distances on a scale of a few nanometers via fluorescence resonance energy transfer (FRET).[9–11] Single molecule tracking[12,13] with sub-wavelength resolution to follow the position as well as the single molecule characteristics of blinking and photo-induced recovery of emitters[14] ultimately led to the development of super-resolution microscopy techniques such as photo-activated localization microscopy (PALM)[15,16] and stochastic optical reconstruction microscopy (STORM).[17] Advances in laser sources as well as opto-electric detectors have made SMS popular and widely used in bio-related research.[18–20]

Studying micro and nanometer-sized objects under physiological conditions typically involves a liquid environment. In solution, free particles and molecules undergo Brownian motion typically causing a quick disappearance from an observation volume as it scales with the molecule's size. A second technique that is often used in combination with SMS enables the study of microscopic objects over extended time periods. A very successful way of confining microscopic objects emerged from the fact that light carries momentum and may thus exert forces. Regarding the so-called optical tweezers,[21–23] which were first experimentally demonstrated in 1986,[24] two types of optical forces are important. Unfavorable scattering forces push the objects of interest in propagation direction, while gradient forces point towards the highest field intensity. For a stable trapping, gradient forces need to exceed the scattering forces. Typically, near-infrared laser light is used in combination with lenses of high numerical aperture to tightly focus the laser light in order to strengthen gradient forces.[25] In the same way as macroscopic tweezers are often used beyond their initial purpose, optical tweezers proved to be much more versatile than just confining objects. In fact, the success of optical tweezers relies on the observation that close to the laser focus, optical forces form a harmonic potential described by a Hookian spring constant.[26] Based on this feature, optical tweezing emerged to the standard tool to measure and exert forces in microscopic systems. Trapping by optical gradient forces, however, can only be achieved for microscopic objects of sufficient polarizability or dielectric contrast to the surrounding medium. A confinement of single biological macro-molecules is hardly possible for feasible laser intensities. The molecules of interest are therefore typically chemically attached to larger micro-meter-sized polystyrene beads. This in turn allows to transmit force to the molecule. Besides atomic force microscopy and magnetic tweezers, this is widely used in single molecule force spectroscopy[27,28] and led to deep insights into fundamental biological processes such as the direct observation of base-pair stepping during RNA polymerase[29] or mechanical folding dynamics of individual proteins.[30] Surface tethering, however, may influence the molecule's nature and can, for instance, alter the structural dynamics of bio-molecular systems.[31] The increasing demand for single molecule trapping as well as the lacking ability of optical tweezers to directly confine single molecules instead of linking them to larger objects leads to the development of new ideas.

Different techniques that directly refine the approach of optical forces to the nanoscale are called plasmonic traps.[32] They involve metallic nano-structures, such as gold pads,[33,34] gap antennas[35,36] or nano-apertures,[37–40] which are excited optically and provide high local intensities and strong field gradients employed for trapping of objects down to single DNA fragments.[39,41] Dielectrophoresis is used to trap individual proteins in radio frequency alternating electric fields.[42] Stable trapping of individual nano-objects was also shown within electrostatic potentials produced by appropriately nano-structured slit surfaces.[43] Paul trapping has been used for decades to trap ions in vacuum[44] and was recently also extended to trap nano-particles in solution.[45] An entirely different approach is the feedback-based hydrodynamic trap,[46] which uses actively controlled hydrodynamic forces to trap particles at a stationary point in the flow field of a microfluidic device. While not all of the mentioned techniques are (yet) capable of trapping single molecules, certainly, each has its own strengths.

A notably powerful technique is the anti-Brownian electrokinetic (ABEL) trap,[47] which uses a four-electrode device to generate an electric field inducing an electrokinetic drift. The electrode voltages are controlled by an optical position feedback to counter act Brownian motion. Beyond a harmonic trapping potential, the optical feedback control allows for the generation of arbitrary force fields.[47] More importantly, the performance of the method today operates at the physical limits of diffraction and shot noise.[31] Sophisticated statistical filtering[48] is employed to maximize localization accuracy enabling trapping of single fluorophores of hydrodynamic radii smaller than one nanometer.[49] Real-time access of the diffusion coefficient and the electrokinetic mobility[50] provides a means to visualize biomolecular interactions in solution such as the binding-unbinding kinetics of a single DNA molecule.[51]

The redundancy of a surface tethering to hold single molecules within a certain detection volume goes along with an inability to apply intra-molecular forces that are for instance exerted by a large polystyrene bead in the harmonic potential of optical tweezers. The homogeneous electric fields of the ABEL trap lead to a displacement of the entire trapped molecule, but the change in conformation is typically negligible.[47,52] While depending on the application, such interactions indeed need to be avoided, altering the conformational dynamics is in general hardly possible, even if demanded.

A promising class of interactions that could complement the toolbox of well-established methods is collected under the umbrella term thermophoresis, also called Soret effect or thermo-diffusion, and describes the response of microscopic particles, molecules or binary mixtures to variations in the local temperature, *i.e.* to temperature gradients. The physicochemical origin of thermophoresis thereby is manifold, but in general leads to a quasi-slip flow along the surface which, in turn, drives the particle or molecule into the opposite direction.[53,54] The different contributions, such as thermoosmosis in the electric double layer,[55] thermoelectric effects[56] or thermally driven depletion forces,[54] are collected within a single coefficient describing the thermophoretic mobility D_T. A different theoretical approach for weak temperature gradients is based on local equilibrium thermodynamics.[55,57–59] None of the existing microscopic theories is yet generally accepted and fundamental issues are still debated.[57,60,61] Phenomenologically, the steady-state particle distribution within an inhomogeneous temperature field is governed by two competing effects, one being thermophoresis, described by D_T, as well as Brownian motion, characterized by the diffusion coefficient D. The relative strength of the two competing effects is measured by the ratio of the individual mobilities, the co-called Soret coefficient $S_{\mathrm{T}} = D_{\mathrm{T}}/D$.[62]

Thermo-diffusion has been studied on various systems, such as colloidal particles,[59,60,62] DNA,[63–65] proteins,[66,67] micelles[67–69] or polymer solutions.[70–74] Attributed to the complex physical and chemical contributions to D_{T}, most microscopic particles or molecules exhibit a finite Soret coefficient. Moreover, the thermophoretic mobility of the bio-molecule sensitively dependents on, for example, conformation, charge, binding state and the chemical composition of the local environment. For this reason, a technique called Microscale Thermophoresis (MST) successfully evolved to a powerful tool for bioanalytics to quantitatively probe molecular interactions in free solution with low sample consumption.[75–78] In addition to the analytical aspect, as thermophoresis is the directed movement along a temperature gradient, the motion of particles or molecules can be influenced by shaping the temperature landscape. In such a way, particles or molecules can be accumulated typically in combination with convective or externally driven flows.[59,62–65,79–81] A third feature of thermophoresis is the ability to apply forces within molecules without the need for a surface attachment. This can be achieved by spatially modulating the temperature gradient over the extend of the molecule. Inducing intramolecular tension by inhomogeneous temperature gradients to stretch or compress single DNA strands has been demonstrated on prestretched DNA in nano-channels,[81,82] on DNA tethered to a surface[83] or on free DNA in combination with thermal convection.[84]

These three aspects, the ability to move objects along temperature gradients, the analytical information that is gained from the response on the gradients and the potential to induce intramolecular forces, make thermophoresis an interesting candidate for both the manipulation and the investigation of bio-molecular properties in the single molecule regime combined in one microfluidic device controlled by optical far-field techniques.

The present doctoral thesis is dedicated to a first step into that direction. The aim is to explore to what extend thermophoresis can be used to efficiently hold and manipulate single nano-objects in solution. For that purpose, sufficient thermophoretic drift velocities need to be induced in an appropriate way to compensate for the fast Brownian motion of nanoscopic particles. As the thermophoretic mobility is a coefficient of the solute-solvent system under study, the parameter which tunes the thermally induced drift is the temperature gradient. Temperature gradients are typically generated by heating a certain spatial region within the sample. The stronger the induced temperature field is localized, the higher the gradients are. Photothermal heating via a focused laser beam leads to heat sources that are diffraction-limited in size. The common way of further minimizing the extend of a heat source is the usage of an absorbing nano-structure.[85] Following these strategies, it is shown that a confinement can be achieved by different heating schemes. In the early experiments, a steady temperature profile that exhibits a local temperature minimum induced by the static illumination of an appropriate gold structure is shown to confine single polystyrene beads. This version represents the initial idea and the basic concept of the so-called thermophoretic trap. In order to increase the performance as well as versatility of the technique, the heating scheme is upgraded and the static illumination of the gold structure is replaced by a dynamic heating by means of a focused laser beam, which is driven in a feedback-free manner showing analogy to Paul trapping. By additionally introducing a software-based feedback of the heating beam position on the particle position, the efficiency of the trap can be increased tremendously. Moreover, the ability to flexibly alter the feedback rules allows for a complex manipulation of the nano-objects. It is also shown that, enabled by the spatially strongly decaying temperature fields, a defined number of multiple particles may be confined in a single trap. Finally, first experiments on the trapping of single DNA macro-molecules are presented that show the applicability of the developed technique for biophysical questions.

The manuscript is structured as follows. Chapter 2 presents background information on the physical concepts being relevant in the context of thermophoretic trapping. This is followed by Chapter 3 dealing with the experimental background necessary to understand the presented experiments and the received results. Chapter 4 presents and discusses the performed experiments. The chapter is thereby structured in three parts following the three major stages of development that are already mentioned above. Finally, a short summary of the results as well as an outlook on the future of thermophoretic single particle trapping is given with Chapter 5.

Chapter 2

Theoretical Background

2.1 Particle Motion on Small Length Scales

The first section introduces the governing equation for the fluid motion on small length scales in viscous media. Then, two different approaches to describe the stochastic motion of particles in a viscous solvent are presented. While both theoretical approaches are equivalent, each provides a different view on the problem of Brownian motion. Theoretical insight is gained either from an averaging over individual realizations of trajectories in the Langevin description or from studying the evolution of the probability density using the Fokker-Planck equation.

2.1.1 Motion at Low Reynolds Numbers

On microscopic length scales, the velocity field within a fluid, due to for example pressure gradients or moving boundaries, are well described by continuum mechanics. For the typical case that the fluid velocity is low compared to the velocity of sound within the fluid, it can be treated as incompressible,[86] $\nabla \cdot \mathbf{v} = 0$. With this assumption, the Navier-Stokes equation (NSE) that results from the conservation of mechanical momentum, takes the form

$$\rho \frac{\partial \mathbf{v}}{\partial t} - \eta \nabla^2 \mathbf{v} + \rho (\mathbf{v} \cdot \nabla) \mathbf{v} = -\nabla P + \mathbf{f}, \tag{2.1}$$

and describes the spatial and temporal evolution of the velocity field $\mathbf{v}(\mathbf{r},t)$. Herein, ρ and η are the mass density and the viscosity of the fluid, respectively. Apart from time-dependent boundary conditions, the fluid field may be driven by a pressure gradient ∇P or an externally applied force density $\mathbf{f}$. Mathematically, the complexity of the NSE is set by the non-linear term $\rho(\mathbf{v} \cdot \nabla)\mathbf{v}$ that results from inertial forces within the liquid.

The strength of the inertial forces (non-linear 3rd term in NSE) over the viscous forces due to momentum diffusion (2nd term in NSE) is quantified by their ratio, the so-called Reynolds number Re. By substituting the gradient with a typical length scale of the system $\nabla \sim l^{-1}$, *e.g.* a particle's diameter, Re is given by

$$\mathrm{Re} = \frac{\rho v^2/l}{\eta v/l^2} = \frac{\rho v l}{\eta}. \tag{2.2}$$

As the viscosity and density of water are of order $\eta \sim 10^{-3}\,\mathrm{Pa \cdot s}$, $\rho \sim 10^3\,\mathrm{kg/m^3}$ and typical velocities in microscopic systems of scale $l \sim 1\,\mu\mathrm{m}$ are $v \sim 1\,\mu\mathrm{m/s}$, the Reynolds number is of order $\mathrm{Re} \sim 10^{-6}$. Thus, inertial forces may be neglected leading to pure a laminar flow. Considering an intrinsic time scale of the system $\tau = l/v$, also the 1st term of the NSE scales with the Reynolds number and can be neglected assuming that the transient behavior is not of interest.[86] If, however, a time dependence is given by an external time scale, *e.g.* due to an oscillating boundary, the time derivative may not be neglected. As the viscous friction in the system dominates, any change of the force field $\mathbf{f}$ or pressure gradient ∇p leads to a quasi-instantaneous response in the velocity field $\mathbf{v}$. The motion is over-damped and now described by the Stokes Equation being linear in the velocity $\mathbf{v}$,

$$\eta \nabla^2 \mathbf{v} = \nabla P - \mathbf{f}. \tag{2.3}$$

The much simpler form allows for an analytical solution of important systems, such as the shear flow between two walls, when one wall is translated (Couette flow), or the pressure-induced fluid flow in

long channels (Poiseuille flow).[86] Also, Equation 2.3 is particularly important to describe phoretic motion such as electrophoresis and thermophoresis as will be seen in Section 2.2.2.
Via Equation 2.3 it can be shown that a microscopic rigid spherical particle of radius R that is dragged through a liquid by an external force $\mathbf{F}$ at a constant velocity $\mathbf{u}$ will induce a long-ranged velocity field around the particle, which decays with one over the distance from the particle, $\mathbf{v} \propto r^{-1}$. The energy of the flow field dissipates to heat due to the shear strain within the liquid leading to a friction coefficient $\gamma = 6\pi\eta R$ for the particle. Typically, this is referred to as Stokes drag characterizing the velocity response $\mathbf{u} = \mathbf{F}/\gamma$ to the external force $\mathbf{F}$.

2.1.2 Brownian Motion and Diffusion

The term Brownian motion denotes the stochastic motion that is shown by a mesoscopic particle dissolved in a liquid or gas. Mesoscopic in that context means, that the particles are too large that the motion directly relies on quantum effects, though too small to be described by classical mechanics. Its name is dated back on the Scottish botanist Robert Brown, who recognized the jittery motion of the pollen of plants in 1828.[87] Over years, abstract theories have been put forward that are today important in all kinds of sciences, not only fundamental physics, but also life science. The theory of Brownian motion may be even applied to the dynamics of economy, such as *e.g.* the stock market.[88, 89] Typically, the Brownian motion is described by hydrodynamic theories, where the microscopic details of the particle-solvent interaction are hidden in a set of parameters such as the temperature or the viscosity of the solvent. It was Einstein in 1905[90] who gave the important relation (Equation 2.4) linking thermal fluctuations of the solvent molecules to the macroscopically visible motion of the Brownian particle described by the diffusion or Einstein coefficient D,

$$D = \frac{k_\mathrm{B} T}{\gamma}, \tag{2.4}$$

with k_B the Boltzmann constant, T the absolute temperature and γ being the friction coefficient. The friction is caused by random collisions of a particle with the solvent molecules leading to a dissipation of kinetic energy to heat, *i.e.* thermal fluctuations, driving Brownian motion. Equation 2.4 is therefore an early representative of a fluctuation-dissipation relation.

Langevin Description An intuitive description which directly follows the microscopic origin of Brownian motion was given by Paul Langevin.[91] The dynamics of the particle or molecule is described by a differential equation in the form of Newtons equation of motion. The random collisions with solvent molecules that drive Brownian motion is expressed as a stochastic thermal force $\xi(t)$ randomly fluctuating in time. Considering a motion with viscous damping, $m\ddot{x} = -\gamma\dot{x}$, where m denotes the mass of the microscopic particle, a micron-sized particle of initial velocity decelerates exponentially on a time scale m/γ that is on the order of $1\,\mu\mathrm{s}$ and displaces less than $1\mathring{A}$. For microscopic systems in a viscous medium, the motion is thus over-damped (high friction limit) and the acceleration is four orders of magnitude faster than the experimentally accessible time scales of the experiments in this thesis ($\tau_\mathrm{exp} \sim 10\,\mathrm{ms}$). The term $m\ddot{x}$ may thus be neglected. The Langevin equation then reads[92, 93]

$$\gamma \frac{\mathrm{d}x}{\mathrm{d}t} = -\frac{\partial U}{\partial x} + \xi(t). \tag{2.5}$$

In the following, the random force term $\xi(t)$ fulfills the requirement of a Gaussian probability distribution with vanishing mean value. Also, the noise is assumed to be Markovian, *i.e.* delta-correlated in time ('white noise'), weighted by the friction γ and thermal energy $k_\mathrm{B}T$.

$$\langle\xi(t)\rangle = 0, \quad \langle\xi(t)\xi(0)\rangle = 2\gamma k_\mathrm{B}T\delta(t) \tag{2.6}$$

The term $-\partial_x U$ describes the force exerted by an externally applied potential. For now, it shall be assumed that $U \equiv 0$. The observable that is often measured experimentally is the particle position $x(t)$. As $\xi(t)$ is a stochastic variable, the particle position $x(t) = x(0) + \frac{1}{\gamma}\int_0^t \mathrm{d}t'\xi(t')$ is a stochastic variable as well and no predictions can be made for individual realizations. In particular, due to the Gaussian noise of vanishing mean, also the mean particle displacement with time vanishes, $\langle\Delta x(t)\rangle = \langle x(t) - x(0)\rangle = 0$. The mean refers to the average over many individual realizations. The second moment of the particle's probability distribution is the variance or mean squared displacement $\left\langle\Delta x^2(t)\right\rangle = \left\langle(x(t)-x(0))^2\right\rangle$, which takes in the case of no external potential the finite value

$$\left\langle\Delta x^2(t)\right\rangle = 2\frac{k_\mathrm{B}T}{\gamma}t = 2Dt. \tag{2.7}$$

The mean squared displacement being linear in t is a common means to calculate the diffusion coefficient D from a measured time trace $x(t)$.

In some cases, it is particularly useful to switch from the time to the frequency domain of a particle's motion by performing a Fourier transform of the particle position $\tilde{x}(f) = \mathfrak{F}(x(t)) = \int_{-\infty}^{+\infty}\mathrm{d}t e^{i2\pi ft}x(t)$. The phase information, however, is typically sacrificed by looking at the power spectral density (PSD) $S(f) = |\tilde{x}(f)|^2$, being the squared magnitude of the Fourier transform.[94] The uncorrelated noise $\xi(t)$ is frequency-independent and has a flat power spectrum ('white noise'). An integration of $\xi(t)$ over time results in a power-law dependence of the PSD for the Brownian motion of the free particle,[95] *i.e.* for $U \equiv 0$, given by

$$S(f) = \frac{D}{\pi^2 f^2}. \tag{2.8}$$

The latter noise is often called 'Brownian noise'.

Particle in a Harmonic Potential A potential which is of fundamental importance not only within this thesis, but generally in physics, is the harmonic potential with

$$U(x) = \frac{k}{2}x^2, \tag{2.9}$$

where k is the curvature of the potential. Most particle traps locally resemble a harmonic potential in good approximation. In the case of optical traps, k is typically referred to as the trap stiffness as it describes the response coefficient (spring constant) for the restoring force $\mathbf{F} = -k\mathbf{x}$ as a function of the displacement from the origin. In preparation of quantitative trapping experiments, *e.g.* to perform optical force spectroscopy,[27,28] the trap needs to be calibrated, meaning that the trap stiffness is characterized. Two standard methods to do so are the calculation of the power spectral density or the mean squared displacement of the particle position in the potential. Integrating the corresponding Langevin equation 2.6 after inserting the harmonic potential 2.9 yields a Lorentzian shape for the PSD,[26,95]

$$S(f) = \frac{D}{\pi^2(f^2 + f_c^2)}, \tag{2.10}$$

where $f_c = k/2\pi\gamma$ is the corner frequency containing the ratio of trap stiffness k and friction coefficient $\gamma = 6\pi\eta R$. Figure 2.1 B plots the PSDs for different curvatures of the harmonic potential given in A. In the high frequency limit $f \gg f_c$, the curves merge with the $1/f^2$-dependence for the free particle, where $U \equiv 0$. Low frequency fluctuations are increasingly suppressed by an increasing trap stiffness due to the localization of the particle. The according relation for the MSD is given by[92,95]

$$\left\langle \Delta x^2(t) \right\rangle = 2\frac{k_B T}{k}\left(1 - e^{-t/\tau_k}\right), \tag{2.11}$$

and contains the same information as the PSD. Herein, $\tau_k = 6\pi\eta R/k = 1/2\pi f_c$ is a relaxation time of the particle in the potential U with stiffness k and is equivalent to the inverse corner frequency. In the short time limit $t \ll \tau_k$, Equation 2.7 is recovered after a Taylor expansion. This shows that on short time scales the motion is dominated by Brownian motion. For long times, the motion is dominated by the confining potential and the MSD saturates to $\left\langle \Delta x^2(t \to \infty) \right\rangle = 2\frac{k_B T}{k}$, which is the equipartition theorem. This behavior is shown in Figure 2.1 C for increasing k and in comparison to a free particle with $U \equiv 0$ (black curve).

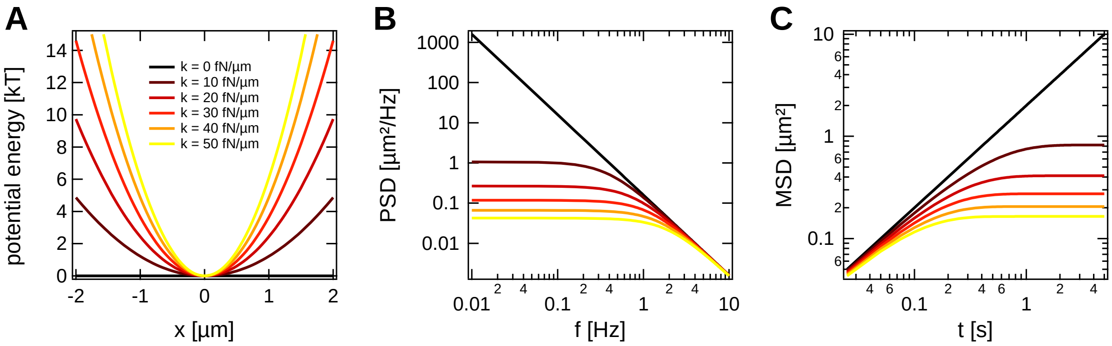

Figure 2.1: Brownian particle in harmonic potential: Potential energy $U(x)$ (**A**), power spectral density $S(f)$ (**B**) and mean squared displacement $\left\langle \Delta x^2(t) \right\rangle$ (**C**) for a diffusion coefficient of $D = 1\,\mu\mathrm{m}^2/\mathrm{s}$ for different trap stiffnesses k. The black curves correspond to zero potential.

Fokker-Planck Description For the commonly assumed case that the stochastic force $\xi(t)$ is given by Gaussian white noise, the Langevin equation can be transformed into a differential equation that describes the evolution of the probability distribution function (PDF) $P(x,t)$ of a Brownian particle. The resulting equation is known as Fokker-Planck equation (FPE).[a] The function $P(x,t)$ describes the probability $P(x,t)\,\mathrm{d}x$ to find a Brownian particle within the interval $x + \mathrm{d}x$ at time t . A normalization is chosen such that $\int_{-\infty}^{\infty} P(x,t)\,\mathrm{d}x = 1$. The FPE may be derived from the Langevin equation by writing the probability density as $P(x,t) = \langle \delta(x - x(t)) \rangle$. The mean again refers to the average over many individual realizations of the stochastic variable $x(t)$. Considering the derivative $\partial_t P(x,t) = -\partial_x \langle \delta(x - x(t))\dot{x}(t) \rangle$ and inserting Equation 2.6 yields[96]

$$\frac{\partial P(x,t)}{\partial t} = \frac{\partial}{\partial x}\left(\frac{1}{\gamma}\frac{\partial U}{\partial x}P(x,t) + D\frac{\partial P(x,t)}{\partial x}\right). \tag{2.12}$$

As the particle does not disappear, the probability is conserved and the FPE can be rewritten in form of a continuity equation $\partial_t P(x,t) = -\partial_x j$, where $j = j_D + j_U$ refers to the probability flux due

---

[a] In some literature the term ‘Fokker-Planck equation’ is used for the probability density $P(\chi,t)$ for a generalized variable χ, that could, for example, also be the velocity of a particle. If $\chi = x$ referees to the position of the particle, the FPE is often called Smoluchowski equation.

to diffusive motion $j_D = -D\partial_x P(x,t)$ as well as the external potential $j_U = -\frac{1}{\gamma}(\partial_x U)P(x,t)$. The steady-state probability distribution takes the shape of a Boltzmann distribution $P(x) \propto \mathrm{e}^{-U(x)/k_\mathrm{B}T}$, which can be directly seen after integrating Equation 2.12 after setting $\partial_t P(x,t) = 0$. Mathematically, this will become important again in the case of thermophoresis, where a temperature field can be thought of as a potential leading to a certain probability distribution.

For non-interacting particles, considering the evolution of the concentration profile $c(x,t)$, a process that is called diffusion, instead of the of the probability distribution $P(x,t)$ is fully equivalent. The solutions vary only by the fact that $P(x,t)$ is normalized.[92] Rewriting Equation 2.12 with $U \equiv 0$ recovers Fick's well known second law $\partial_t c = D\partial_x^2 c$, which predicts how inhomogeneous concentration fields evolve over time.

Brownian Motion with Flow Of particular importance for the analysis of the time traces in the Results chapter is the FPE which accounts for a uniform flow u, whereas no external potential is present ($U \equiv 0$). The flow u does appear in the continuity equation with an additional advection term $j_u = uP(x,t)$. Together with the diffusive flow $j_D = -D\partial_x P(x,t)$, the FPE takes the form

$$\frac{\partial P(x,t)}{\partial t} = u\frac{\partial P(x,t)}{\partial x} + D\frac{\partial^2 P(x,t)}{\partial x^2}. \tag{2.13}$$

Equation 2.13 is readily solved for the initial condition $P(x,t=0) = \delta(x-x_0)$,[97] that means the particle is located at the position x_0 at the time $t = 0$, yielding the advection-diffusion propagator

$$P(x,x_0,t) = \sqrt{\frac{1}{4\pi Dt}}\exp\left(-\frac{(x-x_0-ut)^2}{4Dt}\right). \tag{2.14}$$

The Gaussian probability distribution shows a variance $\sigma^2 = 2Dt$ that spreads in time t. Additionally, the flow u causes a shift of the Gaussian by $\Delta x_u = ut$. Figure 2.2 A displays plots of Equation 2.14 for subsequent times t. Alongside, Figure 2.2 B shows snapshots of Equation 2.14 at a fix time t but for different flow velocities u, which does not effect the width of the probability distribution.

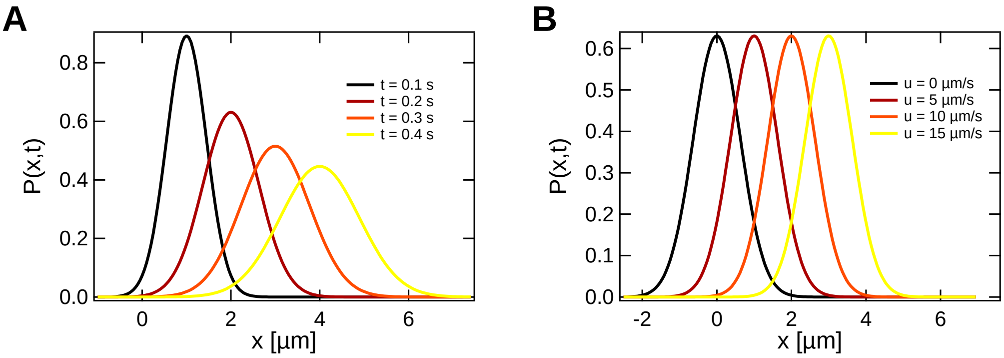

Figure 2.2: **A** Evolution of $P(x,x_0=0,t)$ (Equation 2.14) for a constant flow of $u = 10\,\mu\mathrm{m/s}$. **B** $P(x,x_0=0,t)$ at a constant point in time $t = 0.2\,\mathrm{s}$ for increasing flow velocity u.

2.2 Thermally Induced Motion – Thermophoresis

Additionally to its erratic Brownian motion, a solute typically undergoes a deterministic drift when a temperature gradient is applied to the solvent. This so-called Ludwig-Soret effect is named after the scientists who first discovered the phenomenon.[98,99] Due to its thermal nature, the effect is also called thermophoresis. In the language of non-equilibrium thermodynamics, the temperature gradient gives rise to a generalized force and the mobility D_T is associated with the Onsager coefficient coupling heat and particle flow.[100] The thermophoretic drift induced by applying a temperature gradient is phenomenologically given by $u = -D_\mathrm{T}\nabla T$. By guessing, one might be tempted to assume that the movement is towards the cold region, however, a more thorough examination shows that under certain circumstances also negative thermophoretic mobilities are possible.

The following section will first give a phenomenological description of the thermally induced motion. Later, different approaches to explain the thermophoretic mobility are presented, from a hydrodynamic point of view as well as from thermodynamics by considering a local thermal equilibrium.

2.2.1 Phenomenological Description

In the following, the thermophoretic mobility D_T as well as the diffusion coefficient D are assumed to be temperature-independent. As a result of the thermophoretic drift $u(x) = -D_\mathrm{T}\partial_x T(x)$, the probability flux of a particle due to an applied temperature gradient may be written as $j_\mathrm{T} = u(x)P(x,t) = -D_\mathrm{T}P(x,t)\partial_x T(x)$, where $P(x,t)$ is the probability density for the particle to be at the position x at the time t. Hence, an inhomogeneous temperature field $T(x)$ will distort the probability distribution for a particle. For a positive D_T, particles will migrate to the cold, which in turn will result in a diffusive back-flow $j_\mathrm{D} = -D\partial_x P(x,t)$ (see Figure 2.3). The overall probability flux is then given by

$$j(x,t) = j_\mathrm{D} + j_\mathrm{T} = -D\frac{\partial P(x,t)}{\partial x} - D_\mathrm{T}P(x,t)\frac{\partial T(x)}{\partial x} = -D\left(\frac{\partial}{\partial x} + S_\mathrm{T}\frac{\partial T(x)}{\partial x}\right)P(x,t). \tag{2.15}$$

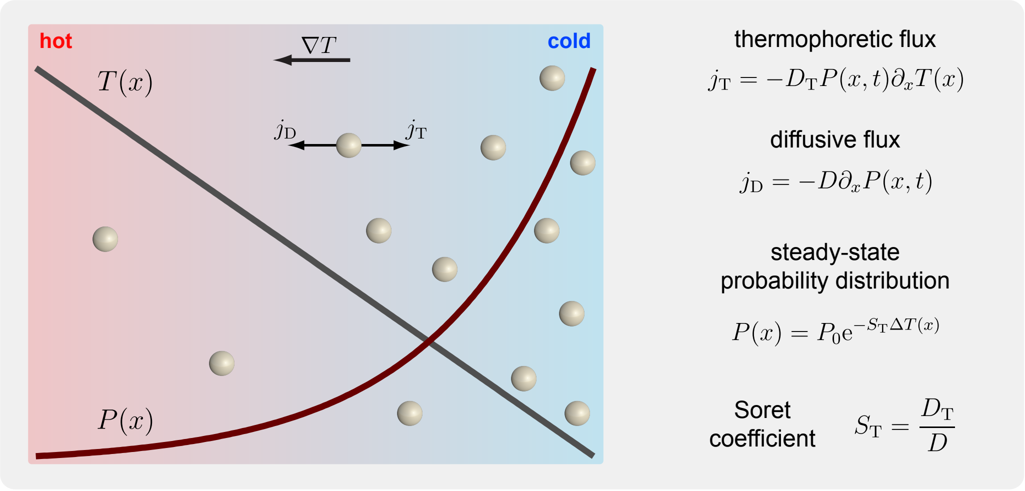

Figure 2.3: Phenomenological description of the motion induced by a temperature gradient.

The Soret coefficient $S_\mathrm{T} = D_\mathrm{T}/D$ is introduced to compare the strength of thermophoresis, characterized by D_T, to normal diffusion with the Einstein coefficient D. In the stationary state, when the fluxes

j_T and j_D compensate, such that $j = j_T + j_D = 0$, the probability density $P(x)$ is solely described by the Soret coefficient together with the shape of the temperature elevation field $\Delta T(x)$,

$$P(x) = P_0 \, \mathrm{e}^{-S_T \Delta T(x)}. \tag{2.16}$$

P_0 appears as a normalization factor. The Soret coefficient may be hence seen as a measure for the thermal separation in the steady state. The time evolution of a particle in a temperature field may be studied by inserting Equation 2.15 into the continuity equation $\partial_x j(x,t) + \partial_t P(x,t) = 0$, which yields the corresponding Fokker-Plank Equation

$$\frac{\partial P(x,t)}{\partial t} = \frac{\partial}{\partial x} D \left(\frac{\partial}{\partial x} + S_T \frac{\partial T(x)}{\partial x} \right) P(x,t). \tag{2.17}$$

Comparing Equation 2.17 with Equation 2.12 shows that, regardless of the mechanisms that lead to thermophoresis (see discussion below) and although no external force is associated with the application of the temperature field, the temperature field itself can be thought of as an effective potential landscape for a particle with $U_{\mathrm{eff}}/k_B T = S_T \Delta T$. This will be particularly useful in the discussion of the results as the induced effective potentials in the thermophoretic trap may be directly compared to competing methods. Also, the solutions of the Fokker-Planck equation for the mean squared displacement and power spectral density that have been calculated for 'real' potentials in Section 2.1.2 may be directly transfered to thermophoresis. The next paragraph will introduce the latter properties of a temperature field that is of notable interest for this thesis.

The Harmonic Temperature Field A special type of temperature field that will often appear within the Results section develops from a temperature gradient that increases linearly with increasing distance to the origin, $\nabla T = \alpha x$. This thus leads to a quadratic temperature field,[101]

$$\Delta T_{\mathrm{Harm}}(x) = T_{\mathrm{Harm}}(x) - T_{\mathrm{Center}} = \frac{\alpha}{2} x^2, \tag{2.18}$$

which is called harmonic temperature field in the following due to the obvious similarity to a harmonic potential. Following Equation 2.16, the steady state probability distribution of a Brownian particle in such a temperature field is found to be Gaussian

$$P(x) = \frac{2\pi}{S_T \alpha} \exp\left(-\frac{S_T \alpha}{2} x^2 \right), \tag{2.19}$$

with a variance $\sigma^2 = 1/S_T\alpha$. A harmonic potential $U(x) = \frac{1}{2} k x^2$ is characterized by its spring constant k, often referred to as trapping stiffness. The parameters α and S_T relate to k of the effective harmonic potential via

$$k_{\mathrm{eff}} = \frac{k_B T}{\sigma^2} = S_T \alpha k_B T. \tag{2.20}$$

From the Fokker-Planck equation 2.17 together with the harmonic temperature field of Equation 2.18, one finds the mean squared displacement

$$\left\langle \Delta x^2(t) \right\rangle = \frac{2}{S_T \alpha} \left[1 - \exp\left(-t/\tau_\alpha \right) \right], \tag{2.21}$$

with $\tau_\alpha = 1/\alpha D_T$ (see SI in Braun et al.[101] for the detailed derivation). Accordingly, the power spectral density is of the same shape as Equation 2.10, except that the corner frequency is now given by $f_c = 1/2\pi\tau_\alpha = \alpha D_T/2\pi$.

2.2.2 Fluid Dynamics Approach

Within the above phenomenological description of thermophoresis, the complex physical and chemical mechanisms leading to thermally induced motion are hidden in the thermophoretic mobility D_T. The approaches to describe the Soret effect on a microscopic scale can be classified in two categories: effects related to a quasi-slip flow on a particle's surface, *i.e.* from hydrodynamics, and a thermodynamic approach. In the following, a brief overview is presented covering the most important aspects.

Hydrodynamics of the Boundary Layer Interactions of the particle with the solvent happen within a boundary layer of thickness λ. For charged particles, where a shielding is caused the accumulation of counter ions, the boundary layer is called electric double layer. Conveniently, a local coordinate system is used on the particle's surface, where the x and z directions are tangential and normal to the particle's surface, respectively. Here, the boundary layer approximation shall be briefly introduced, where the particle is much larger than the characteristic thickness of the boundary layer $\lambda \ll R$. That means, the hydrodynamic quantities vary strongly perpendicular to the surface, but only slowly change along the surface due to external perturbations. Close to the particle, the normal component of the velocity vanishes, $v_z = 0$, and the velocity parallel to the surface weakly depends on x, such that it can be assumed that $v_x = v_x(z)$. The normal component of the Stokes Equation 2.3 thus reads[54, 55]

$$0 = \frac{\mathrm{d}P}{\mathrm{d}z} - f_z \tag{2.22}$$

An integration delivers the excess hydrostatic pressure. The force field f_z may, for example, be due to the electrostatic potential caused by the surface charge, which will be discussed later on. The Stokes equation in tangential direct reduces to

$$\eta \frac{\mathrm{d}^2 v_x}{\mathrm{d}z^2} = \frac{\mathrm{d}P}{\mathrm{d}x} - f_x. \tag{2.23}$$

An integration with stick boundary condition at the surface of the particle and a constant velocity $\mathbf{v}_\mathrm{B}$ beyond the boundary layer tangential to the surface leads to

$$v_\mathrm{B} = \frac{1}{\eta} \int_0^\lambda \mathrm{d}z\, z \left(f_x - \frac{\mathrm{d}P}{\mathrm{d}x} \right). \tag{2.24}$$

As the boundary layer is much smaller than the particle, $\mathbf{v}_\mathrm{B}$ appears as a quasi-slip flow on the surface. In the lab frame, the fluid velocity vanishes at large distances to the particle. According to the reciprocal theorem, the particle moves into the opposite direction as the averaged quasi-slip velocity, $\mathbf{u} = -\langle v_\mathrm{B} \mathbf{e}_x \rangle = -\langle v_\mathrm{B} \sin\theta \rangle$.[54, 102] As the slip flow varies as $v_\mathrm{B} = v_\mathrm{B}^\mathrm{max} \sin\theta$ along the surface of a spherical particle, where $v_\mathrm{B}^\mathrm{max}$ is the maximum occurring velocity in the case that $\mathbf{e}_x$ is parallel to the external perturbation, the velocity of a spherical particle is given by

$$u = -\frac{2}{3} v_\mathrm{B}^\mathrm{max}. \tag{2.25}$$

The velocity field beyond the boundary layer may be obtained by solving the force-free Stokes equation 2.3 with a slip flow at the particle's surface $v_\mathrm{B} = -\frac{3}{2} u \sin\theta$ and a vanishing flow at infinity. This leads to the following relation

$$\mathbf{v}(\mathbf{r}) = u \frac{a^3}{r^3} \left(\frac{1}{2} \sin\theta\, \mathbf{t} + \cos\theta\, \mathbf{n} \right), \tag{2.26}$$

with the normal and tangential unit vectors $\mathbf{n}$ and $\mathbf{t}$.[55] The velocity field due to the phoretic motion is short-ranged as it decays with the inverse distance cubed $\mathbf{v}(\mathbf{r}) \sim r^{-3}$ in comparison to the flow field generated by Stokes friction which decreases with the inverse distance $\mathbf{v}(\mathbf{r}) \sim r^{-1}$.

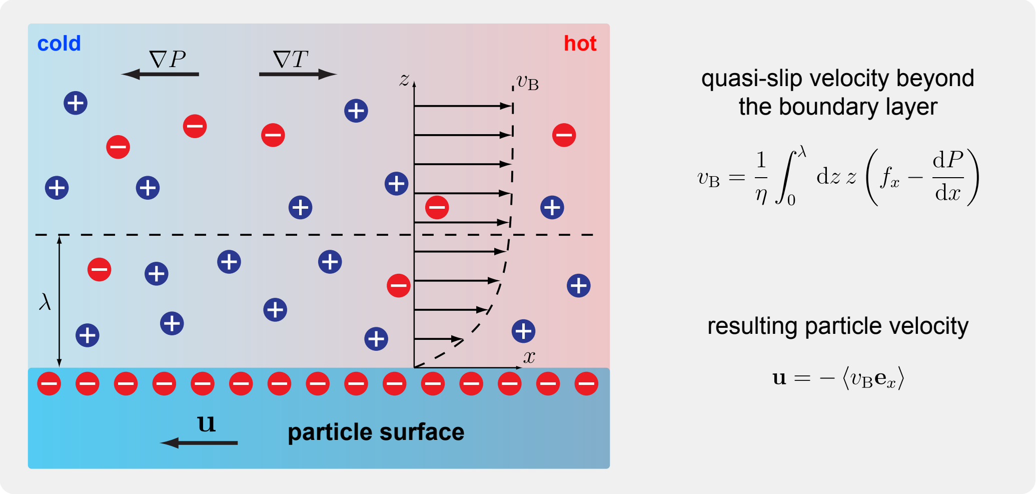

Figure 2.4: Schematic representation of the effects within the electric double layer: The particle's surface charge is shielded by counter ions. A temperature gradient leads to an osmotic pressure gradient. This drives a flow along the surface inducing quasi-slip boundary conditions (quasi-slip velocity v_B) at the particle's surface. As the velocity field needs to vanish at large distances, the particle is driven into the opposite direction at a velocity $\mathbf{u}$.

Thermophoresis of Charged Colloids In the following, a particle of radius R and surface charge density σ_c is assumed. The charge on the surface causes an electrostatic potential ϕ, which is screened by the counter-ions in the solvent resulting in a boundary layer of scale λ. With a bulk salinity of n_0, the excess ion densities of positive and negative ions are given by[56]

$$n_\pm = n_0 \left(\mathrm{e}^{\mp e\phi/k_\mathrm{B}T} - 1 \right). \tag{2.27}$$

The charge density in the boundary layer around the particle is then $\rho = e(n_+ + n_-)$ and the excess density of mobile ions is $n = n_+ - n_-$. In absence of an external perturbation, the shape of the boundary layer is isotropic. Application of an external field (*e.g.* an external electric field $\mathbf{E}_0$, an inhomogeneous temperature field T or a non-uniform concentration of ions n_0) breaks the spherical symmetry around the particle and leads to a non-vanishing force field within the solvent which appears in the Stokes Equation 2.23. The force field in the solvent has contributions from the divergence of the Maxwell tensor that is dependent on the electrostatic potential in the boundary layer as well as an external electric field coupling to the charge. The hydrostatic pressure $P = nk_\mathrm{B}T$, that is found by integration of Equation 2.22, strongly changes in normal direction due to the screening potential, but only weakly varies tangentially to the surface due to the external perturbations. Gathering all contributions to the force field and pressure gradient in the boundary layer yields the following equation[54–56]

$$\mathbf{f} - \nabla P = -(\rho\phi + nk_\mathrm{B}T)\frac{\nabla T}{T} - \frac{1}{2}E^2\nabla\varepsilon - nk_\mathrm{B}T\frac{\nabla n_0}{n_0} + \rho\mathbf{E}_0, \tag{2.28}$$

with ε being the permittivity of the solvent and $E = -|\nabla\phi|$. The force field thus dependents on the external electric field $\mathbf{E}_0$ and the gradients ∇T, $\nabla\varepsilon$ and ∇n_0, which are not independent of each other. For instance, applying a temperature gradient may induce gradients to the other parameters (companion fields), which ultimately influence the thermophoretic mobility.

The electrostatic potential ϕ of a charged particle may be calculated by the Poisson-Boltzmann equation in normal direction to the particles surface $\varepsilon\partial_z^2\phi = -\rho$ and takes the form

$$\phi(z) = \zeta \operatorname{artanh}\left(\mathrm{e}^{-z/\lambda}\right). \tag{2.29}$$

Herein, $\zeta = \frac{2k_\mathrm{B}T}{e}\operatorname{arsinh}(2\pi\sigma_\mathrm{c} l_\mathrm{B}\lambda)$ is the surface potential and $\lambda = (8\pi n_0 l_\mathrm{B})^{-\frac{1}{2}}$ the Debye and Bjerrum length $l_\mathrm{B} = e^2/4\pi\varepsilon k_\mathrm{B}T$. With the approximation, that the permittivity of the solvent is much higher than that of the particle, $\varepsilon_\mathrm{P} \ll \varepsilon_\mathrm{S}$, and that the thermal conductivities of the solvent and the particle are approximately equal, $\kappa_\mathrm{P} \approx \kappa_\mathrm{S}$, the particle velocity is obtained via Equations 2.24 and 2.24 by[54]

$$\mathbf{u} = -\frac{\varepsilon(\zeta^2 - 3\zeta_\mathrm{T}^2)}{3\eta}\frac{\nabla T}{T} + \frac{\varepsilon\zeta_\mathrm{T}^2}{3\eta}\left(\frac{\nabla\varepsilon}{\varepsilon} + \frac{\nabla n_0}{n_0}\right) + \frac{\varepsilon\zeta}{\eta}\mathbf{E}_0, \tag{2.30}$$

where $\zeta_\mathrm{T} = \left(\frac{2k_\mathrm{B}T}{e}\right)^2 2\ln\cosh\left(\frac{e\zeta}{4k_\mathrm{B}T}\right)$ is an abbreviation depending on the surface potential ζ. The first term being proportional to the temperature gradient originates from the anisotropy of the electric double layer. The gradient in the osmotic pressure and the electrostatic energy drives the solvent in the boundary layer to the hot region such that the particle is dragged to the cold. For highly charged particles, the term with $-3\zeta_\mathrm{T}^2$ may be neglected as $\zeta_\mathrm{T} \ll \zeta$. On the contrary, for weakly charged particles when the potential energy of the ions is smaller than the thermal energy $e\phi \ll k_\mathrm{B}T$ (Debye-Hückel approximation), ζ_T takes the value $\frac{1}{2}\zeta$. The second term of Equation 2.30 accounts for the permittivity gradient. As the permittivity is dependent on the temperature, a temperature field will lead to a permittivity landscape described by the relation

$$\frac{\nabla\varepsilon}{\varepsilon} = -\tau\frac{\nabla T}{T}. \tag{2.31}$$

In water, the coefficient $\tau \approx 1.4$ is positive resulting in a quasi-slip to the warm and a subsequent particle motion to cold regions.[54] The third term describes the effect arising from a salinity gradient. A lower ion concentration increases the surface potential and the Debye length, which in the end drives the particle towards higher salt concentrations. The last term describes the electrophoresis induced by the electric field $\mathbf{E}_0$. The effect of the temperature field on the distribution of the ions n_0 as well as the generation of a thermoelectric field is discussed in the following paragraph.

Thermoelectricity – Electrolyte Seebeck Effect Two significant contributions to the thermophoretic drift are caused by the movement of the ions within the solvent as a response to a temperature gradient. First, there is the overall motion that causes a concentration gradient of the ions. Then, the relative motion of positive and negative ions cause a thermoelectric field inducing electrophoretic motion. The latter effects shall be briefly discussed for a binary electrolyte of monovalent ions. The ion flux may be described as follows[54,56,58]

$$\mathbf{J}_\pm = -D_\pm\left(\nabla n_\pm + n_\pm\alpha_\pm\nabla T \mp n_\pm\frac{e\mathbf{E}_0}{k_\mathrm{B}T}\right). \tag{2.32}$$

The first term describes the gradient diffusion of the ions with the diffusion coefficient $D_\pm$. The second term is due to the thermophoretic motions of the ions, where $\alpha_\pm = \frac{Q_\pm^*}{2k_\mathrm{B}T} = TS_{\mathrm{T},\pm}$ is the reduced Soret coefficient of the ions that depends on the ionic heat of transport $Q_\pm^*$. Finally, the last term characterizes the response of the ions on an electric field $\mathbf{E}_0$.

Applying a temperature gradient, the stationary state of the sum of all ion fluxes $\mathbf{J} = \mathbf{J}_+ + \mathbf{J}_- = 0$ leads to

$$\frac{\nabla n_0}{n_0} = -\alpha \frac{\nabla T}{T}, \tag{2.33}$$

where $n_0 = \frac{1}{2}(n_+ + n_-)$ and $\alpha = \alpha_+ + \alpha_-$. As $\alpha > 0$ is positive, the ion concentration gradient leads to a flow of the particle to the cold, which is clear by plugging Equation 2.33 into Equation 2.30. The second effect is known as the electrolyte Seebeck effect. A different Soret coefficient for the different ions leads to a charge separation within the solvent giving rise to an electric field. Implying zero current in the solvent by setting $\mathbf{J}_+ = \mathbf{J}_-$ and using the fact that the solvent is neutral leads to the induced electric field $\mathbf{E} = S\nabla T$ with the Seebeck coefficient[54, 58]

$$S = \frac{k_\mathrm{B}}{e} \frac{\alpha_+ - \alpha_-}{2}. \tag{2.34}$$

From the last term in Equation 2.30 it is clear, that the induced electric field leads to an additional component of the thermophoretic mobility D_T. As an example, the Seebeck coefficient for NaCl takes the value $S_\mathrm{NaCl} \approx 50\,\mu\mathrm{V/K}$ whereas the coefficient for NaOH is $S_\mathrm{NaCl} \approx -210\,\mu\mathrm{V/K}$.[54] Depending on the strength of the other components in Equation 2.30, the electrolyte Seebeck effect may thus change the sign of the thermophoretic mobility D_T.

Diffusiophoresis Another contribution to thermophoresis may be driven by depletion forces leading to diffusiophoresis. Additional molecules, that could be polymers, or smaller colloids will lead to an excess pressure $P = k_\mathrm{B}T(c - c_0)$ in the boundary layer, where $c(x,z) = c_0(x)\mathrm{e}^{-U(z)/k_\mathrm{B}T}$ is the concentration profile on the surface of the particle. $U(z)$ describes the interaction potential of the particle with the dissolved molecules. Via Equation 2.24 one finds the quasi-slip velocity at the surface of the particle due to an external concentration gradient $\partial_x c_0$ of the additional molecules[54]

$$v_\mathrm{B} = -\frac{k_\mathrm{B}T}{\eta} \frac{\partial c_0}{\partial x} \int_0^\infty \mathrm{d}z\, z \left(\mathrm{e}^{-U(z)/k_\mathrm{B}T} - 1 \right). \tag{2.35}$$

Excluded volume effects described as a hard-core potential at radius R lead to a particle velocity $\mathbf{u} = -\frac{k_\mathrm{B}TR^2}{3\eta}\nabla c_0$. This model well-describes the thermophoresis of polystyrene beads in a solution of neutral polyethylene glycol (PEG) polymer chains.[103] Thermophoresis drives the polymers away from a heated spot hence reducing their local concentration as seen from Equation 2.33 with the Soret coefficient of PEG $S_\mathrm{T,PEG} = \alpha_\mathrm{PEG}/T \approx 0.056\,\mathrm{K}^{-1}$. Thus, for small amounts of PEG the Soret coefficient is decreased due to depletion forces. Increasing the PEG concentration further eventually leads to a change in the sign of S_T and the polystyrene beads accumulate in the heated region.

Dispersion Forces An additional contribution to the thermophoretic mobility arises from the inhomogeneous density profile of the solvent due to thermal expansion. Caused by the higher density, the solvent is stronger bound via van-der-Waals interactions to the particle at the cold side leading to a solvent flow along the particles surface. The particle in turn moves in the opposite direction (Reciprocal Theorem, see above). This contribution is typically expected to be low for charged polystyrene spheres in aqueous solution, however, may be significant for the thermophoresis of polymers.[54]

2.2.3 Thermodynamics Approach

Local Thermal Equilibrium As the thermophoretic depletion described by Equation 2.16 follows an exponential steady state probability distribution, the relation can be interpreted as a Boltzmann distribution. This may be understood by assuming local thermal equilibria that are connected by Brownian motion.[62] That means, that thermodynamically the local environment of the particle is isotropic. At weak gradients of order $\nabla T \sim 0.01\,\mathrm{K}/\mu\mathrm{m}$, typical Soret coefficients of $S_\mathrm{T} \sim 1\,\mathrm{K}^{-1}$ and particles of radius $\mathrm{a} \sim 0.1\,\mu\mathrm{m}$, the energy difference over the particle is $aS_\mathrm{T}\nabla T\,k_\mathrm{B}T \sim 0.01\,k_\mathrm{B}T$. However, on a larger scale, the chemical potential depends on temperature and thus on space.[104] Since temperature and concentration differences are small on the local scale, a linearized Boltzmann distribution is assumed with $\delta c/c = -\delta G/k_\mathrm{B}T$ and a comparison to the locally linearized thermophoresis $\delta c/c = -S_\mathrm{T}\delta T$ yields an expression for the Soret coefficient as a function of the particle's energy G (Gibbs free enthalpy)[59,62]

$$S_\mathrm{T} = \frac{1}{k_\mathrm{B}T}\frac{\partial G}{\partial T}. \tag{2.36}$$

Assuming a local equilibrium means that the particle samples the space by random Brownian motion, but prefers regions that are thermodynamically more stable. This assumption is only valid for weak temperature gradients, when the motion is governed by diffusion. This is measured by a Peclet number smaller than unity, $\mathrm{Pe} = av_\mathrm{T}/D = aS_\mathrm{T}\nabla T < 1$.[59,104]

The energy of a charged solute can be expressed on the basis of a simple capacitor model, where the thermophoresis is a result of the temperature-dependent energy stored within the Debye screening length. A simple description has been put forward by Duhr and Braun in 2006,[59] which has been refined later by Dhont et al[105] and very recently by Reichl et al.[57,58] The energy stored in the shielding by the counter ions is given by $W = \frac{Q_\mathrm{eff}^2}{8\pi\varepsilon R}(R/\lambda + 1)$, with R the hydrodynamic radius of the particle or molecule.[58] By normalizing S_T with Z_eff^2/R and λ to the hydrodynamic radius R, a master curve (Equation 2.37) is obtained that is independent of the particular parameters of the molecule.

$$S_\mathrm{T}\frac{R}{Z_\mathrm{eff}^2} = \frac{e^2R/\lambda}{16\pi k_\mathrm{B}T^2\varepsilon_r\varepsilon_0(1+R/\lambda)^2}\left(1 - \frac{\partial\ln\rho(t)}{\partial\ln T} - \frac{\partial\ln\varepsilon_r(t)}{\partial\ln T}\left(1+\frac{2\lambda}{R}\right)\right) \tag{2.37}$$

Assuming a small Debye length compared to the particles hydrodynamic radius $\lambda \ll R$ simplifies Equation 2.37 to

$$S_\mathrm{T} = \frac{Q_\mathrm{eff}^2\lambda}{16\pi k_\mathrm{B}T^2\varepsilon\varepsilon_0R^2}\left(1 - \frac{\partial\ln\rho(t)}{\partial\ln T} - \frac{\partial\ln\varepsilon_r(t)}{\partial\ln T}\right). \tag{2.38}$$

Herein, $Q_\mathrm{eff} \propto R^2$ resembles the particle's effective surface charge which scales with the particle's surface area. Therefore, according to Equation 2.38, the Soret coefficient $S_\mathrm{T} \propto R^2$ grows with the surface as well. As the diffusion coefficient scales as the inverse radius, the thermophoretic mobility $D_\mathrm{T} \propto R$ increases linearly with the particle size. This is in direct contrast to the hydrodynamic approach, where the mobility is caused by a slip flow on the particle's surface. The particle mobility is connected to the slip flow by the reciprocal theorem and hence must not depend on the particle size but only on the length scale λ that describes the interaction with the fluid. Both dependencies have been seen experimentally,[59,60] leading to an ongoing debate in literature.[53,54,57–61,106]

Ideal Gas Term In a dilute system, non-interacting particles in the solvent can be seen as an ideal gas with osmotic pressure $\Pi = -nk_\mathrm{B}T$.[55,105,107] A pressure gradient due to an inhomogeneous temperature hence will lead to a particle flux $\mathbf{j} = -\mu\nabla\Pi = -\mu n k_\mathrm{B}\nabla T$, with $\mu = 1/\gamma$ being the mobility of the particle. A comparison to the definition of the thermophoretic flux $\mathbf{j} = -nD_\mathrm{T}\nabla T$ yields a thermophoretic mobility of $D_\mathrm{T} = \mu k_\mathrm{B}$ and hence with the diffusion coefficient $D = \mu k_\mathrm{B} T$ a Soret coefficient of

$$S_\mathrm{T} = \frac{1}{T}. \tag{2.39}$$

At room temperature, this contribution takes the value of $S_\mathrm{T} \approx 0.003\,\mathrm{K}^{-1}$ and always leads to a migration of particles to the cold regions. It is typically much smaller than, for example, ionic contributions due to the boundary layer interactions, such that the ideal gas term is typically neglected.

2.2.4 Temperature Dependence

The Soret coefficient shows a strong temperature dependence. Often, the sign of S_T changes by simply decreasing the average temperature, such that the thermophobic behavior becomes thermophilic. This effect has been shown in a broad range of experimental parameters such as pH and ionic strength.[67] The switching sign is typically observed in the temperature range from 5° to 30°. For a wide ensemble of experimental systems, an universal temperature dependence for S_T is found with

$$S_\mathrm{T} = S_\mathrm{T}^\infty \left[1 - \exp\left(\frac{T^* - T}{T_0}\right)\right], \tag{2.40}$$

where S_T^∞ describes the thermophobic Soret coefficient at high temperatures, T^* the temperature where the sign changes and T_0 the exponential growth. The latter empirical formula has been experimentally shown to describe the temperature dependence of the Soret effect of proteins,[66,106] DNA,[57,67] polystyrene beads of various sizes[60,67] and micelles.[67] Although or even caused by the universal applicability of Equation 2.40, its physical origin is still unclear. Depending on the particular system, different contributions are discussed in the literature, such as for instance the temperature dependence of the thermoelectric effect,[54] the viscosity (which is however not able to switch the sign of S_T) and thermal expansion.[53,67]

2.2.5 Thermophoresis of Polymers

Thermophoresis of polymers is a widely studied field and has been reported on all kinds of polymer systems, such as synthetic polymers and biopolymers, like DNA or proteins. For many systems of dilute polymers, *e.g.* in non-aqueous solvents, it has been experimentally observed that the thermophoretic mobility rises with increasing molecular weight, however, eventually reaches a maximum D_T^∞ and is constant for high polymers.[72,108–110] This observation is typically explained by the fact, that hydrodynamic interactions of the segments cancel within the polymer chain.[111] The velocity of segment i is given by[107]

$$\mathbf{u}_i = \mathbf{u}_0 + \sum_{k \neq i} \mathbf{v}\left(\mathbf{r}_i - \mathbf{r}_k\right). \tag{2.41}$$

Herein, $\mathbf{u}_0$ is the thermal drift velocity induced by the external temperature gradient and $\mathbf{v}(\mathbf{r})$ the short-ranged flow field induced by a particle due to the phoretic drift u given by Equation 2.26. The shear resulting from $\mathbf{v}(\mathbf{r}_i - \mathbf{r}_k)$ is weak enough to not affect the statistical properties of the polymer chain significantly, high velocity fields are only found within the boundary layer of each segment. Also, the orientational average over the flow field $\langle \mathbf{v}(\mathbf{r}) \rangle_\theta = 0$ at a given radius r vanishes. Hence, for high polymers, where the number of segments is large, the second term in Equation 2.41, which reflects the hydrodynamic interactions of the segments, disappears and the mean velocity of segment i equals the induced thermophoretic velocity of the segment, $\langle \mathbf{u}_i \rangle = \mathbf{u}_0 = -D_\mathrm{T} \nabla T$. That means, the entire polymer drifts at $\mathbf{u}_0$ independently from its length. The scaling of the Soret coefficient with the hydrodynamic radius $S_\mathrm{T} = D_\mathrm{T}/D \propto R_\mathrm{h}$ results from the size dependence of the diffusion coefficient $D \propto R_\mathrm{h}^{-1}$. Recently, it has been shown, that assuming a draining of the coil without interactions of the individual segments is not necessarily needed to explain the constant D_T of high polymers over the molecular weight.[112] Alternatively, a non-draining core of the coil may experience a tangential stress within a draining layer of the polymer coil due to the mechanisms explained above.

Experiments on the thermophoresis of biopolymers has been extensively conducted in the group of Dieter Braun.[57–59,63,64,77,78,113,114] A study of long DNA strands showed that the above observation of constant D_T does not hold for DNA in aqueous buffer solutions.[59] Within the DNA, a long-ranged shielding couples the monomers and the independence of D_T over the chain length is not seen experimentally. Instead, short DNA molecules actually experience a larger thermal drift. The experimental trend is well fitted by the capacitor model on basis of local thermal equilibrium. According to this model, the Soret coefficient scales as $S_\mathrm{T} \propto Q_\mathrm{eff}^2/R_\mathrm{h}^2 \propto L^{0.5}$ as the hydrodynamic radius relates to the length of the DNA via $R_\mathrm{h} \propto L^{0.75}$ and accordingly $D_\mathrm{T} = DS_\mathrm{T} \propto L^{-0.25}$.

2.3 Interaction of Metal Nanostructures with Light – Optical Heating

When light interacts with a microscopic structure, the electromagnetic energy can be redistributed or absorbed. While typically for glass or polymer particles the absorption is neglected in the visible range, both effects are significant for metal nanostructures. For the case that the structure is smaller than the dimension of the light beam, it is convenient to introduce scattering and absorption cross sections by dividing the scattered and absorbed optical power by the incident intensity $I_0 = \frac{cn\varepsilon_0}{2} |\mathbf{E}_0|^2$, $\sigma_{\mathrm{sca}} = W_{\mathrm{sca}}/I_0$ and $\sigma_{\mathrm{abs}} = W_{\mathrm{abs}}/I_0$. Herein, $\mathbf{E}_0$ denotes the incident electric field amplitude of an electromagnetic plane wave. In the case of a light beam illuminating a gold film, the latter cross sections are inappropriate to describe the light-metal interaction. Rather, absorption A, reflection R and transmission T are introduced with the ratios of absorbed, reflected and transmitted intensity to the incident intensity. These normalized quantities are unit-less and obey

$$R + T + A = 1. \tag{2.42}$$

In the following, a short overview of the surface plasmon polarization is given. Then, Fresnels equations are used to calculate the absorption, reflection and transmission for a thin gold film. Finally, the work-flow to derive the absorption of a arbitrarily shaped metal-structure is briefly discussed.

2.3.1 Surface Plasmon Polarization

Metal structures are typically used as microscopic heat sources due to their electronic properties, which allows to couple optical energy W_{abs} to the electrons. Most of the energy is dissipated to heat $Q \approx W_{\mathrm{abs}}$ as the quantum yield is typically negligible.

Metals provide free conduction electrons, which are able to oscillate collectively at the interface between a negative and positive permittivity material, *i.e.* a metal and a dielectric, in a resonant manner. This effect is known as the Surface Plasmon Resonance (SPR) and will be briefly introduced in the following. For that, two semi-infinite non-magnetic media are considered, one is a dielectric (typically water) while the other is a metal (gold). The x axis is chosen along the metal surface and the z axis stands perpendicular on the interface (see Figure 2.5 A). The plasmonic electric field can be written as an evanescent wave propagating along the metal surface,[115]

$$E_j = E_0 \, \mathrm{e}^{-\kappa_i |z|} \exp(i\omega t - ik_x x). \tag{2.43}$$

The plasmon oscillation is characterized by its dispersion relation, *i.e.* the relation between the wave vector k_x and angular frequency ω. Via matching boundary conditions, the electric and magnetic field components parallel to the interface need to be continuous,[116] the dispersion relation is found with

$$k_x = \frac{\omega}{c} \sqrt{\frac{\varepsilon_{\mathrm{m}} \varepsilon_{\mathrm{Au}}}{\varepsilon_{\mathrm{m}} + \varepsilon_{\mathrm{Au}}}}, \tag{2.44}$$

where ω/c represents the vacuum light wave vector. The indexes of the dielectric constants $j = \mathrm{m}$ stands for the medium, such as water or glass, and $j = \mathrm{Au}$ for the metal being gold.

The free conduction electrons within the metal may be described by the Drude-Lorentz-Sommerfeld (DLS) model, which assumes that all free electrons react in phase to an external perturbation of an electromagnetic wave. The DLS model yields an approximation of the complex dielectric function $\varepsilon_{\mathrm{Au}} = \varepsilon_{\mathrm{Re}} + i\varepsilon_{\mathrm{Im}}$ with[117]

$$\varepsilon_{\mathrm{Re}} = 1 - \frac{\omega_{\mathrm{p}}^2}{\omega^2}, \quad \varepsilon_{\mathrm{Im}} = 1 - \frac{\omega_{\mathrm{p}}^2}{\omega^3}\Gamma, \tag{2.45}$$

where Γ is a phenomenological damping constant of the free electrons in the metal. Obviously, the real part of $\varepsilon_{\mathrm{Au}}$ appears to be negative for $\omega < \omega_{\mathrm{p}} = \sqrt{4\pi n_e e^2/m_e}$. Herein, ω_{p} denotes the plasma frequency, n_e the free electron density and m_e the electron mass.

Combining Equation 2.45 with 2.44, Figure 2.5 B plots the dispersion relation of the plasmon wave together with that of light being $\omega = ck$ (gray line). While the blue line represents the dispersion relation of light in the bulk metal, the red curve relates to the dispersion relation of the surface plasmons. At small k vectors it exhibits the same slope as the dispersion relation of light, but converges for large k vectors and for $\varepsilon_{\mathrm{m}} \approx 1$ to the surface plasmon frequency

$$\omega_{\mathrm{sp}} = \omega_{\mathrm{p}}/\sqrt{2} \tag{2.46}$$

at the resonance, where $\varepsilon_{\mathrm{m}} + \varepsilon_{\mathrm{Au}}$ takes a minimum. This condition is fulfilled when the dielectric function of the medium and the real part of the gold match as $\varepsilon_{\mathrm{m}} + \varepsilon_{\mathrm{Re}} = 0$.

Due to the evanescent nature of the plasmonic wave for $\omega < \omega_{\mathrm{sp}}$, no electromagnetic field can propagate within the metal, but only along the surface (x direction). The length scale κ_j on which the electric field decays, called penetration or skin depth, is given by

$$\kappa_j = \frac{\omega}{c}\sqrt{\frac{-\varepsilon_j^2}{\varepsilon_{\mathrm{m}} + \varepsilon_{\mathrm{Au}}}}. \tag{2.47}$$

For example, at $\lambda = 700\,\mathrm{nm}$ wavelength, a skin depth in gold ($\varepsilon_{\mathrm{Re}} \approx -16$) is found with $\kappa_{\mathrm{Au}} = 26\,\mathrm{nm}$ and in water ($\varepsilon_{\mathrm{m}} \approx 1.77$) with $\kappa_{\mathrm{m}} = 238\,\mathrm{nm}$.[115]

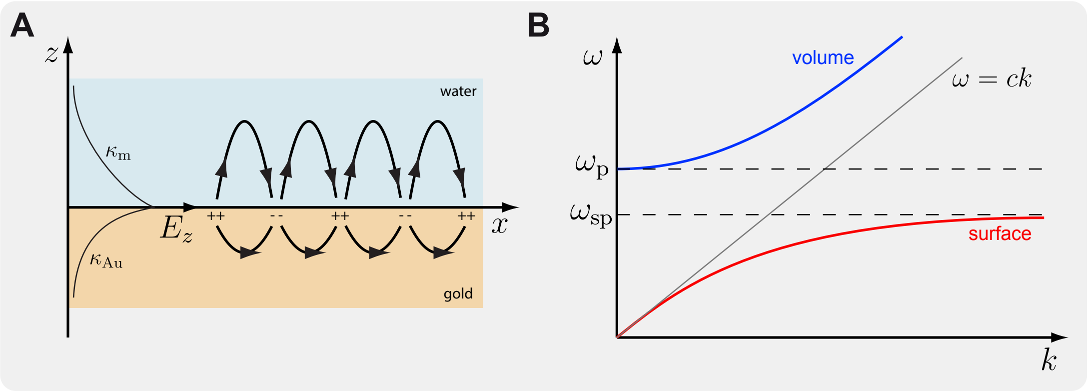

Figure 2.5: **A** Schematic illustration of the evanescent electric field of the surface plasmon at a metal-dielectric interface, which only propagates in x direction, but exponentially decays in z direction. **B** Dispersion relation of the light in the metal (blue) and that of the surface plasmon polarization (red) according to Equation 2.44 combined with 2.45. The diagonal gray line represents the dispersion relation of light, which is approached by the surface plasmon line for small k values. For large k values, the surface plasmon line converges to the surface resonant frequency ω_{sp}.

Note, that the surface plasmon curve is always beneath the light curve without an intersection, such that the k vectors do not match. That means that the optical excitation of surface plasmons is not trivial. Nevertheless, there are several mechanisms that assist external radiation to couple to surface-plasmon polaritons. One way is to use a periodic structure on the gold surface (grating) or the surface roughness to scatter the incident light,[118] which may provide the required k vector via *umklapp* processes.[119] Most popular is the excitation via attenuated total reflection (ATR, also called Kretschmann configuration),[120, 121] where a second interface is introduced, such that the former gold half space reduces to a thin layer between two dielectric media with $\varepsilon_{\mathrm{m1}} > \varepsilon_{\mathrm{m2}}$. This results in two dispersion relations for each gold-dielectric interface. Now, the normal light relation in medium 1 intersects the surface plasmon dispersion relation of gold-medium 2 interface, where thus plasmons can be excited by an appropriate adjustment of the k vector (typically by the incident angle) of the incoming light. A description using Fresnel's equations is presented in the next section. ATR has become the standard method in surface plasmon assisted spectroscopy, where, based on the strong sensitivity on the surrounding dielectric, the plasmon resonance is used as a sensor for changes in the dielectic constant. Due to the optical properties of the evanescent plasmonic wave, the sensor is sensitive to the dielectric constant only within a thin layer above the gold film. Hence, changes in the adsorption characteristics of molecules altering the dielectric constant of the solvent ε at the gold-water interface may be detected.[122, 123]

2.3.2 Absorption by a Thin Metal Film

In the following, thin film optics on the basis of Fresnel's equations is used to calculate the absorption A, reflection R and transmission T of a thin metal film. It shall be considered that a plane wave of amplitude E_{i} is incident from bulk medium 1 and hits a gold film (medium 2) of thickness d under an angle θ_1. Part of the wave is reflected described by $r_{12} = E_{\mathrm{r}}/E_{\mathrm{i}}$. Another part is refracted into the gold film, $t_{12} = E_{\mathrm{t}}/E_{\mathrm{i}}$, changing the angle of propagation according to Snells law, $n_1 \sin\theta_1 = n_2 \sin\theta_2$. The situation is illustrated in Figure 2.6. The Fresnel coefficients are given by[124]

$$t_{12} = \frac{2n_1 \cos\theta_1}{n_2 \cos\theta_1 + n_1 \cos\theta_2} \quad \text{and} \quad r_{12} = \frac{n_2 \cos\theta_1 - n_1 \cos\theta_2}{n_2 \cos\theta_1 + n_1 \cos\theta_2}. \tag{2.48}$$

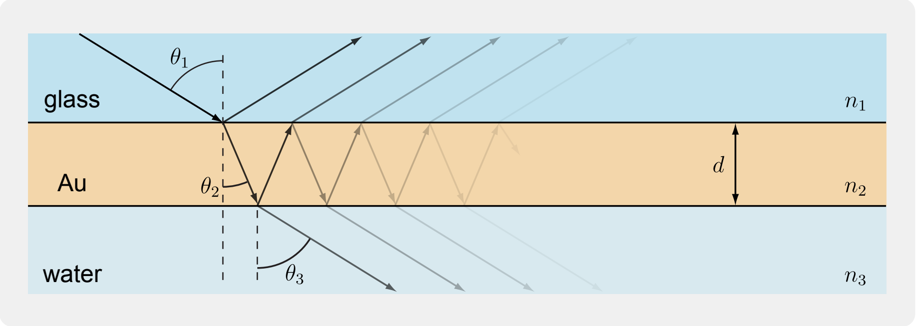

Figure 2.6: Propagation of light (incident angle θ_1) through a thin metal film of thicknes d and complex refractive index n_2 surrounded by two dielectric media (n_1 and n_3) causing reflection and transmission.

Here, only the polarization parallel to the incident plane (TM or p polarization) in considered, as this is the orientation that is able to excite plasmon oscillations. The second interface between gold and a bulk medium 3 leads to an additional reflection and transmission described by r_{23} and t_{23} analog to Equations 2.48. This leads to multiple reflections within the thin film of gold. The total transmission and reflection is described by a series of reflection and transmission coefficients that converges to[124, 125]

$$t = \frac{t_{12} t_{23} e^{i\beta}}{1 + r_{12} r_{23} e^{2i\beta}} \quad \text{and} \quad r = \frac{r_{12} + r_{23} e^{2i\beta}}{1 + r_{12} r_{23} e^{2i\beta}}. \tag{2.49}$$

The parameter $\beta = \frac{2\pi}{\lambda_0} n_2 d \cos\theta_2$ accounts for the phase of the light due to the path difference of two neighboring interfering beams in the gold film.[126] Note, that the gold film shows a complex index of refraction n_2 leading to a non-zero absorption. The transmission and reflection of intensity is then found from the amplitude coefficients via

$$T = \frac{n_3 \cos\theta_3}{n_1 \cos\theta_1} |t|^2 \quad \text{and} \quad R = |r|^2. \tag{2.50}$$

The prefactor for the transmission appears due to energy conservation during refractions of the light. Absorption is calculated via Equation 2.42. The absorption, reflection and transmission is shown in Figure 2.7 for medium 1 being glass of refractive index $n_1 = 1.5$ next to a gold film of thickness $d = 50\,\text{nm}$ and air ($n_3 = 1.0$, A) or water ($n_3 = 1.33$, B) as medium 3. The vacuum wavelength of the incident light is assumed with $\lambda_0 = 532\,\text{nm}$. The case of air shall be discussed first. The dependence of R, A and T on the incident angle is essentially flat until the total reflection internal angle (TR) is reached, where the transmission drops to zero. Accordingly, the reflectance shows a jump as well. Increasing the incident angle further, leads to an abrupt decrease in reflectance that goes along with a resonance in absorption at about $\theta_{SP}^{air} = 48°$. At that angle, surface plasmons are excited by attenuated total reflection as explained in the last Section 2.3.1. An oil immersion objective lens with a numerical aperture of NA $= 1.35$ provides a maximum incidence angle of about $\theta_{NA} \approx 64°$ (O), such that the plasmon resonance could be excited by a focused laser beam. Calculating the same spectra for water as the third medium, one recognizes that the distinct resonance flattens to a shallow maximum at $\theta_{SP}^{water} = 78°$, which is beyond θ_{NA} and can thus not be excited. The shallow resonance is caused by the higher refractive index of water, which is much closer to that of glass compared to the low reflective index of air. Nevertheless, the high absorbence of about 35% over the entire angular spectrum resulting from the high imaginary part of n_2 ensures the potential of the gold film as an efficient heat source, even for the case that no SPR can be excited.

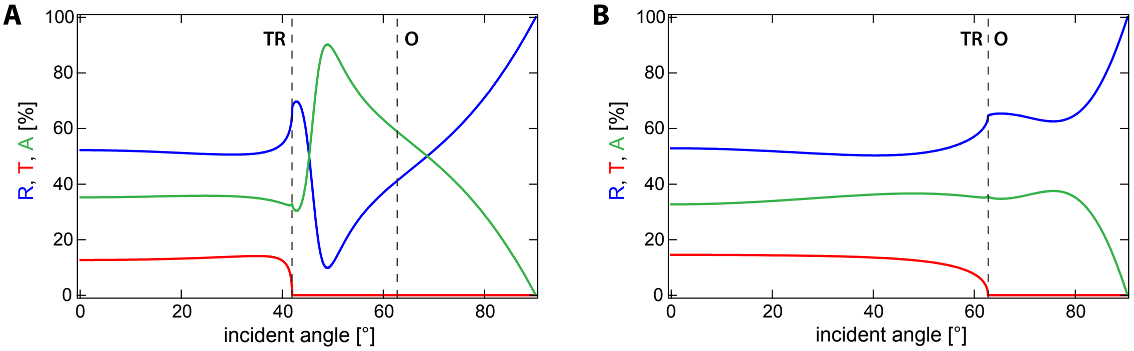

Figure 2.7: A Absorption A, reflection R and transmission T of $\lambda_0 = 532\,\text{nm}$ light incident on a gold film of $d = 50\,\text{nm}$ thickness from glass ($n_1 = 1.5$). The third medium is air with $n_3 = 1.0$. The complex refractive index of gold n_2 is calculated from the dielectric data of gold by Johnson and Christy.[127] The total internal reflection angle is marked with 'TR' and the maximum incident angle that can be provided by a NA $= 1.35$ objective lens with 'O'. **B** Same for water as the third medium with $n_3 = 1.33$.

2.3.3 Absorption by an Arbitrary Metal Structure

For metal structures of sizes that compare to the wavelength of the light, the interaction cross sections can be calculated analytically for a collection of simple shapes including spheres,[117,128] layered spherical[129] or rod-like particles.[128] The absorption properties as well as local field enhancement may be tuned by optimizing the shape of the gold structure often leading to a complex morphology, such as gold shells, bow-tie antennas, star-like particles or nano-cages.[130–133] Independently from the particular morphology, the heat generation in general relates to the Joule effect and is a result of resistive losses. The heat power density $q(\mathbf{r})$ is accordingly given by[85,134]

$$q(\mathbf{r}) = \frac{1}{2}\mathrm{Re}\left[\mathbf{J}^{*}(\mathbf{r})\cdot\mathbf{E}(\mathbf{r})\right]. \tag{2.51}$$

The electronic current density $\mathbf{J}$ may be expressed as the time-derivative of the dielectric polarization density $\mathbf{J} = \partial_t \mathbf{P} = i\omega\mathbf{P}$, with $\mathbf{P} = \varepsilon_0\varepsilon(\omega)\mathbf{E}$. The current density is therefore directly related to the electric field amplitude, such that the heat power density takes to following form

$$q(\mathbf{r}) = \frac{\omega}{2}\varepsilon_0 \mathrm{Im}\left[\varepsilon(\omega)\right]\left|\mathbf{E}(\mathbf{r})\right|^2. \tag{2.52}$$

The overall heat power is calculated via an integration over the metal particles volume, $Q = \int_{\mathrm{NP}} q(\mathbf{r})\mathrm{d}^3 r$. As the heating power is proportional to the intensity of the illuminating wave, $I_0 = \frac{cn\varepsilon_0}{2}\left|\mathbf{E}_0\right|^2$, the absorption cross section $\sigma_{\mathrm{abs}} = Q/I$ is typically used as a particle parameter. The calculation of the amount of heat that is generated by an arbitrary metal structure hence boils down to a calculation of the electric field amplitude within the structure. For that purpose, different numerical methods such as the boundary element method (BEM),[135] the discrete dipole approximation (DDA)[136] or finite difference time domain method (FDTD)[137] have been developed. An overview can be found in the review article of Myroshnychenko *et al.*[138]

2.4 Temperature Distribution Around a Heat Source

The last section treated the generation of heat within metal nano-structures. Such structures are typically embedded in a medium like water, glass or a polymer. The thermal energy that is released by the nanoscopic heat source is thus distributed in the surrounding leading to a specific temperature profile. From the mathematical point of view, the problem of heat diffusion is equivalent to particle diffusion discussed before. The Fokker-Planck equation of Section 2.1.2 may thus be rewritten in the heat diffusion language to calculate temperature profiles instead of concentration or probability density profiles. In the case of water being a liquid, advection due to buoyancy may also be considered to contribute to the heat transport. However, the thin height of the water films used in the experiments prevent buoyancy to play a dominant role.[139] Radiative heat transfer may be also neglected, as a simple estimation shows. Using the Stefan-Boltzmann law, a 100 nm-diameter gold particle heated to about 5 K surface temperature elevation releases its energy by radiation only by a fraction of about $P_{\mathrm{rad}}/P_{\mathrm{abs}} \sim 10^{-6}$. In the following it shall be therefore concentrated on the establishment of temperature profiles via diffusive heat conduction.

2.4.1 Fouriers Law and Heat Equation

The amount of energy or heat that is stored in a particular temperature distribution $T(\mathbf{r},t)$ is given by $u_{\mathrm{th}}(\mathbf{r},t) = \rho c_p T(\mathbf{r},t)$, with ρ and c_p being the mass density and the specific heat capacity of the medium at constant pressure. According to Fourier's law, any gradient in the temperature profile will lead to a flow of thermal energy $\mathbf{j}_{\mathrm{th}}(\mathbf{r},t) = -\kappa \nabla T(\mathbf{r},t)$ proportional to the thermal conductivity κ. The governing equation of heat conduction, the so-called heat equation, directly follows from conservation of energy described with the continuity equation $\partial_t u_{\mathrm{th}}(\mathbf{r},t) + \nabla \cdot \mathbf{j}_{\mathrm{th}}(\mathbf{r},t) = q(\mathbf{r},t)$,[140]

$$\rho c_p \frac{\partial T(\mathbf{r},t)}{\partial t} = \kappa \nabla^2 T(\mathbf{r},t) + q(\mathbf{r},t). \tag{2.53}$$

The source term $q(\mathbf{r},t)$ accounts for the thermal energy provided per volume and time, *i.e.* is a heating power density and may depend on space and time. In particular, $q(\mathbf{r},t)$ represents the thermal coupling to the optically absorbed power described by Equation 2.52. To represent the diffusive nature of heat conduction, the material coefficients κ, ρ and c_p are conveniently combined to the thermal diffusivity $\lambda = \kappa/\rho c_p$, which shares the unit $\mu\mathrm{m}^2/\mathrm{s}$ with the mass diffusion coefficient.

The analogy to mass diffusion (see Equation 2.14) also directly delivers the solution of Equation 2.53 for the evolution of the temperature when the source term is given by $q(\mathbf{r},t) = E_{\mathrm{th}}\delta(\mathbf{r})\delta(t)$, that means the case of a point-like particle at the origin that releases the thermal energy E_{th} at $t = 0$ with $r \equiv |\mathbf{r}|$,[141]

$$T(r,t) = \frac{E_{\mathrm{th}}}{\rho c_p} \frac{1}{(4\pi\lambda t)^{3/2}} \exp\left(-\frac{r^2}{4\pi\lambda t}\right) + T_0. \tag{2.54}$$

As a particle's probability density for mass diffusion (Equation 2.14), the heat that is concentrated in the beginning at the origin exhibits a Gaussian shape at time t and spreads with time. The thermal diffusivity λ gives rise to a characteristic relaxation time, that is discussed in detail in Section 2.4.3.

2.4.2 Steady-State Temperature Profiles

Point Heat Source On the length scale of nanometers, the relaxation of the heat is typically fast (see discussion Section 2.4.3), such that after switching on a steady heat source, the system rapidly converges to its steady-state. Disregarding the time-dependence, Equation 2.53 simplifies to the Poisson equation or steady-state heat equation

$$\kappa\nabla^2 T(\mathbf{r}) = -q(\mathbf{r}). \tag{2.55}$$

The source term is considered with a point heat source embedded in an infinite bulk medium and releases a constant amount of energy per time, $q(\mathbf{r}) = Q\delta(\mathbf{r})$. At infinity, the temperature field has to match the ambient temperature T_0. The according solution of the Poisson equation is well-known from electrostatics text books and is given with a one over distance temperature profile $T(r) = Q/4\pi\kappa r + T_0$.[142] Note, that while a pulsed heating leads to an exponential decay of the temperature profile (Equation 2.54), even the smallest steady heat source induces a long-ranged temperature profile lacking an intrinsic length scale due to the weak algebraic decay of $\sim r^{-1}$. Also, while the temporal evolution of the temperature field is described by the thermal diffusivity λ, the decay of the steady-state temperature profile solely depends on the thermal conductivity κ. Solutions of Equation 2.55 are also known for the special cases that the heat source is embedded in a semi-infinite medium with a boundary to a second medium of different thermal conductivity[143] or placed within an thin slab of a medium in between two different adjacent media.[144] In both cases, the temperature field is not significantly altered as compared to the infinite bulk in the close proximity of the heat source, but is distorted close to the boundaries.[145]

Spherical Particles In reality, even the small plasmonic heat sources exhibit finite sizes. The prototype heat source for many theoretical as well as experimental considerations is the spherical particle embedded in a bulk medium, which keeps its symmetry in the generated temperature field. Assuming a spherical gold particle of radius R_{NP} and thermal conductivity κ_{Au} constantly releasing heat at a rate $Q = q\frac{4}{3}\pi R_{\mathrm{NP}}^3 = \sigma_{\mathrm{abs}} I_0$ embedded in a medium of κ_{w} being typically water, the temperature field is described by the following set of differential equations

$$\kappa_{\mathrm{Au}}\nabla^2 T(r) = -q \quad \text{for} \quad r < R_{\mathrm{NP}}, \tag{2.56}$$

$$\kappa_{\mathrm{w}}\nabla^2 T(r) = 0 \quad \text{for} \quad r > R_{\mathrm{NP}}. \tag{2.57}$$

The latter equation system is solved by the following expression[143]

$$T(r) = \frac{\Delta T_{\mathrm{surf}} R_{\mathrm{NP}}}{r} + T_0, \tag{2.58}$$

wherein $\Delta T_{\mathrm{surf}} = Q/4\pi\kappa_{\mathrm{W}} R_{\mathrm{NP}}$ denotes the surface temperature of the sphere. Outside the particle, the temperature profile exhibits the same shape as the point heat source truncated at the particle's radius. The inner of the particle is practically isothermal due to the high thermal conductivity of gold ($\kappa_{\mathrm{Au}} \ll \kappa_{\mathrm{w}}$). For the case that the particle-medium interface exhibits a finite surface conductivity g which cannot be neglected, the inner of the sphere is hotter than the particle's (outer) surface by the factor $(1+\lambda_{\mathrm{K}})$, where $\lambda_{\mathrm{K}} = \kappa_{\mathrm{w}}/(gR_{\mathrm{NP}})$ is a dimensionless parameter quantifying the Kapitza resistivity $1/g$.[141] The shape of the temperature field outside the particle, however, remains unaffected by g.

Arbitrary Heat Source Despite the simplicity of the Poisson equation, the calculation of the temperature distribution around an arbitrarily shaped particle of known heat source density is not trivial. An analytical approach utilizes the Greens function of Equation 2.55 given by $G(\mathbf{r},\mathbf{r}_i) = 1/4\pi\kappa|\mathbf{r}-\mathbf{r}_i|$. Consider a gold structure consisting of single well-separated gold nano-particles, each releasing a heating power Q_i. Utilizing the linearity of the Poisson equation, the temperature profile is described by[134]

$$T(\mathbf{r}) = \sum_i G(\mathbf{r},\mathbf{r}_i)\,Q_i. \tag{2.59}$$

The temperature of each individual particle is accordingly given by $T(\mathbf{r}_i) = \sum_j G(\mathbf{r}_i,\mathbf{r}_j)\,Q_j$. The attempt of modeling the transition from discrete heat sources to an arbitrary continuous heat source $q(\mathbf{r})$ by replacing the sum in Equation 2.59 by an integral such that the temperature profile would be given by $\Delta T(\mathbf{r}) = \int_{V_{\mathrm{NP}}} G(\mathbf{r},\mathbf{r}')\,q(\mathbf{r}')\,\mathrm{d}^3r'$ fails. The reason for that is the higher thermal conductivity of the gold as compared to the medium, which tends to smoothen the temperature distribution within the gold structure. This is not taken into account with the simple Greens function approach, which, however, can be modified by calculating a fictive heat source density that induces a uniform temperature over the metal structures volume.[134]

In practice, the heat equation 2.53 in its time-dependent form, but also the Poisson equation 2.55, in which the dynamics has been dropped, are often solved by numerical means. Particularly finite element methods (FEM) are widely applied. FEM solve the partial differential equations for given (possibly complex) boundary conditions by dividing the whole problem space in subdomains, called finite elements. Readily compiled software packages, such as COMSOL Multiphysics including advanced add-ons like the heat-transfer module, provide a versatile toolbox with elaborate functionality far beyond the heat equation. After modeling the problem in terms of its geometry, constraints and boundary conditions are set. To gather the shape of the temperature field, typically, the temperature along a surface A (surface of heated gold structure or boundaries with ambient temperature) is set $T(r,t)|_A = T_A(r,t)$. These are called Dirichlet boundary condition. Alternatively, a source term $q_V(r,t) = (\kappa\partial_n T)|_V$ can be directly set describing the heat that enters the system (von-Neumann boundary condition).

2.4.3 Time Scales of Relaxation

The relaxation cascade of optically excited gold structures consist of three steps.[130, 146] Oscillations of the free electrons are excited by the incident light. The first step is the thermalization of the free electron gas which happens on a time scale of 100 fs[141, 147] and increases the electronic temperature, while the photonic temperature is still in equilibrium with the surrounding. In a second step, the absorbed energy is transfered to the lattice via electron-phonon interactions. After a time scale of about 2 ps, the electronic system is in equilibrium with the lattice of metal ions.[148] Still, the energy is not yet released to the surrounding. The latter time scales are only dependent on the material but hardly depend on shape of the metal structure. In a third step, the heat is conducted to the surrounding media by thermal diffusion. This process is described by Equation 2.53 and thus dependent on the length scale of the system. A dimensional analysis yields a typical time scale of the thermal relaxation of $\tau_{\mathrm{th}} = \frac{\rho c}{\kappa}L^2 = \frac{L^2}{\lambda}$. As the thermal diffusivity of gold is about three orders of magnitude higher than that of water ($\lambda_{\mathrm{Au}} = 127\cdot 10^{-6}\,\mathrm{m^2/s}$ vs. $\lambda_{\mathrm{water}} = 0.143\cdot 10^{-6}\,\mathrm{m^2/s}$),[141] the relaxation is faster in the gold by the same factor. In terms of fast heat release, the limit is thus given by the surrounding medium, *i.e.* typically water or glass. As can be seen from Equation 2.58, the temperature field decays over the length scale comparable to the size of the heat source. Small structures of less than 100 nm, hence, establish their temperature field in less than 100 ns and may be assumed as instantaneous compared to the experimental time scales relevant for this thesis, *i.e.* the feedback update rate of $\tau_{FB} = 10\,\mathrm{ms}$ limited by the CCD camera. For larger length scales, the time to reach a steady state temperature distribution increases significantly. However, even for distances over a few micron, the relaxation time is more than an order of magnitude faster than τ_{FB} (see Figure 2.8). A more thorough analysis of the interplay of time scales and also the influence of interracial resistivity may be found in the paper of Baffou and Rigneault.[141]

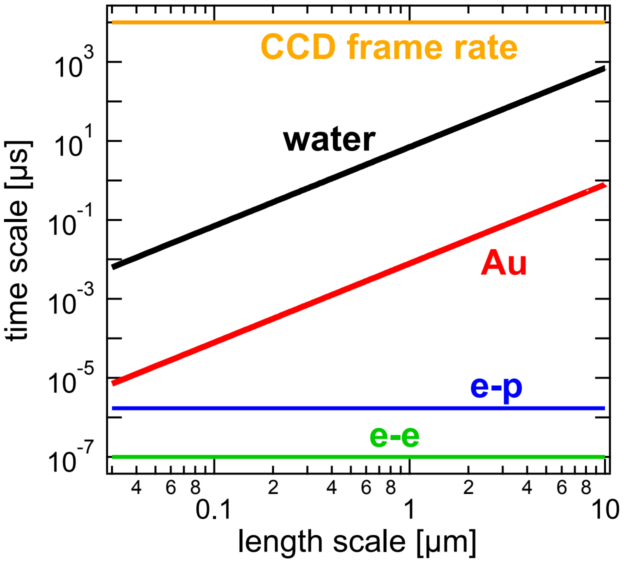

Figure 2.8: Overview over the time scales of the different relaxation processes: electron-electron (e-e, green) and electron-phonon (e-p, blue) relaxation within the metal structure, relaxation by thermal diffusion in the metal (Au, red) and water (black). All discussed time scales are well below the minimum CCD exposure time of about 10 ms.

2.5 DNA as a Model System for Linear Polymer Chains

Along with proteins and saccharides, deoxyribonucleic acid (DNA) is one of the major biopolymers and is generally known for its property of carrying genetic information. It is therefore of fundamental interest in life sciences, such as biology or biochemistry. Beyond that, its long-chained appearance, well-defined structure as well as unique biophysical properties make DNA interesting in polymer physics, as it is prototypical for a linear unbrached polymer chain. The following section will first give a very brief overview of the structural properties of DNA. Then, a few basic concepts of how to physically describe a single polymer chain will be introduced. Throughout this section, DNA is considered as dilute in aqueous solutions assumed as good solvents.

2.5.1 Fundamental Properties of DNA

Monomers of DNA are called nucleotides and consist of three components: a phosphate group, a five-carbon sugar (deoxyribose) and one of the nucleobases cytosine (C), guanine (G), adenine (A) and thymine (T). A single strand is called polynucleotide. The backbone of the DNA strand is made from alternating phosphate and sugar residues which are covalently bound. The nucleotides only differ in the nucleobases, which is why typically the abbreviations C, G, A and T are used. The physical properties are typically assumed to be independent of the particular base sequence. DNA molecules naturally consist of two strands coiled to the form of a double helix, of which different forms exist (*A*-DNA, *B*-DNA or *Z*-DNA). The most common and being the only relevant form for this thesis is *B*-DNA. Often, the term double-stranded DNA, short dsDNA, is used to differentiate from a single strand accordingly termed single-stranded DNA or ssDNA. Within the double helix, the strands are connected over complementary base pairs (A with T and C with G) via hydrogen bonds. This molecular structure was first described by Watson and Crick in 1953,[149] who found a spacing between neighboring nucleotides of 0.34 nm as well as a diameter of the double helix of about 2.0 nm. One turn of the helix comprises about 10 base pairs and thus exhibits a pitch of 3.4 nm. Depending on its origin, a single dsDNA molecule may be very large and can consist of millions of base pairs. The hydrogen bonding between the base pairs may be overcome by thermal energy. This melting process typically happens between 45°C and 60°C and leads the dsDNA to fall apart into two single strands of DNA. This process is reversible and the dsDNA-forming binding process is called annealing.[150]

For this thesis, λ-DNA was used, which refers to the genome of the enterobacteria phage λ, a bacterial virus infecting Escherichia coli (E. coli). The linear DNA molecule contains 48 490 base pairs of dsDNA. Both ends consist of 12 base ssDNA segments, such that the whole molecule is made of 48 502 base pairs.[151] This corresponds to a contour length of 16.5 µm. Its base sequence has been known since 1982.[152]

2.5.2 Physical Description of a Single Polymer Chain

Depending on the purpose, a polymer chain can be modeled on different levels of accuracy. Due to the vast amount of possible configurations that are randomly taken by the polymer chain, it is reasonable to use statistical descriptions. In the following, the most important terms and concepts of two simple models needed in the last part of the thesis shall be briefly introduced.

Freely-Jointed Chain The ideal or freely-jointed chain is the simplest way to model a polymer, as all kinds of interactions between the monomers, such as excluded volume effects, are neglected. A chain consists of $n+1$ monomers that are assumed as jointed rigid rods, each of length b. The conformation is described by bond vectors $\mathbf{r}_i = \mathbf{R}_i - \mathbf{R}_{i-1}$, where $\mathbf{R}_i$ denotes the position of the i-th monomer. The contour length is accordingly given by $L_\mathrm{c} = \sum_i |\mathbf{r}_i| = nb$. The angles between subsequent bond vectors are arbitrary. The chain is therefore represented by a 3D random walk of constant step-size b.

The size of an individual polymer chain configuration may be characterized by different parameters, of which one is the end-to-end distance

$$\mathbf{R}_\mathrm{ee} = \sum_i \mathbf{r}_i = \mathbf{R}_n - \mathbf{R}_0. \tag{2.60}$$

The bond vectors are assumed to be independent of each other, $\langle \mathbf{r}_i \cdot \mathbf{r}_j \rangle = \delta_{ij} b^2$, and their mean vanishes, $\langle \mathbf{r}_i \rangle = 0$. It can be shown that, due to the central limit theorem, the end-to-end distance has a Gaussian probability distribution of vanishing mean, $\langle \mathbf{R}_\mathrm{ee} \rangle = 0$.[92, 153] A meaningful characterization of the polymer coil dimension is thus given by the mean squared end-to-end distance that takes the value $\langle \mathbf{R}_\mathrm{ee}^2 \rangle = nb^2$. The root mean squared (rms) end-to-end distance therefore scales as $\bar{R}_\mathrm{ee} = \sqrt{\langle \mathbf{R}_\mathrm{ee}^2 \rangle} \propto n^{1/2}$.

Caused by the high level of coarse-graining, the ideal chain model fails at the microscopic scale of single monomers and is not a priori suited to describe dsDNA. The bending energy between the nucleotides are not negligible compared to $k_\mathrm{B}T$, however, no bending stiffness was considered. Physically, a finite bending stiffness increases the rms end-to-end distance of a polymer. Within the ideal chain model, this may be considered by the introduction of an artificial parameterization, which effectively accounts for a bending stiffness. This is achieved by combining monomers to segments and introducing an effective number of repeat units $n_\mathrm{K} < n$ smaller than the number of monomers n as well as a length over which the polymer appears to be stiff, called the Kuhn length L_K. In that way, the contour length $L_\mathrm{c} = n_\mathrm{K} L_\mathrm{K}$ is preserved. The single Kuhn segment exhibits the length $L_\mathrm{K} = \sigma b$ and is rescaled by a factor $\sigma > 1$ accounting for short-ranged orientation correlations. The number of segments decreases accordingly. Essentially, the segmental length has been renormalized such that the polymer is stiff on length scales smaller L_K, but there is no orientational correlation between the Kuhn segments. The mean squared end-to-end distance then reads[154]

$$\langle \mathbf{R}_\mathrm{ee}^2 \rangle = nb^2\sigma = n_\mathrm{K} L_\mathrm{K}^2 = L_\mathrm{c} L_\mathrm{K}. \tag{2.61}$$

Besides $\bar{R}_\mathrm{ee}$, another quantity to measure the extend of a polymer chain is the radius of gyration, which is defined as the root-mean-squared deviation of the monomers from the chains center of mass, $R_\mathrm{G} = \sqrt{\langle (\mathbf{R}_i - \langle \mathbf{R}_i \rangle)^2 \rangle}$. In the case of freely-jointed chains, the radius of gyration is given by $R_\mathrm{G} = \sqrt{\frac{1}{6} nb} = \sqrt{\frac{1}{6} n_\mathrm{K} L_\mathrm{K}} = \sqrt{\frac{1}{6} L_\mathrm{c} L_\mathrm{K}}$. Thus, the ratio between the rms end-to-end distance and the radius of gyration is given by $\bar{R}_\mathrm{ee}/R_\mathrm{G} = \sqrt{6}$.[92, 150]

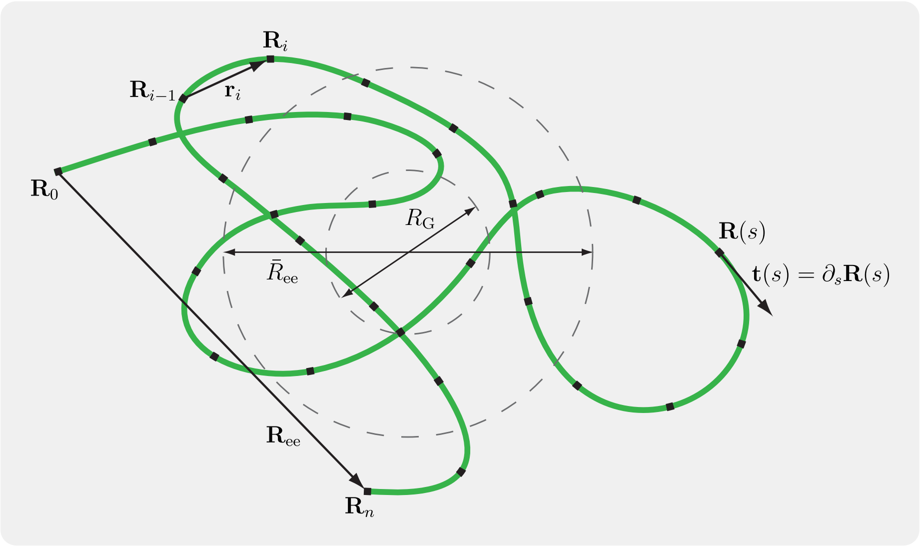

Figure 2.9: Sketch of a polymer chain, illustrating the main quantities and parameters described within this section. The $\mathbf{R}_i$ parametrization is used in the freely-jointed chain model, while for the worm-like model the $\mathbf{R}(s)$ parametrization is introduced.

Worm-like Chain Like dsDNA, Polymer chains often obey Hook's elasticity law under small deformations. A model which intrinsically includes a bending rigidity is the worm-like chain model. Here, the polymer is considered as a continuous chain of length L_c. The chain is parameterized by a parameter s, such that $s = 0$ and $s = L_\mathrm{c}$ correspond to the two ends and the conformation of the chain is continuously described by $\mathbf{R}(s)$. To mathematically define the persistence and the bending energy, it is useful to introduce the tangential vector along the polymer's path, $\mathbf{t}(s) = \partial_s \mathbf{R}(s)$. Due to the choice of the parameterization, the contour length is $L_\mathrm{c} = \int_0^{L_\mathrm{c}} |\mathbf{t}(s)|\,\mathrm{d}s$, and it follows that the tangential vector automatically is a unit vector, $|\mathbf{t}(s)| = 1$. The total bending energy of the polymer chain is then given by[92, 150]

$$U_\mathrm{bend} = \frac{1}{2} E \int_0^{L_\mathrm{c}} \left| \frac{\mathrm{d}\mathbf{t}(s)}{\mathrm{d}s} \right|^2 \mathrm{d}s, \tag{2.62}$$

where E in units of Nm^2 describes the bending rigidity of the chain. In thermal equilibrium, the conformational probability distribution obeys a Boltzmann statistics with[92]

$$P\left[\mathbf{u}(s)\right] \propto \exp\left(-\frac{U_\mathrm{bend}}{k_\mathrm{B}T}\right) = \exp\left[\frac{1}{2} L_\mathrm{p} \int_0^{L_\mathrm{c}} \left| \frac{\mathrm{d}\mathbf{t}(s)}{\mathrm{d}s} \right|^2 \mathrm{d}s\right], \tag{2.63}$$

wherein $L_\mathrm{p} = E/k_\mathrm{B}T$ is the persistence length of the chain. For DNA molecules in aqueous solvents, a bending rigidity of $E = 2 \cdot 10^{-28}\,\mathrm{Nm}^2$ leads to a persistence length of about $L_\mathrm{p} = 50\,\mathrm{nm}$.[92, 150] Its physical interpretation becomes immediately clear when considering the angular correlation function between two sites s_1 and s_2 along the polymer which decays over the persistence length,[92, 154]

$$\langle \mathbf{t}(s_1) \cdot \mathbf{t}(s_2) \rangle = \exp\left(-\frac{|s_2 - s_1|}{L_\mathrm{p}}\right). \tag{2.64}$$

The persistence length is thus characteristic for the decay of the direction of the tangential vector, *i.e.* for the strength of the bending. The rms end-to-end distance of the polymer can be directly calculated from Equation 2.64 to[92, 154]

$$\bar{R}_{\mathrm{ee}} = \sqrt{2L_{\mathrm{c}}L_{\mathrm{p}} - 2L_{\mathrm{p}}^{2}(1 - \mathrm{e}^{-L_{\mathrm{c}}/L_{\mathrm{p}}})}. \tag{2.65}$$

In the case that the polymer chain is much longer than the persistence length (coil-like polymer, ideal chain limit), $L_{\mathrm{c}} \gg L_{\mathrm{p}}$, Equation 2.65 reduces to $\bar{R}_{\mathrm{ee}} = \sqrt{2L_{\mathrm{c}}L_{\mathrm{p}}}$. This is in particular the case for λ-DNA. Comparing with Equation 2.61 of the freely-jointed chain model, the Kuhn length in this limit is twice the persistence length, $L_{\mathrm{K}} = 2L_{\mathrm{p}}$. Accordingly, the radius of gyration is related to the persistence length via $R_{\mathrm{G}} = \sqrt{\frac{1}{3}L_{\mathrm{p}}L_{\mathrm{c}}}$. In the opposite limit with $L_{\mathrm{p}} \gg L_{\mathrm{c}}$ (rigid rod-like polymer), the rms end-to-end distance obviously equals the contour length, *i.e.* $\bar{R}_{\mathrm{ee}} = L_{\mathrm{c}}$.

Diffusion Coefficient In solution, a polymer chain undergoes Brownian motion. Each segment is subjected to collisions with the solvent molecules inducing a random force (see Section 2.1.2). Due to the Stokes drag, each monomer induces a flow field which decays with one over distance. Nevertheless, the diffusion coefficient for the center of mass (com) of the polymer chain can be described by a Stokes-Einstein relation

$$D_{\mathrm{com}} = \frac{k_{\mathrm{B}}T}{6\pi\eta R_{\mathrm{h}}}. \tag{2.66}$$

Herein, the hydrodynamic radius R_{h} is a measure for the effective size of the macro-molecule in terms of internal hydrodynamic interactions. The polymer chain is thus much slower than a single monomer as the macro-molecule drags a volume $\frac{4}{3}\pi R_{\mathrm{h}}^{3}$ of solvent with it. Within the Zimm theory, which models the dynamical chain behavior and includes hydrodynamic interactions between the single monomers, it can be shown, that R_{h} is given by the relation[155]

$$\frac{1}{R_{\mathrm{h}}} = \left\langle \frac{1}{|\mathbf{R}_i - \mathbf{R}_j|} \right\rangle. \tag{2.67}$$

The average is performed over all conformations as well as over all pairs of monomers $i \neq j$ of a particular configuration. For the ideal chain, the relations between the radius of gyration, the rms end-to-end distance and the hydrodynamic radius are given by $R_{\mathrm{h}} = \frac{3\sqrt{\pi}}{8}R_{\mathrm{G}} \approx 0.66\,R_{\mathrm{G}} \approx 1.63\,\bar{R}_{\mathrm{ee}}$.[155]

Chapter 3

Experimental Background

The present chapter treats experimental prerequisites, which are specific to the experiments associated with the thesis and may support the understanding of the results. First, the sample preparation is discussed followed by a description of the experimental setup.

3.1 Sample Preparation

Preparation of Gold Nano-Structures For the preparation of the microscopic heat sources, *i.e.* the gold structures, a simple approach commonly called micro-sphere lithography is pursued.[156] The most important steps are schematically shown in Figure 3.1 A. Glass cover slides (Carl Roth No. 1, 22×22 mm) are cleaned with aceton, isopropanol, ethanol as well as deionized water and are dried under a nitrogen stream. The slides are held by a special mount that is installed into a vacuum chamber in which a 5 nm chromium adhesion layer is coated by thermal evaporation (1). After that, the slides are removed from the vacuum and are placed in a plasma chamber for 10 s to induce a hydrophilic surface. Polystyrene micro-particles ($5 - 15\,\mu$m, Microparticles GmbH) are spin-coated at 8000 rpm from aqueous solution onto the chromium layer (2). The concentration is adjusted such, that the beads are mainly isolated on the chromium layer (see Figure 3.1 B).

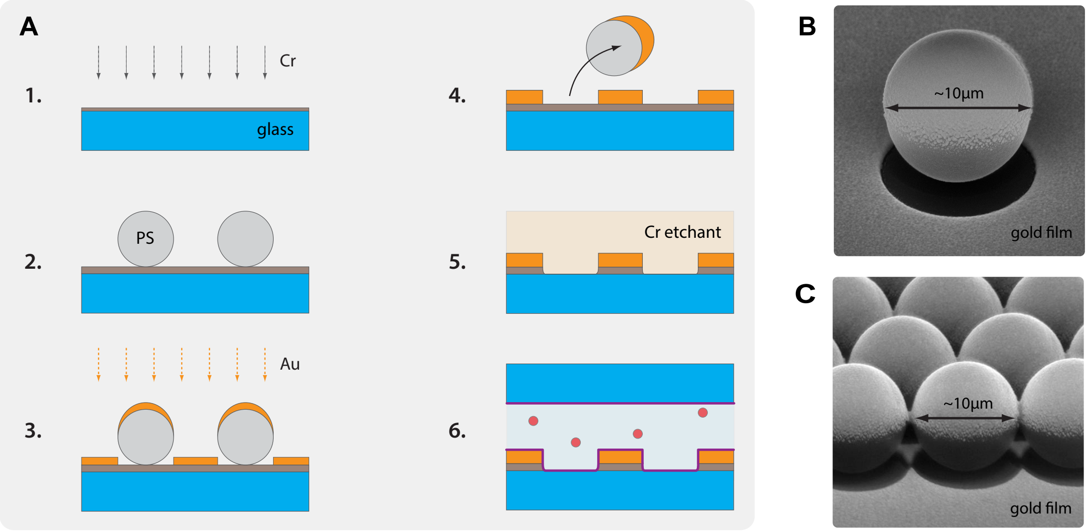

Figure 3.1: **A** Procedure to prepare gold nano-structures by micro-sphere lithography. **1.** Coating of a 5 nm chromium adhesion layer. **2.** Spin-coating of micro-beads. **3.** Coating of a 50 nm gold layer. **4.** Removal of the micro-beads. **5.** Removal of the chromium layer by etching. **6.** Passivation of the surfaces by Pluronic F-127 (purple) and assembly of the fluid chamber. Note that the schematic representation is not to scale. **B** Electron micrograph of a polystyrene bead coated with a gold film. The shadow leaves a circular gold structure in the gold film covering a glass slide. **C** Same a in A, but closed packed layer of polystyrene beads to prepare a patchy array of gold triangular islands.

A 50 nm gold film is evaporated on top (3). After the glass slides are removed from the vacuum chamber, polystyrene particles are removed by sonication in a bath of deionized water (4). Note, that the same procedure is used to produce extensively studied hybrid micro-particles, that consist of a polystyrene bead covered by a gold hemi-sphere ('Janus particles').[157, 158] The removal of these particles should not take longer than about 30 s, as the gold film may lift off from the adhesion layer. This is due to the two-step coating procedure, in which the chromium layer oxidizes during its contact to air. Residual polystyrene beads are dissolved by toluene. What remains is a gold film that contains circular holes at the sites of the removed polystyrene micro-spheres. The uncovered chromium layer within the holes is removed by etching (5) using Chromium Etch No. 1 purchased from MicroChemicals GmbH. Also a patchy structure of isolated triangular gold islands in a hexagonal array can be achieved by spin coating a less dilute solution to form a closed packed mono-layer of beads (see Figure 3.1 C).

Sample for the Experiment All current versions of the thermophoretic trap are 2-dimensional in that sense that the confinement by means of thermal gradients can only be realized in lateral directions. The third direction thus needs to be limited spatially. In the experiments, the solvent is confined to a film of 500 nm to 1 µm height between two glass cover slides. While one carries the gold nanostructures that can be heated optically, the second slide (also Carl Roth No. 1, 22x22 mm) is coated in the outer regions with a layer of spray paint, that acts as a spacer of a few hundred micron in height. Therefore, a 2 cent euro coin of 19 mm diameter is used as a mask. The two cover slides are assembled to confine the solvent and the specimen and are placed into a sample holding device, that is able to apply gentle pressure to the upper glass slide, which in turn bends controlled by a micrometer screw to adjust the water film thickness to the desired value (see Figure 3.2). A stamp made of polydimethylsiloxane (PDMS) prevents a hard contact between the micrometer screw and the glass that possibly breaks the glass slide. Depending on the purpose of the experiment, it is possible to assemble the fluid chamber such that the gold structure is on the top or on the bottom (2nd case is shown in the Figure). The latter configuration has the advantage that a radiation-pressure-induced spatial lateral confinement can be immediately excluded, as potential radiation pressure would push particles to the upper glass slide without a gold structure. However, particles outside the trapping region are hardly visible, because their fluorescence is blocked by the gold film. Therefore, in the first proof-of-principle experiments, a gold-on-the-bottom configuration was used, whereas later the opposite is used. The glass and gold surfaces are passivated by Pluronic F-127 (Sigma-Aldrich) to avoid an adhesion of the colloids. To do so, both cover slides are placed in a bath containing a 4 wt. % aqueous solution of Pluronic for at least 60 minutes after 20 s of treatment with a plasma cleaner for hydrophilization.

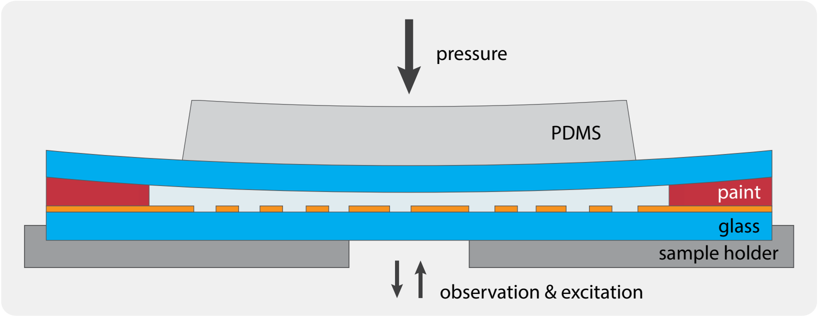

Figure 3.2: Schematic representation of the fluid chamber.

The film of solvent, that is deionized water (Milli-Q, resistivity 18.2 MΩ · cm), contains the particles or molecules that shall be trapped. For most experiments, dye-doped colloidal particles (Invitrogen FluoSpheres) of size 28 nm, 200 nm and 460 nm are used.

For the DNA trapping experiments the samples are prepared as follows. $\lambda-$DNA (NEB, N3011) of 16.3 μm contour length is stained with the bisintercalating fluorescence dye POPO-3 (life technologies, P3584) at a ratio 1 dye/8 base pairs in 100 mM phosphate buffer (sodium phosphate buffer: 18.8 mM $NaH_2PO_4 \cdot H_2O$, 81.3 mM $Na_2HPO_4 \cdot 2H_2O$, resulting in a pH of 7.5) at a final DNA concentration of 1.28 nM. This solution is incubated for at least 1 hour at 50 °C in order to ensure homogeneous staining. The contour length of the DNA is expected to increase to approximately 19 μm due to intercalation of POPO-3. For the trapping experiments the DNA was further diluted with H_2O by a ratio of 1 : 30.

3.2 Experimental Setup

The setup on which the trapping experiments are performed is specifically designed to fulfill two major demands. First, the objects of interest, particles or molecules, need to be observed, which is realized via fluorescence. Second, the gold structure needs to be heated locally to create the temperature profiles able to confine the object of interest. The latter is achieved by absorption of a laser beam. Especially in the latest version of the trap, the two characteristics are connected via a feedback. The following section will cover the experimental setup as well as the interplay of its individual components.

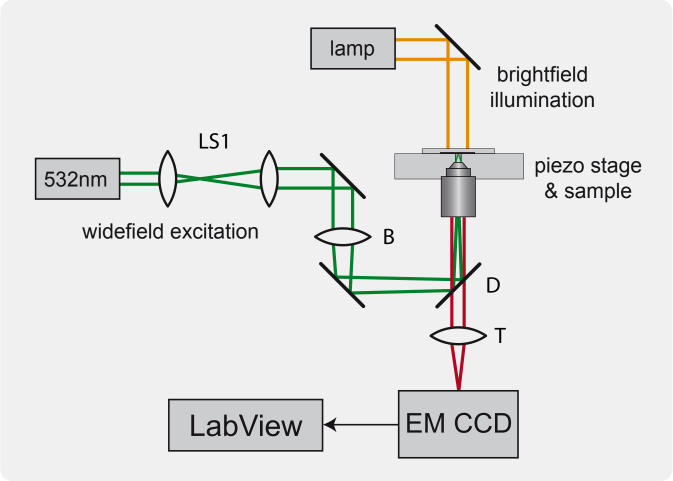

Figure 3.3: Cartoon representation of experimental setup for thermophoretic trapping using a steady heating by an expanded laser beam.

Microscopy Setup The entire experimental setup schematically shown in Figure 3.3 is built around a modified inverted microscopy stage (Olympus IX70) mounted on a pneumatically stabilized optical table. The original tube lens of $f = 18\,\mathrm{cm}$ focal length has been replaced by a $f = 50\,\mathrm{cm}$ achromatic lens (T). The same objective lens (Olympus lens 100/NA1.3, adjustable aperture) is used for the detection as well as the excitation. The replaced tube lens leads to an effective magnification of 278x. For imaging, an electron multiplying charge-coupled device (EMCCD camera, Andor iXon3 897) of 16 µm pixel pitch is employed. Typically, the exposure time is set to $\tau_{\mathrm{exp}} = 0.01\,\mathrm{s}$, which leads to a frame time of $\tau_{\mathrm{frame}} = 0.01091\,\mathrm{s}$ in frame transfer mode. Also, in most experiments, a 2x2 or 4x4 pixel binning is used. The images are read out by a dedicated LabView 8.5 program via a controller board installed to a personal computer (Intel i7, 16GB memory, 256GB solid-state drive, Windows 7). The sample holder, to which was already commented above, is mounted to a 3-axes piezo stage, that is able to travel 20 µm in vertical (*e.g.* for focusing purposes) and 100 µm in lateral directions. The stage is mainly needed to adjust the gold structure in the field of view. For excitation of fluorescent nano-objects a laser beam of 532 nm wavelength ($P_{\mathrm{max}} = 50\,\mathrm{mW}$) is expanded by a pair of lenses (LS1). An additional lens (B) is used to focus the beam to the back-focal plane of the objective lens such that a parallel illumination with Gaussian intensity profile of width $\omega_{0,w} \approx 20\,\mu m$ is achieved in the sample plane. A suited dichroic mirror (D) reflects the excitation beam into the objective lens. An optional brightfield illumination from the top helps to visualize the metal structure on demand.

In the first generation of the thermophoretic trap (see Results Chapter 4), the expanded laser beam is not only used for excitation of the fluorescence but also for heating of the circular gold structure. While such an illumination leads to a heating of the entire gold structure, for the second and third trap generation, a localized heating is employed. For this purpose, the setup is extended with an additional focused 532 nm laser beam ($\omega_{0,h} \approx 1\,\mu$m), which can be steered within the sample plan by means of an 2D-acousto-optic deflector (2D-AOD) purchased from Brimrose USA. The advanced setup is shown in Figure 3.4. The parallel laser beam is expanded by a pair of lenses (LS2) to adapt the size of the crystals within the acousto-optic deflector. The AOD is able to deflect the beam in two directions by 2.3° and has an access time of 15 µs. To ensure that the focused laser beam is scanned properly in the sample plane, another system of lenses (LS3) is used such that the center of the AOD is imaged to the back-focal plan of the objective lens.

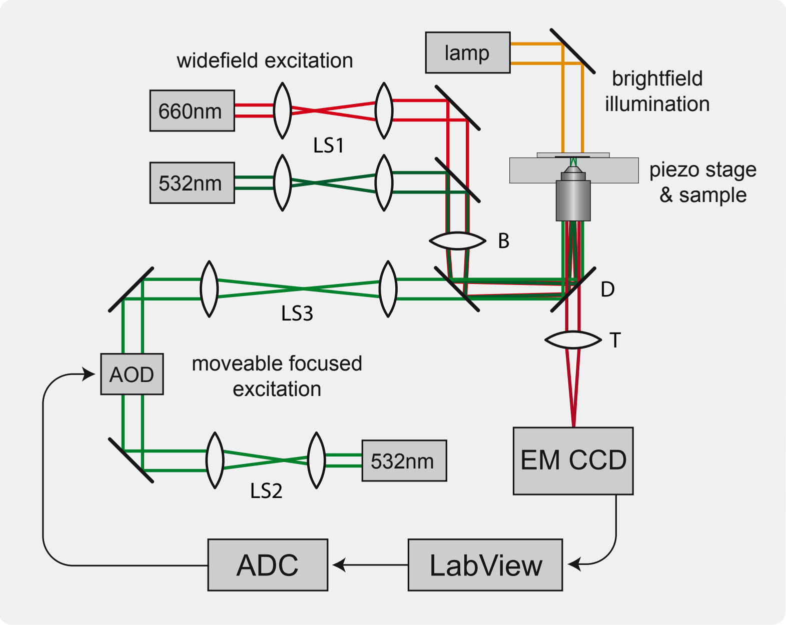

Figure 3.4: Schematic representation of experimental setup for thermophoretic trapping using a dynamic heating by a focused laser beam.

Calibration of the AOD The acousto-optic deflector (AOD) is used to steer the beam in two dimensions. Therefore, a certain voltage at the AOD controller input corresponds to a certain deflection angle of the beam. The AOD consists of two independent deflection units, thus, two voltages are needed for the x and y direction, both provided as analog signals by the ADC (AdWin, see below). The relation between control voltage, deflection angle and hence the beam position in the sample plane (in pixel) is however not trivial and needs to be calibrated before each experiment. To do so, a matrix of voltage values for the deflection in x and y direction is assigned and the resulting beam positions are acquired by tracking the appearing spots on a fluorescing film. Figure 3.5 A and B show the data for an example calibration. Obviously, a tilt is present between the corresponding matrices of the voltages and the tracked beam positions, which can be attributed to a slight tilt between the stage to which the AOD is mounted and the CCD camera. Each coordinate component hence depends on both, the x and y voltage. After correction for this tilt angle, that is $-0.557°$ in the calibration presented in Figure 3.5, the beam's x position only depends in good approximation on the voltage controlling the x component (respectively for the y component). An averaging then yields the calibration curves for the x (black) and y (green) direction shown in Figure 3.5 C which appear strongly non-linear. The curves are fitted by polynomials of 10th order and the resulting parameters together with the tilt angle are later used to steer the beam to the desired position. The resulting intensity distribution in the sample plane appears inhomogeneous as can be seen from Figure 3.5 D. The optical components however can be adjusted such that the intensity distribution shows a distinct maximum in the center of the field of view. In the experiments performed, the beam is always steered on a circular path around the maximum, such the beam intensity along the path is approximately constant at 82% of the maximum intensity with a relative standard deviation of 2% (see Figure 3.5 C, red curve).

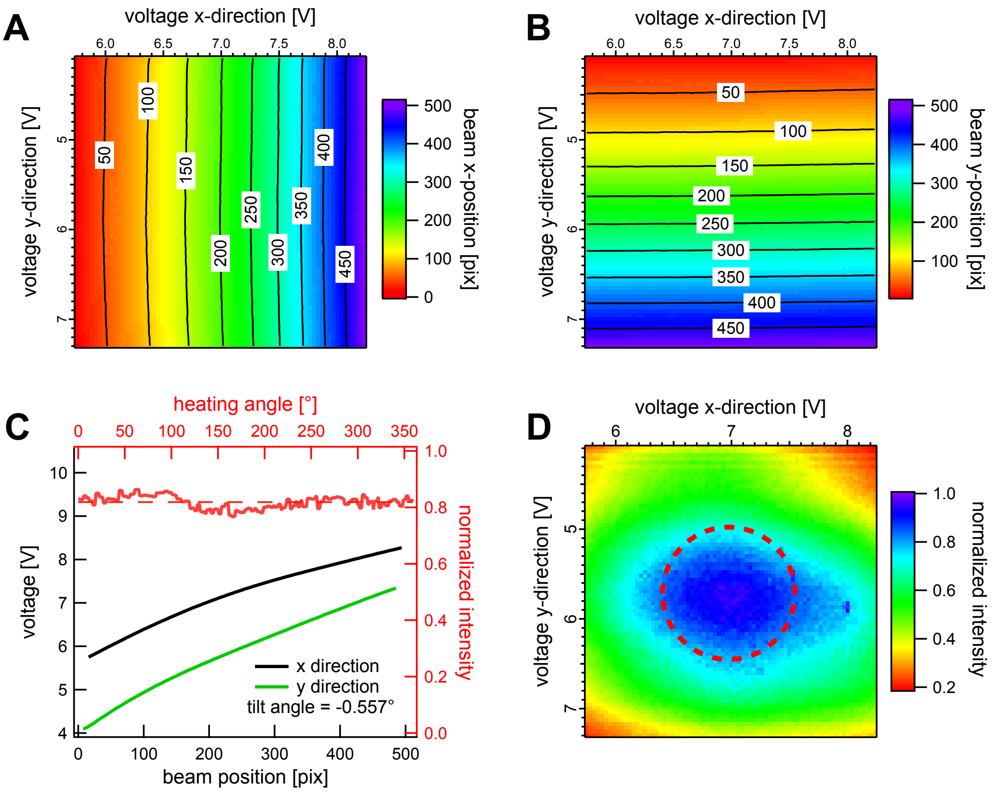

Figure 3.5: **A** Tracked x component of the beam illuminating a fluorescent film in the sample plane in dependence on the x and y control voltages. **B** Same for y component. **C** Non-linear relations between control voltage and beam position after correction for the tilt angle (here $-0.557°$). The red curve with the colored axes shows the angular intensity distribution along the dashed circle in D. **D** Intensity distribution within the sample plane normalized to the maximum.

Interplay of Components The interplay of the different devices of the setup is regulated by the PC running a dedicated LabView program as well as an ADwin-Gold II real-time processing device, which will be introduced below. The self-made LabView program represents the control center for the setup as most parameters relevant for the experiment are set. Important parameters related to the CCD camera are the exposure time, pixel binning, region of interest or the number of frames to capture. Also, the LabView program grabs the frames of the camera via a Bruxton SIDX 6 software interface. The acquired camera frames are processed in real-time. The processing includes real-time multi-particle tracking. For that purpose, the NI Vision toolbox is used. The threshold can be set manually.

Alternatively, the threshold can be set automatically, oriented on the maximum intensity in the frame. In that case, a minimum value ensures the threshold to be above the noise level. Before applying the threshold, a median filter is used to reduce noise. The ADwin-Gold II, Jäger Messtechnik GmbH, is not only a real-time processing device, but also an AD/DA converter with eight 16bit channels each for analog input and output. The ADwin is connected to the PC via Ethernet and is able to run autarkic programs written in a Basic-like programming language called ADBasic. Running ADBasic programs may communicate with the LabView program via a dedicated software development kit, which allows for an exchange of parameters and data arrays. This is used, for instance, to transmit the AOD calibration data or the particle position gained from particle tracking. The ADWin is used for the different tasks, such as the calculation of position of the heating laser beam in dependence on the particle position according to the particular feedback algorithm. Also, the control voltages for the AOD and the piezo stage are calculated and set. The positional sensors of piezo stage can be read out on demand. A photo diode signal is a read out to track the heating laser power. Some hardware related parameters are set in the LabView program and the Adwin is used to control devices (laser power, manual AOD deflection, manual piezo stage positioning).

Chapter 4

Results and Discussion

The following chapter constitutes the main part of the dissertation as the results are treated in detail. The discussion closely follows the order of increasing complexity of the thermal trap. The Results and Discussion chapter is therefore divided in three major sections, each orients on a particular iteration of the trap.

The first working generation of the trap directly relies on the idea of trapping a nano-object within a local temperature minimum. Yet, the experimental realization is easy and may in principle be copied in every laser-based widefield fluorescence microscope. A simple gold structure, consisting of a circular hole in a gold film, is employed as a heat source. The resulting temperature field exhibits a dip in the center in which a particle is confined. The heating is achieved via absorption of a steady laser beam expanded to illuminate the entire gold structure. The results are published in the following article.

- **M. Braun**, F. Cichos (2013): *Optically Controlled Thermophoretic Trapping of Single Nano-Objects*, ACS Nano **7**(12), 11200-11208.

The second generation technically constitutes an intermediate step to the feedback-controlled version of the thermophoretic trap. The heating of the gold structure by an expanded laser beam is discarded in favor of a local heating by means of a focused laser beam. As the temperature field produced by such a heating scheme yields an effective potential that is for typically positive Soret coefficients purely repulsive, the laser beam is steered in order to confine a single particle. As a simple strategy, it is possible to rotate the laser beam along the circumference of the gold structure, *i.e.* in circles, at a certain frequency. The behavior of a trapped particle is studied in detail and a non-trivial dynamics is found. The phenomenology of the motion thereby exhibits similarities to the Paul trapping of ions. The major result can be found in

- **M. Braun**, A. Würger, F. Cichos (2014): *Trapping of Single Nano-objects in Dynamic Temperature Fields*, Phys. Chem. Chem. Phys. **16**, 15207-15213.

The third and to date most advanced iteration of the trap essentially uses the same hardware as the second one. The difference lies in the strategy of how the heating laser beam is steered. Now, an optical feedback couples in real-time the heating laser position on the position of the trapped object. This increases the trapping efficiency tremendously and effectively reduces the temperature rise needed to stably confine a particle. Beyond a simple trapping of nano-objects, the optical feedback allows for a versatile manipulation of the trapped object, as it can now be steered freely within the trapping region. As will be shown, the effective trapping potential can be shaped in almost arbitrary ways by modifying the applied feedback rules. The feedback heating can also be modified such that multiple particles can be trapped simultaneously, a feature that is almost unique to the thermal trap. As a step towards potential applications, it is shown that single and multiple macro-molecules can be confined, demonstrated by trapping λ-DNA strands. The major results are collected in a third publication.

- **M. Braun**, A. Bregulla, K. Günther, M. Mertig, F. Cichos (2015): *Single Molecules Trapped by Dynamic Inhomogeneous Temperature Fields*, Nano Lett. **15**(8), 5499-5505.

4.1 Thermophoretic Trapping by Steady Temperature Fields

The confinement of a microscopic objects at a certain position in solution requires a compensation of the erratic Brownian motion. As Brownian motion enhances for smaller particles, an counteracting fast drift velocity is needed to drive the particle back to the region of interest. In the course of this monograph, thermophoretic interactions with local temperature gradients are used to confine Brownian motion of microscopic objects. The effects that lead to thermophoresis (see discussion in Section 2.2) all have in common, that a temperature gradient induces a particle drift, typically towards colder regions. Temperature gradients, however, can only be induced by rising the temperature locally. While it seems counter-intuitive to trap a particles by elevating the temperature, as Brownian motion speeds up as well, it will be shown, that local temperature fields can be used to stably confine a single particle. Local heating may be realized by different means. As an optical detection of the object of interest is employed, it seems convenient to also use an all-optical control of the heating. Often, a liquid is heated directly by the absorption of a laser beam.[59,65,159] The temperature profile, however, cannot decay faster than the size of the heat source which in that case is diffraction limited and thus at least a few hundred nanometers in size. A different approach exploits the plasmonic interaction of laser light with a metal nano-structure, typically constituting heat sources much smaller than the diffraction limit which results in strong temperature gradients in their local proximity. The key to thermophoretic trapping is the establishment of a temperature field shaped such that the negative gradient and therefore the thermophoretic drift points towards a stable position. In other words, a local temperature minimum is essential to represent an effective trapping potential. This demands a metal structure of special shape. A realization of such a geometry is schematically shown in Figure 4.1 A. The gold structures of circular symmetry are fabricated via micro-sphere lithography (see Section 3.1). In the first realized version of the thermophoretic trap, the structures are illuminated by an expanded laser beam in a fixed and continuous (*i.e.* steady in space and time) manner, often referred to as wide-field (WF) illumination. The next Section 4.1.1 will show, that such a heating scheme indeed produces a temperature field fulfilling the upper demand. The experimental realization is then presented in Section 4.1.2.

4.1.1 Temperature Distribution Within the Sample

The technique of micro-sphere lithography is used to produce two basic kinds of micro-structures. Single holes in a gold film (Figure 4.1 A) are produces by spin-coating a dilute solution of polystyrene beads of a few micron in size. Also a patchy structure of isolated triangular gold islands in a hexagonal array (Figure 4.1 B) is achieved by spin coating a less dilute solution to form a closed packed monolayer of beads (for details of sample preparation see Section 3.1). Both are potential candidates for the realization of a thermophoretic trap. Within this section, the expected temperature fields upon optically heating the latter gold structures shall be examined. For that purpose, FEM simulations are performed using the software suite COMSOL Multiphysics 4.0 and in particular the Heat Transfer Module. The steady-state heat equation 2.55 is solved for a modeled geometry, that resembles the actual sample used in the experiment including the glass cover slides, the gold structure as well as the water film in between. The size of the model is larger than the actual gold structure to avoid boundary effects (x- and y-direction $(-20...+20)$ µm and in z-direction $(-10...+10)$ µm, where the center of the hole in the gold film coincides with the origin). As the environment effectively acts as an infinite heat bath, the external boundaries are set to ambient temperature. Convection within the water film is neglected due to the thickness below 1 µm.[139] In this first realization of the thermophoretic trap, the entire circumference of the gold structure is used as a heat source. The heat source density within the gold film is identified with the Gaussian profile of the excitation beam (beam waist $\omega \approx 20\,\mu$m). It's magnitude can be chosen arbitrarily as the resulting temperature fields later are normalized to the surface temperature rise at the gold edge.

A simulated temperature map for the single-hole gold structure is shown in Figure 4.1 C. While the gold structure itself is near isothermal in the surrounding, the temperature drops into the hole direction leading to a local minimum. It will be referred to, in the following, as 'closed' gold structure. A temperature map produced by the second patchy structure is depicted in Figure 4.1 D. As can be seen, the radial symmetry disappears. The patches seem to produce stronger temperature gradients than produced by the closed structure. In between the patches, the temperature drops, which is why it will be referred to the patchy structure as 'open' gold structure in the following.

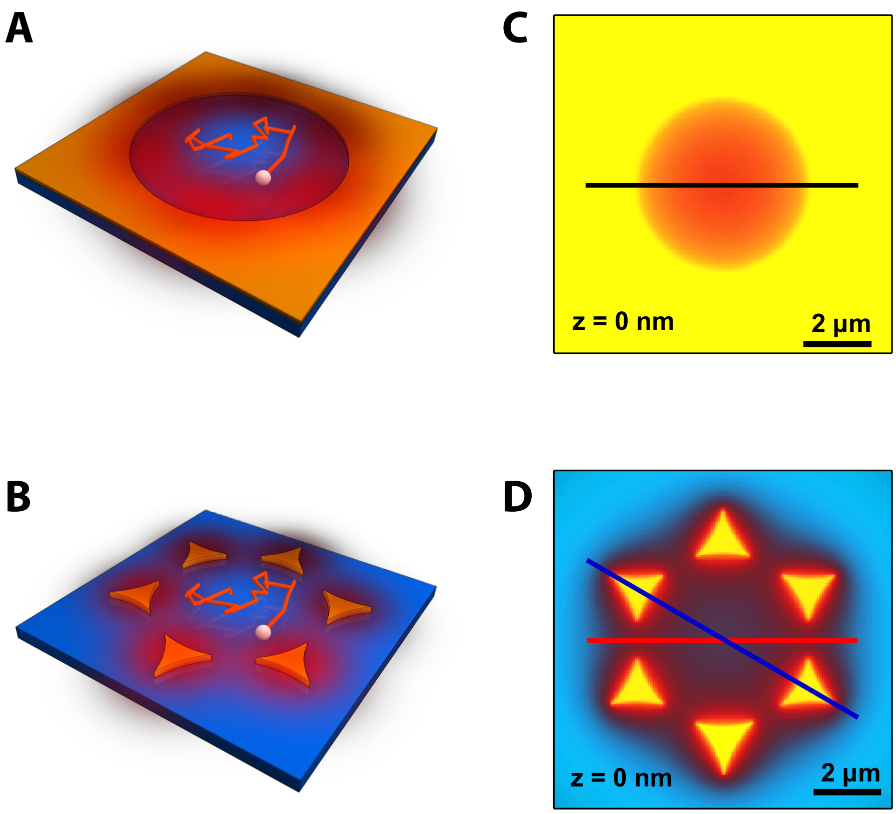

Figure 4.1: **A** Scheme of a closed gold structure photothermally heated to produce a radially symmetric temperature field. **B** FEM-simulation of a temperature field produced by a closed gold structure with 5.3 µm diameter in the lateral plane of the lower glass slide which carries the gold structure ($z = 0$). The black line indicate the path of the line profile shown in Figure 4.3 A. **C** Scheme of an optically heated open gold structure. **D** FEM-simulation of a temperature field produced by an open gold structure of the same diameter in the plane $z = 0$. The red and blue lines indicate the paths of the line profiles plotted in Figure 4.3 B. The color scales may be read from the line profiles in Figure 4.3.

Before going into detail, it is helpful to introduce some notations, which will be used throughout the monograph. Figure 4.2 shows a scheme including the most important parameters such as ambient temperature T_0, the temperature rise at the gold surface ΔT_{Au} and the temperature rise in the center of the hole in the gold film $\Delta T_{\mathrm{Center}}$, which is the local temperature minimum. To quantify the temperature fields, it is convenient to use a normalization to the temperature rise at the gold structure which results in unit-less relative temperatures. Doing so decouples the shape of the temperature field from its magnitude, which is directly proportional to the heating power used. As will be seen, the local temperature field may be approximated by a parabola in the proximity of the temperature minimum,

$$\Delta T_{\mathrm{Harm}}(r) = \frac{\alpha}{2} r^2 + \Delta T_{\mathrm{Center}}, \tag{4.1}$$

with α being the curvature of the temperature field, which may also be expressed by a relative curvature $\alpha^{\mathrm{rel}} = \alpha/\Delta T_{\mathrm{Au}}$ in units of $\mu\mathrm{m}^{-2}$. Likewise, the relative temperature gradient $\nabla T^{\mathrm{rel}} = \nabla T/\Delta T_{\mathrm{Au}}$ will appear in units of $\mu\mathrm{m}^{-1}$.

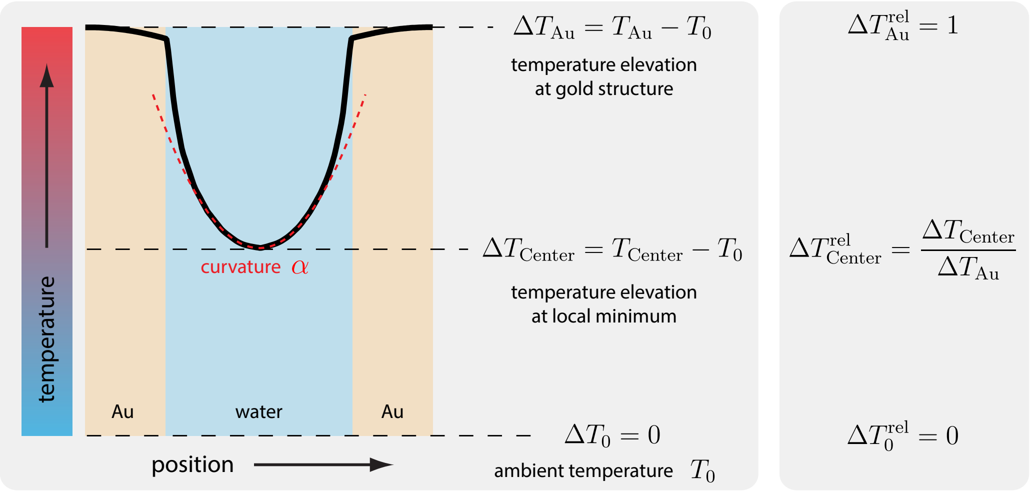

Figure 4.2: Scheme illustrating the notations of the temperatures used throughout the thesis. The temperature elevation at the gold structure is denoted with ΔT_{Au}, the ambient temperature with T_0. The temperature elevation at the local minimum which later resembles the center of the trap will be described by $\Delta T_{\mathrm{Center}}$. Often, relative temperature increases will be used (right side), which are nomalized by ΔT_{Au} and are denoted by $^{\mathrm{rel}}$, such that $\Delta T^{\mathrm{rel}}_{\mathrm{Au}} = 1$ and $\Delta T^{\mathrm{rel}}_{\mathrm{Center}} = \Delta T_{\mathrm{Center}}/\Delta T_{\mathrm{Au}}$. The curvature of the temperature field at the local minimum will be called α and will also appear normalized as $\alpha^{\mathrm{rel}} = \alpha/\Delta T_{\mathrm{Au}}$ in units of $\mu\mathrm{m}^{-2}$.

Closed gold structure Figure 4.3 A shows temperature line profiles at along the black line of Figure 4.1 B directly on (black) and 300nm above (black dashed) the gold structure in the water film. The according temperature gradient in the gold structure plane (red) appears to be linear in the center, leading to a parabolic temperature field of relative curvature $\alpha^{\mathrm{rel}} = 0.027\,\mu\mathrm{m}^{-2}$. For the given geometry and materials, a relative temperature contrast quantifying the depth of local temperature minimum is found to be $\Delta T^{\mathrm{rel}}_{\mathrm{Depth}} = \Delta T^{\mathrm{rel}}_{\mathrm{Au}} - \Delta T^{\mathrm{rel}}_{\mathrm{Center}} = 0.17$. The remaining difference to ambient temperature leads to a center temperature rise $\Delta T^{\mathrm{rel}}_{\mathrm{Center}} = 0.83$ which does not effect the trapping directly, but only increases the temperature that the trapped species is at. Regions far from the center deviate from the harmonic approximation and show even stronger temperature gradients. The latter values are simulated for a trap diameter of $5.3\,\mu\mathrm{m}$, a dependence on the size of the gold structure is discussed later in Section 4.1.6. While the center temperature rise is almost constant in the vertical direction in the center of the gold structure, it linearly decreases above the gold film (about 5% over the $\delta z = 300\,\mathrm{nm}$ between the curves). The shape of the parabolic temperature field close to the trap center is conserved over the height of the water film.

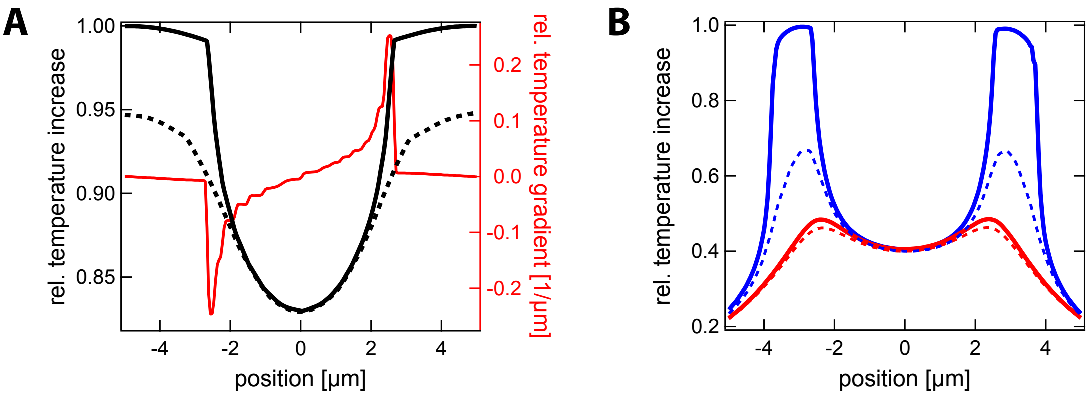

Figure 4.3: **A** Lateral temperature profiles along the line drawn in Figure 4.1 B (black) of the temperature field produced by the closed gold structure in the plane of the gold structure and 300 nm above (dashed). Corresponding temperature gradient (red). **B** Analogous temperature profiles according to the lines drawn in Figure 4.1 D.

Open gold structure Compared to the closed structure, the open gold structure produces a much lower center temperature rise of $\Delta T^{\mathrm{rel}}_{\mathrm{Center}} = 0.37$ (Figure 4.3 B, blue curves). Also, the temperature difference between the heated gold pads and the local minimum is huge with $\Delta T^{\mathrm{rel}}_{\mathrm{Depth}} = \Delta T^{\mathrm{rel}}_{\mathrm{Au}} - \Delta T^{\mathrm{rel}}_{\mathrm{Center}} = 0.63$ producing strong temperature gradients. However, the bottle neck regarding this specific geometry is the gap between the gold islands, where the relative temperature difference is only $\Delta T^{\mathrm{rel}}_{\mathrm{Gap}} - \Delta T^{\mathrm{rel}}_{\mathrm{Center}} = 0.08$ (red curves). That means, while a particle can efficiently be repelled thermophoretically from the gold islands into the trapping region, it may escape through the gaps in between the gold pads, where the effective temperature difference is much less, being a disadvantage for the stable trapping of particles. This, though, does not mean that the open structure is discarded. Trapping is not only possible as will be seen with the second generation trap (see Section 4.2.1), but the structure may even be beneficial for a potential parallelization and cooperation of nearby traps. Also, by introducing an additional step to the sample preparation, such as oxygen plasma treatment of the micro-spheres before the evaporation step, the geometry of the gold structure may be altered to achieve a ‘semi-open’ structure, where the gaps in between the gold islands are replaced by thin gold bases.

Due to the simplicity of the closed gold structure in terms of preparation but also because of the radial symmetry of the temperature profile, which is broken in the open structure, however, the first experiments presented in the following will concentrate on that structure.

4.1.2 Steady-State Properties – Positional Distribution

Within the next sections, the fundamental behavior of a particle in a static thermophoretic trap shall be investigated. For that purpose, the trapping of a 200 nm-diameter polystyrene (PS) bead is demonstrated, which is chosen for various reasons. PS beads are commercially available in different sizes and may be doped by different dyes. Due to the large dye content, they are neither prone to blinking nor bleaching and may be observed via fluorescence for hours. The size of 200 nm is chosen for a relatively large Soret coefficient of order $1\,\mathrm{K}^{-1}$, while still being small enough to demonstrate trapping of objects being challenging to trap by well-established methods such as optical tweezing. The size of the trap is given by the diameter of the hole in the gold film being $5.3\,\mu\mathrm{m}$. The exposure time of the frame-transfer CCD camera is set to $\tau_{\mathrm{exp}} = 0.01\,\mathrm{s}$ such that the Brownian motion of the particle is sufficiently resolved. Also, the camera is used with a 2×2-binning resulting in scale factor of $0.1152\,\mu\mathrm{m}/\mathrm{pixel}$. The sample was assembled according to the description in Section 3.1. Once a particle diffuses by chance over the trapping region, the heating laser is manually switched on resulting in a confinement for the particle. Movies of the trapping are acquired for increasing heating laser power each with a length of 270 s consisting of 25 000 frames. Particle positions are extracted from the movie files by a home-made tracking software. The single position of the particle in each frame is assembled to a trajectory which can be analyzed.

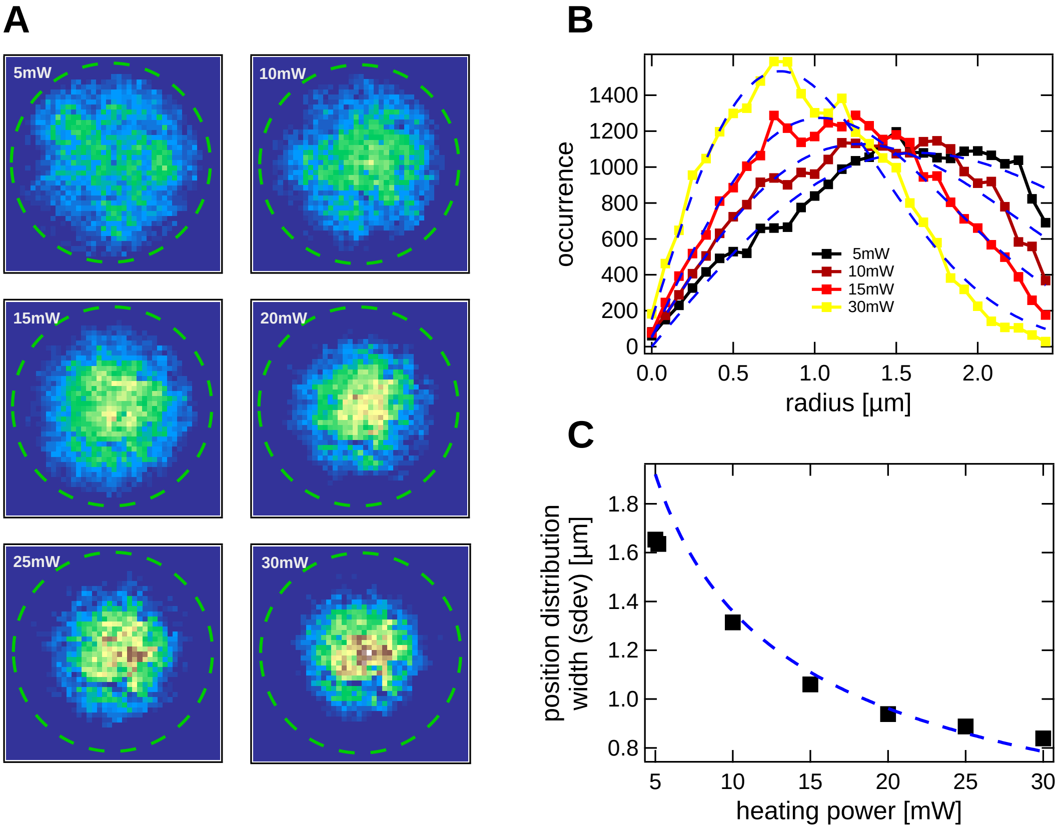

Figure 4.4: Trapping of a single 200 nm polystyrene particle for increasing heating laser power. **A** Positional distribution histograms over all trajectory points. The green dashed circles indicate the edges of the gold structure of $5.3\,\mu\mathrm{m}$ diameter. **B** Radial position distribution in dependence on the radial distance to the center of the trap. **C** Width of the position distribution $\sigma = (S_{\mathrm{T}}\alpha)^{-1/2}$ (black squares) gained from fitting Equation 4.2 to the data of B, fitted by the theoretical prediction $\sim P_{\mathrm{Heat}}^{-1/2}$ (dashed blue line).

The following pages give a detailed presentation and discussion of the performed experiment, beginning with the steady-state properties that can be obtained from the position distribution of the bead within the trapping region. Two-dimensional position distribution histograms are depicted in Figure 4.4 A. For low heating intensities, the bead positions are distributed over the entire trapping region. For increasing heating laser power, the increasing confinement is visible already by eye. The distributions follow the steady-state density described by Equation 2.16. The radial position distributions for a few heating intensities are shown in Figure 4.4 B. The probability to find the bead within the radial interval $[r, r+\mathrm{d}r]$ is accordingly given by $P_{\mathrm{rad}}(r)\,\mathrm{d}r = P(r)\cdot 2\pi r\,\mathrm{d}r$. Inserting the harmonic temperature field with Equation 4.1 and normalizing such that $\int_0^\infty P_{\mathrm{rad}}(r)\,\mathrm{d}r = 1$ yields the following expression

$$P_{\mathrm{rad}}(r) = S_{\mathrm{T}}\alpha r \exp\left(-\frac{S_{\mathrm{T}}\alpha}{2} r^2\right). \tag{4.2}$$

The width $\sigma = (S_{\mathrm{T}}\alpha)^{-1/2}$ of the distribution is dependent on the Soret coefficient and the curvature of the absolute temperature field, which both are not known at this point. A fitting of Equation 4.2 to the experimentally obtained data shown in Figure 4.4 B yields the widths σ in dependence of the heating power plotted in Figure 4.4 C. While the Soret coefficient may depend on the absolute temperature, the dependence is assumed to be weak in the given experimental temperature range. S_{T} thus is considered to be constant. Then, the confinement is determined solely by the curvature of the temperature field. Since the curvature is linearly related to the temperature rise and therefore also to the heating power $\alpha = \alpha^{\mathrm{rel}}\Delta T_{\mathrm{Au}} \propto P_{\mathrm{heat}}$, the width of the distribution ideally decreases with the square root of the heating power $\sigma \propto P_{\mathrm{heat}}^{-1/2}$. This theoretical dependence is shown in the same plot with the blue dashed line and fits the experimental data reasonably well. The main contribution of the visible deviation is attributed to the present anharmonicity of the temperature field in the outer region close to the gold structure which the particle probes especially for low heating intensities. Also, the neglected temperature dependence of the Soret coefficient may cause a deviation.

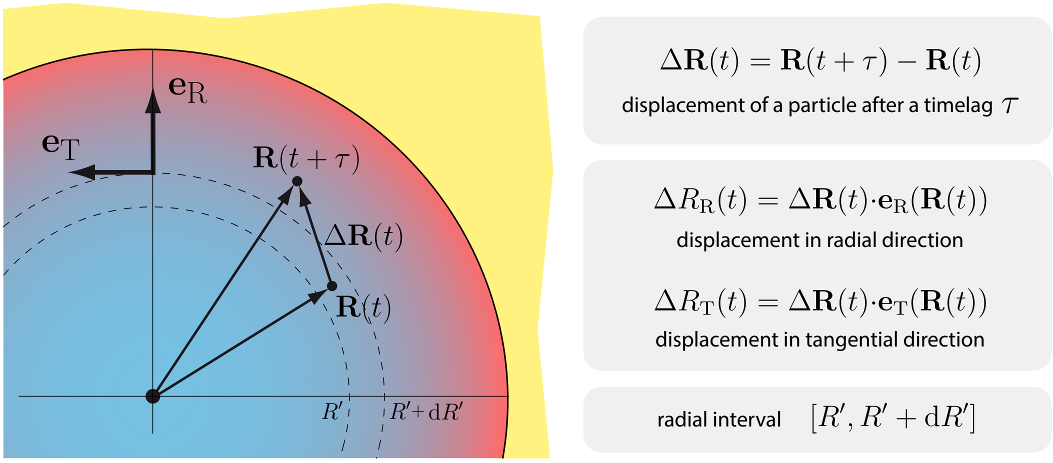

Figure 4.5: Illustration and overview of the parameters being relevant for step size analysis. $\mathbf{R}(t+\tau)$ and $\mathbf{R}(t)$ are two subsequent trajectory positions with τ being the inverse frame rate.

4.1.3 Dynamic Properties – Thermophoretic Drift

Additionally to the overall positional distribution, dynamic properties are of particular interest such as the diffusion coefficient and the photothermally induced thermophoretic drift velocity. Both may be studied by investigating the trajectory constructed from the tracked particle position in each frame. More precisely, the step size distribution is determined by both the diffusion coefficient and the thermal drift. The step-size distribution is a synonym for the probability density $P_{\mathrm{adp}}(\mathbf{R}(t+\tau), \mathbf{R}(t))$ for detecting a particle at a time $t+\tau$ at the position $\mathbf{R}(t+\tau)$ if it was at a position $\mathbf{R}(t)$ at time t. This probability density may be described by the advection-diffusion propagator[97] (see Section 2.1.2) of Gaussian shape[a)]

$$P_{\mathrm{adp}}\left(\mathbf{R}(t+\tau),\mathbf{R}(t)\right) \propto \exp\left(-\frac{\left|\mathbf{R}(t+\tau)-\mathbf{R}(t)-\mathbf{v}_{\mathrm{T}}\tau\right|^2}{4D\tau}\right). \tag{4.3}$$

Considering a constant flow velocity $\mathbf{v}_{\mathrm{T}}$, the width is solely determined by the diffusion coefficient D. The center of the distribution is shifted from the origin by $\mathbf{v}_{\mathrm{T}}\tau$ due to the deterministic thermal drift. To apply this concept to an inhomogeneous velocity field (such as produced by the heated circular gold structure), it is important to note, that Equation 4.3 only holds true, if the timelag τ is sufficiently short, such that the displacement $\Delta\mathbf{R}(t) = \mathbf{R}(t+\tau) - \mathbf{R}(t)$ is small and the drift velocity can be considered as constant. For a frame time (inverse frame rate) of $\tau = 0.01\,\mathrm{s}$ and a typical drift velocity of $v_{\mathrm{T}} = 5\,\mu\mathrm{m/s}$, a displacement on the order of 50 nm is expected. Over such length scales, the temperature gradient can be considered as constant such that Equation 4.3 may be applied locally. Because of the radial symmetry of the temperature field (see Section 4.1.1), it is convenient to project each displacement $\Delta\mathbf{R}(t)$ in radial $\mathbf{e}_{\mathrm{R}}$ and tangential $\mathbf{e}_{\mathrm{T}}$ direction with respect to the trap center located at the temperature minimum (see Figure 4.5). Without such a projection, the thermal drift would average out and disappear in a broadened step size distribution.

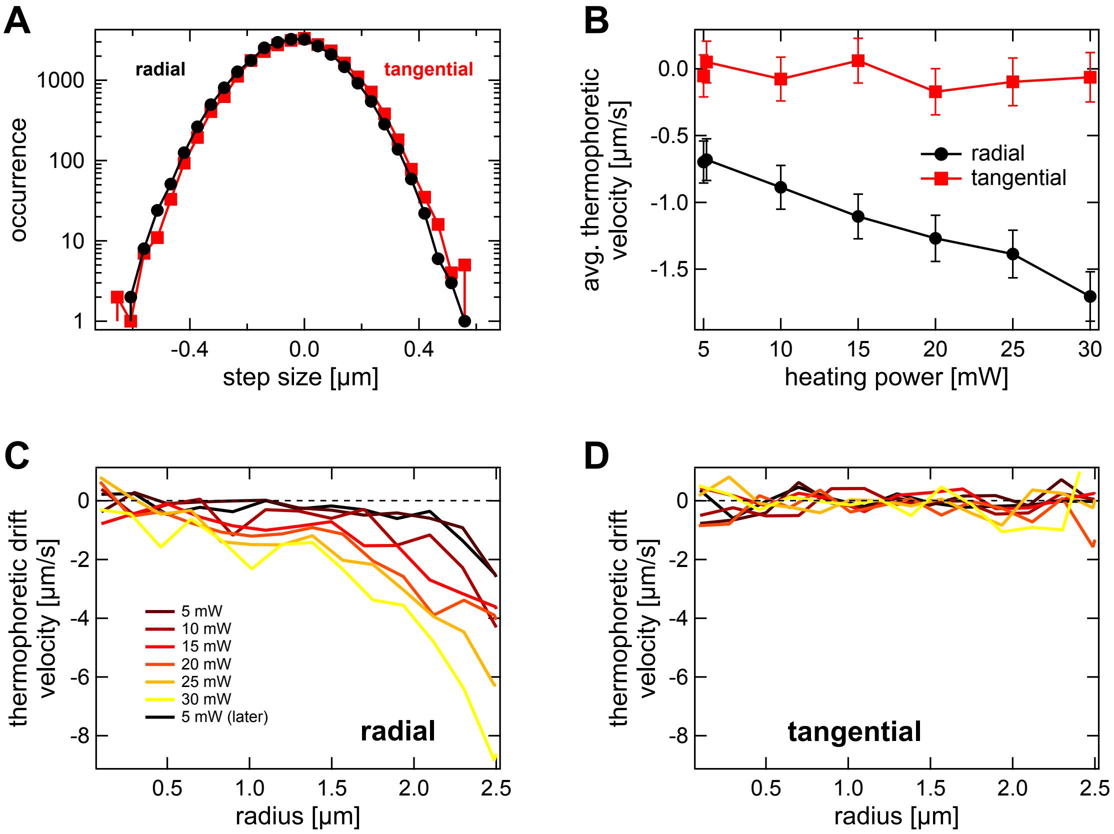

Figure 4.6: **A** Distribution of step lengths after projection in radial (black circles) and tangential (red squares) direction. **B** Average thermophoretic drift velocity in radial (black circles) and tangential (red squares) direction. **C** Radial thermophoretic drift velocity as a function of the radial distance to the trap center for different heating laser powers. **D** Same as in C for the tangential direction.

[a)] Note, that the normalization factor for the 3-dimensional advection-diffusion propagator differs from the 1-dimensional case given in Section 2.1.2 with Equation 2.14.

Figure 4.6 A shows the position distributions after projection in radial (black) and tangential (red) direction. According to Equation 4.3, the width is a measure for the diffusion coefficient, which is discussed within the next section 4.1.4. While the red curve seems to be centered at the origin, the black curve is shifted to negative values. The shift divided by the inverse frame $\tau = 0.01\,\mathrm{s}$ leads to the thermophoretic drift velocity. Here, the average drift in radial and tangential direction is measured, as the histograms include all steps within the trapping region. The dependence of this average drift is plotted in dependence of the heating laser power in Figure 4.6 B. Clearly visible, the average tangential drift disappears for all heating intensities. The average radial drift increases linearly for increasing heating power. This is plausible as the radial drift is parallel and proportional to the temperature gradient $\nabla T \propto P_{\mathrm{heat}}$. Performing this step size analysis under restriction of the starting point of a step $\mathbf{R}(t)$ to a certain radial interval $[R', R' + \mathrm{d}R']$ leads to a more detailed picture of the distribution of the thermal drift velocity field within the trapping region. Figures 4.6 C and D show the dependence of the thermally induced drift in radial and tangential direction, respectively. The tangential drift disappears for all radial distances and heating powers, which is consistent with the shape of the temperature field. Due to the radial symmetry of the gold structure no temperature gradient in tangential direction is expected. In contrast, the radial thermophoretic drift disappears in the center of the trap, but increases in magnitude with increasing radial distance to the trap center R', to about $2\,\mu\mathrm{m/s}$ for the lowest heating power of $5\,\mathrm{mW}$ and about $8\,\mu\mathrm{m/s}$ for the highest measured heating power of $30\,\mathrm{mW}$. As already seen in the average values, the radial drift is always negative corresponding to flow towards the center of the trap. Qualitatively, this distribution is also consistent with the shape of the simulated temperature gradient field. While the temperature gradient disappears in the center at the temperature minimum, it increases linearly with the distance to the center and for longer distances the gradient rises even stronger than linear. A quantitative comparison will be given in Section 4.1.5.

4.1.4 Dynamic Properties – Diffusion Coefficient and Induced Temperatures

While the last section treated the deterministic motion of the particle, *i.e.* the thermal drift induced by the temperature gradient, this section will investigate the additional Brownian motion. This erratic motion is quantified by the diffusion coefficient that can also be accessed via step-size analysis. At a given inverse frame rate τ, the width of the advection-diffusion propagator (Equation 4.3), $\sigma^2 = 2D\tau$, is a measure of the diffusion coefficient D. Analyzing the width after projecting each step in tangential direction leads to the values plotted in Figure 4.7 A. Considering only the step size distribution in tangential direction ensures a decoupling from the thermal drift not present in this direction. As seen from the figure, the diffusion coefficient increases from $0.75\,\mu\mathrm{m}^2/\mathrm{s}$ at the lowest heating power of $5\,\mathrm{mW}$ to $1.08\,\mu\mathrm{m}^2/\mathrm{s}$ for the highest heating power measured being $30\,\mathrm{mW}$. This increase is a result of the rising average temperature the particle is exposed to while it is trapped. To find a relation between the heating power and the temperature rise in the trapping region, the measured trend of diffusion coefficients are compared to a theoretical model, where the Stokes-Einstein relation is considered together with a Vogel-Fulcher (VFTH) temperature dependence for the viscosity of water,

$$D(\Delta T) = C_{\mathrm{B}} \cdot \frac{k_{\mathrm{B}}\,(T_0 + \Delta T)}{6\pi\eta\,(T_0 + \Delta T)\,R} \propto \frac{(T_0 + \Delta T)}{\eta\,(T_0 + \Delta T)}. \tag{4.4}$$

Herein, $\eta(T) = \eta_\infty \exp A/(T - T_{\mathrm{VF}})$ denotes the viscosity with the coefficients $\eta_\infty = 0.0298376\,\mathrm{mPa\cdot s}$, $A = 496.889\,\mathrm{K}$ and $T_{\mathrm{VF}} = 152.0\,\mathrm{K}$.[160] The artificial factor C_{B} accounts for a decreased mobility due to the hydrodynamic interactions of the particle with the nearby glass surfaces.[161,162] This effects can be assumed to be temperature independent and does therefore not influence the relation between temperature rise and heating power. Also, a reduction of D due to the thermal expansion (less than one percent) of the particle is neglected. As the increase in fluctuations is relatively small due to the small temperature rise ΔT compared to the absolute temperature $T \sim T_0$, the major contribution to the temperature dependence originates from the decreasing viscosity. At a given heating power, the temperature in the local proximity of the particle varies by just a few K, which is why the relative error of the absolute temperature is small ($\Delta T/T < 2\%$). Therefore, the deviation from thermal equilibrium is small and Equation 4.4 may be used. To influence the diffusion coefficient noticeably by out-of-equilibrium effects, much stronger temperature gradients are necessary in the direct vicinity of the Brownian particle as is the case *e.g.* for Hot Brownian Motion.[160]

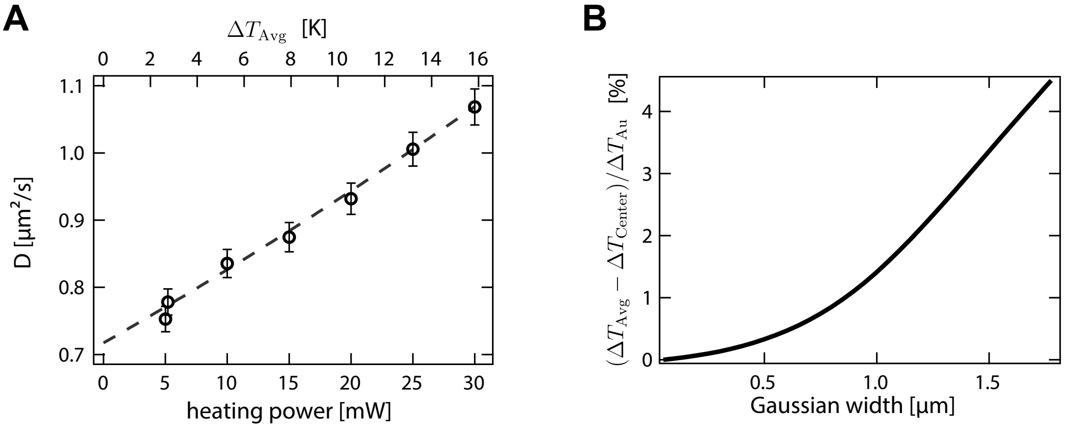

Figure 4.7: **A** Diffusion coefficient obtained from step size analysis in dependence on the heating power. Dashed line according to Equation 4.4 for $\Delta T_{\mathrm{Avg}}/P_{\mathrm{heat}} = 0.53\,\mathrm{K/mW}$ and $C_{\mathrm{B}} = 0.35$. **B** Relative increase in average temperature $(\Delta T_{\mathrm{Avg}} - \Delta T_{\mathrm{Center}})/\Delta T_{\mathrm{Au}}$ in dependence on the width σ of the position distribution in the trap.

Matching Equation 4.4 with the experimental data in Figure 4.7 A yields a temperature rise with heating power of the trapped particle of $\Delta T_{\mathrm{Avg}}/P_{\mathrm{Heat}} = 0.53\,\mathrm{K/mW}$. This temperature increase with heating power is averaged over the entire trajectory. However, averaging the measured position distribution over the simulated temperature field, $\Delta T_{\mathrm{Avg}}(\sigma) = \int \Delta T(\mathbf{r})\, p(\mathbf{r};\sigma) \mathrm{d}r$ shows that for a typical confinement of less than $\sigma \sim 2\,\mu\mathrm{m}$ the average temperature rise ΔT_{Avg} increases less than 5% from the temperature increase in the local minimum $\Delta T_{\mathrm{Center}}$ (see Figure 4.7 B), because the particle is mostly located in the central region of the trap. Hence, the average temperature rise a particle experiences may be identified with the temperature rise at the center of the trap $\Delta T_{\mathrm{Avg}} \approx \Delta T_{\mathrm{Center}}$. For the highest heating power used in the experiment being 30 mW, an average temperature rise of 15.8 K is measured. Considering the shape of temperature field which was simulated in Section 4.1.1, where it was found that $\Delta T^{\mathrm{rel}}_{\mathrm{Center}} = \Delta T_{\mathrm{Center}}/\Delta T_{\mathrm{Au}} = 0.83$ for a trap diameter of 5.3 µm, the temperature rise at the surface of the gold structure is 19.0 K, accordingly. The particle is thus effectively trapped in a temperature difference of about 3 K. The resulting effective trapping potential will be discussed in the next section.

4.1.5 Soret Coefficient and Effective Trapping Potential

With the knowledge of the absolute temperature rise gained from the last section, now, the Soret coefficient can be quantified. Therefore, two independent approaches can be used. Either, S_T is calculated from the steady-state position distribution described by Equation 2.19, or, by measuring the thermophoretic drift velocity. While the position distribution is solely determined by the Soret coefficient if the temperature field is known, the thermal drift is actually dependent on the thermodiffusive coefficient D_T. The Soret coefficient $S_T = D_T/D$ may be then obtained by dividing by the diffusion coefficient. The positional distribution is given by the histogram of a trajectory positions, *i.e.* no dynamic information is needed. Contrarily, measuring the thermophoretic drift velocity by analyzing the step size distribution relies on dynamic information only. Thus, the two ways of calculating the Soret coefficient from the same data set are fully independent, however, both rely on the same absolute temperature measured before.

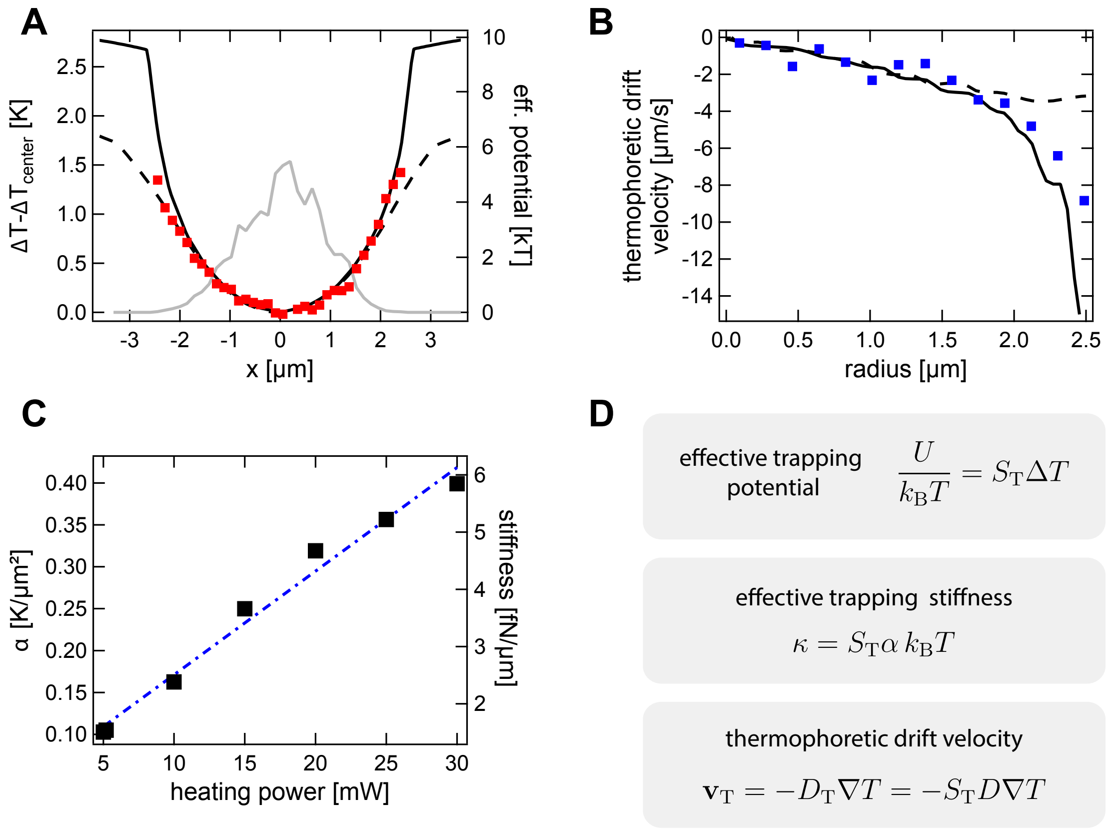

$$\frac{U}{k_B T} = S_T \Delta T$$

$$\kappa = S_T \alpha \, k_B T$$

$$\mathbf{v}_T = -D_T \nabla T = -S_T D \nabla T$$

Figure 4.8: **A** Temperature distribution (red squares) calculated from the position distribution of a trapped particle for a heating laser power of 30 mW (gray and in arbitrary units) and a Soret coefficient of $S_T = 3.56\,\mathrm{K}^{-1}$. Simulated temperature field in the plane of the gold structure (black) and 300 nm above (dashed) with a central temperature rise of $\Delta T_{\mathrm{Center}} = 15.8\,\mathrm{K}$. **B** Comparison between radial thermophoretic drift velocity measured from step size analysis (30 mW heating power, blue squares) and drift expected from the simulated temperature field in the plane of the gold structure (black) and 300 nm above (dashed) for a Soret coefficient of $S_T = 3.56\,\mathrm{K}^{-1}$ and a diffusion coefficient of $D = 1.08\,\mu\mathrm{m}^2/\mathrm{s}$. **C** Curvature of the temperature field α and corresponding effective trapping stiffness k versus heating laser power P_{heat} for the same Soret coefficient. **D** Overview of important parameters plotted in A, B and C.

As the shape of the temperature profile is known from simulations, the absolute applied temperature field for a heating power of 30 mW is fully determined with the measured $\Delta T_{\mathrm{Center}} = 15.8\,\mathrm{K}$ and is plotted in Figure 4.8 A as the black line (gold surface plane) and the dashed black line (300 nm above the gold structure). The measured data for the position distribution (grey line in a.u.) matches the temperature field with $\Delta T(x) = -1/S_{\mathrm{T}} \ln(P(x)) + \mathrm{const.}$ best for a Soret coefficient of $S_{\mathrm{T}} = 3.56\,\mathrm{K}^{-1}$ (red squares). Figure 4.8 B shows the experimental data (blue squares) of the thermal drift velocity for the same heating power. The temperature gradient profile $\nabla T(r)$ is calculated from the temperature field in A. The expected drift velocity $v_{\mathrm{T}}(r) = -S_{\mathrm{T}} D \nabla T(r)$ for the above-gained Soret coefficient and a diffusion coefficient of $D = 1.08\,\mu\mathrm{m}^2/\mathrm{s}$ is plotted as the black line. The dashed black line again corresponds to the expected drift velocity 300 nm above the gold structure. As can be seen from Figure 4.8 A and B, both independent methods deliver a consistent match to the temperature field for the same $S_{\mathrm{T}} = 3.56\,\mathrm{K}^{-1}$. The measured Soret coefficient appears to be about a factor of three larger as compared to the literature.[60, 62] However, due to interactions of the particle with the glass surfaces, the diffusion coefficient, which relies on flow fields decaying with one over distance, is decreased by a factor of three compared to free diffusion. As the Soret coefficient is the ratio of the thermodiffusive coefficient and the diffusion coefficient, D_{T} remains thus unchanged as it is determined by the much shorter ranged interfacial flows and is therefore consistent with the literature.

The positional distribution can also be translated into an effective trapping potential. Due to the phoretic nature of thermodiffusion the term “effective” is used, since it is not meant to be a real potential in that sense that $-\nabla U$ resembles an external force acting on the particle. Instead, complex mechanisms lead to a thermophoretic drift of the particle in an external temperature gradient and typically the particle is overall force-free (see Section 2.2). Also, due to the local temperature gradients used for trapping, the system is not in thermal equilibrium. Nevertheless, the particle is trapped in a local temperature inhomogeneity of a few K which is considered to be a only a small deviation to the absolute temperature being about 300 K. The position distribution of the particle may be thus compared to a Boltzmann distribution to gage the strength of the presented thermal trap,

$$\frac{P(\mathbf{r})}{P_0} = \exp\left(-S_{\mathrm{T}} \Delta T(\mathbf{r})\right) \sim \exp\left(-\frac{U(\mathbf{r})}{k_{\mathrm{B}} T}\right). \tag{4.5}$$

This has been done in Figure 4.8 A (see left scale). The particle sampled the potential up to $5\,k_{\mathrm{B}}T$, the overall depth is extrapolated to about $9.5\,k_{\mathrm{B}}T$ for 30 mW heating power in the plane the gold structure and about $6.5\,k_{\mathrm{B}}T$ at a height of 300 nm above the gold film. Note, that the absolute potential depth increases linearly with the temperature rise and therefore with the heating power. Considering an effective harmonic potential in the center of the trap, $U(r) = \frac{\kappa}{2} r^2$, an effective trapping stiffness may be defined with $\kappa = S_{\mathrm{T}} \alpha k_{\mathrm{B}} T$, which is directly proportional to the curvature α of the temperature field in the center of the trap. The experimental values of α and κ are plotted in Figure 4.8 C. In the particular experiment presented here, the curvature of the temperature field is on the order of $0.1\,\mathrm{K}/\mu\mathrm{m}^2$ such that an effective trapping stiffness of several fN/µm is achieved. These values that are achieved by the steady state heating scheme are about a factor 10^3 smaller than the stiffness that can be reached by optical tweezing[163] leading to a broader position distribution. While the trapping stiffness is important, for example, in force spectroscopy, the stability of the trap is governed by the depth of the temperature minimum, *i.e.* the effective trapping potential. The effective trapping stiffness may be tuned by changing the size of the gold structure as will be seen in the next section.

4.1.6 Radius Dependence of the Temperature Distribution

The simulated temperature fields presented in the beginning of this chapter are resulting from a modeled geometry that should match the experimental condition. In particular, the diameter of the gold structure is 5.3 µm, resulting from the size of the PS beads used for micro-sphere lithography. Within the present section, further simulations are presented which deliver insight in how the temperature field alters with changing diameter of the circular hole in the gold film and to what extent this influences the effective trapping potential and stiffness.

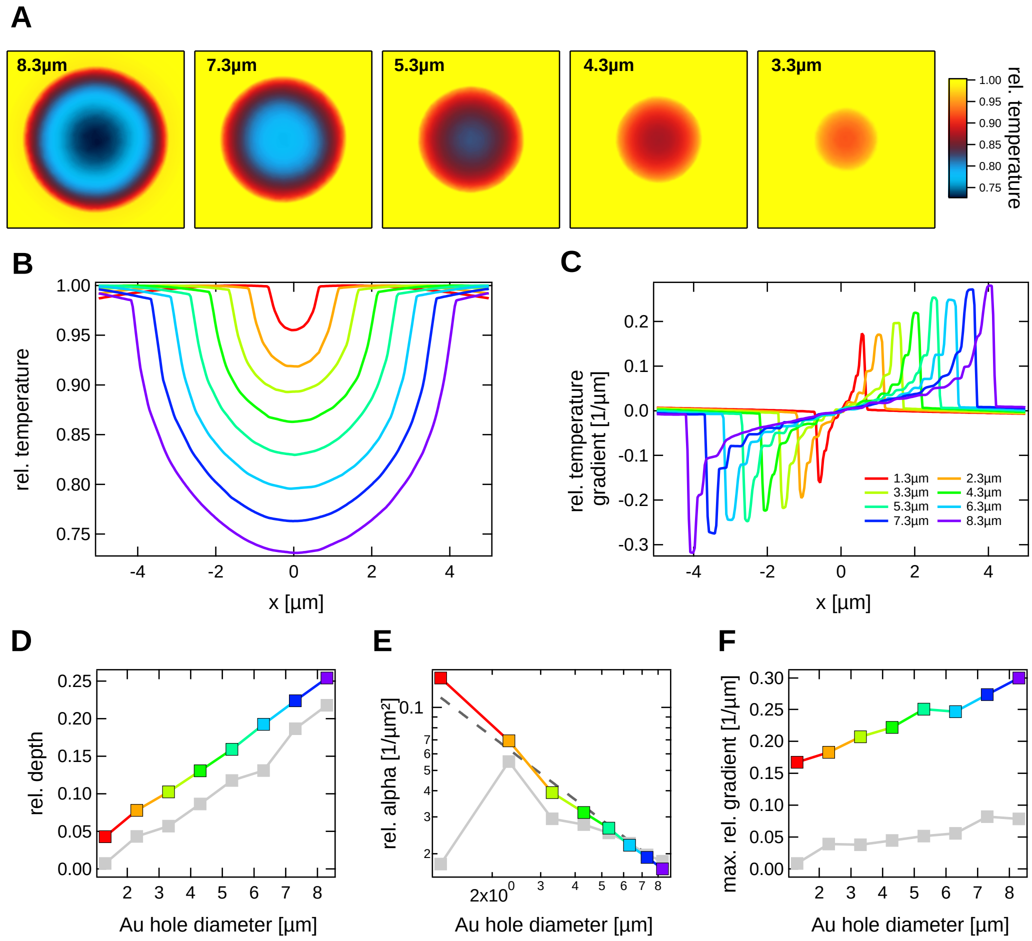

Figure 4.9: **A** Lateral map ($z = 0$) of the relative temperature rise $\Delta T/\Delta T_{\mathrm{Au}}$ for different trap diameters. **B** Line profiles through the center of the relative temperature maps shown in A for trap diameters between 1.3 µm (red) and 8.3 µm (purple). **C** Corresponding relative temperature gradients $\nabla T(x)/\Delta T_{\mathrm{Au}}$. **D** Relative depth of the temperature field $(\Delta T_{\mathrm{Au}} - \Delta T_{\mathrm{Center}})/\Delta T_{\mathrm{Au}}$ for increasing diameter of the gold structure. **E** Relative curvature $\alpha^{\mathrm{rel}} = \alpha/\Delta T_{\mathrm{Au}}$ of the temperature field. **F** Maximum relative temperature gradient at the edge of the gold structure. Each grey data curve corresponds to the same quantity, but is calculated from the lateral temperature fields at $z = 300\,\mathrm{nm}$.

Again, a normalization of all temperatures, temperature gradients and curvatures to the temperature rise at the gold structure ensures that in each case only the shape remains independently from the magnitude, *i.e.* from a particular heating power in the experiment (see Section 4.1). Figure 4.9 A shows the relative temperature fields induced by heated gold structures of different sizes. Line profiles through the center of these fields are plotted in Figure 4.9 B for increasing trap diameters ranging from 1.3 µm to 8.3 µm. The corresponding relative temperature gradients are depicted alongside in

Figure 4.9 C. As readily seen from the temperature field line profiles, the relative depth strongly increases with increasing diameter, which is quantified in Figure 4.9 D in the plane of the gold structure (color-coded) and 300 nm above (grey). Both curves show a linear dependence of approximately the same slope of $0.030\,\mu\mathrm{m}^{-1}$. Between these two planes, the relative difference in depth is 0.04, independently from the diameter as the temperature field decays approximately linear in z-direction. For the above measured Soret coefficient of $S_\mathrm{T} = 3.56\,\mathrm{K}^{-1}$ and a moderate temperature rise of the gold structure of $\Delta T_\mathrm{Au} = 10\,\mathrm{K}$, a potential depth of about $1.0\,k_\mathrm{B}T$ per µm diameter of the gold structure is achieved. The difference in the effective potential energy in z-direction between the gold structure plane and 300 nm above is about $1.4\,k_\mathrm{B}T$. The relative curvature decreases approximately with the inverse diameter $\alpha^\mathrm{rel} = 0.145/\mu m \cdot D^{-1}$ as seen from Figure 4.9 E. Above a diameter of about 2 µm, the curvatures are approximately the same in the two considered planes, since the linear decay of the temperature in z-direction has in first order no influence on the curvature if the structure is sufficiently large. Again, for $S_\mathrm{T} = 3.56\,\mathrm{K}^{-1}$ and $\Delta T_\mathrm{Au} = 10\,\mathrm{K}$, the stiffness per inverse micron diameter is $\kappa = 21.2\,\mathrm{fN}/D$. Overall, a deeper trapping potential has the trade-off of a less stiff trap, or *vice versa*. The choice of the trap diameter thus depends on the particular application. Stiff traps are typically needed for force spectroscopy. Since the main objective of the studied trapping method is to keep an object within a certain region for an extended time periods, typically a larger traps are of interest.

The temperature gradient is linear in the center of the trap, which leads to a harmonic effective trapping potential. Closer to the gold structure, the temperature gradient rises stronger than linear. Here, the temperature gradient can easily exceed a few K/µm even for a moderate heating of the gold structure of $\Delta T_\mathrm{Au} = 10\,\mathrm{K}$ (see Figure 4.9 F). This, however, holds true only within the lateral plane of the gold structure. Looking at the plane 300 nm above, thermal diffusion blurs the distinct peak and the maximum gradient is about a factor of 5 lower (grey data points). Having said that, a stably trapped object rarely enters this region, but is trapped in the center as seen in the experiment.

4.2 Thermophoretic Trapping by Dynamic Temperature Fields

The presented experimental data of the last sections treated the thermophoretic trapping of a single particle by means of a static temperature profile, steady in space and time. Such a heating scheme exhibits unfavorable disadvantages. The main issue is the temperature rise in the center of the trap, that is unavoidable when the entire circumference is heated. Though, this temperature rise does not contribute to the trapping directly. Rather, thermal fluctuations are increased which enhances Brownian motion and may harm, for example, biological material in potential applications. Perspectively, it is therefore the aim to reduce the unwanted temperature rise by providing the temperature gradients needed for trapping by a different heating scheme. It should be noted beforehand, that this issue cannot be solved until the third trapping generation. This second generation, however, constitutes an important intermediate step. Another disadvantage, although only of technical nature, is that with the proposed steady heating scheme the trapped particle is always under direct illumination by the heating beam, which has its maximum intensity in the central trapping region and leads to fast photobleaching. While this problem may also be solved via beam shape engineering or using different wavelengths for fluorescence excitation and heating, it to a large extend disappears with the second trap generation that is presented in the following. Instead of heating the entire gold structure at the same time, only a small area close to the circumference is illuminated by a focused laser beam resulting in a much more localized temperature field as it is sketched in Figure 4.10. The thereby induced temperature gradients are much stronger. Typically the Soret coefficient is positive leading to a decreased particle concentration in the hot region. That means, by steadily heating a single position, particles are repelled and no trapping is achieved. In order to establish a confining potential, the laser beam (and therefore the temperature field) is steered dynamically.

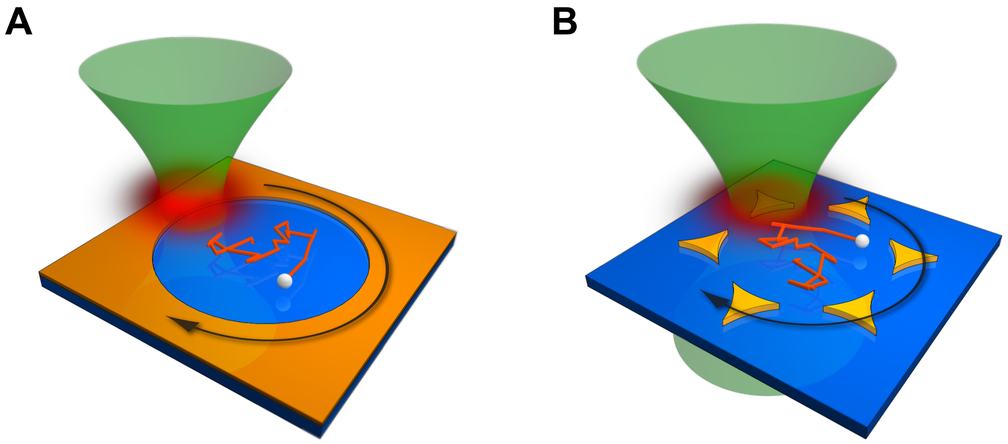

Figure 4.10: Scheme of the thermophoretic trapping by means of a focused laser beam. A confinement of a particle is achieved by periodically driving the laser beam **A** along the rim of a closed gold structure or **B** over the single islands of an open gold structure.

The principle that is treated in the following is inspired by Paul trapping, where a quadrupole electric field produced by four electrodes leads to a saddle-shaped potential for ions in vacuum[44,164] or particles in liquid.[45] While such a potential is attractive in one direction, it is repulsive into the perpendicular direction such that trapping by a steady field is also not possible. By applying a AC voltage to the electrodes, the saddle potential rotates and may generate a stable confinement depending on complex stability parameters. In a similar fashion, to achieve a confinement by purely repulsive thermophoretic flow fields, the focused heating laser beam can be steered in circles at a certain frequency $f = \omega/2\pi$ along the circumference of the closed gold structure, or, in the case of an open gold structure, over the gold patches (Figure 4.10). The expanded laser beam is now only used at low intensities for fluorescence excitation. As will be shown, the rotation of the repulsive thermal potential has a net inward component resulting in an effective steady trapping potential. It is also found that trapped particles dynamically behave similar to particles or ions in a Paul trap.

4.2.1 Introducing a Dynamic Heating Scheme

As an introduction experiment, Figure 4.11 shows the feasibility of trapping a 200 nm-diameter polystyrene particle in an open gold structure. The heating of the single gold islands by means of the focused laser beam is thereby more efficient. A trapping using the expanded laser beam was not possible due to a lack of power of the particular laser used in the setup.

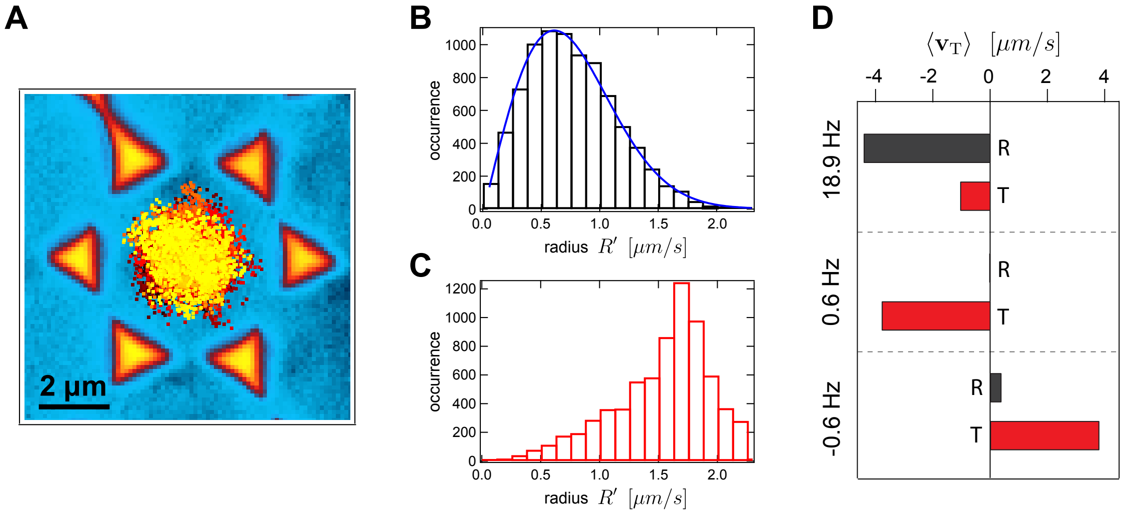

Figure 4.11: Trapping of a 200 nm-diameter polystyrene particle in an open gold structure by dynamic temperature fields. **A** False-color rendering of a bright field micrograph showing the single gold patches. In the center the trajectory points for a single particle are depicted (color coded time). **B** Radial position distribution for a laser rotation frequency of 18.9 Hz. **C** Radial position distribution for a laser rotation frequency of 0.6 Hz. **D** Overview over average radial (R) and tangential (T) drift velocities measured by step size analysis. Positive frequencies indicate a clock-wise rotation, while a negative frequency refers to a counter clock-wise rotation.

Similar as for the closed trap, a Gaussian confinement of $\sigma = (0.60 \pm 0.01)\,\mu\mathrm{m}$ standard deviation is achieved at a laser rotation frequency of $f = 19\,\mathrm{Hz}$. The radial position distribution is well-described by Equation 4.2 (blue curve). At a trap diameter of 5.3 µm and a laser circle radius of about 6.0 µm, the velocity of the rotating temperature field is about 700 µm/s. This is much faster than a typically induced thermophorec drift of a few µm. Hence, to estimate an effective trapping potential depth, it is obvious to assume that the particle effectively feels a steady-state temperature as simulated in Figure 4.3 B. An additional argument for this assumption is the Gaussian particle distribution indicating an effective harmonic temperature profile. With a Soret coefficient of $S_\mathrm{T} = 3.56\,\mathrm{K}^{-1}$ measured in Section 4.1.5 (the same particle solution and sample geometry is used) and a confinement $\sigma = 0.60\,\mu\mathrm{m}$, a curvature of the temperature field of $\alpha = 1/S_{\mathrm{T}}\sigma^2 = 0.78\,\mathrm{K}/\mu\mathrm{m}^2$ is calculated. Simulations of the temperature profile yield a value for the normalized curvature of $\alpha' = \alpha/\Delta T_{\mathrm{Au}} = 0.034\,\mu\mathrm{m}^{-2}$. An average temperature rise at the gold structure is then estimated to be $\Delta T_{\mathrm{Au}} = 23.1\,\mathrm{K}$. Note, that this is not the instantaneous temperature rise of a gold island but an average over one cycle. Accordingly, the average temperature increase in the center of the trap is about $\Delta T_{\mathrm{Center}} = 9.2\,\mathrm{K}$. Using a much lower frequency of $f = 0.6\,\mathrm{Hz}$ leads to a much broader distribution. Also, radial position distribution deviates from Equation 4.2. Looking at average drift velocities, one recognizes for the high frequency a fast inward radial drift and a small tangential drift, probably a component due to the rotation of the laser beam. In contrast, for the low frequency, essentially no radial drift is measured, while there is a high tangential drift present switching its sign when changing the rotation direction of the heating beam. The drift velocity of the particle is hence directly related to the motion of the laser beam. The velocity of the laser beam for the low frequency is about $20\,\mu\mathrm{m/s}$ and much closer to the induced drift velocity.

This experiment shows that the dynamics of a particle trapped by a dynamically steered laser beam is not trivial and raises the following issues. It is not clear if the steady-state approximation for high frequencies is indeed allowed. Even if so, in which frequency range is the transition from fast to slow. From the technical point of view, a slow steering is easier to realize. While an acousto-optic deflector is typically fast, galvo-based beam scanners are slower due to inertia of mirrors. Also, is there a stability condition, *i.e.* a minimum frequency for which the trap works at all? These open questions shall be addressed in the following. Due to the radial symmetry, which is much easier to model theoretically, the next experiments are performed on a closed gold structure.

4.2.2 Temperature Profile by a Focused Laser Beam

Upon illumination of the gold structure by a focused laser beam, a temperature field is generated in the proximity of the heated spot. To get an impression of the temperature distribution, the steady-state heat Equation 2.55 is studied numerically via FEM simulations performed analogous as described in Section 4.1.1. Here, the heat source density $q(\mathbf{r})$ is modeled by a 2D-Gaussian function of width $\sigma = 1.0\,\mu\mathrm{m}$ to account for the focused laser beam illuminating the circumference of the gold structure. Figure 4.12 presents the results for a $8.3\,\mu\mathrm{m}$-diameter gold structure (white dashed circle), which is heated at a radial distance to the center of about $9\,\mu\mathrm{m}$. Figure 4.12 A shows the lateral temperature maps in the plane of the gold structure. In the following, all temperature fields and gradients again are normalized to ΔT_{Au}, which now refers to the hottest point on the gold structure. Compared to the expanded laser illumination, where the rim of the gold structure is isothermal (Figure 4.12 B, dashed red), here, the circumference reaches half the temperature rise at about 30° (black and grey). This localization of the heat source leads to a faster decay of the temperature into the trapping region (Figure 4.12 C) and goes along with stronger temperature gradients as shown in Figure 4.12 D. An additional important difference to the expanded heating scheme is that the temperature gradient does not disappear nor changes sign in the center. That means in particular, that no static temperature minimum is present. As a consequence, the particle will quickly escape from the trapping region if the heating beam is not steered in an appropriate way, *e.g.* by a rotation along the gold edge. The dynamical properties of a particle trapped by a rotating temperature field are studied in the following.

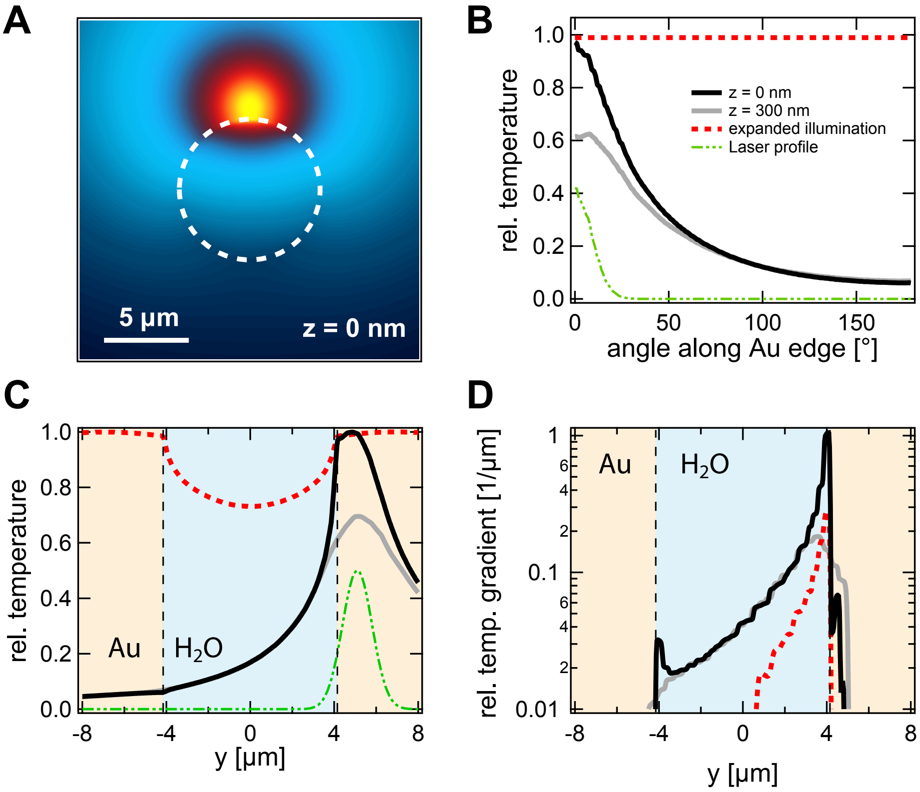

Figure 4.12: FEM simulation of the temperature field produced by a laser beam focused to the rim of the gold structure (8.3 µm diameter). **A** Lateral temperature elevation map in a plane directly above the gold structure. **B** Relative temperature rise along the circumference of the gold structure (black) for heating by a focused laser beam (indicated in green in arbitrary units) and 300 nm above (gray). The red dashed line indicates the isothermal circumference for heating of the entire gold structure. **C** Vertical temperature line profiles through the laser spot and the center of the trap. Same color coding as in B. **D** According relative temperature gradients.

4.2.3 Motivation of a Rotating Frame

The following two sections approach the dynamics of the particle by trapping experiments of single 460 nm-diameter polystyrene beads. The relatively large size is chosen to reduce Brownian motion compared to the induced thermophoretic flow field. Figure 4.13 A and B show the positional distribution of two trapping events of the same particle at a heating power of 2.0 mW, that only differ in the laser rotation frequency. In A, a fast rotation with $f = 100\,\text{Hz}$ was used, while B shows the result for $f = 0.7\,\text{Hz}$. As already recognized in Section 4.2.1, the distribution broadens for the low frequency ($\sigma_{100\text{Hz}} = (1.23 \pm 0.05)\,\mu\text{m}$ vs. $\sigma_{0.7\text{Hz}} = (1.48 \pm 0.06)\,\mu\text{m}$). The confinement results from the induced thermal drift, which is in its magnitude only dependent on the heating power, but is independent of the rotation frequency. The weaker confinement suggests that the inward component of the thermal drift is decreased for a slower rotation. This is confirmed in Figure 4.13 C, where the radial thermal drift velocity for both frequencies is plotted in black. Also, while for the high frequency no tangential drift is measured, it is clearly seen, that the tangential component dominates for the low frequency, as was already recognized for the open gold structure (Figure 4.11). However, due to the time dependence and the lost radial symmetry of the temperature field, the projection of the thermally induced drift velocity in radial and tangential direction is not anymore suited to access the full dynamics of the trapped object. Instead, the dynamics of the particle may be resolved when transforming the trajectory into a rotating frame, in which the laser beam and therefore the temperature field is steady, but the sample rotates about the center of the trap.

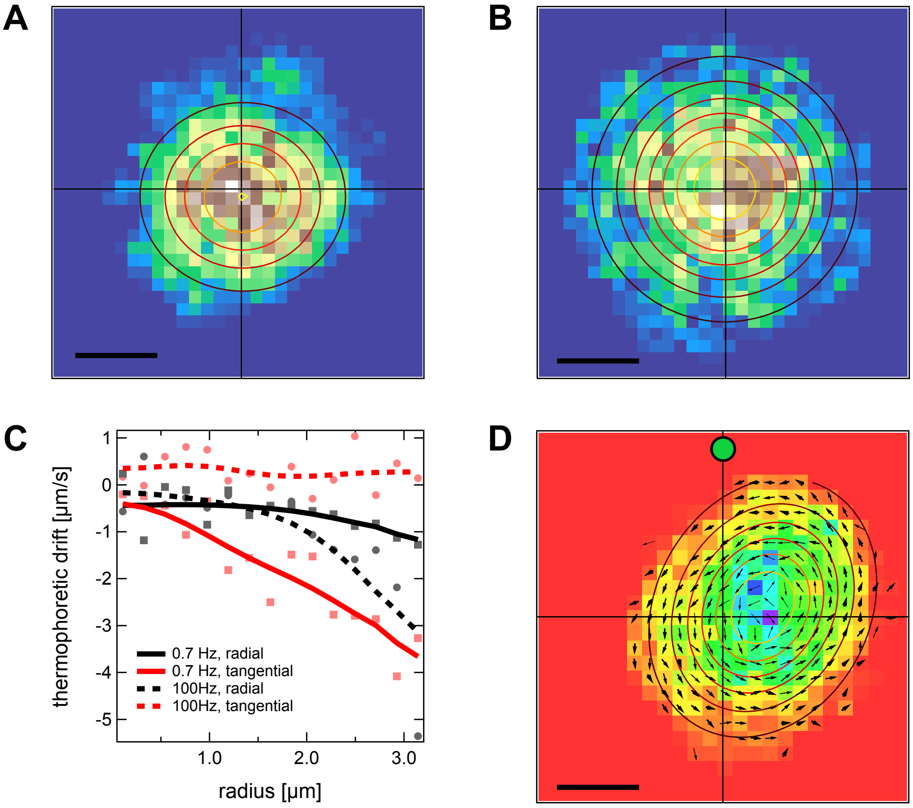

Figure 4.13: Positional distribution of a 460 nm-diameter polystyrene bead trapped in a trap of 8 µm diameter for a laser rotation frequency of 100 Hz in **A** and 0.7 Hz in **B**. Scale bars measure 2 µm. The horizontal and vertical lines indicate the center of the trap. **C** Thermophortic drift velocity in radial (black) and tangential (red) direction for a laser rotation frequency of 100 Hz and 0.7 Hz (dashed). The curves show a median of the raw data (circles and squares in the background). **D** Positional distribution of the particle trapped at 0.7 Hz after switching to the rotating frame. The arrows indicate the average flow field of the particle. To improve the distinction, a different color scale is used within the rotating frame. Contour lines reveal an eccentricity of the position distribution.

To do that properly, the trajectory of the laser beam rotating along the circumference of the hole in the gold film is acquired by tracking the induced fluorescence on the gold film and is afterwards transfered to the rotating frame. The needed parameters such as frequency, phase and center of the rotation are optimized until the trajectory collapses onto a single point. The gained parameters are then used to transform the trajectory of the particle into the same rotating frame. Following the latter procedure, the position distribution for the trajectory of the trapping at $f = 0.7$ Hz in the rotating frame is depicted in Figure 4.13 D. Note that a different color scale is chosen for the distribution histograms in the rotating frame. The focused laser beam is fixed on the top, the position is indicated by the green dot. The position distribution in the rotating frame is obviously not centered with the origin in contrast to the distribution in the lab frame. Also, the distribution is Gaussian, but appears to be anisotropic and tilted by about 45°. Averaging out the erratic Brownian motion, the velocity field of the particle is indicated by the arrow field revealing a circular motion, not around the center of the trap, but around the center of the position distribution. Qualitatively, these features may be understood such that, due to the repulsive character of the temperature field and the advective flow resulting from the rotation of the sample, the particle is always held ‘in front of’ the heated spot. By transforming the position distribution back to the lab frame (or via a rotation average), the anisotropy disappears and the broadened and symmetric position distribution is received.

4.2.4 The Rotating Frame – Theory vs. Experiment

The next section gives a detailed theoretical description of the particle dynamics which is directly verified by dedicated experiments. The theoretical description that will be presented is the result of a collaboration with Prof. Alois Würger.[a)] The understanding benefits from a direct discussion of the theory together with the experimental counterpart.

In the first part, Brownian motion will be neglected and only the deterministic motion of the particle is considered. The influence of the erratic motion on the trapping is discussed later on. Also, due to the low Reynolds number of about $\mathrm{Re} \sim 10^{-6}$, viscous motion dominates over inertial effects as discussed in the Section 2.1.1. Inertia is thus be neglected such that the particle instantaneously follows the thermophoretic and advective drifts.

Stationary Points in the Flow Field The flow field in the rotating frame $\mathbf{u}$ consists of two components that are the thermal drift $\mathbf{v}_\mathrm{T} = -D_\mathrm{T}\nabla T$ generated by the local heating and the advection $\omega \times \mathbf{r}$ resulting from the rotation of the sample about the origin, as illustrated in Figure 4.14 A.

$$\mathbf{u} = \mathbf{v}_\mathrm{T} + \omega \times \mathbf{r} \tag{4.6}$$

For the sake of simplicity, the temperature profile generated by the heating beam is approximated with the analytic expression for a point heat source (see Section 2.4.2)

$$T(\mathbf{r},t) = T_0 + \frac{P_\mathrm{Abs}}{4\pi\kappa\,|\mathbf{r} - \mathbf{r}_\mathrm{L}(t)|}. \tag{4.7}$$

Herein, $\mathbf{r}_\mathrm{L}(t)$ denotes the trace of the heating laser beam. In the rotating frame, the heat source is steadily located at the rim of the gold structure of radius a, indicated with a green dot in Figure 4.14 A. The temperature gradient is then given with $\nabla T = -P_\mathrm{Abs}/(4\pi\kappa R^2)$, where $R = |\mathbf{r} - a\mathbf{e}_y|$ is the distance to the heat source. As it will turn out, it is convenient to define a unit-less parameter

$$\xi = \frac{\omega a}{u_\mathrm{T}}, \tag{4.8}$$

which compares the tangential laser velocity ωa to the thermophoretic velocity $u_\mathrm{T} = D_\mathrm{T} P_\mathrm{Abs}/(4\pi\kappa a^2)$ at a distance a from the heat source. The resulting velocity field $\mathbf{u}$ is plotted for the upper-right quadrant of the trap and for $\xi = 6$ in Figure 4.14 B. Two positions in the flow field are notable (blue and red dots in Figure 4.14 B), where the thermal drift and the advective flow compensate such that the velocity vanishes, $\mathbf{u} = 0$. The top stationary point marked in blue is unstable in that sense that any slight perturbation will drive the particle either to infinity or towards a second stationary point marked in red, which appears to be stable. The flow field in the proximity of the latter stable point resembles a spiral and will be later discussed in detail. Disregarding Brownian motion, once a particle reaches

---

[a)] Visiting professor in Leipzig (Leibniz-Professur, summer semester 2013).

the lower stable point, it is steady in the rotating frame but shows a circular motion around the trap center when transformed back to the lab frame.

Being of particular interest for the trapping, the frequency dependence of the locations of the stationary points is investigated. Using the approximated temperature field of Equation 4.7 and setting Equation 4.6 to zero, $\mathbf{u} = 0$, returns a cubic $\xi^2 y(a-y)^2 = a^3$ as well as a quadratic equation $x^2 = y(a-y)$. The latter resembles a half-circle, which is indicated in orange in Figure 4.14 B. Solving these equations yields the positions of two stationary points within the radial distance a from the origin.

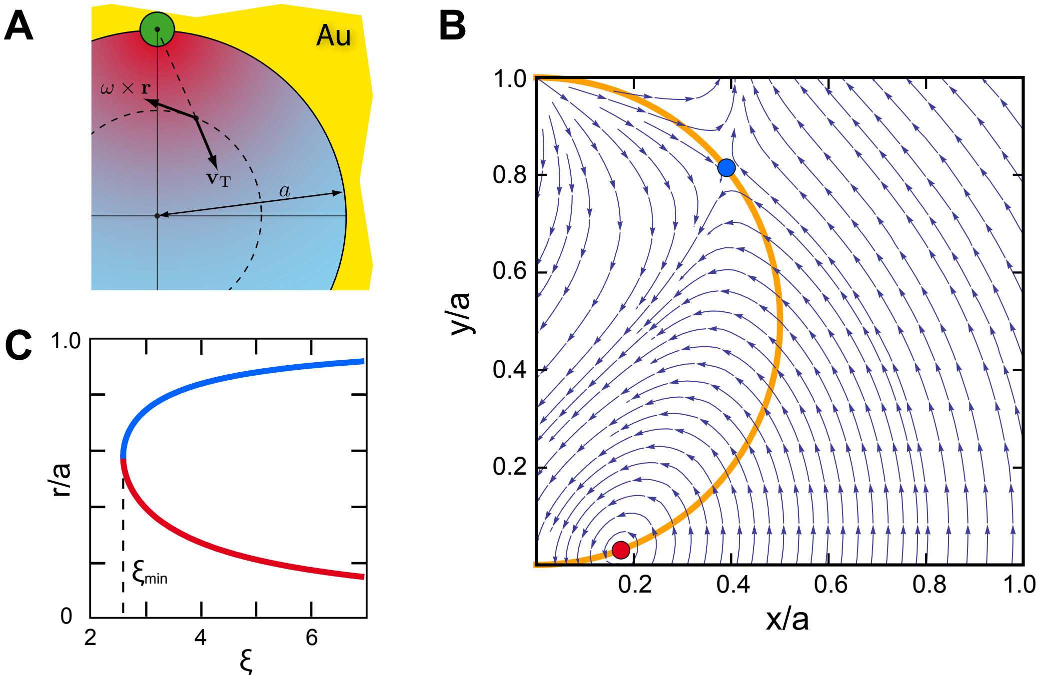

Figure 4.14: **A** Scheme of the trap in the rotationg frame. The position of the laser beam and therefore the heat source is marked as the green dot. The direction of the advective flow $\omega \times \mathbf{r}$ tangentially about the center and the thermal drift radially away from the heat source is indicated by the arrows. **B** Flow field $\mathbf{u}(x,y)$ observed in the rotating frame for $\xi = 6$. The orange curve represents the half circle $x^2 = y(a-y)$. With increasing frequency, the unstable stationary point (blue dot) shifts along the orange line towards the laser beam, while the stable point (red dot) wanders towards the center. For decreasing frequency, the points merge for $\xi = \xi_\mathrm{min} \approx 2.6$. **C** Radial distance of the stable (red) and unstable (blue) stationary point to the trap center in dependence on ξ.

For sufficiently large ξ, the two points are well-separated, but approach each other on the half-circle for decreasing ξ, until they eventually meet for a minimum ξ of $\xi_\mathrm{min} = \sqrt{27/4} \approx 2.6$. This dependence is depicted in Figure 4.14 C, where the radial distance of the stable and unstable stationary points are plotted in red and blue, respectively. No stationary points exist for smaller values of ξ. At a given trap diameter and heating power, this defines a minimum frequency for which a trapping can be achieved. For lower frequencies, the laser rotation is to slow to prevent an escape of the particle due to the thermophoretic drift driving the particle radially away from the heat source. Hence, $\xi > \xi_\mathrm{min}$ gives a theoretical stability condition for the trapping of a particle. Note, that only the repulsive character of the thermal potential causes the instability for lower frequencies as Brownian motion is yet neglected. With typical thermal drifts of order $u_\mathrm{T} \sim \mu\mathrm{m/s}$ and trap radii of $a \sim \mu\mathrm{m}$, the minimum frequency is of order $\omega/2\pi \sim$ Hz. With increasing ξ, the stable point approaches the center of the trap, whereas the unstable one converges to the position of the heat source (see Figure 4.14 B and C). The coordinates of the stable point may be expressed by a power series in ξ, and therefore in dependence on the frequency ω, with $y_0 = a\left(\xi^{-2} + 2\xi^{-4} + \ldots\right)$ and $x_0 = \sqrt{y_0(a - y_0)}$. Paying attention to the radial symmetry of the trap, the coordinates may also be transfered to polar coordinates with r_0 being the distance to the trap center

$$\frac{r_0}{a} = \frac{1}{\xi} + \frac{1}{\xi^3} + \ldots \tag{4.9}$$

and the angle φ_0 with

$$\tan\varphi_0 = \frac{1}{\xi} + \frac{3}{2\xi^3} + \ldots . \tag{4.10}$$

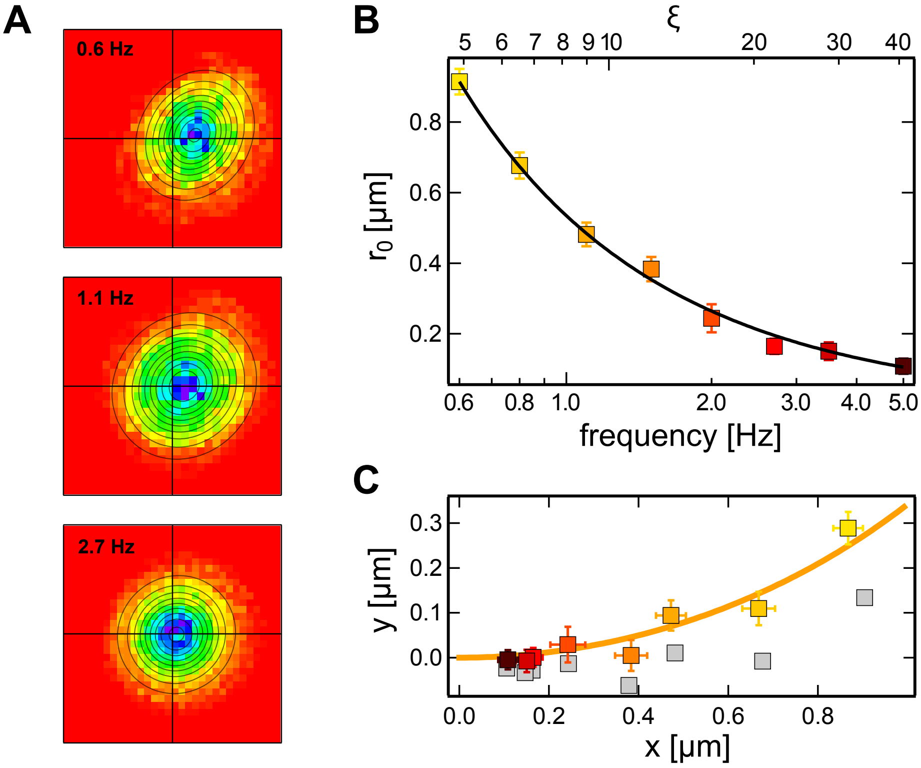

Figure 4.15: A Positional distribution histograms in the rotating frame for a 460 nm diameter polystyrene bead for the laser rotation frequencies 0.6 Hz, 1.1 Hz and 2.7 Hz. **B** Radial distance of the central point of the position distributions (which coincides with the stable stationary point) versus the laser rotation frequency. A fit of Equation 4.9 yields a thermal drift at a distance from the heat source of $a = 4.3\,\mu\text{m}$ of $u_\text{T} = (3.3 \pm 0.1)\,\mu\text{m}$. **C** Position of the central point for the different frequencies (color-coded). The raw data (gray) was tilted by 10° about the center in order to correct the effect of the extended heat source. Again, the orange curve plots the half circle $x^2 = y(a - y)$.

In order to verify the gained theoretical insight, the following experiment was performed. A 460 nm diameter polystyrene particle is thermophoretically trapped in a water film above a closed gold structure of radius $a = 4.3\,\mu\text{m}$. The heating laser power is held constant at moderate $P_\text{heat} = 1.7\,\text{mW}$. Movies are acquired for rotation frequencies ranging from 0.6 Hz to 5.0 Hz. The particle and laser positions are extracted from the movie files afterwards. Each trajectory of the particle is then transfered to the rotating frame following the procedure explained in the last Section 4.2.3. Figure 4.15 A presents the corresponding position distribution histograms for three rotation frequencies in the rotating frame. The position of the stable point is identified with the maximum of the distribution. The decreasing shift of the distribution from the center with increasing frequency is clearly visible. The radial distance r_0 in dependence on the frequency $f = \omega/2\pi$ is plotted in Figure 4.15 B. Fitting Equation 4.9 yields a thermophoretic drift velocity of $u_\mathrm{T} = (3.3 \pm 0.1)\,\mu\mathrm{m}$ at a distance of $a = 4.3\,\mu\mathrm{m}$ from the heat source. This value is consistent with the temperature rise at the center of the trap of $\Delta T_\mathrm{Center} = 12\,\mathrm{K}$ estimated using the simulated temperature profile.

As can be seen from Figure 4.15 C, the absolute x and y positions (grey data points) of the maximums deviate from the theoretically predicted half circle plotted in orange. The deviation is stronger for decreasing frequencies. The observation, that the radial distance matches the theoretical description, implies that the measured phase angle precedes the angle given by Equation 4.10. This is explained with the finite size of the heat source and the high thermal conductivity of the gold film, which results in a spatially extended temperature field in contrast to the theoretical assumption of a point heat source (Equation 4.7). The data is corrected by introducing an additional shift angle $\Delta\varphi_0$, which is assumed to only depend on the real shape of the temperature field and in particular not on the frequency ω[a)] . Doing so (color-coded data points) yields a sound agreement with the theoretical prediction for $\Delta\varphi_0 = 10^\circ$ (orange line).

Motion Close to the Stable Point The trapping of a particle is achieved at the stable stationary point. Theoretically, onces the particle reaches the stable point it performed a circular motion around the center in the lab frame. The present paragraph explores the motion of a particle while it is close to the stable point. Here again, Brownian motion is still neglected but will be discussed in the next paragraph.

By introducing a new coordinate system in the rotation frame shifted by the coordinate of the stable stationary point, $\hat{\mathbf{r}} = \mathbf{r} - \mathbf{r}_0$, the flow field close to $\mathbf{r}_0$ can be expanded in $1/\xi$, which in first order yields the expression

$$\mathbf{u} = \omega \times \hat{\mathbf{r}} + \frac{\omega}{\xi}(\hat{x}\mathbf{e}_x - 2\hat{y}\mathbf{e}_y) + \ldots . \tag{4.11}$$

Herein, the first term resembles a simple rotation about the stationary point. The second term is independent of the rotation frequency since $\omega/\xi = u_\mathrm{T}/a$, however, is of particular importance for the trapping, because it describes the radial drift driving a particle towards the stable point. While the contribution in $\hat{x}$ direction is pointing outwards, the flow in $\hat{y}$ has twice the magnitude and points inwards (negative sign), hence resulting in a net inward flow when averaging over one cycle. An integration of Equation 4.11 yields the following expressions for the trajectory of a particle in the proximity of the stable point $\mathbf{r}_0$,

$$\begin{aligned} \hat{x}(t) &= A\,\mathrm{e}^{-\Gamma t}\cos(\Omega t - \phi), \\ \hat{y}(t) &= B\,\mathrm{e}^{-\Gamma t}\sin(\Omega t). \end{aligned} \tag{4.12}$$

The latter equations describe a spiral. That means, still neglecting Brownian motion, the particle will converge to the stable point in the long time limit $t \to \infty$. A and B refer to the initial position of the particle. The phase $\phi = 3/(2\xi)$ characterizes the anisotropy or skewness of the spiral. In the

---

[a)] This is fulfilled as long as the heat propagation is much faster than the laser trace velocity, which is well-fulfilled for the used frequencies ω of a few Hz.

high-frequency limit $\xi \to \infty$, the phase vanishes $\phi = 0$ and the anisotropy disappears. The frequency $\Omega = \omega\sqrt{1-\phi^2}$ of the particle in the spiral differs from the laser rotation frequency ω depending on the phase ϕ. The coefficient $\Gamma = \omega/(2\xi) = u_T/(2a)$ describes the damping or the speed of the relaxation of the particle towards the stable point and is independent of the laser rotation frequency ω. Note, that neither the shape of the flow field nor the position of the stationary points are dependent on the particle size. The only particle characteristic appears via D_T describing the interaction of the trapped particle with the temperature gradient. Particle size, however, will influence the effects of Brownian motion that are discussed later.

Figure 4.16 A presents a vectorial plot of the velocity field $\mathbf{u}(x,y) = (u_x(x,y), u_y(x,y))$ calculated from the experimentally obtained trajectory for the lowest measured frequency in the rotating frame. The frequency of $f = 0.6\,\text{Hz}$ corresponds to $\xi = 4.9$. Averaging out Brownian motion, the arrows indicate the mean direction of the particle obtained from step size analysis in the particular spatial region. The speed is represented by the color beneath the arrows, where darker regions indicate a faster flow. The position of the heat source is given by the green dot on the top. Clearly visible, the particle appears to be spiraling around the stable point, where the velocity field vanishes. For a quantitative comparison to the theory given by the Equations 4.11 and 4.12, the vector field extracted from the experimental data is projected in x and y direction and plotted along the horizontal (green) and vertical (violet) lines in Figure 4.16 B and C, respectively. Therein, the corresponding theoretical prediction is represented by the black curves, being in remarkable accord with the experimental data. Note, that the curves are not fitted, but are calculated with no free parameters using $u_T = 3.3\,\mu\text{m}$, which has been extracted before from the experiment (see Figure 4.15 B) and a trap radius of $a = 4.3\,\mu\text{m}$ measured in the movie file.

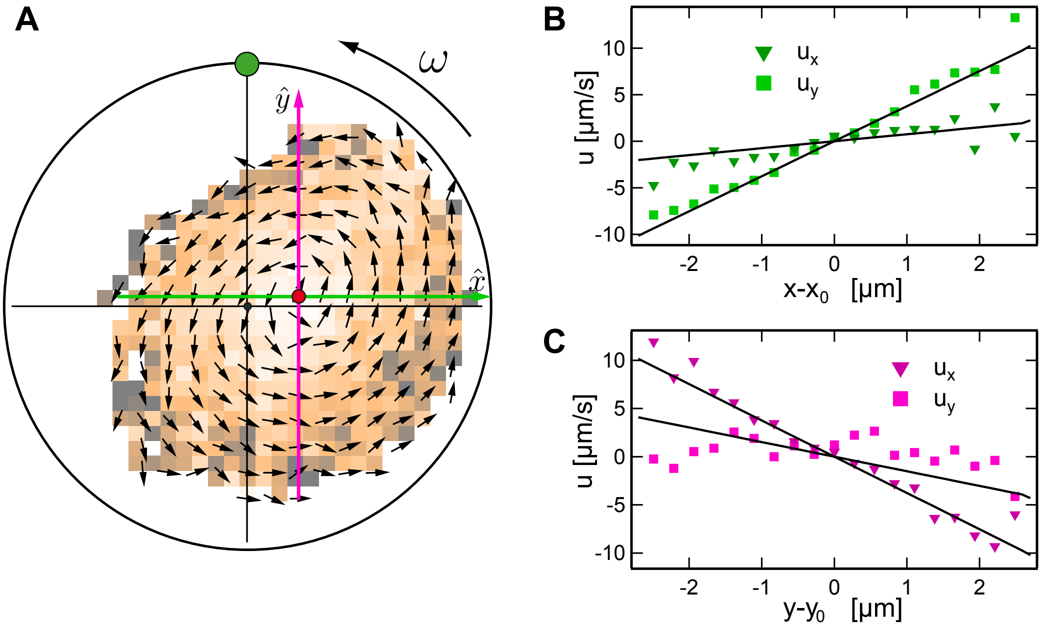

Figure 4.16: **A** Flow field obtained by step-size analysis of the trajectory for $f = 0.6\,\text{Hz}$, where Brownian motion has been averaged out to a large extend. The arrows show the direction of the flow $\mathbf{u}/u$, while the color scale indicates the magnitude $u = |\mathbf{u}|$. The red dot marks the position of the stationary point. **B** x and y component of the flow fields along the horizontal line in A (green). The black lines are calculated from Equation 4.12 for a trap size of $a = 4.3\,\mu\text{m}$ and a thermal drift of $u_T = 3.3\,\mu\text{m}^2/\text{s}$. **C** Same as B but along the vertical line (magenta) in A.

Below, the analogy to the dynamics in a Paul trap shall be pointed out. Paul trapping employs a saddle potential to confine a objects. This saddle in attractive in one direction, but repulsive into the other, which is why the saddle potential is rotated at a high frequency in order to confine a particle or ions.[45,165] The motion of a trapped object is described by two frequencies. Depending on the complex stability parameters, ions trapped in a Paul trap in vacuum are forced on non-trivial trajectories.[44,166] Typically, a macro-motion is observed superimposed with a circular micro-motion at the driving frequency commonly on the order of MHz. Although the frequency range used to trap an object thermophoretically is at a totally different order of several Hz, nevertheless, a similar observation is made. Switching to the rotating frame decouples a micro-motion at the laser frequency ω from the harmonic oscillation of the particle in the rotation frame at a different frequency Ω, which is analogous to the macro-motion in the Paul trap. Due to the viscous medium, an additional damping factor appears, such that the distance of the particle to the stable point decreases exponentially with time until it is eventually reached. Then, the macro-motion disappears and a circular motion of the particle around the trap center is theoretically observed in the lab frame. The analog effect for the trapping of particles using a Paul trap in a viscous medium has been reported as well.[167] This macro-motion not only disappears in the long time limit, but in general for sufficiently large ω due to the disappearance of the phase ϕ. This can be immediately seen from the Equations 4.12, which for $\phi = 0$ exactly resemble the transformation from the lab to the rotating frame since the stable point also converges to the center ($\mathrm{r}_0 \to 0$ for large ω). That means in particular, that the dynamic thermophoretic trap operated at a high frequency ω, such that $\xi \gg \xi_{\mathrm{min}}$, may be treated as if the particle is trapped by a steady heating of the entire gold structure, hence being refereed to as 'quasi-steady' heating. That implies that the unwanted temperature rise in the center of the trap can not be substantially reduced by the new heating scheme. Only a little drop in $\Delta T_{\mathrm{center}}$ of a few percent can be achieved by using a focused laser beam compared to an expanded one that effectively heats a larger area of the gold film as shown later in Figure 4.22. The macro-motion also explains the appearance of the tangential drift for a sufficiently low frequency in Figures 4.11 and 4.13, where the distance of the stable point to the trap center is $r_0 > 0$, while only a radial component is measured for high frequencies. The measured tangential drift is, however, less meaningful for uncovering the dynamics of the particle, since it represents a tangential average of the flow field in the rotating frame.

The trajectory described by Equations 4.12 is the deterministic solution for an anisotropic two-dimensional damped harmonic oscillator, which accordingly suggests a harmonic potential. Adding Brownian motion, the position distribution of a particle within such a potential should resemble a anisotropic Gaussian. This was readily observed in Figure 4.15, but will be studied in detail in the next paragraph.

Brownian Motion and Particle Distribution In reality, Brownian motion spreads any point-like initial probability distribution for a particle in the trap. Practically, this drives the particle away from the stable point. With regard to a stable confinement, this effective outward flow needs to be compensated, which is achieved by the already discussed inward component of the velocity field 4.11 driving the particle towards the stable stationary point.

The detailed theoretical derivation of the relation describing the positional distribution within the rotating frame is given in the publication[168] and is only briefly presented here. The interplay of advection and diffusion is described the a stationary Smoluchowski equation (see Section 2.1.2),

$$\nabla\cdot\mathbf{j} = 0, \quad \mathbf{j} = P\mathbf{u} - D\nabla P, \tag{4.13}$$

where P and $\mathbf{j}$ represent the particle probability density and the corresponding probability flux, D the diffusion coefficient and $\mathbf{u}$ the velocity field in the rotating frame (Equation 4.11). A linearization of $\mathbf{u}$ in powers of $\hat{x}$ and $\hat{y}$ and a projection in radial ($\mathbf{e}_{\hat{r}}$) and tangential direction ($\mathbf{e}_\varphi$) with respect to the stable point yields

$$u_{\hat{r}} = \frac{\omega}{\xi}\frac{\hat{x}^2 - 2\hat{y}^2}{\hat{r}} = \frac{u_\mathrm{T}}{a}\frac{\hat{x}^2 - 2\hat{y}^2}{\hat{r}} \quad \text{and} \quad u_\varphi = \omega\hat{r}. \tag{4.14}$$

This again shows that the radial drift shows outwards in $\hat{x}$ direction, while showing inwards in $\hat{y}$ direction. Also, the radial drift is independent of the frequency ω and is slow compared to the angular motion for any $\xi > \xi_\mathrm{min}$. Hence, during a single cycle, the change in the radial distance to the stable point $\hat{r}$ is weak (*i.e.* the damping is negligible as $\mathrm{e}^{-\Gamma/\Omega} \approx 1$) such that $u_{\hat{r}}$ may be replaced with its time average

$$\bar{u}_{\hat{r}} = -u_\mathrm{T}\frac{\hat{r}}{2a}. \tag{4.15}$$

The negative sign indicates an effective inward flow towards the stable point, which is in steady-state compensated by the diffusive outward flow, $\bar{j}_{\hat{r}} = P\bar{u}_{\hat{r}} - D\mathrm{d}P/\mathrm{d}\hat{r} = 0$. Adapting the problem in skew coordinates $\hat{r}_\pm = \frac{1}{\sqrt{2}}(\hat{x} \pm \hat{y})$, which is possible due to the ellipticity along the diagonal (see Equations 4.12) and taking into account the anisotropy by the non-zero correlation $\overline{\hat{x}\hat{y}} = \frac{1}{2}\hat{r}^2\sin\phi$ yields the following expression for the probability distribution of a particle in the rotating frame,

$$P(\hat{x},\hat{y}) = P_0\exp\left(-\frac{\hat{r}_+^2}{2\sigma_+^2} - \frac{\hat{r}_-^2}{2\sigma_-^2}\right) \tag{4.16}$$

with the mean-squared displacement

$$\sigma_\pm^2 = (1 \pm \sin\phi)\frac{2Da}{u_\mathrm{T}}, \tag{4.17}$$

where $\sin\phi$ may be approximated with $\sin\phi \sim \phi = 3/(2\xi) \propto 1/\omega$. The position distribution therefore shows a distinct anisotropy in diagonal direction for low frequencies, which vanishes for sufficiently high frequencies. Then, an isotropic position distribution is observed with equal widths of $\sigma^2 = \frac{2Da}{u_\mathrm{T}}$. In contrast to the position of the stationary points, the width of the position distribution is dependent on the size of the particle, which appears within the diffusion coefficient $D = k_\mathrm{B}T/(6\pi\eta R)$, such that $\sigma \propto R^{-1}$.

Fitting a 2D-Gaussian to the positional distributions in the rotating frame in Figure 4.15 yields the experimental values for $\sigma_\pm$ which are plotted in Figure 4.17 A as the black squares (σ_+) and red circles (σ_-). The black and red lines plot the according theoretical prediction of Equation 4.16 for a trap size of $a = 4.3\,\mu\mathrm{m}$, a thermophoretic drift of $u_\mathrm{T} = 3.3\,\mu\mathrm{m/s}$ and the according diffusion coefficients which are obtained from step size analysis and are of average $D = 0.59\,\mu\mathrm{m}^2/\mathrm{s}$. Both σ_+ and σ_- are of the expected order, however, do not show a quantitative agreement. The anisotropy σ_+/σ_- is shown alongside in Figure 4.17 B. While the experimentally measured anisotropy follows the theoretical prediction reasonably well for high frequencies, a lower anisotropy is obtained for frequencies below 1.5 Hz. These are the frequencies, where the particle probes the regions in the trap that are closest to the gold edge. Hence, the major deviation is again attributed to the spatially extended heat source, whereas a point source was modeled. The difference in the resulting temperature fields are strongest close to the rim of the gold structure. A stronger inward component of the real temperature gradient along the gold edge compresses the long direction of the position distribution which leads to the decreased anisotropy.

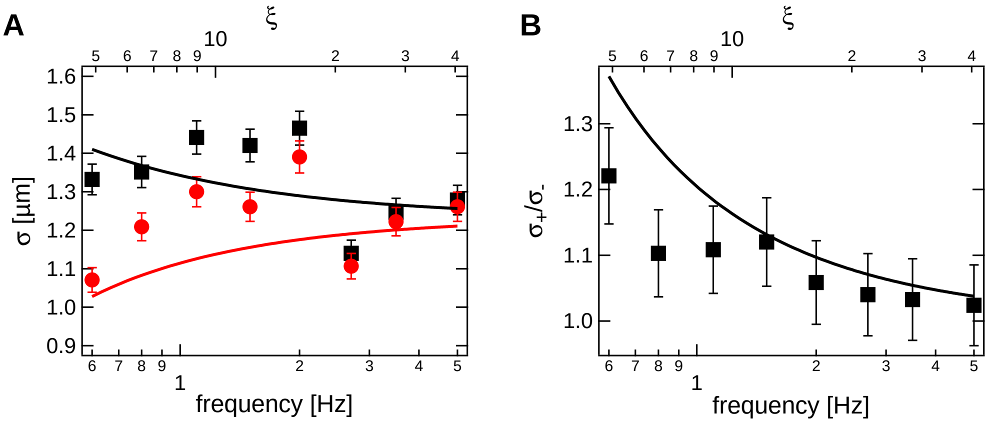

Figure 4.17: **A** Widths σ_+ (black) and σ_- (red) of the positional distributions in Figure 4.15 in the rotating frame in dependence on the laser rotation frequency. The according curves are calculated from Equation 4.17. **B** Anisotropy σ_+/σ_- of the positional distribution versus the laser rotation frequency f.

Finally, a publication by Duhr and Braun in 2006[65] shall be mentioned, where, in order to accumulate particles, a local thermophoretic (repulsive) drift field generated by an optothermal heating of the fluid is superimposed by a linear fluid flow in a micro-channel resulting in a one dimensional confinement. The rotating laser beam in our case produces an analog advection field to achieve a trapping in two dimensions. The theoretical descriptions are alike.

4.2.5 Trapping Above a Plain Film of Gold

The advanced heating scheme allows for more flexibility in terms of the heat source. With a heating by an expanded laser beam, a hole-like structure is essential in order to achieve a local temperature minimum. However, the hole in the gold film may be obsolete due to the local excitation. Often, a focused infrared laser beam is used to locally heat water, also resulting in a repulsive effective potential.[59,63,65] The produced temperature gradients are typically smaller due to the lack of a sharp edge from an absorbing medium to an non-absorbing one. Nevertheless, since an implementation in existing setups would be particularly easy, it shall be demonstrated, that single particles may also be trapped without the need for a non-absorbing micro-structure. Since no appropriate infrared laser beam was available for a direct heating of the water film, a plain gold film without a hole structure is used, producing a comparable temperature field upon local heating. By cycling the focused laser beam along a circular trace on the absorbing gold film, an effective local temperature minimum is achieved.

Single 200 nm-diameter polystyrene particles are confined by a temperature field, which is produced by a focused laser beam driven in circles over a plain gold film at a frequency of $f = 100\,\mathrm{Hz}$. The radius of the circle is varied between 7 µm and 13 µm. Movies of 10000 frames per radius are recorded at a frame rate of 50 Hz resulting in trajectories of 200 s length. Figure 4.18 A shows the position distribution histograms for three different laser traces (green dashed circles). Obviously, the confinement decreases for increasing laser circle diameter. Each distribution resembles a Gaussian, indicating an effective harmonic trapping potential in the central region. The corresponding effective trapping potentials $U/k_BT = -\ln P/P_0$ are plotted in Figure 4.18 B for the according radii. The quadratic fits (dashed black) readily prove the harmonicity of the potentials.

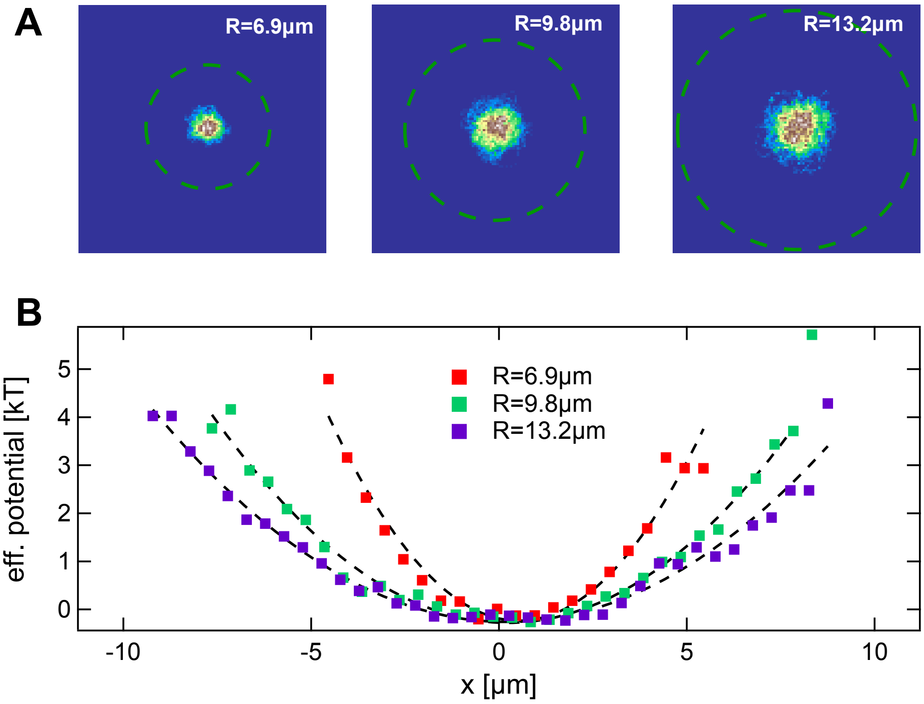

Figure 4.18: A Positional distribution of a 200 nm polystyrene particle confined by a rotating laser beam focused to a plain gold film (no hole structure) for different circle radii (6.9 μm,9.8 μm and 13.2 μm). **B** Corresponding effective trapping potentials $\Delta U/k_BT = -\ln(P/P_0)$ calculated from the postion distribution.

In order to describe the measured distributions theoretically, the produced temperature fields are calculated numerically by a similar FEM simulation described in the Sections 4.1.1 and 4.1.6. Figure 4.19 A shows the lateral temperature field above the gold film produced by the focused laser beam. To create the circular heating profile, experimentally, the laser beam is subsequently steered to 36 positions, *i.e.* in 10° steps, on a ring with the particular radius. A step frequency of 3600 Hz results in an effective laser rotation frequency of 100 Hz. Due to the high frequency, the particle feels the time-averaged temperature field as was shown in the last Section 4.2.4. Hence, the according temperature field results from a super-position of the field shown in A is duplicated to 36 positions along the circle of the particular radius, shown in Figure 4.19 B for different radii. Figure 4.19 C depicts temperature line profiles normalized to the maximum of the rotated temperature field $\Delta T_{\mathrm{Au,Rot}}$. For consistency, the same notation for the subscript ΔT_{Au} is used for the maximum temperature rise although here the gold film covers the entire trapping region. For a heating by means of the focused laser beam, the temperature increment per heating power $\Delta T_{\mathrm{Au}}/P_{\mathrm{Heat}} = 29\,\mathrm{K/mW}$ is known from a measurement that will be presented later in Section 4.3.3. The averaged maximum temperature rise along the circle $\Delta T_{\mathrm{Au,Rot}}$ due to the laser rotation is much lower than the instantaneous temperature rise at the position of the laser beam ΔT_{Au} and is a priori not known. However, it is clear, that the center temperature must be the same for the case of a rotating and a steady focused laser beam, since the absolute distance to the heat source is in both cases the same at any time. Adjusting $\Delta T_{\mathrm{Au,Rot}}$ accordingly (Figure 4.19 D) allows for the calculation of the ratio $\Delta T^{\mathrm{rel}}_{\mathrm{Au,Rot}} = \Delta T_{\mathrm{Au,Rot}}/\Delta T_{\mathrm{Au}}$, which is plotted in Figure 4.19 E.

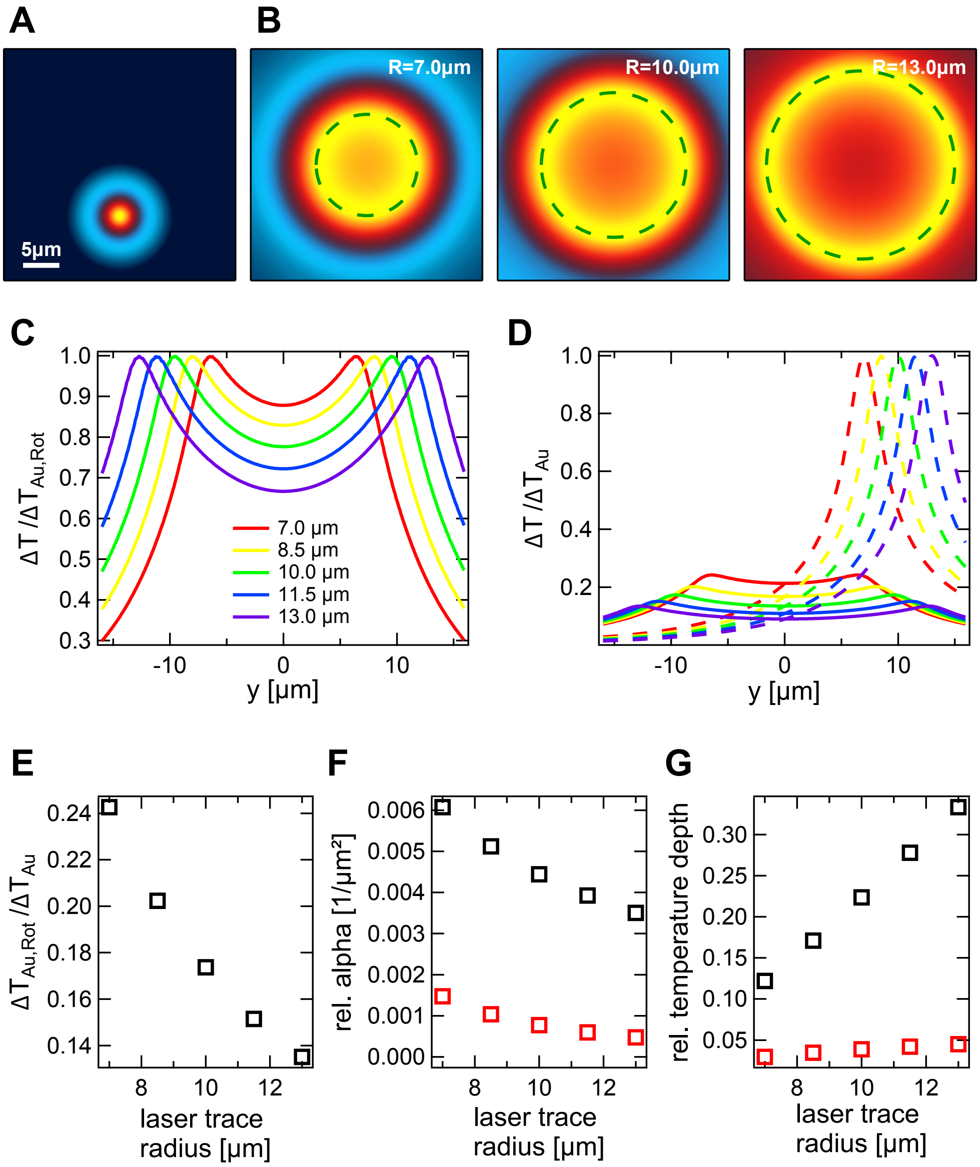

Figure 4.19: **A** Temperature field map of a single spot heating by a focused laser beam. **B** Rotation-averaged temperature field after rotation of the focal spot for different radii. **C** Line profiles through the rotation-averaged temperature profiles for increasing laser rotation radius. **D** Scaled line profiles to match the center temperature rise with the profile of the steady focused heating. **E** Ratio of the temperature rise at the gold structure for rotation-averaged temperature field to the maximum temperature rise of a heated spot. **F** Relative curvature of the temperature field with respect to $\Delta T_{\mathrm{Au,Rot}}$ (black) and ΔT_{Au} (red). **G** Relative depth of the temperature field relative to $\Delta T_{\mathrm{Au,Rot}}$ (black) and ΔT_{Au} (red).

Obviously, the average temperature rise decreases for increasing radius due to the distribution of the same heating power onto a larger circumference. The curvatures of the temperature field may be obtained from fitting a second-order polynomial to the temperature fields and are plotted in Figure 4.19 F normalized to $\Delta T_{\mathrm{Au,Rot}}$ (black) and ΔT_{Au} (red). The effective trapping potential is related to the relative depth of the local minimum $\Delta T_{\text{Au}} - \Delta T_{\text{Center}}$ plotted in Figure 4.19 G again with a normalization to $\Delta T_{\text{Au,Rot}}$ (black) and ΔT_{Au} (red). While the curvature of the temperature field, which is a measure for the trapping stiffness, decreases with increasing laser trace diameter, the relative depth and therefore the trapping potential energy increases. A similar dependency is already found in Section 4.1.6 for the temperature fields produced by the closed gold structure of different hole sizes. The dependencies found from the latter simulations can be directly compared with the presented experimental data. The width (standard deviation) of the position distributions in Figure 4.18 A are plotted in Figure 4.20 A. At a heating power of $P_{\text{Heat}} = 7\,\text{mW}$, the confinement ranges from about $\sigma = 1.7\,\mu\text{m}$ for a laser trace radius of 6.9 µm to about $\sigma = 3.0\,\mu\text{m}$ for a radius of 13.2 µm. Trapping of particles at lower radii over extended periods was not possible or relatively unstable. The theoretical prediction $\sigma^2 = 1/(S_T\alpha)$ for a Soret coefficient of $S_T = 1.1\,\text{K}^{-1}$ and $\alpha = \alpha^{\text{rel}}\Delta T_{\text{Au}} = \alpha^{\text{rel}}\frac{\Delta T_{\text{Au}}}{P_{\text{Heat}}}P_{\text{Heat}}$ is plotted as the dashed line. Due to a large affinity of the particles to adhere to the gold surface, each trace was acquired with a different particle at a different site on the gold surface leading to the visible deviation of the experimental data to the theoretical curve. The temperature profiles reconstructed by the experimental position distribution $\Delta T = -\frac{1}{S_T}\ln\left(\frac{p}{p_0}\right)$ is shown in Figure 4.18 B and compared to the simulated temperature profiles. Each shows a reasonable agreement.

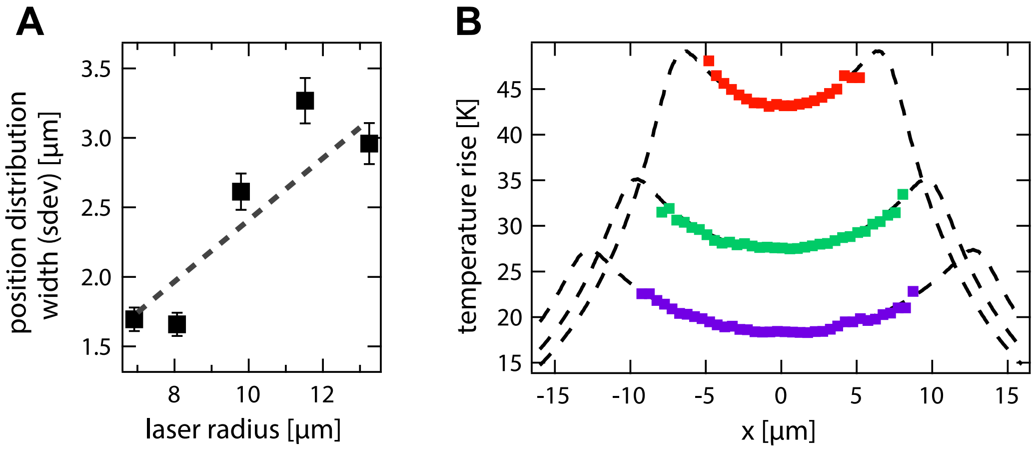

Figure 4.20: A Width of the position distributions plotted in Figure 4.18. Gray dashed line is the theoretical prediction calculated from the curvature of the simulated temperature fields for a Soret coefficient of $S_T = 1.1\,\text{K}^{-1}$. **B** Simulated temperature profiles for an instantaneous temperature rise at the gold structure with heating power of $\Delta T_{\text{Au}}/P_{\text{Heat}} = 29\,\text{K/mW}$ (see Section 4.3.3).

A heating power as high as $P_{\text{Heat}} = 7\,\text{mW}$ leads to an instantaneous maximum temperature rise of about $\Delta T_{\text{Au}} = 200\,\text{K}$. However, while driving the laser along the circle, the average maximum temperature rise of the gold decreases depending on the radius from 49 K for a radius of 7 µm to 27 K for a radius of 13 µm. Since the particle is trapped a few µm away from the heat source, the average temperature rise of the particle accordingly ranges from 43 K to 18 K, accordingly.

The presented experiment together with the simulation proves the feasibility of a trap consisting of a rotating temperature maximum without the need for a hole structure. While trapping using a hole structure can already be realized with trap diameters as small as 5 µm, here, a large diameter is needed to achieve a sufficient depth of the temperature field. However, without the need for a hole-like structure, the presented trapping scheme may readily be implemented into existing setups by only changing software.

4.3 The Feedback-Assisted Thermophoretic Trap

A typical temperature field induced by a laser beam focused onto the gold film near a circular hole is shown in Figure 4.21 A. In addition to the gain in temperature gradient, the relative temperature rise in the center of the gold structure is much lower as compared to the steady heating of the entire circumference as can be seen from the temperature line profiles in Figure 4.21 B, being 14% for focused beam versus 67% for expanded beam for the particular geometry shown of 10 µm-trap size. However, illuminating a single spot only will drive the particle rapidly out of the trapping region due to the thermophoretic repulsion for typically positive Soret coefficients.

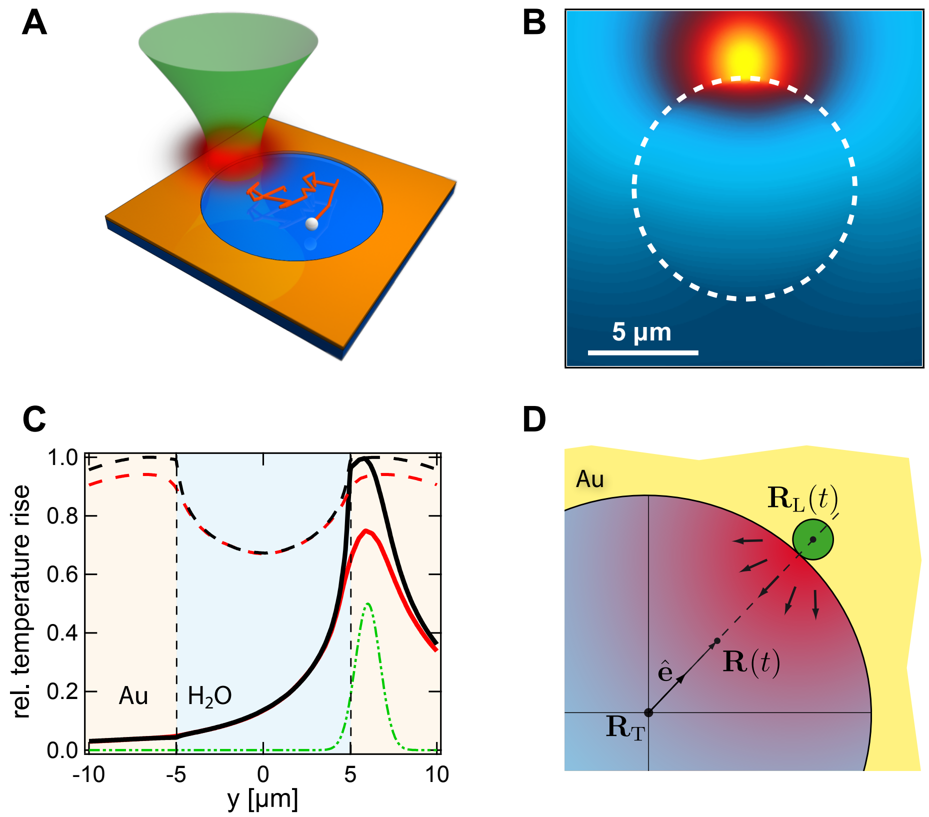

Figure 4.21: **A** Sketch of the focused laser beam heating the edge of the gold structure. This creates an effective repulsive potential for a particle due to thermophoretic interactions. **B** Simulated lateral temperature elevation map through the gold structure. The white circle indicates the edge of the circular hole in the gold film with a diameter of 10 µm. **C** Simulated lateral line profiles of the relative temperature increase through (black curve) and 300 nm above (red curve) the gold structure. The green curve indicates the profile of the heating beam (in arbitrary units). The dashed curves represent the temperature profiles for a heating of the entire gold structure by an expanded laser beam accordingly. **D** Illustration of the parameters used in the following: position of the particle $\mathbf{R}(t)$, position of the target $\mathbf{R}_\mathrm{T}$, position of the heating laser beam $\mathbf{R}_\mathrm{L}(t)$, director pointing from the target towards the heated spot $\hat{\mathbf{e}}(t)$. The arrows indicate the direction of the thermal drift $\mathbf{v}_\mathrm{T}$. For convenience the coordinate origin is located in the center of the circular hole in the gold film.

To keep a particle within the trapping region, the focused beam needs to be moved. In a simple mode, the beam is steered in circles along the gold structure[168] as was demonstrated within the last sections. For the purpose of trapping, this heating scheme is most efficient for high rotation frequencies, where the velocity of the beam is much faster than the induced thermal drift and, thus, the particle feels a time-averaged temperature field of the same shape as for the steady heating. Hence, the advantages of the stronger temperature gradients and the lower relative center temperature are no longer significant due to the effective averaging of the temperature field. Additionally, while periodic fields are easy to produce, micro and macro motion of the trapped particle is induced in a similar manner as for Paul trapping.[167] To exploit the full potential of the focused heating beam and the instantaneous local temperature field, yet another heating scheme is introduced. In order to study a particle, it needs to be observed in any case which is done typically via a fluorescent labeling. Hence, the step to a real-time observation is small. The effort to track the particles position in real-time pays off, as steering the local temperature field accordingly may push the limit of the method tremendously. Also, by modifying the particular feedback rules, the method is extended from the pure ability of trapping towards a versatile tool to manipulate objects in liquids. The aim of the following sections is to explore the thermophoretic trapping of particles and molecules using a feedback-controlled optical heating of the gold structure.

4.3.1 Trapping by Active Dynamic Heating – The Feedback Trap

As the local temperature field decays radially from the heat source, the thermophoretic drift points radially away from the heat source as well. To guide a particle towards the center of the gold structure, the location of the heating beam is controlled by the real-time feedback (FB) loop such that the generated temperature gradient pushes the particle at the position $\mathbf{R}(t)$ towards the target $\mathbf{R}_\mathrm{T}$ in the center of the trap according

$$\mathbf{R}_\mathrm{L}(t) = R_\mathrm{Trap}\hat{\mathbf{e}}(t). \tag{4.18}$$

Herein, R_Trap is the radius of the gold structure and $\hat{\mathbf{e}}(t) = \frac{\mathbf{R}(t)-\mathbf{R}_\mathrm{T}}{|\mathbf{R}(t)-\mathbf{R}_\mathrm{T}|}$ the director pointing from the target to the position of the heating laser beam $\mathbf{R}_\mathrm{L}(t)$. A scheme of the geometry is shown in Figure 4.21 D. By that, an effective temperature profile is produced, which depends on the particle position. Its shape is shown for instantaneous feedback, *i.e.* for high feedback update frequencies, in Figure 4.22 with the black line. This one-dimensional representation consists of two parts. The left arm results from the heating at the left if the particle is located left from the center and *vise versa*. That means, only one position is heated at a time, which leads to a central kink caused by the non-zero temperature gradient in the center. The extension of the instantaneous temperature field for the heating laser being placed on the right side is plotted with the black dashed line, but does not contribute to the now '*virtual*' effective temperature field. A heat diffusion coefficient of water $D_\mathrm{Heat}^{\mathrm{H_2O}} \approx 0.14 \cdot 10^6\ \mu\mathrm{m}^2/\mathrm{s}$ being much higher than the particle diffusion of order $D \sim 1\ \mu\mathrm{m}^2/\mathrm{s}$ allows for a fast switching of the temperature fields within microseconds (see Section 2.4.3). Thus, at a typical feedback cycle time of 10 ms, the temperature fields can be assumed to be generated instantaneously. The scheme in Figure 4.22 also shows the effective temperature profiles for static (red) and quasi-static (red dashed) heating for the same ΔT_Au. Both exhibit a much higher center temperature rise. Due to the exploitation of the information of the particle position and the heating at the single position that is most efficient to drive the particle to the center, a heating of all other positions is omitted with the feedback-controlled heating scenario, which is not the case for a steady or quasi-steady heating (red lines in Figure 4.22). The absolute temperature rise in the center of the trap therefore decreases significantly.

In the upcoming discussion of the results, a similar notation to quantify the temperature fields is used, summarized in Figure 4.22. The maximum temperature rise at the heated spot of the gold structure is again denoted by ΔT_{Au}. The simulated temperature profiles and gradients often appear normalized to ΔT_{Au}, such that $\Delta T^{\mathrm{rel}} = \Delta T/\Delta T_{\mathrm{Au}}$ and $\nabla T^{\mathrm{rel}} = \nabla T/\Delta T_{\mathrm{Au}}$.

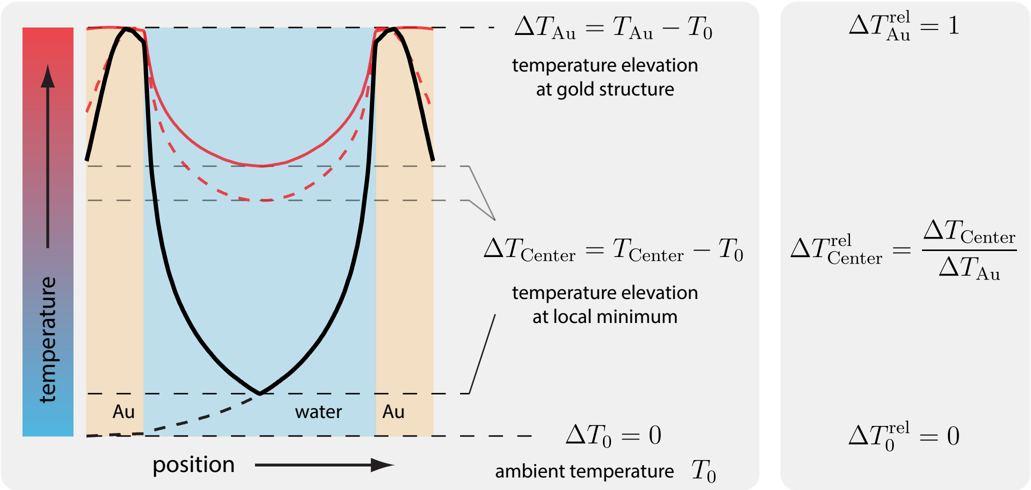

Figure 4.22: Effective temperature profile produced via feedback heating (black) in comparison to steady heating of the entire gold structure (red) and quasi-steady heating (red dashed).

4.3.2 Comparison of Quasi-Steady vs. Feedback-Controlled Heating

To highlight the improvement, the confinement of a 200 nm-diameter polystyrene bead in a 10 µm-diameter trap is compared for two different heating scenarios. First, the laser focus is steered in circles along the gold edge at a rotation frequency of 200 Hz. The velocity of the laser beam is much faster than the induced thermal drift which is why the particle only feels the time-averaged temperature field having the a similar shape as for a wide-field illumination of the entire gold structure and is hence in the quasi-steady heating regime (QS heating). Second, the same bead is trapped using the feedback rule (FB heating) described above, where the laser beam is placed in dependence on the particles position according to Equation 4.18. Aside from the respective heating scheme, the experiments are exactly identical. The feedback cycle time of $\tau_{\mathrm{FB}} = f_{\mathrm{CCD}}^{-1} = 0.01092\,\mathrm{s}$ is given by the inverse frame rate of the CCD camera.

Figures 4.23 A and B compare the positional distribution histograms for QS and FB heating, respectively. For both, the data approximately follow Gaussian distributions, implying a harmonic equivalent trapping potentials. The narrower distribution for the FB heating scheme can clearly be seen from radial position distribution histograms in C yielding the rms-widths $\sigma_{\mathrm{QS}} = (1.47 \pm 0.02)\,\mu\mathrm{m}$ and $\sigma_{\mathrm{FB}} = (0.432 \pm 0.002)\,\mu\mathrm{m}$. Also, a more than four times higher average radial drift of $\langle \mathbf{v}_{\mathrm{T,FB}} \cdot \mathbf{e}_r \rangle = (-6.1 \pm 0.1)\,\mu\mathrm{m/s}$ is measured for the feedback scheme as compared to the quasi-steady heating with $\langle \mathbf{v}_{\mathrm{T,QS}} \cdot \mathbf{e}_r \rangle = (-1.4 \pm 0.1)\,\mu\mathrm{m/s}$. This results from the stronger temperature gradients for the FB heating compared to the decreased gradients for the QS heating due to the rotation-averaging of the temperature field.

By calculating the equivalent trapping stiffness $\kappa = k_{\mathrm{B}}T/\sigma^2$, *i.e.* the curvature of the effective trapping potential shown in Figure 4.23 D, it is seen that for the same heating beam power, the stiffness for the FB heating ($\kappa_{\mathrm{FB}} = 22.0\,\mathrm{fN/\mu m}$) is about an order of magnitude higher than for the QS heating

($\kappa_{QS} = 1.90\,\mathrm{fN/\mu m}$). Hence, with the real-time FB, in the given experiment 10 times less heat deposition is necessary to achieve the same trapping stiffness as for a QS heating, as the trap stiffness is proportional to the absolute temperature rise $\kappa \propto \Delta T_{Au}$. The effective trapping stiffness achieved with the feedback heating scheme is comparable to that reported for the first generation ABEL trap.[169]

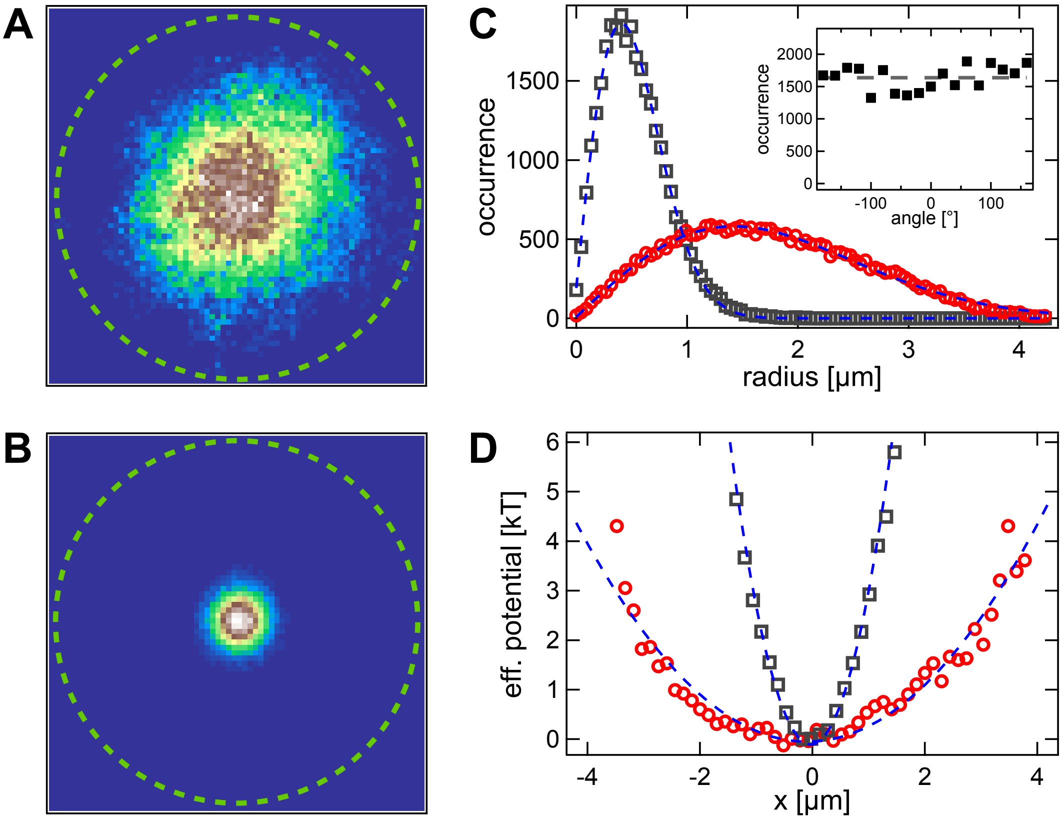

Figure 4.23: **A** Positional distribution histogram of a 200 nm-diameter polystyrene particle for a quasi-steady heating at a laser rotation frequency of 200 Hz. The rms-distance from the center of the trap measures $\sigma_{QS} = (1.47 \pm 0.02)\,\mu\mathrm{m}$ at a heating beam power of $P_{heat} = 3.0\,\mathrm{mW}$. **B** Same as for A but laser beam is feedback-loop controlled at a feedback cycle time of $\tau_{FB} = 10.92\,\mathrm{ms}$. rms-displacement reduces to $\sigma_{FB} = (0.432 \pm 0.002)\,\mu\mathrm{m}$. **C** Radial positional distribution histogram for QS (red) and FB (black) heating fitted by Equation 4.2. **Inset** Probability of heating at a certain angle along the circumference of the gold structure. The gray dashed line shows the average. **D** Effective trapping potentials $\Delta U/k_B T = -\ln(P/P_0)$ for QS (red) and FB (black) heating, each with second order polynomial fit (harmonic approximation).

Figure 4.24 shows the effective temperature profiles calculated from FEM simulations together with the experimental data, *i.e.* the temperature profiles calculated from the position distribution via $\Delta T = -\ln(P/P_0)/S_T$. Both match for a Soret coefficient of $S_T = 1.6\,\mathrm{K}^{-1}$. The knowledge of the temperature rise per heating power is necessary for the calculation of the theory plots as the simulation delivers a relative temperature profile normalized to ΔT_{Au} but can be scaled then with the heating power according to $\Delta T_{Au}/P_{Heat} = 29\,\mathrm{K/mW}$. The origin of this factor is discussed in detail within the next section. The depth of the effective temperature fields determining the height of the confining potential differs strongly as can be directly seen from Figure 4.24 ($\Delta T_{Depth,FB} = 74.6\,\mathrm{K}$ for the feedback heating versus $\Delta T_{Depth,QS} = 8.1\,\mathrm{K}$ for the quasi-steady heating). Note, that the instantaneous temperature rise of the gold structure and hence the average center temperature is approximately the same in both heating scenarios. Also, the probability for heating at a certain angle is equally distributed along the rim of the gold hole in both cases (see inset in Figure 4.23 C for FB, trivial for QS). That implies, that the average temperature profile, which directly resembles the effective temperature profile for the QS heating, is the same for both scenarios. The shape of the effective temperature profile for the FB heating, however, is different and results from the active steering of the laser beam. The increase in effective temperature depth by about a factor of 10 as well as the increase in trapping stiffness by the same factor is thus only due to the active positioning of the heating beam with feedback on the real-time position of the trapped object.

Theoretically, the temperature field exhibits a kink in the trapping center which also should be directly visible in the experiment. However, the calculation represents the temperature field for an infinite feedback update rate. In the experimental data, the sharp kink is blurred by Brownian motion within one frame, but also from an inaccuracy of the tracking of the bead as well as the heating position of the laser beam.

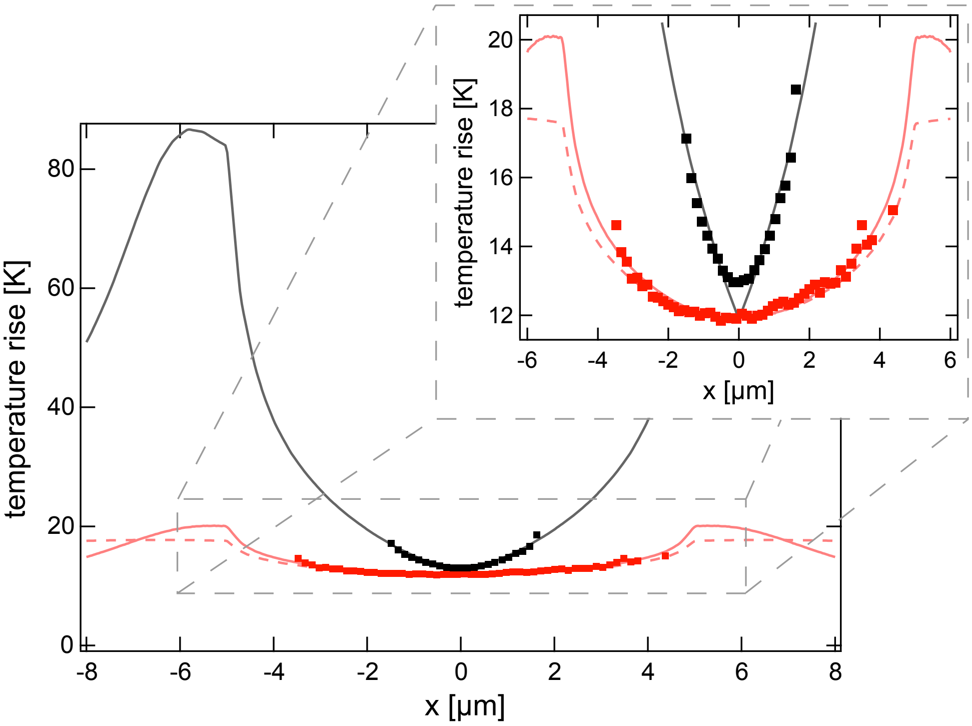

Figure 4.24: Temperature profiles reconstructed from the positional distribution for a Soret coefficient of $S_T = 1.6\,\mathrm{K}^{-1}$ for FB (black) and QS (red) heating and comparison to effective theoretical temperature fields. The dashed red line represents the equivalent temperature field for a steady heating of the entire gold structure.

4.3.3 Steady-State and Dynamic Properties of the Feedback Trap

The last section demonstrated the feasibility of a thermophoretic feedback trap and gave a direct comparison to the quasi-steady heating scheme. Within the this section, the steady-state and dynamic properties of the feedback trapping scheme are investigated in detail in the same manner as was presented in the Sections 4.1.2 to 4.1.5 for the steady heating scheme. These properties include the achievable confinement, the induced thermal drift velocities as well as the diffusion coefficient and the generated temperature rise, also allowing the measurement of the Soret coefficient. All the latter concerns may be addressed by studying the confinement of a particle in dependence on the heating power. To be consistent with the previous experiments, the same polystyrene bead size of 200 nm diameter is chosen. The trap size is $d_{\mathrm{Trap}} = 8.2\,\mu\mathrm{m}$ and the heating powers used are between 0.6 mW and 3.0 mW. The feedback cycle time of $\tau_{\mathrm{FB}} = f_{\mathrm{CCD}}^{-1} = 0.01092\,\mathrm{s}$ again is determined by the inverse frame rate f_{CCD}^{-1} of the CCD camera. For each heating power, a movie of 40000 frames is acquired, resulting in trajectories of 435 s length after tracking the particle's position.

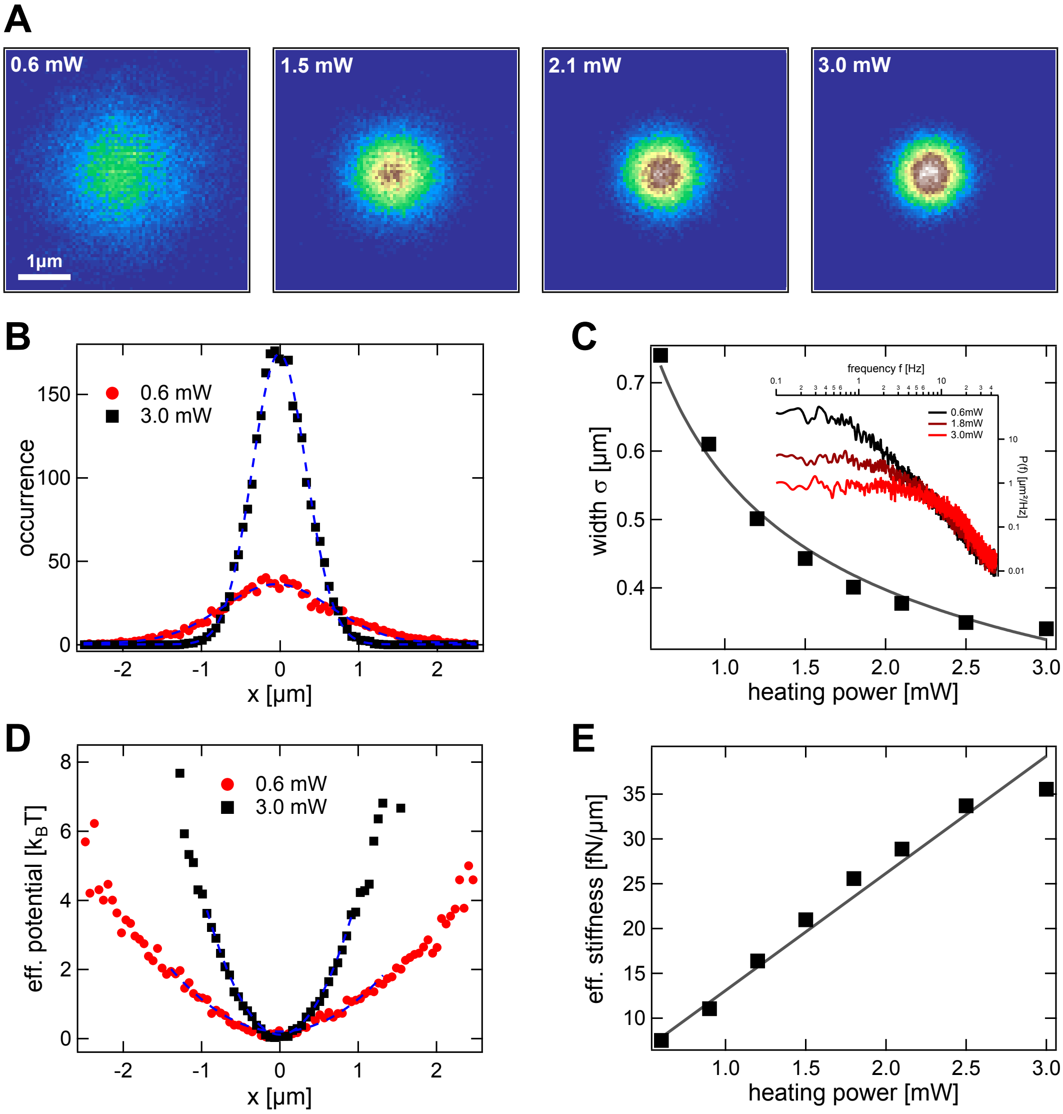

Figure 4.25: **A** Position distribution of a 200 nm polystyrene particle confined in a 8.3 µm trap using feedback-controlled laser heating of the gold structure for increasing heating powers. **B** Position distribution line profiles for the highest (black) and lowest (red) heating power together with Gaussian fits. **C** Width (standard deviation from the center) of the position distributions fitted by $\sigma \propto P_{\mathrm{Heat}}^{-1/2}$. Inset: Power spectral density of the particle's motion in the trap. **D** Effective trapping potentials $\Delta U / k_{\mathrm{B}}T = -\ln(p/p_0)$ calculated from the position distributions in B. **E** Effective trapping stiffness calculated from the width in C with linear fit yielding a slope of $\kappa / P_{\mathrm{Heat}} = (13.1 \pm 0.6)\,\mathrm{fN}/(\mu\mathrm{m}\cdot\mathrm{mW})$.

Positional Distribution Figure 4.25 A presents positional distribution histograms for increasing heating powers. The increase in confinement is directly visible. The distributions approximately follow a Gaussian, as can be seen from the line profiles in Figure 4.25 B. The width of the confinement with rising heating power is plotted in Figure 4.25 C and decreases from about 0.74 µm for 0.6 mW heating power to about 0.34 µm for 3.0 mW.

Under the assumption of instant feedback and that the temperature field can be approximated by a parabola in the center of the trap, $\Delta T_{\mathrm{Harm}}(r) = \frac{\alpha}{2}r^2 + \Delta T_{\mathrm{Center}}$, with $\alpha \propto \Delta T_{\mathrm{Au}} \propto P_{\mathrm{Heat}}$ the curvature of the temperature field, the width $\sigma \propto P_{\mathrm{Heat}}^{-1/2}$ goes as the inverse square root of the heating power (see discussion in Section 4.1.2). At a finite feedback cycle time, an over-compensation at high heating intensities may broaden the position distribution. An over-shooting over the target position is directly visible in the power spectral density (PSF) of the particle as a resonance peak.[170, 171] From the inset in Figure 4.25 C it can be seen, that no peak is visible in the experimental data. The PSD for the highest heating power (red curve) used shows a little neck beyond frequencies of 10 Hz, marking the beginning of the over-compensation. Finite feedback cycle times will be discussed in detail in Section 4.3.5. The one-over-square-root-power-dependence well fits the experimental data in Figure 4.25 C. The effective trapping potentials $\Delta U(\mathbf{r})/k_{\mathrm{B}}T = -\ln(p/p_0)$ are calculated from the positional distributions. Two examples are plotted in Figure 4.25 D for the lowest and highest measured heating powers. Assuming a temperature independent S_{T}, the effective potential resembles the shape of the temperature field $\Delta U(\mathbf{r})/k_{\mathrm{B}}T = S_{\mathrm{T}}\Delta T(\mathbf{r})$. The sharp kink in the theoretically expected effective temperature field in the center of the trapping region again appears to be blurred in the experimental data (see last Section 4.3.2). Under the assumption of a harmonic effective trapping potential, the effective stiffness is calculated from the width of the position distribution via $\kappa = k_{\mathrm{B}}T/\sigma^2$ and is plotted in Figure 4.25 E. Consistently with the theoretical expectation ($\kappa = S_{\mathrm{T}}\alpha k_{\mathrm{B}}T \propto P_{\mathrm{Heat}}$), a linear relation with the heating power is recognized with a slope of $\kappa/P_{\mathrm{Heat}} = (13.1 \pm 0.6)\,\mathrm{fN}/(\mu\mathrm{m}\cdot\mathrm{mW})$.

Thermophoretic drift The drift velocities that are induced by the temperature gradients are extracted from the trajectory via step size analysis, which was already explained in detail in Section 4.1.3. In short, the probability of finding a particle at a position $\mathbf{R}(t+\tau)$ if it has been at the position $\mathbf{R}(t)$ in the previous frame is given by the advection-diffusion propagator $p_{\mathrm{adp}}(\mathbf{R}(t+\tau), \mathbf{R}(t)) \propto \exp\left(-\frac{|\mathbf{R}(t+\tau)-\mathbf{R}(t)+\mathbf{v}_{\mathrm{T}}\tau|^2}{4D\tau}\right)$ exhibiting a Gaussian shape. Its width $\sigma^2 = 2D\tau$ is determined by Brownian motion, which will be discussed later on. First, it shall be concentrated on the drift velocity given by the shift $\mathbf{v}_{\mathrm{T}}\tau$ of the distribution. To account for the symmetry of the effective temperature field, each step $\mathbf{R}(t+\tau) - \mathbf{R}(t)$ is projected in radial and tangential direction.

Figure 4.26 A shows the radial and tangential drift velocity averaged over the entire trapping region. While no tangential component is detected, the radial component increases linearly with the heating power. The negative sign reveals the flow towards the trap center. This is in accord with the effective temperature profile generated by the feedback-controlled heating (Equation 4.18), which steers the laser beam such that the tangential component of the temperature gradient disappears while only the radial component survives. Since the radial component is proportional to the temperature rise at the gold structure $\Delta T_{\mathrm{Au}} \propto P_{\mathrm{Heat}}$, the radial drift also increases linearly with the heating power. The spatially resolved radial drift velocity is plotted in Figure 4.26 B as a function of the distance to the trap center. Clearly visible is the (negative) increasing velocity for growing distances to the center, which is consistent with the higher temperature gradient radially towards the gold rim. From the effective temperature fields for the feedback heating (see Figure 4.22), a finite temperature gradient is expected, leading to a finite drift velocity in the center of the trap. However, this is not observed in the experimental data, which is addressed to the fact that the closer the particle is to the trap center, the higher is the relative error in the determination of the heating position director $\hat{\mathbf{e}} = \frac{\mathbf{R}-\mathbf{R}_T}{|\mathbf{R}-\mathbf{R}_T|}$ (see Figure 4.21 D) due to Brownian motion within one frame cycle and tracking uncertainty. This also leads to the measurement of the blurred kink in the effective temperature profiles. Figure 4.26 C shows that the tangential drift not only disappears on average, but for every distance to the trap center at any heating intensity.

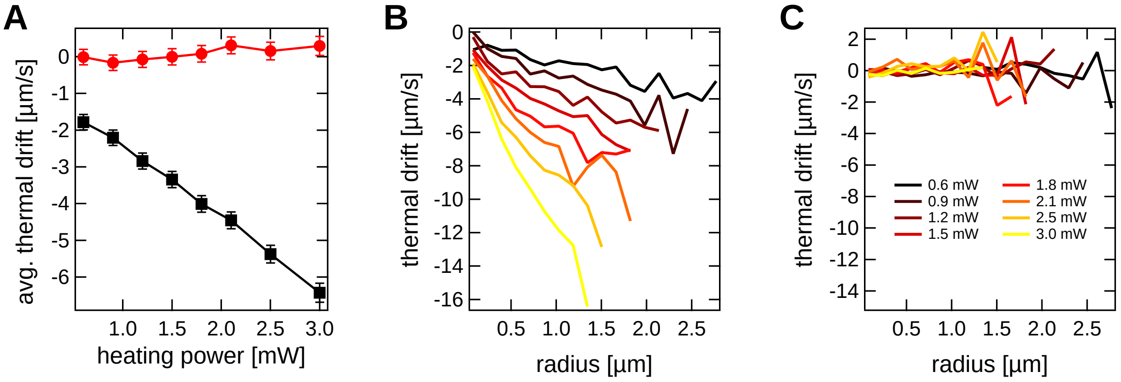

Figure 4.26: **A** Averaged thermophoretic drift velocity yielded from step size analysis after projecting each step in radial (black) and tangential (red) direction. **B** Thermophoretic drift velocity in radial direction in dependence on the distance to the trap center for increasing heating power. **C** Same as B but in tangential direction. Color coding is the same as in B.

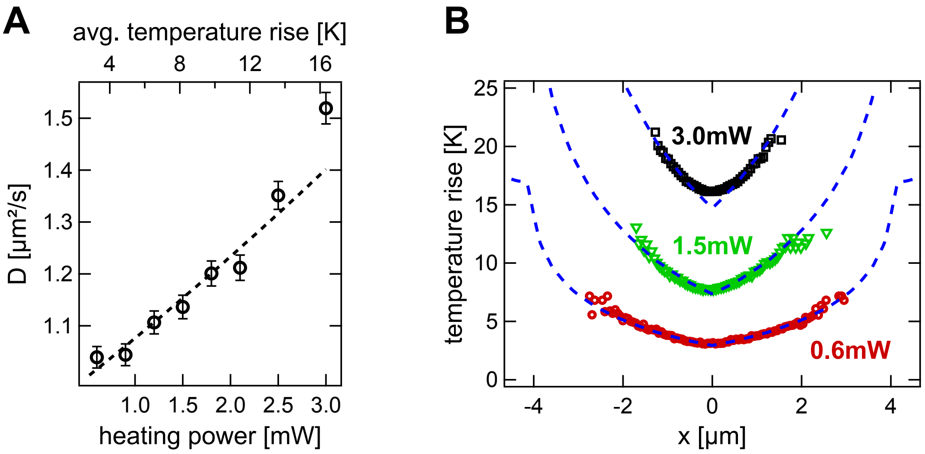

Figure 4.27: **A** Diffusion coefficient as a function of the heating laser power. Dashed line according to Equation 4.4 yielding an average temperature rise of the particle per heating power of $\Delta T_{\mathrm{Avg}}/P_{\mathrm{Heat}} = 5.4\,\mathrm{K/mW}$ (top axis). **B** Relative termperature profiles from FEM simulations scaled with the temperature rise at the gold structure ΔT_{Au} together with the temperature profiles reconstructed from the position distributions in Figure 4.25 for a Soret coefficient of $S_T = 1.5\,\mathrm{K}^{-1}$.

Diffusion Coefficient and Effective Temperature Field An analysis of the width $\sigma^2 = 2D\tau$ of the step size distribution $p_{\mathrm{adp}}(\mathbf{R}(t+\tau), \mathbf{R}(t))$ yields the diffusion coefficient D. To ensure a decoupling of the Brownian steps from the thermophoretic drift, which may result in a broadening, the width is analyzed after a projection in tangential direction, where no temperature gradient is present and the thermal drift thus disappears. Figure 4.27 A plots the diffusion coefficient in dependence on the used power of the focused laser beam, which varies between $D = 1.04\,\mu\mathrm{m}^2/\mathrm{s}$ for the lowest heating power of 0.6 mW and $D = 1.52\,\mu\mathrm{m}^2/\mathrm{s}$ for 3.0 mW. The main effect results from the decreasing viscosity for increasing heating power, while the increase in thermal fluctuations is relatively small ($k_\mathrm{B}\Delta T/k_\mathrm{B}T_0 < 5\%$). To obtain a measure for the temperature rise at a given heating power, a Stokes-Einstein relation with temperature-dependent viscosity is fitted (Equation 4.4, see discussion in Section 4.1.4) yielding an average temperature rise of $\Delta T_\mathrm{Avg}/P_\mathrm{Heat} = 5.4\,\mathrm{K/mW}$ for the particular trap diameter of 8.2 µm. For the measured particle distributions, the average temperature of the particle ΔT_Avg is well-approximated by the center temperature rise ΔT_Center, which will be shown later (Figure 4.28). From the shape of the simulated effective temperature profile, a temperature rise at the gold structure with the heating power is calculated to $\Delta T_\mathrm{Au}/P_\mathrm{Heat} = 29\,\mathrm{K/mW}$. While this value is dependent on experimental parameters such as laser wavelength, beam diameter or gold film thickness, it is independent of the trap size and may hence be used to calculate the center temperature rise $\Delta T_\mathrm{Center}/P_\mathrm{Heat}$ for different trap sizes. Figure 4.27 B shows the absolute temperature fields calculated from the simulated relative temperature profiles for the particular trap size of 8.2 µm diameter together with the experimental data obtained from the positional distributions via $\Delta T = -\ln(p/p_0)/S_\mathrm{T}$ for three different heating powers. The simulated and experimentally obtained temperature profiles fit well for a Soret coefficient of $S_\mathrm{T} = 1.5\,\mathrm{K}^{-1}$ for all heating intensities, which agrees with literature for the given particle size.[60,62] The lower Soret coefficient compared to the experiment for the static heating is a result of a higher water film thickness (see discussion in Section 4.1.5).

Average Temperature Rise and Trap Size Dependence In the last paragraph, the assumption was made that the average temperature of the particle ΔT_Avg does not significantly differ from the center temperature rise ΔT_Center. This claim shall be discussed in the following supported by a simple calculation, which was already performed for the steady-state heating scheme in Section 4.1.4. As seen from Figure 4.25, the positional distribution approximately follows a Gaussian distribution $p(\mathbf{r};\sigma)$ of standard deviation σ. The effective temperature profiles for the three different trap diameters used, *i.e.* 8.3 µm, 10.3 µm and 15.3 µm, are shown in Figure 4.28 A. The average temperature rise a particle experiences in the trapping region can be then estimated by an integration of the positional distribution (indicated for $\sigma = 1.0\,\mu\mathrm{m}$ by the gray dashed curve) over the effective temperature profile

$$\Delta T_\mathrm{Avg}(\sigma) = \int \Delta T(\mathbf{r})\, p(\mathbf{r};\sigma)\mathrm{d}r. \tag{4.19}$$

Figure 4.28 B plots the average temperature rise normalized to ΔT_Au for an increasing Gaussian width σ for the different trap sizes. The respective relative center temperature rises $\Delta T^\mathrm{rel}_\mathrm{Center}$ are plotted as the dashed lines. The relative increase in average temperature $\Delta T^\mathrm{rel}_\mathrm{Avg} - \Delta T^\mathrm{rel}_\mathrm{Center}$ is the strongest for the smallest trap size, but is for typical widths $\sigma < 1\,\mu\mathrm{m}$ (see Figure 4.25) below 5%. Generally, the center temperature rise and therefore the average temperature of the particle decreases for increasing trap sizes, which is plotted in Figure 4.28 C as the red curve. Also, the depth of the temperature field $(\Delta T_\mathrm{Au} - \Delta T_\mathrm{Center})/\Delta T_\mathrm{Au}$ increases with increasing trap size (black curve). This behavior was already found for the steady heating scheme (see Figure 4.9). However, a comparison of the values for an 8 µm-diameter trap reveals the more distinct effective temperature minimum for the feedback-controlled heating ($\Delta T^\mathrm{rel}_\mathrm{Depth,Steady} = 0.25$ vs. $\Delta T^\mathrm{rel}_\mathrm{Depth,FB} = 0.83$) going along with considerably less center temperature rise ($\Delta T^\mathrm{rel}_\mathrm{Center,Steady} = 0.75$ vs. $\Delta T^\mathrm{rel}_\mathrm{Center,FB} = 0.17$). Table 4.1 presents an overview of the absolute temperature increment in the center of the trapping region for the different trap sizes used, which can be calculated from the effective temperature profiles plotted in

Figure 4.28 together with the temperature rise of the gold structure upon laser illumination $\Delta T_{\mathrm{Au}}/P_{\mathrm{Heat}}$ found in the last paragraph (Figure 4.1.4). Due to the larger average distance to the heat source, the center temperature rise is lowest for large trap sizes. For the trapping of temperature-sensitive material such as biomolecules, it is thus advisable to use a large trapping diameter. Also, the height of the effective trapping potential $\Delta U/k_{\mathrm{B}}T = S_{\mathrm{T}}\Delta T_{\mathrm{Depth}}$ slightly increases for increasing trap sizes, which is shown with the right column in Table 4.1. Both the advantages of large traps go along with a broader particle distribution within the trapping region due to decreasing trapping stiffness with growing trap size. Stiffness becomes important to measure forces *e.g.* in force spectroscopy using optical tweezers, but is typically less meaningful for the pure confinement of objects in a well-defined spatial region over extended time periods.

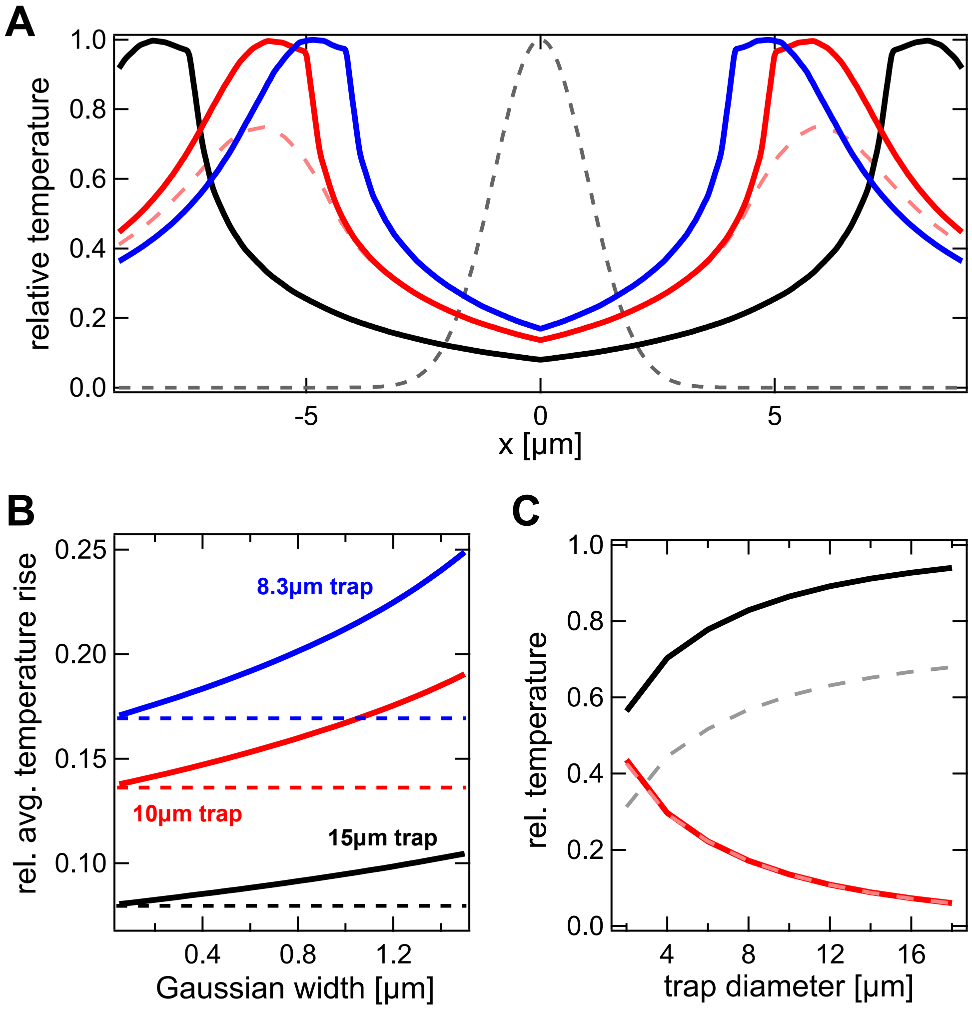

Figure 4.28: **A** Simulated temperature profiles assuming an instant feedback for the trap diameters 8.3 µm (blue), 10 µm (red) and 15 µm (black). The gray dashed curve represents a Gaussian probability distribution with $\sigma = 1$ µm (in arbitrary units). **B** Relative average temperature rise of a trapped particle for an increasing width of the probability distribution for the different trap sizes. The dashed lines mark the relative temperature rise in the center of the trap. **C** Relative depth of the temperature field $(\Delta T_{\mathrm{Au}} - \Delta T_{\mathrm{Center}})/\Delta T_{\mathrm{Au}}$ (black) and relative temperature rise in the center $\Delta T^{\mathrm{rel}}_{\mathrm{Center}} = \Delta T_{\mathrm{Center}}/\Delta T_{\mathrm{Au}}$ (red) as a function of the trap diameter in the plane of the gold structure. Dashed lines show the equivalent data for the plane 300 nm above the gold structure.

trap diameter [µm]	$\Delta T_{\mathrm{Center}}/P_{\mathrm{Heat}}$ [K/mW]	$\Delta U/(S_{\mathrm{T}}P_{\mathrm{Heat}})$ [$\mathrm{k_B T \cdot K/mW}$]
8	5.4	24.6 (16.9)
10	4.2	25.4 (17.8)
15	2.4	27.4 (19.5)

Table 4.1: Center column: Center temperature rise per heating power for the different trap sizes used for trapping via feedback-controlled heating calculated from the simulated effective temperature profiles and $\Delta T_{\mathrm{Au}}/P_{\mathrm{Heat}} = 29.6\,\mathrm{K/mW}$. **Right column:** Effective trapping potential depth in the plane of the gold structure per Soret coefficient and heating power. Values in parentheses are for 300 nm above the gold film.

4.3.4 Shaping the Trapping Potential

The above discussion showed that the thermophoretic trapping by means of a feedback-loop controlled heating yields a huge gain in efficiency. Although being technically more demanding, in addition to its higher efficiency, it also has tremendous impact on the methods versatility. The ability of positioning the heating beam in real-time enables an interactive shaping of temperature gradients within the trapping region and by that allows for the formation of almost arbitrary effective virtual trapping potentials. A few examples shall be given in the following.

Point Target Steering particles within the trapping region can be realized by assigning target positions $\mathbf{R}_{\mathrm{T}}$ that differ from the center of the trap and may also be time-dependent $\mathbf{R}_{\mathrm{T}}(t)$. For that purpose, the simple feedback rule given by Equation 4.18 is extended. The new situation is illustrated in Figure 4.29 A. By basic geometrical considerations, one finds the position of the heating laser beam $\mathbf{R}_{\mathrm{L}}$ to[172]

$$\mathbf{R}_{\mathrm{L}} = \mathbf{R}_{\mathrm{T}} + d\hat{\mathbf{e}}, \quad \text{with} \quad d = -\mathbf{R}_{\mathrm{T}} \cdot \hat{\mathbf{e}} + \sqrt{R_{\mathrm{Trap}}^2 - |\mathbf{R}_{\mathrm{T}}|^2 + |\mathbf{R}_{\mathrm{T}} \cdot \hat{\mathbf{e}}|^2} \tag{4.20}$$

the distance and $\hat{\mathbf{e}} = \frac{\mathbf{R}-\mathbf{R}_{\mathrm{T}}}{|\mathbf{R}-\mathbf{R}_{\mathrm{T}}|}$ the director pointing from the target $\mathbf{R}_{\mathrm{T}}$ to the position to heat $\mathbf{R}_{\mathrm{L}}$. For the case that the target coincides with the center of the trap, $\mathbf{R}_{\mathrm{T}}(t) \equiv 0$, Equation 4.20 reduces to Equation 4.18. The resulting effective temperature profile is depicted in Figure 4.29 B. Note, that the virtual temperature profile appears to be discontinuous due to the different distances to the heat source for different heating angles ϕ (see Figure 4.29 A). Hence, the negative temperature gradient determining the thermal drift still points inwards, but is anisotropic and depends on the heating angle ϕ.

The experimental implementation of Equation 4.20 is readily demonstrated by trapping a 200 nm polystyrene bead at different positions within the trap being $\mathbf{R}_{\mathrm{T}} = (0,0)$, $\mathbf{R}_{\mathrm{T}} = (1.3,0)\,\mu\mathrm{m}$ and $\mathbf{R}_{\mathrm{T}} = (2.6,0)\,\mu\mathrm{m}$. Figure 4.30 A shows the according positional distribution histograms. The shift towards the gold rim is clearly visible. Histograms over the applied heating angles are given in B. While the angles are nearly equally distributed for a central trapping, a pronounced anisotropy is visible for increasing displacements of the target from the trap center. The probability of heating is lower in regions where the target is closer to the gold rim which is due to the higher drift velocity driving a particle faster to the target. Hence, even though the particle is trapped closer to the gold structure, the average temperature remains about the same as for the heating at the center. A remaining anisotropy for the central trapping may result from a misaligned gold structure but is mostly attributed to a slightly inhomogeneous heating power over the circumference (see Calibration of the AOD in Section 3.2).

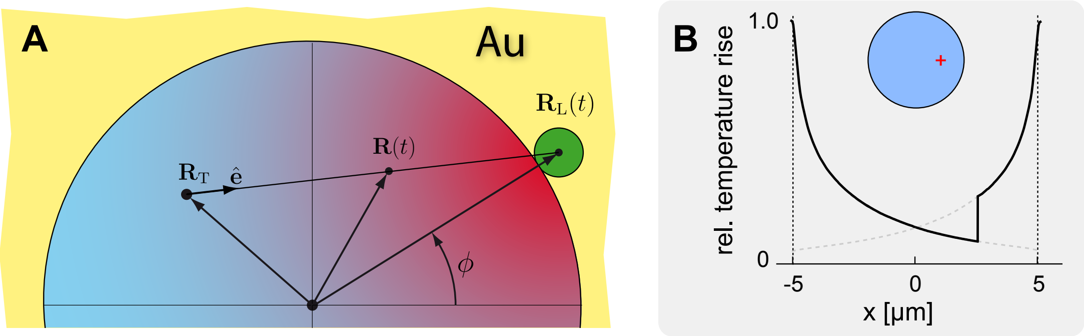

Figure 4.29: **A** Schematic illustration for the off-center feedback trapping. The laser beam is placed such, that a particle at the position $\mathbf{R}(t)$, the target $\mathbf{R}_\mathrm{T}$ as well as the laser position $\mathbf{R}_\mathrm{T}(t)$ form a straight line. Note, that two positions at the gold rim fulfill this criterion, but only the one closer to the particle will lead to a confinement. The heating angle ϕ is defined as shown in the Figure. **B** Effective virtual temperature profile that is applied due to the feedback heating to trap a particle at the position $x = 2.5\,\mu\mathrm{m}$.

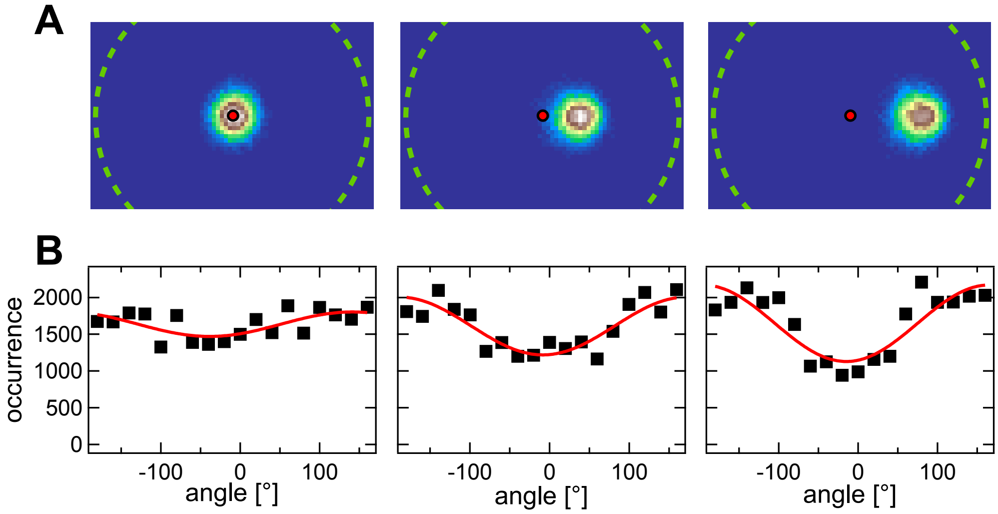

Figure 4.30: **A** Lateral positional distribution histograms for three different targets being $\mathbf{R}_\mathrm{T} = (0,0)$ (left), $\mathbf{R}_\mathrm{T} = (1.3,0)\,\mu\mathrm{m}$ (center) and $\mathbf{R}_\mathrm{T} = (2.6,0)\,\mu\mathrm{m}$ (right). **B** Distribution of the applied heating angles ϕ for the according targets.

The horizontal line profiles through the positional distribution of Figure 4.30 A, which are plotted in Figure 4.31 A, still approximately follow Gaussian distributions, yet the standard deviation from the target position increases from $\sigma = (0.59 \pm 0.01)\,\mu\mathrm{m}$ for trapping at the center to $\sigma = (0.70 \pm 0.01)\,\mu\mathrm{m}$ for the trapping at a target shifted from the center by $2.6\,\mu\mathrm{m}$ (Figure 4.31 B). By analyzing the step-size distribution of the trajectories, the thermophoretic drift velocities can be measured and are shown for the x direction in Figure 4.31 C. For a trapping at the center, the drift appears to be symmetric around the center and is positive for negative x coordinates and *vice versa*. Both, the positive and the negative branches have the same slope. Although the directions behave analog for the off-center trapping, the slopes are different on the respective negative (steeper) and positive (shallower) branch, which is directly related to the higher temperature gradients close to the gold structure, while the gradients are less when the gold structure is heated on the opposite side and the distance to the heat source is longer. Figure 4.31 D presents the corresponding effective trapping potentials calculated from the positional distribution. Again, the asymmetry for the off-center trapping is visible as the potentials are steeper on the side that is closer to the gold rim. The effective trapping potentials resemble effective temperature profiles $\Delta U_{\text{eff}}/k_{\text{B}}T = S_{\text{T}}\Delta T_{\text{eff}}$, however, without the discontinuity at the target position. This is expected, since the shape of the effective temperature profile only results from the applied feedback-rule. At a given point in time, the gold structure is heated only at a single point producing a single repulsive potential. Hence, the temperature at $\mathbf{R}_{\text{T}}$ is colder if the distance to the heat source is larger. The absolute temperature itself then again has no direct influence on the confinement which is only caused by the temperature gradient via a thermophoretic drift such that a jump in the effective potential is neither measured nor expected.

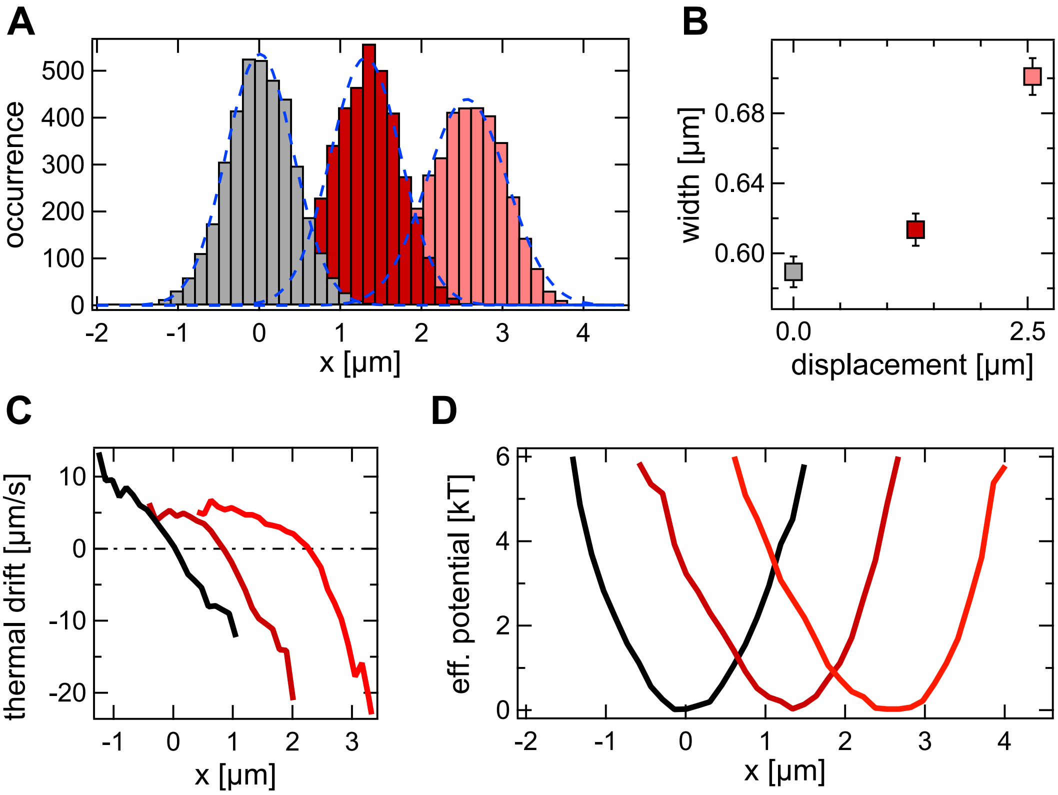

Figure 4.31: **A** Line profiles of the position distribution in Figure 4.30 for the targets at $\mathbf{R}_{\text{T}} = (0,0)$ (gray), $\mathbf{R}_{\text{T}} = (1.3,0)$ µm (dark red) and $\mathbf{R}_{\text{T}} = (2.6,0)$ µm (light red) with Gaussian fits. **B** Width σ of the Gaussian fits in A. **C** Thermophoretic drift velocity in x direction. **D** Effective trapping potentials.

Double Well Target The last paragraph showed the ability to define arbitrary target positions $\mathbf{R}_{\text{T}}$ for a particle within the trapping region. Introducing a time dependence to the target position $\mathbf{R}_{\text{T}} = \mathbf{R}_{\text{T}}(t)$, the particle can be steered along an externally scheduled trajectory. Moreover, it is possible to couple the target to the particle's real-time position. This shall be demonstrated in the following with the realization of an effective double well potential. For that, two target positions $\mathbf{R}_{\text{T}+}$ and $\mathbf{R}_{\text{T}-}$ are defined (see Sketch in Figure 4.32 A). For simplicity, both are chosen to be equally displaced from the center of the trap along the x axis by $|\Delta x_{\text{T}\pm}| = d_{\text{T}}/2$, such that the distance between the targets is d_{T}. The steering of the heating laser beam is then controlled by the feedback rule given by Equation 4.20.

Which target being used at the time t is decided by the particle position $\mathbf{R}(t)$. If the particle is detected in the positive x space, the gold structure is heated to guide the particle to $\mathbf{R}_{\mathrm{T}+}$ and *vice versa*,

$$\mathbf{R}_{\mathrm{T}}(t) = \begin{cases} \mathbf{R}_{\mathrm{T}+} & \text{if} \quad \mathbf{R}(t) \cdot \mathbf{e}_x > 0 \\ \mathbf{R}_{\mathrm{T}-} & \text{if} \quad \mathbf{R}(t) \cdot \mathbf{e}_x < 0. \end{cases} \tag{4.21}$$

Theoretically, this will result in an effective temperature profile plotted in Figure 4.32 B. Disregarding the discontinuities in the temperature field, which have no direct influence on the trapping (see last paragraph), two local minima appear separated by a barrier.

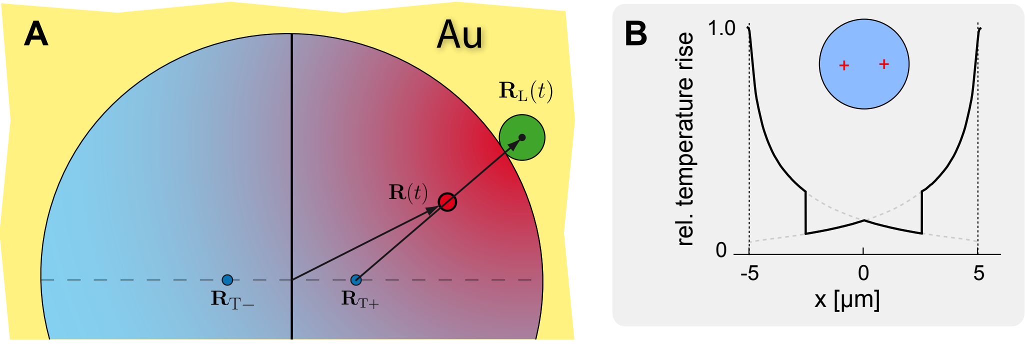

Figure 4.32: **A** Scheme illustrating the target positioning to create an effective double well potential. **B** Effective temperature profile applied by the feedback-controlled heating beam.

Figure 4.33 presents an experiment, where a 200 nm polystyrene bead is trapped in the above-described double well temperature field for two different separations d_{T} of the targets $\mathbf{R}_{\mathrm{T}+}$ and $\mathbf{R}_{\mathrm{T}-}$ resulting in a different height of the barrier. While the height of the barrier may be also changed by adjusting the heating laser power, this would change the shape of the local minima, *i.e.* the curvature, as well. Changing the target separation d_{T} practically preserves the curvature of temperature field and only changes the height of the barrier ΔU.

A typical time trace for the x direction is shown in Figure 4.33 A. The hopping between two states is clearly visible. The position distribution in B reveals the two preferred regions of the particle at the target positions. The potential landscape $\Delta U/k_{\mathrm{B}}T = -\ln(p/p_0)$ calculated from the position distribution is plotted in Figure 4.33 C for the x direction. Analyzing the trajectories with a threshold at $x = 0$ yields the dwell times that the particles stay in one of the wells. Histograms over the obtained dwell times are shown in Figure 4.33 D. An exponentially distribution can be seen, except for very short dwell times $\tau < 0.5\,\mathrm{s}$, where the particle only samples the local proximity of the saddle point, but does not enter one of the wells. Via an exponential fit, the mean dwell times are measured with $\tau = (13.3 \pm 2.1)\,\mathrm{s}$ for the shorter separation of $d_{\mathrm{T}} = 2.73\,\mu\mathrm{m}$ and $\tau = (19.2 \pm 3.6)\,\mathrm{s}$ for $d_{\mathrm{T}} = 3.34\,\mu\mathrm{m}$. The dwell times may be interpreted as first passage times, *i.e.* the first time the particle reaches the saddle point while exploring a potential well. For very short dwell times the starting point of the trajectory is important for the shape of the dwell time distribution. With the starting point after each transition being the saddle point, the probability of an immediate subsequent transition is high, whereas the probability for an instant transition vanishes for a hypothetical starting point in the center of the well.[173] On long time scales, however, when the particle practically samples a large fraction of the potential well, the influence of the starting point is negligible and the distribution obeys an exponential dependence.

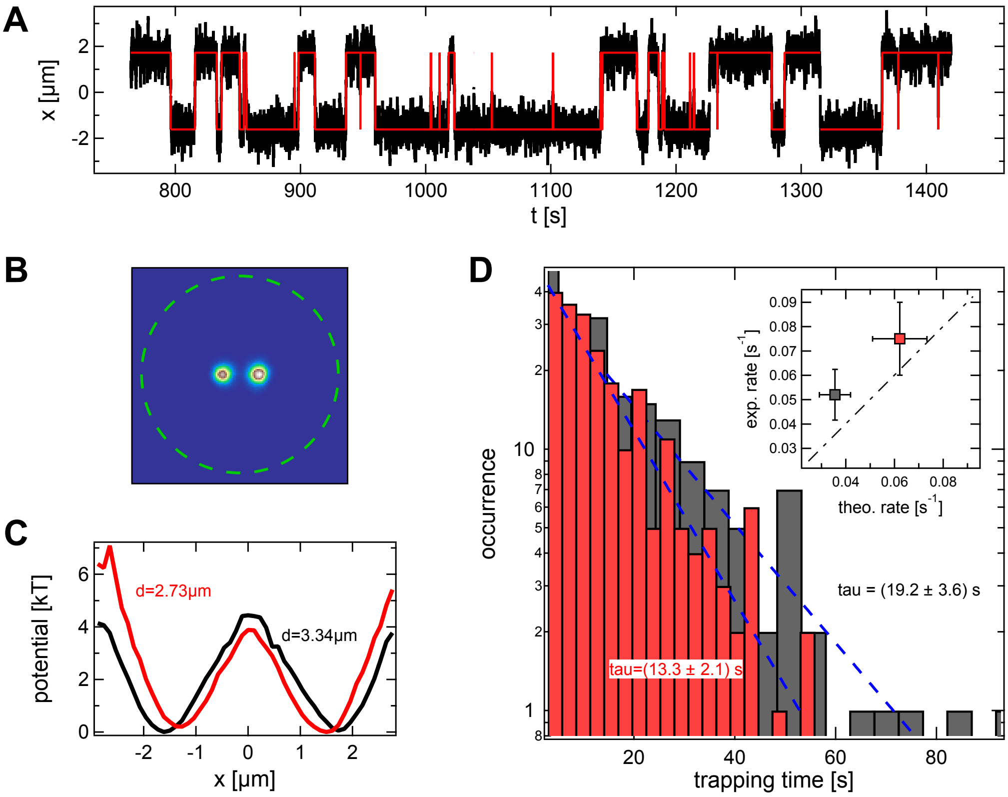

Figure 4.33: **A** Cut-out of a typical trajectory (x component). The red trace shows which well the particle is assigned to after thresholding. **B** Positional distribution for a target separation of $d_\mathrm{T} = 3.34\,\mu\mathrm{m}$. The green circle represents the edge of the gold structure. **C** Effective trapping potential along the x axis for a target separation of $d_\mathrm{T} = 2.73\,\mu\mathrm{m}$ (red) and $d_\mathrm{T} = 3.34\,\mu\mathrm{m}$ (black). **D** Histograms over dwell times (times in between transitions) for a target separation of $d_\mathrm{T} = 2.73\,\mu\mathrm{m}$ (red) and $d_\mathrm{T} = 3.34\,\mu\mathrm{m}$ (black). Exponential fits in blue. **Inset** Experimental transition rate $k_\mathrm{exp} = 1/\tau$ extracted by the exponential fit of the dwell time histograms vs. the theoretical prediction according to Equation 4.22.

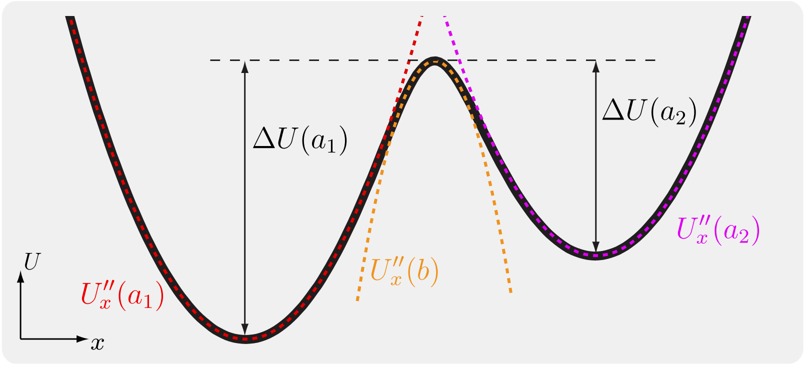

Figure 4.34: Illustration of the parameters determining the transition rate between the potential wells. $\Delta U(a_i)$ denotes the depth of the potential wells with respect to the saddle point and $U''_j(a_i)$ the local curvatures of the potential landscape with $i = 1,2$ and $j = x,y$. The experimental parameters (target positions and heating power) are chosen such that $\Delta U(a_1) \approx \Delta U(a_2)$ and $U''_j(a_1) \approx U''_j(a_2)$.

The problem of the mean first passage time, *i.e.* the mean dwell time or inverse transition rate, directly leads to the Kramers escape rate, which has been studied since the 1940s. For the particular two dimensional potential of the described experiment, the Kramers rate in the overdamped limit reads[174, 175]

$$k_{2\mathrm{D}} = \frac{1}{\tau} = \frac{D}{2\pi k_\mathrm{B}T}\sqrt{\frac{U_x''(a)\,U_y''(a)\,|U_x''(b)|}{U_y''(b)}} \cdot \exp\left(-\frac{\Delta U}{k_\mathrm{B}T}\right), \tag{4.22}$$

where $U_j''(a)$ and $U_j''(b)$ are the curvatures of the effective potential at the local minimum $x = a$ and the saddle point $x = b$ in the particular direction $j = x, y$. ΔU denotes the potential difference between the minimum and the saddle point. These parameters are illustrated in the scheme of Figure 4.34. The drag coefficient γ appears within the prefactor but is replaced with $\gamma = k_\mathrm{B}T/D$, since the diffusion coefficient D is easily extracted from the trajectories. In the experiment, the double well potential are chosen such, that the potential difference to the saddle point $\Delta U(a_1) \approx \Delta U(a_2)$ as well as the curvatures $U_x''(a_1) \approx U_x''(a_2)$ are approximately the same for both the wells. A summary of the parameters extracted from the potentials of Figure 4.33 C is given with Table 4.2. Using these parameters together with Equation 4.22, the theoretically expected transition rates between the potential wells are calculated and compared to the rates measured with the experiment in the inset of Figure 4.33 D. Although the values match the diagonal within the error bars, the experimentally obtained rates are about a factor of 1.3 higher than the theoretical prediction. If this deviation is of systematic nature, *e.g.* caused by the thermal non-equilibrium or the virtual potential due to the feedback-trapping, or if it is due to a lack of statistics can, however, not be judged with the given experimental data.

d_T [µm]	$\Delta U(a_i)$	$U_x''(a_i)$	$U_x''(b)$	$U_y''(a_i)$	$U_y''(b)$
2.73	3.8 ± 0.1	4.07 ± 0.15	-6.56 ± 0.38	3.84 ± 0.15	1.96 ± 0.16
3.34	4.5 ± 0.1	3.99 ± 0.14	-6.48 ± 0.32	2.86 ± 0.13	1.13 ± 0.11

Table 4.2: Overview of the parameters characterizing the experimental double well potentials: ΔU in units of $k_\mathrm{B}T$ and U'' in units of $k_\mathrm{B}T/\mu\mathrm{m}^2$.

Area Target Oftentimes in experiments there is the aim to keep an object within a certain region, but measure an unperturbed local property, *e.g.* the diffusion coefficient to study local viscosity. This demand may be satisfied by specifying an area target rather than a single point. Due to the radial symmetry of the gold structure, the realization of a disc-like target is particularly easy.

For that purpose, a certain maximum radial distance to the trapping center R_max within the trapping region is defined (critical radius). If the nano-object of interest leaves the inner region such that $|\mathbf{R}(t)| > R_\mathrm{max}$, the heating laser is set such that the particle is driven back to the central region, *i.e.* Equation 4.20 with $\mathbf{R}_\mathrm{T} \equiv 0$ is used to calculate the heating position $\mathbf{R}_\mathrm{L}(t)$. Once the particle enters the region where $|\mathbf{R}(t)| < R_\mathrm{max}$, the heating laser is switched off. The by that applied effective temperature profile is shown in Figure 4.35 A. Temperature gradients are only applied in the outer region. According to the described feedback rule the particle is at room temperature while being located in the central region.

The positional distribution of a 200 nm polystyrene particle which is trapped within the central region with radius $R_\mathrm{max} = 2.7$ µm is shown in Figure 4.35 B. The gold structure is heated only if the particle exceeds the white dashed circle. The resulting effective trapping potential is given in Figure 4.35 C and appears to be box-like radially symmetric about the center. Analyzing the step size distribution, it is concluded on the induced thermal drift velocity in radial and tangential direction (Figure 4.35

D). The tangential component vanished overall since the temperature gradient is applied such that the target, the particle as well as the heated spot form a straight line, which ensures that no tangential temperature gradients are present. Strong radial drift velocities up to about $20\,\mu\mathrm{m/s}$ are measured in the outer region with $|\mathbf{R}(t)| > R_{\max} = 2.7\,\mu\mathrm{m}$. Below the threshold for $|\mathbf{R}(t)| < R_{\max}$, a heating of the gold structure is omitted causing zero drift.

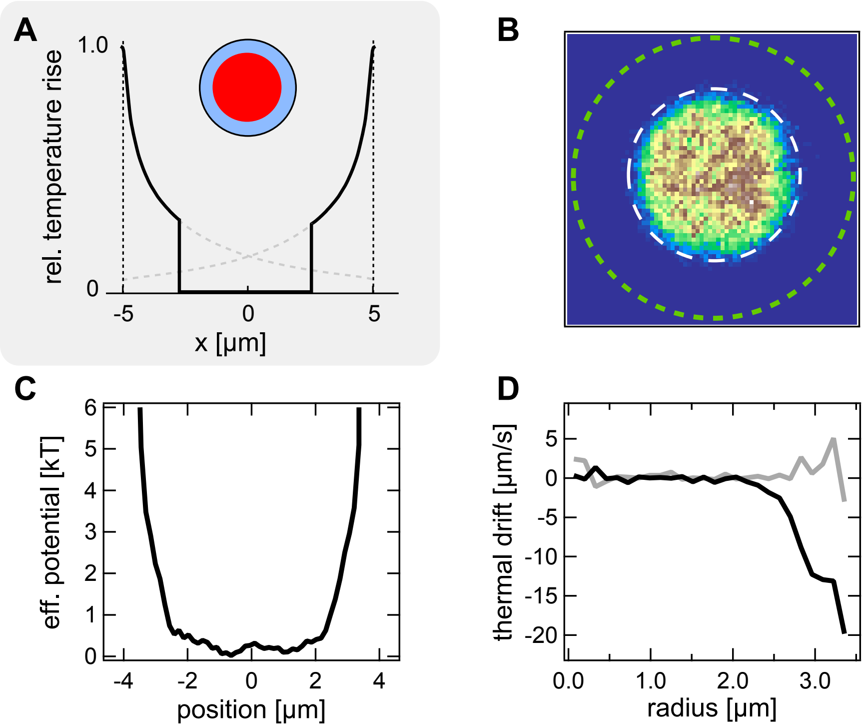

Figure 4.35: **A** Effective temperature field applied via the feedback-controlled heating beam to create a box-like trapping potential. **B** Positional distribution for FB trapping of a 200 nm-diameter polystyrene particle: the laser beam only heats the gold structure if the particle is located outside a radial distance to the center of $R_{\max} = 2.7\,\mu\mathrm{m}$, resulting in a disc-like particle distribution. **C** Effective trapping potential along y axis. **D** Measured radial (black) and tangential (gray) thermal drift velocities as a function of the distance to the trapping center for disc-like positional distribution. Trap diameter $d_{\mathrm{Trap}} = 10\,\mu\mathrm{m}$.

For the particular experiment presented here, the gold structure is only heated about 6.7% of the time to keep the particle within the region with $|\mathbf{R}(t)| < R_{\max}$ and only the strongest temperature gradients near the heated gold structure are used to confine the particle. Note, that the same rms-width of the position distribution may be achieved by a continuous heating with decreasing the beam intensity. However, here, the gold structure is not heated at all most of the time, in which the particle's motion is free and can be studied under no external perturbations.

Time traces of the on-off periods of the heating laser beam are depicted in Figure 4.36 A for three different radii $R_{\max} = 1.4\,\mu\mathrm{m}$, $R_{\max} = 2.9\,\mu\mathrm{m}$ and $R_{\max} = 4.4\,\mu\mathrm{m}$. Already by eye, it is visible, that a more frequent heating is necessary if the particle is confined within an area of smaller radius. Also, the ratio of the total heating time to the time of the time trace decreases for increasing critical radius as can be seen from Figure 4.36 C. A histogram of the durations that the heating laser is switched off reveals an exponential decay for times longer than a few seconds. The bin width of the histograms has been adjusted for each radius $R_{\max}$ due to a different mean decay time.

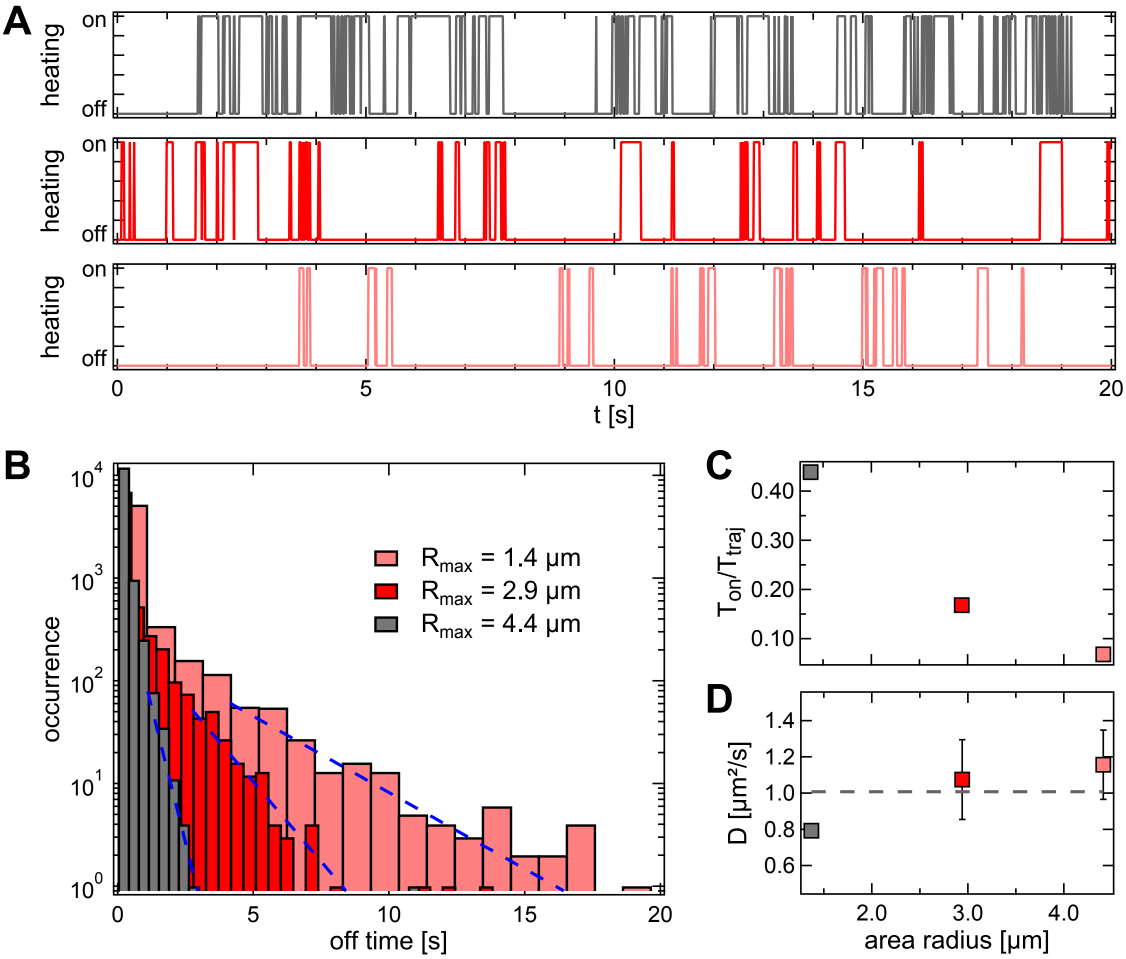

Figure 4.36: **A** Heating status time traces for three different radii $R_{\max} = 1.4\,\mu\text{m}$ (top), $R_{\max} = 2.9\,\mu\text{m}$ (center) and $R_{\max} = 4.4\,\mu\text{m}$ (bottom). **B** Histograms of the off-time durations with fits of Equation 4.23. **C** Ratio of the total heating duration to the time of the trajectory. **D** Diffusion coefficient gained from a fit of Equation 4.23 to the long time tails of the histograms in B. Trap diameter $d_{\text{Trap}} = 15\,\mu\text{m}$.

The off-time distributions resemble a typical two-dimensional first passage problem. Here, the first passage time distribution describes the probability that the particle needs a certain time τ_{off} to reach the circular border of the area $|\mathbf{R}(t)| < R_{\max}$. The first passage time distribution can be described by an analytical expression for the case that the particle starts in the center[176,177] (center to edge diffusion). In the experiment, the first passage time is identified with the laser off-time τ_{off} measured from the point when the particle enters the circular area $|\mathbf{R}(t)| < R_{\max}$ until it leaved the area again (edge to edge diffusion). However, numerical simulations performed by Schuster et al.[173] showed, that the long time tail of the first passage time distribution, *i.e.* for events when the particle explores a large amount of the inner area $|\mathbf{R}(t)| < R_{\max}$ instead of leaving it immediately, exhibits the same exponential decay described by

$$p(\tau_{\text{off}}) = p_0 \exp\left(-\frac{\tau_{\text{off}}}{\tau_{\text{D}}}\right), \tag{4.23}$$

where $\tau_{\text{D}} = R_{\max}^2/(\alpha_1^2 D)$ is the characteristic diffusion time with $\alpha_1 = 2.4$ and D being the diffusion coefficient. Fitting Equation 4.23 to the long time tails of the laser off-time distributions in Figure 4.36 B yields the diffusion coefficient (Figure 4.36 D) of the particle without the need of analyzing the trajectory of the particle at all.

Line Target Due to the symmetry of the gold structure, radially symmetric potentials are particularly easy to realize. Above, trapping at zero and two-dimensional targets has been demonstrated. A quasi-one-dimensional target may be conceived by defining a minimum distance to the trapping center R_{min} in addition to R_{max}. If the particle is located within the region $|\mathbf{R}(t)| < R_{\mathrm{min}}$, the gold structure is heated on the opposite side by setting $\mathbf{R}_{\mathrm{L}}$ to $-\mathbf{R}_{\mathrm{L}}$, which induces a positive radial drift velocity to push the particle towards the outer region. The effective temperature profile along an arbitrary axis through the center is shown in Figure 4.37 A. No heating of the gold structure is performed within $R_{\mathrm{min}} < |\mathbf{R}(t)| < R_{\mathrm{max}}$. Setting $R_{\mathrm{min}} = R_{\mathrm{max}} = R_{\mathrm{line}}$ creates a quasi-one-dimensional line target resulting in a Sombrero-like trapping potential.

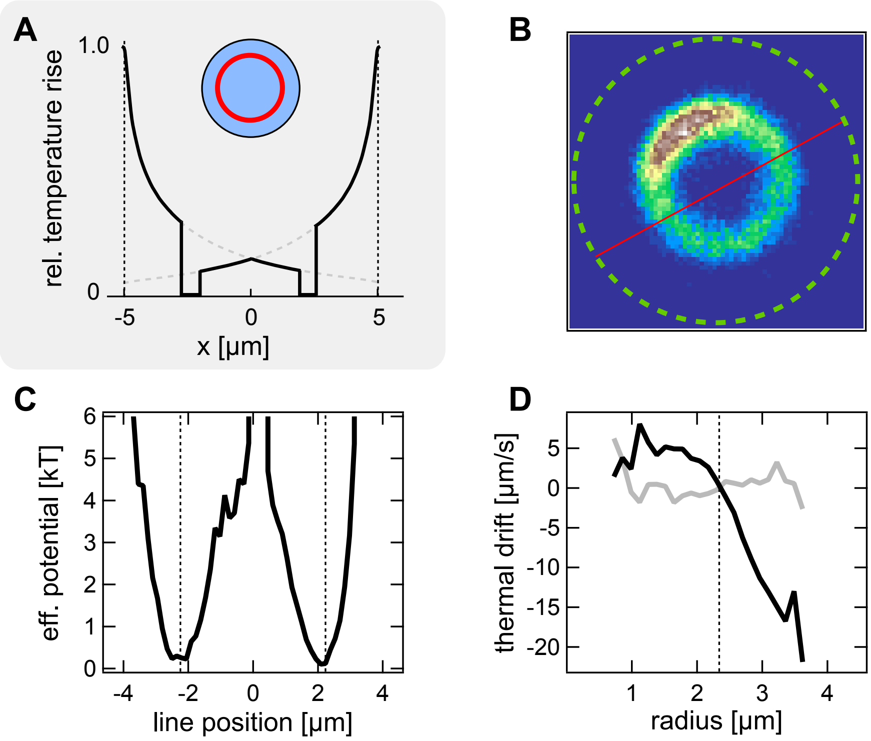

Figure 4.37: **A** Effective temperature field applied via the feedback-controlled heating beam to create a ring-like trapping potential. **B** Position distribution of a 200 nm PS particle in a 10 μm-diameter trap (green dashed circle) with $R_{\mathrm{line}} = 2.3\,\mu\mathrm{m}$. An asymmetry is resulting from a slightly varying heating power along the circumference of the gold structure. **C** Effective trapping potential along the red line in B. **D** Induced thermophoretic drift velocities in radial (black, negative means towards the center) and tangential direction (gray). The dashed lines in C and D indicate R_{line}.

Applying the described feedback rule with $R_{\mathrm{line}} = 2.3\,\mu\mathrm{m}$ in an experiment locates the 200 nm polystyrene particle on a ring-like trace as can be seen from Figure 4.37 B. The positional distribution shown in Figure 4.37 and appears asymmetric due to an remaining asymmetry in the heating beam power (see Calibration of the AOD in Section 3.2) that located the particle preferably on one side of the ring. The effective trapping potential shows a distinct circular minimum at $R_{\mathrm{line}} = 2.3\,\mu\mathrm{m}$, which can be seen from Figure 4.37 C. The slope of the potential in the inner region with $|\mathbf{R}(t)| < R_{\mathrm{line}}$ is shallower resulting from the longer distance to the heat source on the opposite side of the gold structure. Figure 4.37 D shows the transition from positive to negative radial drift velocity at R_{line}. Here, the same argument as for the shallower slope of the potential holds for the positive drift in the inner region, which appears slower in its magnitude. As expected, no tangential thermophoretic drift is measured.

While the latter examples of artificial trapping potential are relatively easy to realize, almost arbitrary (2D) potentials may be generated on demand by designing more complex criteria where and when to heat the Au structure with respect to the particle's position. Also, the heating intensity could be controlled for particular feedback rules.

4.3.5 Limits of Feedback-Controlled Trapping

Different parameters limit the thermophoretic trapping of small objects. Generally, physical and chemical properties of the particle-solvent system determine the Soret coefficient. While the Soret coefficient can certainly be optimized, for example by tuning the composition the solvent, the maximum temperature increment that can be exerted to a particle is typically limited, in particular for biological applications. A limitation of the maximum temperature then again constrains the temperature gradient which can be generated to confine a small object in solution. Otherwise, the trapping is technically limited by a finite update rate of the optical particle position feedback. In the following, the physical limits are discussed considering an instant feedback of the temperature field on the particles position, *i.e.* considering a steady-state temperature field, followed by a discussion of the influence of a finite feedback cycle time in an experiment.

Limitation Considering an Instant Feedback The positional distribution function (PDF) of a particle within the thermal trap for instant feedback is purely determined by the shape of the temperature field ΔT and the Soret coefficient $S_\mathrm{T} = D_\mathrm{T}/D$. An approximation of the temperature field in the trap center with a parabola $\Delta T \sim \frac{\alpha}{2}x^2 + \Delta T_\mathrm{Center}$ leads to the positional distribution function

$$p_\mathrm{TP}(x) = p_\mathrm{TP,0}\exp\left(-S_\mathrm{T}\Delta T\right) = p_\mathrm{TP,0}\exp\left(-\frac{x^2}{2\sigma_\mathrm{TP}^2}\right), \tag{4.24}$$

exhibiting a width $\sigma_\mathrm{TP} = 1/\sqrt{S_T\alpha}$ determined by the two counteracting effects being a diffusive outward drift characterized by D compensated by a thermophoretic inward drift $v_\mathrm{T} = -D_\mathrm{T}\nabla T = -D_\mathrm{T}\,\alpha x$. The curvature of the temperature field $\alpha = \alpha' \cdot \Delta T_\mathrm{Au} \propto P_\mathrm{heat}$ thereby is proportional to the excess temperature at the gold structure and hence the heating power. In simple words, a particle is efficiently trapped, if the width of the positional distribution, *i.e.* the probability distribution function, does not exceed about half the trap size $\sigma_\mathrm{TP} < R_\mathrm{Trap}/2$. However, an overlap of the PDF with the trap borders leads to a finite probability for a particle to escape from the trap. The mean time a particle is held within the trap region may be estimated via Kramers escape theory.[178,179] The theory generally relies on thermal equilibrium processes. Here, an inhomogeneous temperature profile is utilized to trap a nano-object. The relative temperature rise over ambient temperature, however, is typically weak and in the order of a few Kelvin. Also, in Section 4.3.4 Kramers escape rate was already successfully applied to the artificial double well potential in the thermal trap. At ambient temperature T_0, Kramers escape rate for the one-dimensional potential landscape sketched in Figure 4.38 reads

$$k = \frac{D}{2\pi k_\mathrm{B}T_0}\left[U''(a)|U''(b)|\right]^{1/2} e^{-\frac{\Delta U}{k_\mathrm{B}T_0}}, \tag{4.25}$$

with

$$U''(a) = \frac{\partial^2 U}{\partial x^2}|_a \tag{4.26}$$

and

$$U^{''}(b) = \frac{\partial^2 U}{\partial x^2}|_b \tag{4.27}$$

being the curvatures of the potential landscape at the minimum ($x = a$) and the barrier ($x = b$). $\Delta U = U(b) - U(a)$ describes the potential contrast between the minimum and th barrier. As discussed in Section 2.2.2, a particle in the thermal trap is driven via a phoretic drift rather than an external body force. Nevertheless, from the particle's positional distribution it may be concluded on an effective trapping potential $U(x) = k_B T_0 S_T \Delta T(x)$ by a comparison to a Boltzmann distribution.

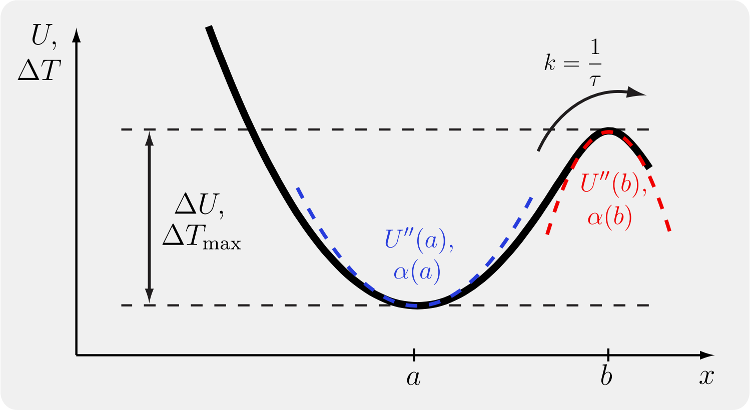

Figure 4.38: Schematic illustration of the parameters used within the present paragraph. The Kramers relation is applied to thermophoresis, where a temperature well acts as an effective potential well. Curvature of the potential $U''(x)$ in the minimum ($x = a$) and the local maximum ($x = b$) corresponds to the curvature of the temperature field $\alpha(x)$. The depth of the potential ΔU is represented by the contrast in temperature ΔT_{max}. Both parameters influence the escape rate k and the mean trapping duration τ according to Equation 4.28.

The trapping center is identified with the position $x = a$, whereas $x = b$ represents the temperature barrier at the gold structure being heated optically. At these positions, the local temperature field may be in first order approximated by parabolic functions, $\Delta T(x) = \frac{\Delta T_{\mathrm{Au}} \alpha'}{2} x^2 + T_0$. The curvatures are then replaced with $U^{''}(x) = k_{\mathrm{B}} T_0 S_T \alpha(x)$ and accordingly the potential depth with $\Delta U = k_B T_0 S_T \Delta T_{\mathrm{max}} = k_B T_0 S_T \Delta T^{\mathrm{rel}}_{\mathrm{max}} \Delta T_{\mathrm{Au}}$. Inserting the above considerations into Equation 4.25 delivers the mean trapping time τ or the escape rate k with

$$\tau = \frac{1}{k} = \frac{2\pi}{D_{\mathrm{T}}\, \Delta T_{\mathrm{Au}}} \frac{1}{\sqrt{\alpha'(a)\,|\alpha'(b)|}} e^{S_{\mathrm{T}} \Delta T^{\mathrm{rel}}_{\mathrm{max}} \Delta T_{\mathrm{Au}}}. \tag{4.28}$$

For a given set of parameters $\alpha'(a)$ and $\alpha'(b)$, that means for a fixed shape of the temperature field, the mean trapping duration of a particle increases exponentially with the Soret coefficient as well as the depth of the temperature field ΔT_{max}. In order to increase the trapping time, thus, it is more beneficial to increase the Soret coefficient or the depth of the temperature field than tuning the curvatures of the temperature field.

Figure 4.39 A plots the effective temperature profile produced by a 15 µm-diameter trap upon feedback-controlled heating. The parameters α' for the particular positions as well as the depth of the temperature field are given within the plot. Using these parameters, the mean trapping time may be calculated from Equation 4.28 as a function of the depth of the temperature field and the Soret coefficient, which is depicted as $\log(\tau/s)$ in Figure 4.39 B. As can be seen, particles with a Soret coefficient of order $S_{\mathrm{T}} \sim 1\,\mathrm{K}^{-1}$ or higher can be virtually trapped forever, even for moderate temperature increments, which was also qualitatively observed, for example, within the experiments of the

Sections 4.3.2 to 4.3.4, which took several hours and were each performed on a single particle. Considering a typical thermodiffusion coefficient of $D_\mathrm{T} = 1\,\mu\mathrm{m}^2/\mathrm{Ks}$ and a Stokes-Einstein relation for the diffusion coefficient $D = k_\mathrm{B}T/6\pi\eta R$, the mean trapping time τ may also be plotted in dependence on the particle radius R (see Figure 4.39 C).

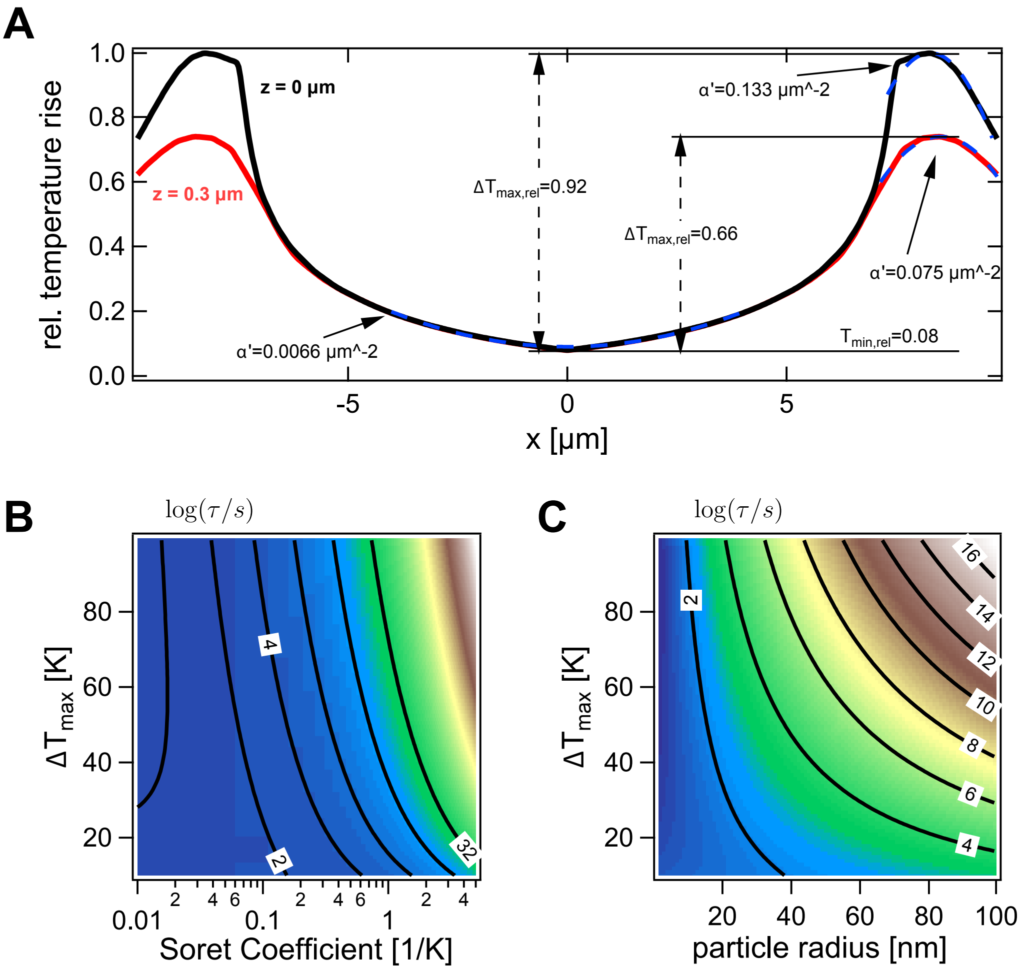

Figure 4.39: **A** Effective temperature profile applied in a 15 µm-diameter trap for instant feedback update in the plane of the gold structure (black) and 300 nm above. The temperature profiles are normalized to the maximum temperature increment at the gold structure. Relative curvatures of the temperature fields are found by fitting 2nd order polynomials (dashed blue) to the minimum and the temperature wells. The extracted parameters are used to estimate the mean trapping durations (see B and C) via Equation 4.28. **B** Logarithm of the mean trapping time (Equation 4.28) for the parameters extracted from A in dependence on the absolute maximum temperature increment and the Soret coefficient. **C** Same as C, but $S_\mathrm{T} = D_\mathrm{T}/D$ was replaced with a typical value $D_\mathrm{T} = 1\,\mu\mathrm{m}^2/\mathrm{Ks}$ and $D = k_\mathrm{B}T/6\pi\eta R$ to plot $\log(\tau)$ in dependence on the particle radius R.

For a depth of the temperature field of $\Delta T_\mathrm{max} \sim 40\,\mathrm{K}$, which leads to a temperature rise in the trap center of about $\Delta T_\mathrm{Center} \sim 3\,\mathrm{K}$ for a 15 µm-diameter trap, an $R \sim 50\,\mathrm{nm}$ particle is trapped with a mean trapping duration of $\tau \sim 10^4\,\mathrm{s}$.

Influence of a Finite Feedback Cycle Time The influence of the feedback cycle time on the trapping is readily checked with an experiment. A 200 nm polystyrene particle is trapped in a 10 µm-diameter trap at a constant heating laser power of $P_\mathrm{Heat} = 5\,\mathrm{mW}$ for an increasing feedback cycle times (*i.e.* a decreasing update rate), which coincide with the frame time of the CCD camera. The particle's trajectory for each exposure time is analyzed and the rms-displacement from the trapping center is plotted in Figure 4.40 (squares). As it turns out, the positional distribution width rises approximately linear with increasing feedback cycle time $\sigma \propto \tau_{\mathrm{FB}}$.

In a simple consideration, the broadening may result from the Brownian motion of the particle during the feedback cycle time, given by $\sigma_{\mathrm{FB}} = \sqrt{4D\tau_{\mathrm{FB}}}$. Hence, additionally to the width that is given by the steady-state temperature field, the position distribution should spread with $\sqrt{\tau_{\mathrm{FB}}}$. This argument was given by Cohen and Moerner for the ABEL trap.[47] The trapping scheme is analogue, but the driving force is different (temperature gradient instead of electric field). However, the dependence does not match the experimental data, such that the spread cannot solely be attributed to the Brownian motion within a feedback period. The argument fully neglects the deterministic drift exerted by the trap.

In 2012, Jun and Bechhoefer published a theoretical description of feedback traps utilizing virtual potentials.[171] Herein, in the simplest case of no feedback delay, the width steady-state position distribution in a virtual harmonic potential is found in dependence of the feedback cycle time τ_{exp} with the expression

$$\langle x^2 \rangle = \frac{2D\tau_{\mathrm{FB}}}{\beta(2-\beta)}, \tag{4.29}$$

where $\beta = \tau_{\mathrm{FB}} k/\gamma$ denotes the feedback gain and $\gamma = 6\pi\eta R$ the Stokes friction coefficient. Equation 4.29 converges to the width predicted by the equipartition theorem $\langle x^2 \rangle = k_{\mathrm{B}}T/k$ for $\beta \ll 1$, but diverges for $\beta = 2$ due to an overshooting over the target. In addition to τ_{exp}, it is also considered that the feedback update exhibits a certain delay described by the delay time τ_{delay}. A finite delay leads to an additional broadening of the position distribution. A corresponding analytical expression is found for the case that $\tau_{\mathrm{delay}} = \tau_{\mathrm{FB}}$,[171]

$$\langle x^2 \rangle = 2D\tau_{\mathrm{FB}} \frac{1+\beta}{\beta(1-\beta)(2+\beta)}. \tag{4.30}$$

The latter relation also converges to the equipartition width for small β, but diverges already at $\beta = 1$. Equations 4.29 and 4.30 are plotted in Figure 4.40 A for the experimental parameters ($k = 35.8\,\mathrm{fN}/\mu\mathrm{m}$, $D = 1.21\,\mu\mathrm{m}^2/\mathrm{s}$) in red and black, respectively. In the experiment, the feedback delay is measured to $\tau_{\mathrm{delay}} = 10.9\,\mathrm{ms}$ and is independent of the feedback cycle time. Hence, the ratio $\tau_{\mathrm{delay}}/\tau_{\mathrm{FB}}$ is about unity for the fastest update rate, but decreases with longer feedback cycle times (Figure 4.40 B). Accordingly, the experimental data should match the black curve for short cycle times but approach the red curve for longer times. This qualitatively behavior is indeed found. The skipping between the regimes lead to a linear dependence by coincidence. Yet, the experimental data still seems to be close to the black curve, which diverges at $\beta = 1$. Hence, at the slowest update rate measured with $\beta > 0.6$, an overshooting over the target should be already present. Over-compensation of the particle's positional fluctuation is visible in the power spectrum as a pronounced resonance. However, no signature of overshooting is found in the power spectra as can be seen from Figure 4.40 C.

The additional broadening in the width is interpreted such, that a tangential thermophoretic drift drives the particle not directly towards the target, leading to a broader position distribution. This effect is not covered by the theoretical description in the description of Jun and Bechhoefer.[171] A finite tangential component may result due to the Brownian motion of the particle, which drives the particle away from the target-laser line (see Figure 4.41 A, dashed line). Due to the radially decaying temperature field, once the particle left this line, it experiences a tangential temperature gradient additionally to the radial gradient that is intended to drive the particle towards the center. This effect is not expected for the ABEL trap, where a constant electric field along the particle-target direction is generated within the trapping region. Hence, no or very little tangential component is produced.

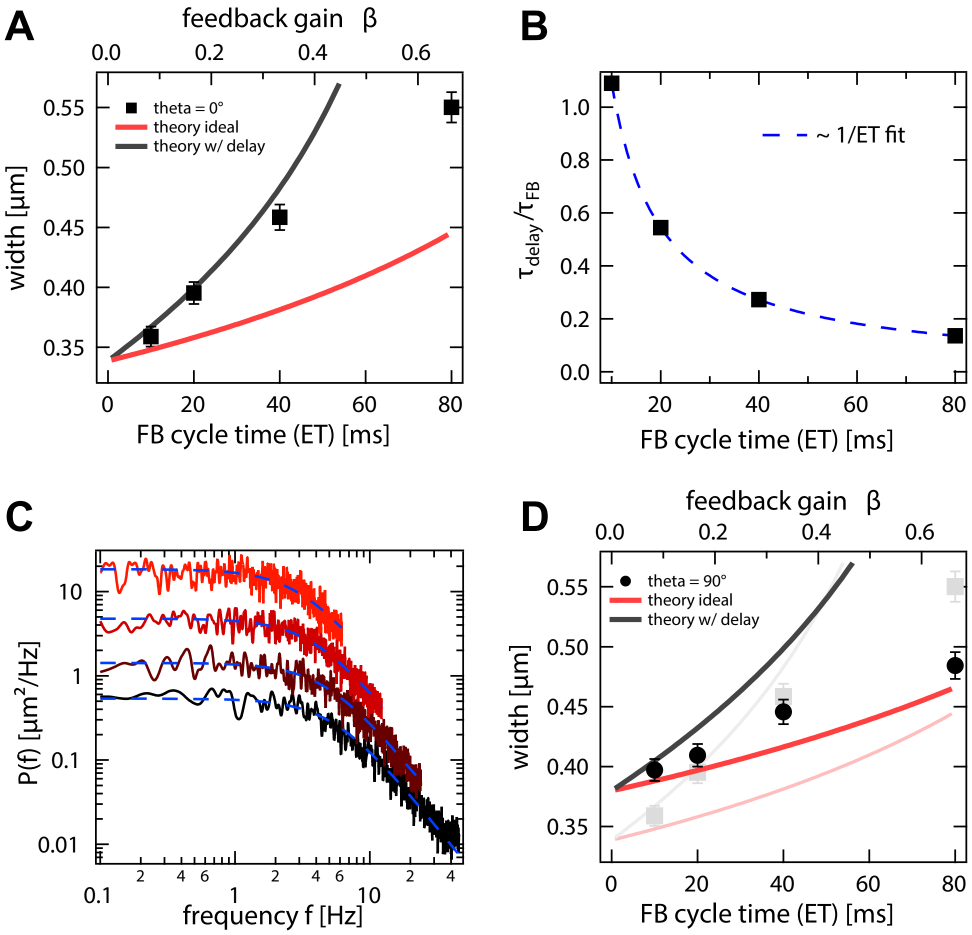

Figure 4.40: Trapping of a single 200 nm PS bead for increasing feedback cycle time τ_{FB} at a heating laser power $P_{\mathrm{Heat}} = 5\,\mathrm{mW}$. **A** Sdev-width of the position distribution for increasing τ_{FB}, *i.e.* decreasing update rate, for heating of a single spot ($\vartheta = 0$). Upper axis: feedback gain $\beta = \tau_{\mathrm{FB}} k/\gamma$. Theory curves calculated from Equation 4.29 (red) and 4.30 (black). **B** Ratio of delay time τ_{delay} and feedback cycle time versus feedback cycle time τ_{FB} (*i.e.* the exposure time). **C** Power spectral density of the particle's motion for different τ_{FB} (10 ms (black) to 80 ms (red)). No signature of over-compensation (resonant peak) is visible. **D** Same as in A, but for the heating of an angular region of $\vartheta = 90°$. For comparison, the data of A is shown again with low opacity.

This effect may also be diminished for the thermophoretic trap. For that purpose, the effective temperature field is redesigned in the following way. Instead of illuminating a single spot at the gold structure (see Figure 4.41 A and C), a certain angular region is heated as shown in Figure 4.41 B, which is achieved by a fast steering of the laser beam along the angular interval $[\phi + \vartheta/2, \phi + \vartheta/2]$. The simulated temperature profiles induced by such a heating scheme are plotted in Figure 4.41 D for $\vartheta = 90°$. For the purpose of trapping, a temperature gradient is only favorable in radial direction, *i.e.* along the dashed line in Figure 4.41 C and D. The red curves in Figures 4.41 F and G present the temperature and temperature gradient profiles along the red line in C. Due to the effective point heat source, the particle experiences also tangential temperature gradients once it leaves the dashed line (*e.g.* due to Brownian motion before the laser position is updated after τ_{FB}) driving the particle past the target.

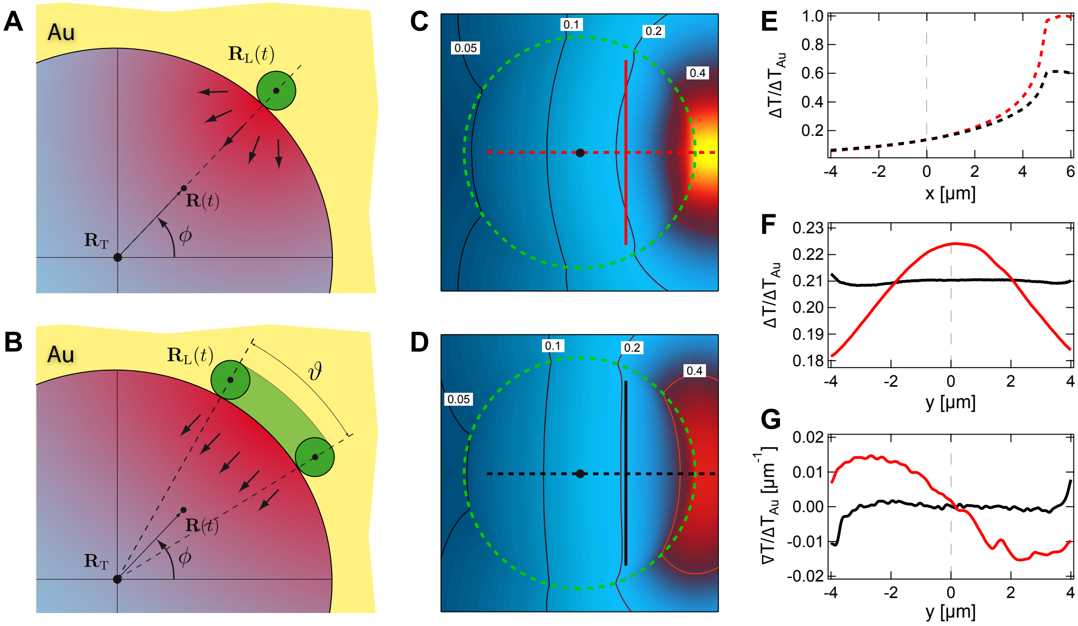

Figure 4.41: **A** Conventional feedback heating scheme. A single diffraction limited spot is heated according to Equation 4.20. **B** By steering the focused laser beam along the circumference of the gold structure, an angular region $[\phi - \vartheta/2, \phi + \vartheta/2]$ can be heated to avoid tangential temperature gradients. **C** Simulated temperature map for the heating of a single spot (*i.e.* $\vartheta = 0°$) at $\phi = 0°$, normalized to the maximum temperature ΔT_{Au}. **D** Temperature map for the heating of an angular region with $\phi = 0°$ and $\vartheta = 90°$. The temperature field is normalized such, that the temperature in the trap center matches with the center temperature in C (central black dots). At this position, the distance to the heat source in both cases is the same. The heating of the broad region with the same power leads on average to a decreased maximum temperature. **E** Line profile of the relative temperature rise along the dashed lines in C and D (radial direction). **F** Line profile of the relative temperature rise along the vertical lines in C and D (tangential direction). **G** Relative temperature gradient along the vertical lines in C and D (tangential direction).

Heating of an angular region as shown in Figure 4.41 D straightens the temperature profile within the trapping region compared to the point source as can be seen already from the iso-temperature contour lines. A direct comparison of the temperature profiles and gradients are given in Figure 4.41 E (radial direction), F and G (tangential direction). Obviously, due to the spatial distribution of the heating laser beam, the effective temperature rise at the gold structure decreases to 61% of the instantaneous temperature rise of the gold structure (compare color scales in C and D and see E). That also leads to a diminished radial temperature gradient and results in a decreased effective curvature of the temperature field and therefore to a lower trapping stiffness k. However, the unwanted tangential temperature gradients are effectively reduced (see G).

In the experiment, the combination of these two effects can be seen in Figure 4.40 D, where the dependence of the positional distribution width on the feedback cycle time is plotted for the heating of an angular region. The black and red curve again represent the calculations from Equations 4.29 ($\tau_{\mathrm{delay}} = 0$) and 4.30 ($\tau_{\mathrm{delay}} = \tau_{\mathrm{FB}}$). For comparison, the data for the single-spot heating of Figure 4.40

A is shown faded in the background. While the diffusion coefficient D and the τ_{delay} are the same, the effective force constant k decreases for the angular heating, resulting in a shallower slope of the width σ with β, even without considering a tangential drift (compare theory curves in Figure 4.40 D for $\vartheta = 0°$ and $\vartheta = 90°$). Also, an increased width for zero cycle time is recognized ($\sigma \propto k^{-1/2}$ for $\tau_{\mathrm{FB}} = 0$, equipartition limit). Due to the suppression of the tangential component of the thermal drift, the data points converge significantly faster to the red curve for large feedback cycle times, where the ratio $\tau_{\mathrm{delay}}/\tau_{\mathrm{FB}}$ is small and the feedback delay is thus negligible.

The two experimental data sets show an intersection at a feedback cycle time of about $\tau_{\mathrm{FB}} = 30\,\mathrm{ms}$ corresponding to a feedback gain of about $\beta \sim 0.28$, which is caused both by the decreased force constant k reducing a potential over-compensation and the suppression of the tangential thermal drift driving the particle past the target. Hence, for slow feedback update rates it can be beneficial to heat an angular region instead of a single spot on the gold structure.

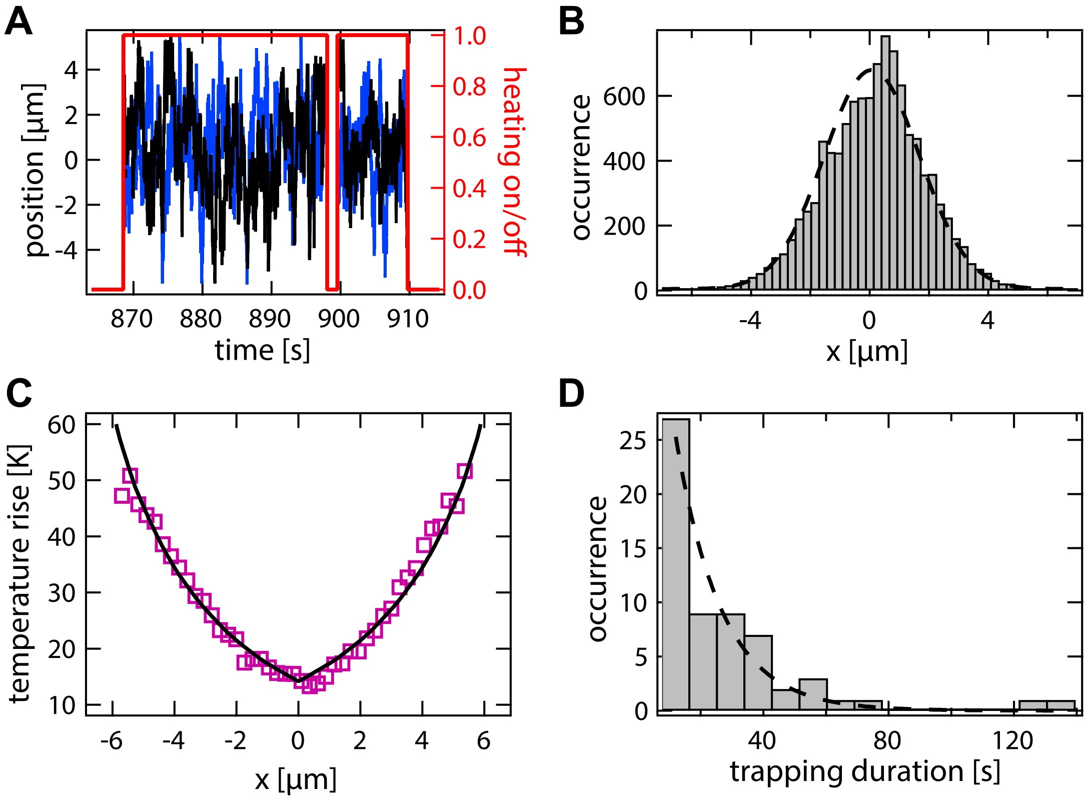

Figure 4.42: Trapping of single 28 nm-diameter polystyrene beads in a $d_{\mathrm{Trap}} = 15\,\mu\mathrm{m}$ gold structure. **A** Extract of the time trace (x and y position) showing two typical trapping events. **B** Positional distribution averaged over all 113 measured trapping events showing an rms displacement of the beads from the trap center of $\sigma = (1.61 \pm 0.08)\,\mu\mathrm{m}$. **C** Temperature profile reconstructed from the position distribution. Comparing the data to the theoretically expected temperature profile yields an ensemble-averaged Soret coefficient of $S_{\mathrm{T}} = 0.13\,\mathrm{K}^{-1}$. **D** Histogram over the duration of the single trapping events with exponential fit yielding a mean trapping duration of $\tau = (14.6 \pm 1.9)\,\mathrm{s}$.

The smallest particles tested with the thermophoretic feedback trap are polystyrene nanobeads of 28 nm diameter. A 15 µm-diameter trap structure was used at a constant heating power of $P_{\mathrm{heat}} = 6.0\,\mathrm{mW}$. The focused laser beam heats an angular region of $\vartheta = 60°$ as explained above. Due to fast Brownian motion, particles may escape the trap after a certain trapping duration. If a particle escapes, the feedback stops and the heating is switched off automatically until a particle by chance enters the trap again, which reactivates the feedback-controlled heating. Figure 4.42 A shows the time trace of two subsequent trapping events. A line profile of the positional distribution of the beads within the trapping region is given in Figure 4.42 B, which shows a sdev-width of $\sigma = (1.61 \pm 0.08)\,\mu\mathrm{m}$. Reconstructing the temperature profile from the positional distribution yields an ensemble-averaged Soret coefficient of $S_{\mathrm{T}} = 0.13\,\mathrm{K}^{-1}$ and an average temperature rise of the trapped beads of about 20 K (see Figure 4.42 C). By monitoring 113 trapping events, a mean trapping duration of $\tau = (14.6 \pm 1.9)\,\mathrm{s}$ is measured. The measured Soret coefficient compares to that of ssDNA and dsDNA oligonucleotides of a about hundred base pairs in length, depending on the buffer condition.[57,59]

Apart from the finite feedback cycle and delay time, additional technical aspects limit the trapping of small or weakly fluorescent objects. Blinking may occur in the case of single quantum dots or molecules (used for labeling), but was no issue with the experiments presented here. Bleaching ultimately limits the trapping duration as the real-time position tracking is indispensable for the update of the feedback. Tracking accuracy is shot-noise-limited $\Delta x = \Delta x_{\mathrm{psf}}/\sqrt{n}$, where Δx_{psf} denoted the diffraction-limited image size of the trapped object, as it increases with the number of collected photons n. A low accuracy further broadens the positional distribution of the particle in the trap leading to a higher escape probability. Even if a sufficient amount of photons is provided by the fluorescent object (as is the case of dye-doped polystyrene particles), the signal-to-noise or signal-to-background ratio is decreased by fluorescence of the gold structure upon the optical heating. Experimentally, the latter aspects could be addressed by modifying the detection scheme. A spectral separation of the laser beams responsible for the excitation of fluorescence of the trapped object and the heating the metal structure would be beneficial to minimize the fluorescence background and bleaching, improving both the tracking accuracy as well as the mean trapping duration. The feedback latency is determined by the time that is needed to acquire and analyze a particular frame. A faster acquisition of the particle or molecule position could be realized using a beam-steering-based detection controlled by a field-programmable gate array as is used in modern ABEL traps.[49–51] Ultimately, the feedback update rate is limited by the time scale to establish the temperature profile, *i.e.* by the heat diffusion in the solvent (see Section 2.4.3). Assuming an instant feedback, the trapping duration is physically limited by the maximum amount of heat that can be brought into the system depending, for example, on the damage threshold in a particular application.

4.3.6 Feedback-Controlled Trapping Above a Plain Gold Film

Already in Section 4.2.5 the question was raised if the gold structure is at all needed for a stable trapping. Oftentimes, water is heated within microscopic regions of a sample by a focused infrared laser beam.[59,63,65,77] While such a laser is not available in the trapping setup used, the direct heating of the water may be mimicked by heating a plain gold film in the same way as done in Section 4.2.5, where the quasi-steady heating scheme was tested. Here, it is shown, that for the feedback heating scheme a particle can be trapped without a gold structure. Advantages and disadvantages over the gold-structure-based trap are discussed.

Figure 4.43 A shows simulated temperature profiles for the case that a circular hole in the gold film is present and a site close to the circumference is heated by a focused laser beam (black). Also, the figure plots the equivalent temperature profiles where the gold film is heated without a hole structure present. The differently colored curves correspond to an increasing distance to the defined trapping center (in the following also referred to as laser radius).

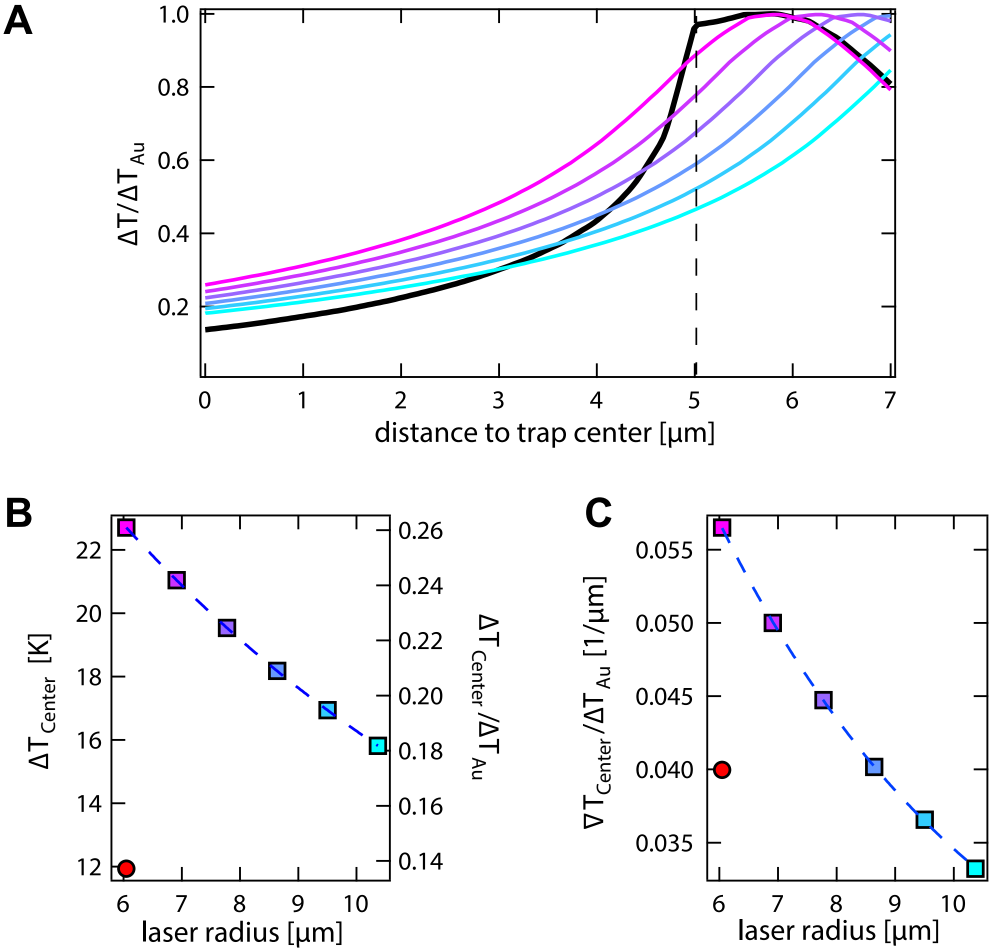

Figure 4.43: Feedback trapping above a plain gold structure. **A** Simulated temperature profiles along the line connecting the trapping center and the position of the heating beam (maximum temperature). All temperatures appear normalized to the maximum temperature rise at the gold structure ΔT_{Au}. The colored curves show the relative temperature profiles for increasing radius of the heating laser circle. The black curve represents the profile for the case that a hole of 10 µm diameter is present in the gold film. **B** Relative center temperature rise (right axis) in dependence on the laser trace radius. The left axis represents the absolute temperature rise for the experiment presented. The color encodes the laser trace radius used in A. The red dot corresponds to the temperature profile through the conventional gold structure (black curve in A). The dashed line shows an exponential fit, as the $\Delta T_{\mathrm{Center}}$ approaches zero (ambient temperature) for large laser rotation radii. **C** Same as in B but for the relative temperature gradient close to the trap center.

As can be clearly seen, the decay of the temperature field into the trapping region in the case where the hole is present (black) is much stronger than for the plain gold film, because of the sharp border between an absorbing (gold) to a non-absorbing (water) material. This leads to a stronger average temperature gradient as well as a lower excess temperature in the center as can be seen from Figure 4.43 B. For the same distance of the laser beam from the center of the trap, the center temperature rise is almost halved in the case of a 10 µm-diameter hole structure. For increasing distances of the laser spot, the temperature rise in the center decreases and ultimately converges to ambient temperature (not shown). The blue dashed line represents an empiric exponential fit. The normalized temperature gradient close to the trapping center decreases with increasing laser radius in the case of the plain gold film as well (Figure 4.43 C). According to the simulated temperature profiles, the gradient produced by the plain gold film is even higher than for the gold structure for comparable laser radii. The expected gradient for the heating of the gold structure of 10 µm-diameter (red dot) is equivalent to the gradient produced by a plain gold film for a laser radius of about 8.6 µm laser radius. Remember, that the center temperature rise is significantly higher in any case.

Experimental data of the trapping of a 200 nm-diameter polystyrene bead are presented in Figure 4.44. The colloid first is trapped in a 10 µm-diameter hole structure by feedback-controlled heating. Subsequently, by means of the piezo translation stage, the trapped particle was driven with activated feedback into a region, where no hole was in the near proximity but only a plain gold film, which ensures that the temperature field is not distorted. The heating power has been kept constant throughout the experiment at $P_{\text{heat}} = 3.0\,\text{mW}$. The sdev-width of the measured particle distribution is shown in Figure 4.44 A, in red for the trapping in the conventional gold structure and in black for the trapping above the plain gold film. The width for the plain gold film trapping increases approximately linear with the laser radius due to the decreasing temperature gradient. For all measured radii, the width is broader than for the trapping in the conventional gold structure. Since the trapping is driven by the temperature gradient, from Figure 4.43 C one would suggest that the width of the gold-structure-assisted trapping is in between the data for the trapping above the gold film, which is not the case in the experiment.

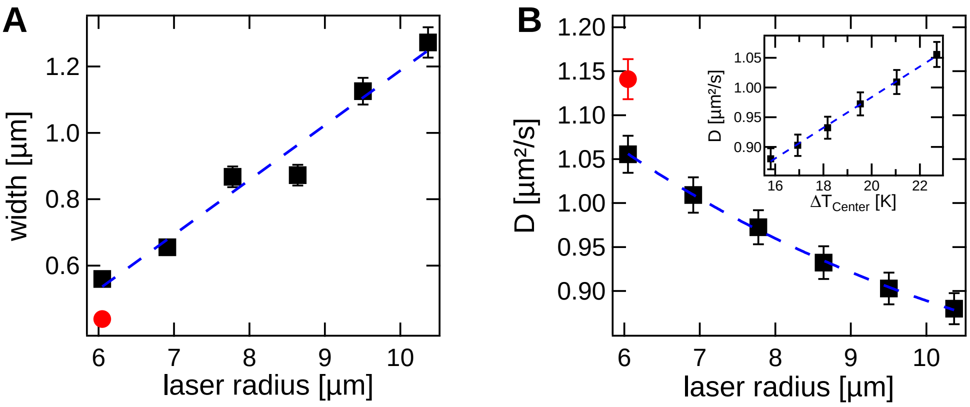

Figure 4.44: Feedback trapping of a 200 nm PS bead above a plain gold structure at a feedback update rate of 100 Hz. **A** rms displacement of the bead from the trap center (width of the position distribution) for a feedback-controlled heating of the gold structure ($P_{\text{heat}} = 3.0\,\text{mW}$) for increasing radius of the heating laser circle. The red data point represents the width of the same particle trapped in a hole in the gold film. **B** Diffusion coefficient in dependence on the laser trace radius fitted by an empirical exponential function. Again, the red data point corresponds to a trapping using a hole in the gold film. **Inset:** Diffusion coefficient plotted versus the center temperature rise ΔT_{Center} calculated from the simulations of Figure 4.43 with $\Delta T_{\text{Au}}/P_{\text{heat}} \approx 29\,\text{K/mW}$ (see Section 4.3.3). The dashed line represents a linear fit.

The characteristics of the center temperature rise is directly related to the diffusion coefficient. The trend of the diffusion coefficient obtained from a step-size analysis of the trajectories is given in Figure 4.44 B. The decrease is correlated with the decreasing center temperature rise for increasing laser radius. The inset plots the diffusion coefficient versus the expected excess temperature in the center and shows approximately a linear relation which is expected within the relative small temperature range (see Figures 4.7 and 4.27). The diffusion coefficient for the gold structure trapping (red dot) is obviously higher. An expected lower center temperature, however, would lead to a lower diffusion coefficient. Also the narrower position distribution contradicts the higher diffusion coefficient, which would lead to a broader distribution since $\sigma \propto 1/\sqrt{S_\mathrm{T}} \propto \sqrt{D}$. This inconsistency is explained with the changed environment. Despite the heating power has been kept constant, the temperature rise for the heating of the plain gold film could be less due to a decreased plasmon excitation when no edge in the gold film is present. Hence, the temperature is lower than expected above, explaining an increased width. Additionally, at a lower center temperature, the mean diffusion coefficient decreases, which matches to the experimental finding. Also, a thinner water film (due to additional gold film, thickness may also vary over the sample) may lead to a secondary decrease in the diffusion coefficient due to stronger friction.

Although a quantitative comparison to the trapping in a conventional gold structure is obviously not trivial due to the change in the absorption properties, the data showed that a feedback trapping above a plain gold structure is possible without further changes in the setup. The experimental data well matches the theoretical expectations. The temperature in the center of the trap is higher than for the gold-structure-assisted trapping, which limits the heating power that can be applied and is possibly unwanted in most applications. However, if a broader position distribution is not obstructive in a particular application, this simpler version of the feedback trap is readily integrated in existing setups that comprise a beam-steering unit. A direct heating of the solvent instead of a gold-structure-assisted heating could also open the possibility for a 3D thermophoretic trap in solution. The feedback-controlled driving of the heating beam on a circle could then be expanded to a sphere by employing a 3D beam steering unit.

4.3.7 Trapping of Multiple Objects

Studying the interaction of micro- and nanoscopic objects is of growing importance for soft matter sciences. Via well-established trapping methods, typically, either a single particle is trapped or particles/molecules are accumulated in a certain spatial region. Achieving a confinement of a small defined number of particles or molecules is yet not trivial. However, a trapping of a well-defined small amount of particles (*e.g.* two or three) could mimic high concentrations to ensure frequent molecular encounters, while still working at the single molecule level. The most common trapping technique, *i.e.* optical tweezing, exerts an attractive potential (gradient force) to the objects present in solution. Trapping a single particle practically means to dilute the particle concentration of the solution to ensure that its unlikely to trap several particles. In order to trap for instance two particles, one would need to increase the concentration, but then again it becomes likely that a third particle is attracted to the trapping volume as well. That means, while an optical trap is in principle capable of trapping several objects, it is hard to control the exact quantity of particles as the potential is purely attractive. Exploiting a feedback trap reacting to several particles may help to control their number. Therefore, each particle needs to be detected and addressed by a driving force field individually. While it is certainly possible to track the position of several particles, it is however hardly possible to address different objects with the conventional electrode geometry in an ABEL trap, as the applied electric field is homogeneous. Hence, the same drift is exerted to all particles in the trapping region and no individual net inward drift can be produced. It has been shown that an arrangement of many electrodes together with a advanced feedback algorithm can be used to create electric fields of higher modes, which are then able to independently address different particles within the trapping region[180, 181] by complex feedback algorithms.[182]

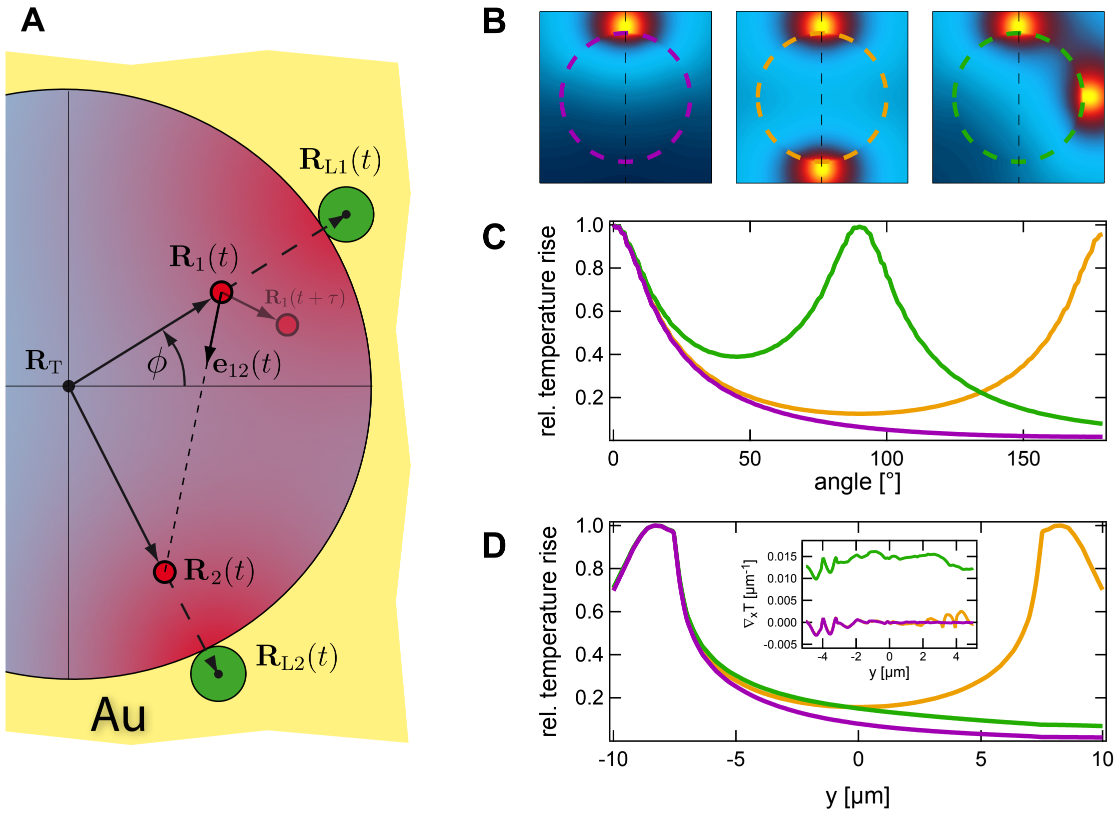

Figure 4.45: **A** Sketch illustrating the parameters important for multi-particle trapping: Two particles (red dots) at positions $\mathbf{R}_1(t)$ and $\mathbf{R}_2(t)$ are trapped by heating two positions of the gold structure $\mathbf{R}_{L1}(t)$ and $\mathbf{R}_{L2}(t)$ (green dots) according to Equation 4.20. The corresponding heating angle ϕ is measured counter clock-wise from the x-axis. **B** Simulated temperature maps in the plane of the gold structure normalized to the maximum temperature. Left: Single heated spot at $\phi = 90°$. Center: Two heated spots at $\phi = 90°$ and $\phi = -90°$. Right: Two heated spots at $\phi = 0°$ and $\phi = 90°$. The dashed circles represent the edges of the gold structure. **C** Relative temperature rise along the edge of the gold structure for the three cases shown in B (see color coding). **D** Relative temperature rise along the dashed lines in B. **Inset:** Relative temperature gradient in x direction along dashed lines in B.

The thermophoretic trap by design features strongly localized and thus inhomogeneous temperature fields. A particle close to the heat source is therefore more affected by the heating beam and experiences a stronger temperature gradient than a particle which is farther away. This allows for the usage of several focused laser beams to address different particles within the trapping region. The sketch in Figure 4.45 A illustrates the feedback scheme that is used to trap two single particles in the thermophoretic trap. Consider two particles (red dots) being located at the positions $\mathbf{R}_1(t)$ and $\mathbf{R}_2(t)$. Both shall be driven to the target at $\mathbf{R}_T$. In order to do so, two focused laser beams illuminate the gold structure at the positions $\mathbf{R}_{L1}(t)$ and $\mathbf{R}_{L2}(t)$ according to Equation 4.20. Simulated temperature maps of two example configurations of the two beams are shown as heat maps in Figure 4.45 B (center and right) in comparison to the temperature field produced by a single laser spot (left). Figure 4.45 C presents the angular distribution of the excess temperature along the circumference of the gold structure, which is indicated as dashes lines in B. For both the configurations of the laser beams $\Delta\phi = 180^\circ$ and $\Delta\phi = 90^\circ$, the temperature maximums are well-separated despite the high thermal conductivity of the gold structure. For smaller $\Delta\phi$, the two spots merge, but that means that the two particles shall be driven into approximately the same direction anyway. Vertical line profiles along the dashed black lines in temperature maps of B are shown in Figure 4.45 D. For $\Delta\phi = 180^\circ$ (yellow), the gold structure is heated on opposite sides. Hence, the temperature profile shows two maximums at the corresponding spots of the gold structure and a distinct minimum in the center. The center temperature increment $\Delta T_{\mathrm{Center}}/\Delta T_{\mathrm{Au}}$ increases from 8% in the case that a single spot is heated to 16% for the case a dual beam heating. Accordingly, the relative temperature contrast determining the depth of the effective trapping potential decreases slightly to 84% compared to 92% for a single heated spot. These two parameters are independent of the particular configurations of the two heating beams. However, the case where the particles are on one line with the center is special, as this leads to a configurations of the laser beam which only produce radial components driving both particles to the center. In all other cases, a cross talk is induced, since a heating at $\mathbf{R}_{\mathrm{L}1}$ will influence the particle at $\mathbf{R}_2$ and *vise versa*. From the Inset in Figure 4.45 D it can be seen that in the case of $\Delta\phi = 90^\circ$ (green) an additional temperature gradient is present in x direction perturbing the particle that shall be driven by the laser beam at $\phi = 90$. Note, that for a typically positive Soret coefficient, the temperature field in any case effectively produces a repulsive potential to the environment. Thus, outside particles are kept away from the trapping region such that it is unlikely for an unwanted particle to enter the trap.

While the above described perturbation could be certainly balanced with a dedicated change in the feedback algorithm, it is neglected in the experiments that will be presented in the following. Figure 4.46 gives snapshots of a dataset, where two 200 nm-diameter polystyrene colloids (central bright spots) are trapped in a 15 µm-diameter gold structure (green dashed circle). The heated spots at the gold structure can be seen as bright spots outside the green circle caused by the fluorescence of the gold film upon illumination by the focused laser beam. In the used setup, only a single heating beam is available but can be steered rapidly between the two spots due to the fast access time of the acousto-optic deflector ($\tau_{\mathrm{AOD}} \approx 14\mu s$) compared to the inverse feedback update rate $\tau_{\mathrm{FB}} = 11\,\mathrm{ms}$. The beam is switched between the positions $\mathbf{R}_{\mathrm{L}1}(t)$ and $\mathbf{R}_{\mathrm{L}2}(t)$ every 200 µs to distribute the power homogeneously between the two spots over the duration of one feedback cycle τ_{FB}.

The snapshots presented in Figure 4.46 A are for a continuous heating by the laser beam (point target), only the positions $\mathbf{R}_{\mathrm{L}1}(t)$ and $\mathbf{R}_{\mathrm{L}2}(t)$ are updated. As will be seen later, this trapping scheme leads approximately to an effective harmonic-like trapping potential similar to the equivalent single particle trapping scheme. The three typical frames of the acquired movie show different configurations of the heating beams according to the positions of the particles: from opposite directions (left), $\Delta\phi \approx 60^\circ$ (center) and a heating from practically the same direction with a small $\Delta\phi$ (right).

An effective box-like potential can be realized employing the area-target trapping mode (intermitted heating) as described in Section 4.3.4. Therefore, the gold structure is only heated to drive the particular particle if it leaves a certain central area within the trapping region, marked by red circles in Figure 4.46 B. This mode could be of particular interest for keeping two or more particles close to each other on the one hand, but study their dynamics in an unperturbed environment on the other hand, in particular without the heating beams. The three pictures present the three scenarios, where either both particles are located within the central region (left), one particle is within the red circle while the other particle overcomes the critical radius and is driven back, or, both particles leave the central region and are thus driven back by both the laser beams being switched on.

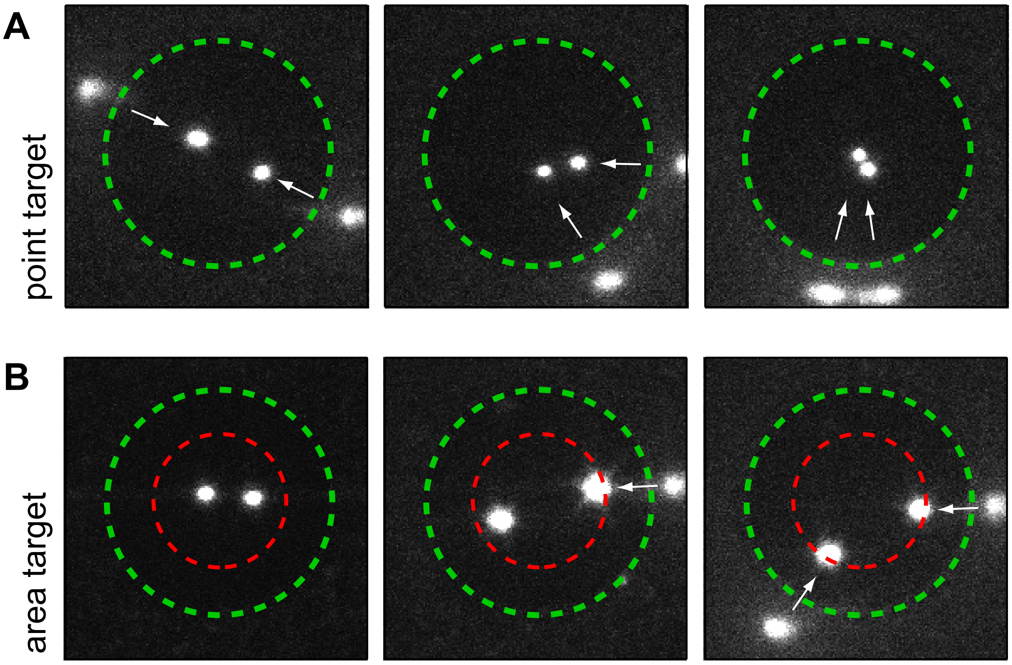

Figure 4.46: Feedback trapping of two polystyrene beads in a $d_{\mathrm{Trap}} = 15\,\mu\mathrm{m}$-diameter trap (green circle). **A** Three typical snapshots for continuous (harmonic-like potential) illustrating the different heating beam configurations. Heating from opposite directions with $\Delta\phi \approx 180°$ (left), $\Delta\phi \approx 60°$ (center) and from about the same direction with a small $\Delta\phi$. **B** Feedback trapping of two particles for intermitted heating (box-like potential) with $R_{\mathrm{Max}} = 3.9\,\mu\mathrm{m}$ (red circle). Left: Both heating beams are switched off as $R_1(t) < R_{\mathrm{Max}}$ and $R_2(t) < R_{\mathrm{Max}}$. Center: One particle is located beyond $R_1(t) > R_{\mathrm{Max}}$ and thus driven back to the central region. Right: Both particles are driven back to the center by the laser beams. The beam power is equally distributed to both the heating beams.

Figure 4.47 A shows the positional distributions for the trapping of a single particle (SP) for $P_{\mathrm{heat}} = 3.0\,\mathrm{mW}$ (top) and $P_{\mathrm{heat}} = 1.5\,\mathrm{mW}$ (center) as well as two particles (MP) with the point target (bottom), where the heating power $P_{\mathrm{heat}} = 3.0\,\mathrm{mW}$ is distributed to both the laser beams. The single particle distributions show a width of $\sigma_{\mathrm{SP,harm}} = (0.76 \pm 0.01)\,\mu\mathrm{m}$ and $\sigma_{\mathrm{SP,harm}} = (1.26 \pm 0.01)\,\mu\mathrm{m}$ for half the power. The width for the two-particle trapping distribution is expected to be as for half the heating power of the single particle trapping, since the full power is distributed to two beams. The perturbation due to the cross talk that was described above could lead to a broadening. Interestingly, the measured value for the rms-displacement of $\sigma_{\mathrm{MP,harm}} = (1.23 \pm 0.01)\,\mu\mathrm{m}$ is slightly below the single-particle value for 1.5 mW heating power. The reason becomes clear when looking at the effective potentials calculated from the positional distributions via $\Delta U / k_{\mathrm{B}}T = -\ln(p/p_0)$ plotted in Figure 4.47 B. While the potentials for SP (black for $P_{\mathrm{heat}} = 1.5\,\mathrm{mW}$) and MP (red) trapping approximately match in the center, the MP potential tightens in the outer region and is in between the 1.5 mW and 3.0 mW (grey) curves of the SP potentials. This can be explained when considering the different configurations shown in Figure 4.46 A. While the MP potential in the outer region does not significantly differ from the SP potential for large $\Delta\phi$ (see temperature fields in Figure 4.45 D), the heating power effectively doubles for configurations with small $\Delta\phi$ leading to a higher temperature gradient. These events thus lead to the tightening of the effective potential and the smaller width in the position distribution. A slight broadening in the central region (hardly visible in Figure 4.47 B) is attributed to the mentioned cross talk as well as a higher center temperature rise as compared to the single particle trapping at $P_{\mathrm{heat}} = 1.5\,\mathrm{mW}$ enhancing Brownian motion. With the discussed deviation from the single-particle potentials, the effective two-particle potential is approximately harmonic (see fit in Figure 4.47 B) with an effective stiffness of $\kappa_{\mathrm{MP,harm}} = (2.59 \pm 0.04)\,\mathrm{fN}/\mu\mathrm{m}$.

The heat maps in Figures 4.47 C plot the corresponding positional distributions for the area target, both for a heating power of $P_{\mathrm{heat}} = 3.0\,\mathrm{mW}$. The distributions in both cases are flat as expected. The width, which is essentially determined with the adjusted critical radius $R_{\mathrm{Max}} = 3.9\,\mu\mathrm{m}$ slightly increases from $\sigma_{\mathrm{SP,box}} = (2.08 \pm 0.01)\,\mu\mathrm{m}$ for the trapping of a single particle to $\sigma_{\mathrm{MP,box}} = (2.31 \pm 0.01)\,\mu\mathrm{m}$ in the case that two particles are trapped, which is due to the decreased temperature gradients in the case that both the particles are outside R_{Max} and the heating power is distributed to both beams. The heating time ratio $\tau_{\mathrm{Heating\,On}}/\tau_{\mathrm{Exp}}$ increases from 13.4% for the SP trapping to 24.4% for MP trapping. Still, both beams are switched off in about 75% of the trapping time, where the interaction of the particle may be studied without a thermal perturbation.

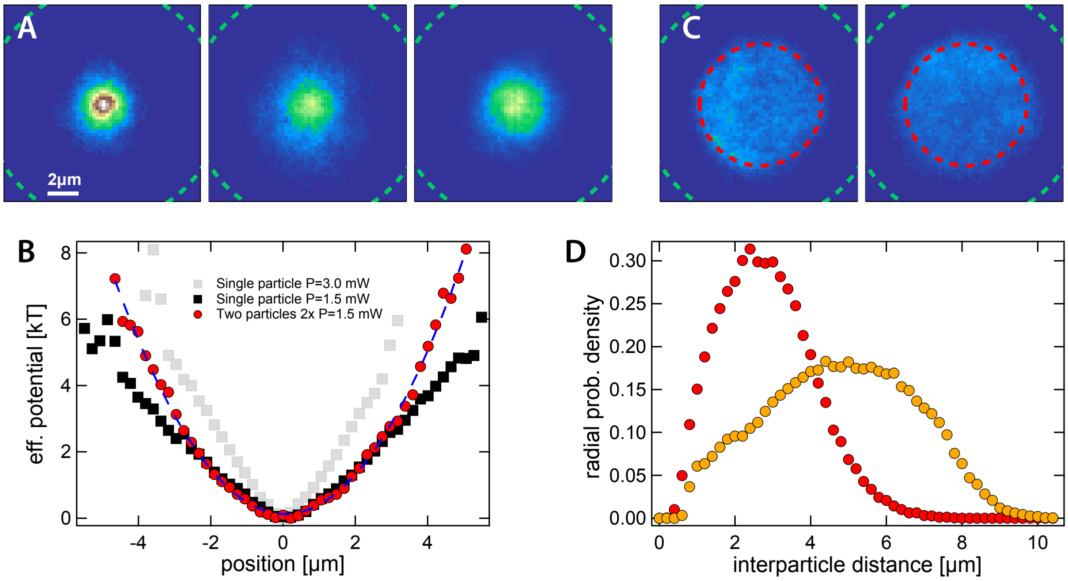

Figure 4.47: **A** Left: Position distribution maps for the feedback trapping of a single 200 nm PS bead for a heating power of $P_{\mathrm{heat}} = 3.0\,\mathrm{mW}$ and a feedback update rate of 100 Hz. Center: Same for $P_{\mathrm{heat}} = 1.5\,\mathrm{mW}$. Right: Position distribution maps for two 200 nm PS beads (continuous heating) at a heating power of $P_{\mathrm{heat}} = 1.5\,\mathrm{mW}$ per heating beam. **B** Effective trapping potentials calculated from the position distributions in A via $\Delta U/k_{\mathrm{B}}T = -\ln(p/p_0)$ for the single particle trapping in gray ($P_{\mathrm{heat}} = 3.0\,\mathrm{mW}$) and black ($P_{\mathrm{heat}} = 1.5\,\mathrm{mW}$). Same for the trapping of two beads in red with a 2nd-order polynomial fit. **C** Position distribution maps for the feedback trapping of a single 200 nm PS bead (left) for a heating power of $P_{\mathrm{heat}} = 3.0\,\mathrm{mW}$ and a feedback update rate of 100 Hz for intermitted beating (critical radius $R_{\mathrm{Max}} = 3.9\,\mu\mathrm{m}$ indicated by the red circle) and for two PS particles (right) at $P_{\mathrm{heat}} = 1.5\,\mathrm{mW}$ per beam. **D** Histograms over the interparticle distances $d = \mathbf{R}_2 - \mathbf{R}_1$ for continuous (harmonic-like potential, red) and intermitted heating (box-like potential, orange). Trap diameter $d_{\mathrm{Trap}} = 15\,\mu\mathrm{m}$.

Figures 4.47 D shows the probability density to find a certain interparticle distance for the continuous (red) as well as the intermitted heating (orange). Since the position distributions are symmetric around the trapping center with $\langle \mathbf{R}_1 \rangle = \langle \mathbf{R}_2 \rangle = 0$, also the average (signed) distance $\langle d \rangle = \langle \mathbf{R}_2 - \mathbf{R}_1 \rangle$ cancels.

Therefore, it makes sense to measure the root mean square (rms) distance $d^{\mathrm{rms}} = \sqrt{\langle d^2 \rangle}$ in between the particles, which may be traced back to the width of the positional distribution via

$$\left\langle d^2 \right\rangle = \left\langle (\mathbf{R}_2 - \mathbf{R}_1)^2 \right\rangle = \left\langle \mathbf{R}_2^2 \right\rangle + \left\langle \mathbf{R}_1^2 \right\rangle - 2 \left\langle \mathbf{R}_1 \cdot \mathbf{R}_2 \right\rangle . \tag{4.31}$$

The first two terms are directly connected to the width of the positional distribution $\left\langle \mathbf{R}_1^2 \right\rangle = \left\langle \mathbf{R}_2^2 \right\rangle = \left\langle x_{1,2}^2 \right\rangle + \left\langle y_{1,2}^2 \right\rangle = 2\sigma_{\mathrm{MP}}^2$. The last term will disappear if the particle positions $\mathbf{R}_1$ and $\mathbf{R}_2$ are fully independent of each other. This is, however, not the case since two laser beams are employed for the trapping which are connected to the particle positions via the optical feedback. Figure 4.48 A shows the correlation functions $\langle \mathbf{R}_1(t+\tau) \cdot \mathbf{R}_2(t) \rangle$ for the harmonic-like potential (red) and the box potential (orange). In both cases, a distinct negative correlation is visible, which decays with a correlation time of $\tau_{\mathrm{harm}} = (1.68 \pm 0.03)\,\mathrm{s}$ for the harmonic potential and $\tau_{\mathrm{box}} = (4.9 \pm 0.2)\,\mathrm{s}$ for the box potential. That means, that the particles are artificially coupled by the laser beams. If the particles are located on the same side with respect to the trap center (small $\Delta\phi$, as *e.g.* in Figure 4.46 A right hand side), both the heating beams are located near each other and effectively twice the temperature gradient is exerted to the particles due to the higher induced temperature. Thus, the particles are faster driven to the center than in the case where the particles are located in opposite directions ($\Delta\phi \sim 180°$, see *e.g.* Figure 4.46 A left hand side). This on average increases the probability that the particles are located on opposite directions with respect to the center explaining the negative correlation. Since the relaxation of the particle positions in the box potential is purely governed to Brownian motion once the heating beams are switched off, the correlation times are much longer as compared to the harmonic potential, where the particles are actively driven towards the center.

With the cross term being the correlation function for $\tau = 0$ and the measured widths of the positional distributions, a value of $d_{\mathrm{harm}}^{\mathrm{rms}} = (3.10 \pm 0.06)\,\mu\mathrm{m}$ is expected from Equation 4.31 for the continuous heating mode, whereas a value of $d_{\mathrm{harm}}^{\mathrm{rms}} = (3.19 \pm 0.07)\,\mu\mathrm{m}$ is measured directly analyzing the trajectories. Similarly, for the two particles trapped in the box potential, the positional distribution and the cross term deliver a rms distance of $d_{\mathrm{box}}^{\mathrm{rms}} = (5.17 \pm 0.08)\,\mu\mathrm{m}$ again matching the measured value with $d_{\mathrm{box}}^{\mathrm{rms}} = (5.25 \pm 0.16)\,\mu\mathrm{m}$. The slightly larger values may be attributed to the fact that interparticle distances smaller than a few 100 nm cannot be detected by the used particle tracking method (see histograms in Figure 4.47 D) due to the finite spot size in the movies. The lack of small distances, introduces a bias to the averaging and thus broadens the apparent rms distance.

Finally, it shall be turned towards the dynamics of the particles. In the following the motion of the particles relative to each other $\Delta\mathbf{R}_{\mathrm{IP}} = \Delta\mathbf{R}_2 - \Delta\mathbf{R}_1$ shall be investigated. In the same way as for the interparticle distance, it is useful to look at the rms interparticle step $\Delta\mathbf{R}_{\mathrm{IP}}^{\mathrm{rms}} = \sqrt{\langle \Delta\mathbf{R}_{\mathrm{IP}}^2 \rangle}$, which leads to the following expression

$$\left\langle \Delta\mathbf{R}_{\mathrm{IP}}^2 \right\rangle = \left\langle (\Delta\mathbf{R}_2 - \Delta\mathbf{R}_1)^2 \right\rangle = \left\langle \Delta\mathbf{R}_2^2 \right\rangle + \left\langle \Delta\mathbf{R}_1^2 \right\rangle - 2 \left\langle \Delta\mathbf{R}_1 \cdot \Delta\mathbf{R}_2 \right\rangle . \tag{4.32}$$

The first two terms describe the mean squared displacement of the single particles due to Brownian motion with $\left\langle \Delta\mathbf{R}_1^2 \right\rangle = \left\langle \Delta\mathbf{R}_2^2 \right\rangle = 4D\tau$. The last term is a measure for the instantaneous correlation of the particle steps. A positive value signifies that the particle on average move together in the same direction. A negative value corresponds to an average motion of the particles either towards or apart each other as both the direction lead to the same sign. Interaction of the particles are expected at the length scale of the Debye length, which is smaller than 100 nm even for low ion concentrations used in the experiments. There is, thus, no physical interaction expected at the distances being accessible here. Any measured interaction would be introduced artificially by the feedback-controlled position of both the laser beam introducing a cross talk between the particles. Figure 4.48 B shows the correlation functions of the interparticle steps $\langle \Delta\mathbf{R}_1(t+\tau)\cdot\Delta\mathbf{R}_2(t)\rangle$ for the harmonic-like potential (red) and the box potential (orange). While the absolute positions of the particles are correlated (see Figure 4.48 A), no correlation is detectable for the relative movement, which is why the last term in equation 4.32 disappears. Therefore, Equation 4.32 reduces to $\left\langle \Delta\mathbf{R}_{\mathrm{IP}}^2\right\rangle = \left\langle \Delta\mathbf{R}_2^2\right\rangle + \left\langle \Delta\mathbf{R}_1^2\right\rangle = 8D\tau \equiv 4D_{\mathrm{IP}}\tau$ and, thus, in the frame of one of the particles, a diffusion coefficient $D_{\mathrm{IP}} = 2D$ is measured which is twice as high as the diffusion coefficient of a single particle (SP). Indeed, analyzing the step sizes of the particles yields a SP diffusion coefficient of $D_{\mathrm{harm}} = (1.12 \pm 0.02)\ \mu\mathrm{m}^2/\mathrm{s}$, while the interparticle coefficient is $D_{\mathrm{IP,harm}} = (2.16 \pm 0.04)\ \mu\mathrm{m}^2/\mathrm{s}$ for the continuous heating mode. The diffusion coefficients for the intermittent heating modes (effective box potential) are $D_{\mathrm{box}} = (1.02 \pm 0.02)\ \mu\mathrm{m}^2/\mathrm{s}$ for the single particles and $D_{\mathrm{IP,harm}} = (2.05 \pm 0.04)\ \mu\mathrm{m}^2/\mathrm{s}$ for the particles relative to each other. As expected, for both the heating schemes, the interparticle diffusion is twice as fast as for the single particles. Note, that diffusion coefficients for the box potential appears to be lower due to the lower average temperature rise of the particles, since the heating beam is switched off in about 75% of the time.

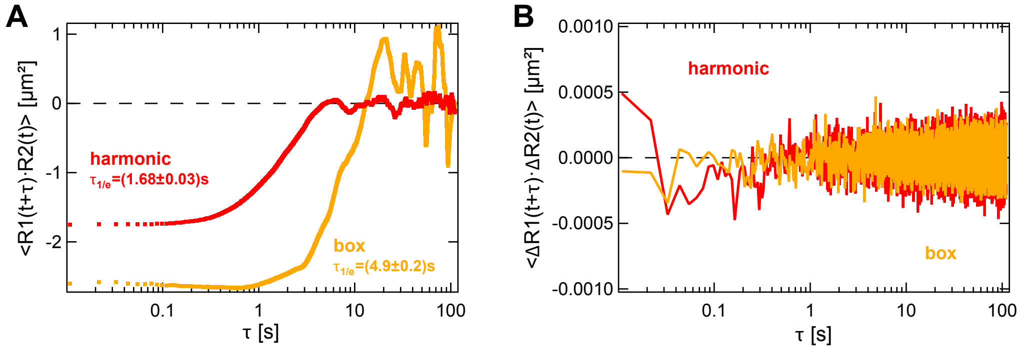

Figure 4.48: **A** Cross correlation of the particle positions $\mathbf{R}_1(t)$ and $\mathbf{R}_2(t)$ for continuous (harmonic-like potential, red) and intermitted heating (box-like potential, orange). **B** Cross correlation of the particle steps $\Delta\mathbf{R}_1(t) = \mathbf{R}_1(t+\tau_{\mathrm{ET}}) - \mathbf{R}_1(t)$ and $\Delta\mathbf{R}_2(t) = \mathbf{R}_2(t+\tau_{\mathrm{ET}}) - \mathbf{R}_2(t)$ for continuous (harmonic-like potential, red) and intermitted heating (box-like potential, orange) with τ_{ET} being the exposure time of the CCD.

To further study the relative motion of the particles, the particle step $\Delta\mathbf{R}_1(t) = \mathbf{R}_1(t+\tau_{\mathrm{ET}}) - \mathbf{R}_1(t)$ is projected on the director $\mathbf{e}_{12}(t) = \frac{\mathbf{R}_2(t)-\mathbf{R}_1(t)}{|\mathbf{R}_2(t)-\mathbf{R}_1(t)|}$ pointing from $\mathbf{R}_1$ to $\mathbf{R}_2$ (see Figure 4.45 A). That means, now a positive value corresponds to a motion towards the other particle and *vise versa*. Figure 4.48 plots $\Delta\mathbf{R}_1(t)\cdot\mathbf{e}_{12}(t)$ over the interparticle distance $|\mathbf{R}_2(t) - \mathbf{R}_1(t)|$ for the harmonic-like (A) and the box-like potential (B). The raw data points are shown in gray. Their vertical spread is dominated by diffusive steps being equally likely in both positive and negative direction. Applying a median filter to average out the Brownian steps leads to the black curve. The corresponding relative drift velocities towards each other is shown in dependence on the interparticle distance underneath in C and D.

For the harmonic-like potential in A and C, it is clearly visible that for increasing distances in between the particles, the function $\Delta\mathbf{R}_1(t)\cdot\mathbf{e}_{12}(t)$ is on average positive (see deviation from the red dased zero line), *i.e.* the particles on average approach each other. This can be understood as follows. For increasing interparticle distances it becomes more likely for the particles to be in opposite regions within the trap with respect to the origin. That again means that the laser beams are on opposite sites of the trap circumference due to the applied feedback rule. As the particles are both driven towards the center of the trap, they are effectively driven towards each other. If the particles are close to each other, no relative motion is induced, because, either they are both located in the outer regions, then they are driven into the same direction, or, if they are located in the central region, the temperature gradients are much weaker and induce no significant relative drift.

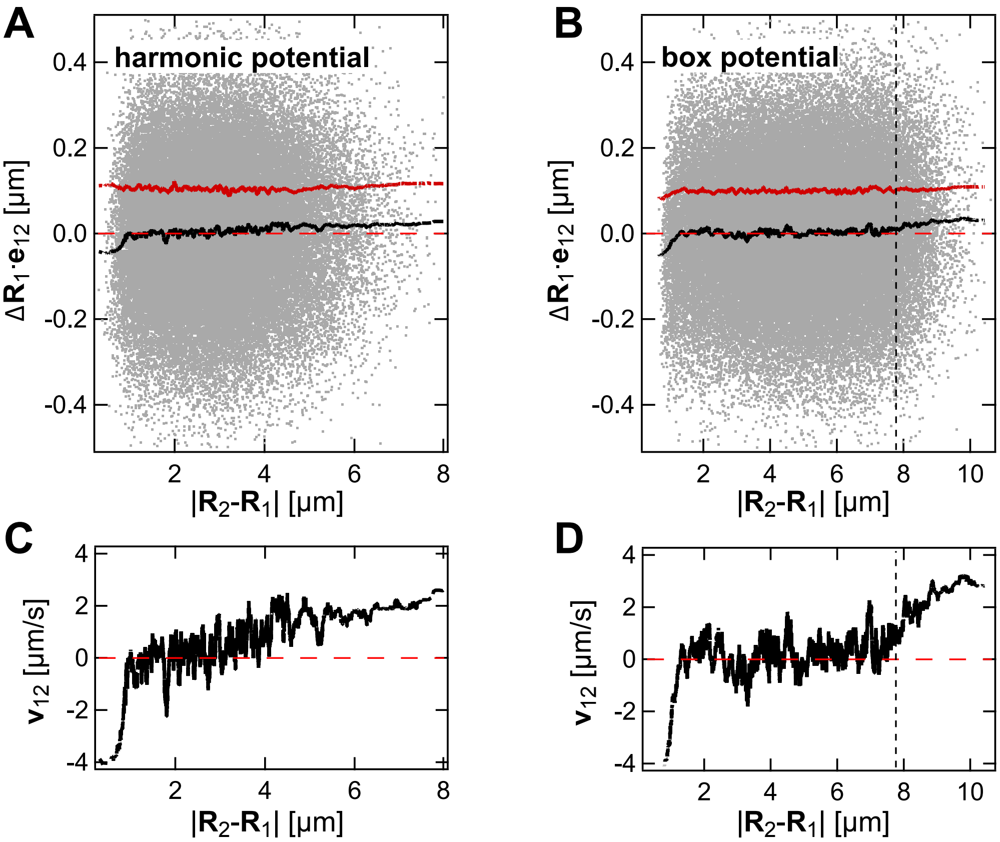

Figure 4.49: **A** Projection of the particle step onto the director between the particles $\Delta\mathbf{R}_1(t)\cdot\mathbf{e}_{12}(t)$ in dependence on the interparticle distance for the harmonic-like potential. The horizontal dashed red line indicated zero drift. The raw data is shown with the gray dots. The black curve represents a median average of the data. The dark red curve shows the rms-width of the Brownian noise. **B** Same for the box potential. The dashed vertical line indicated twice the critical radius $2R_{\text{max}} = 7.8\,\mu\text{m}$. **C** Corresponding median-averaged relative drift velocity $\langle v_{12}\rangle = \langle \Delta\mathbf{R}_1(t)\cdot\mathbf{e}_{12}\rangle/\tau_{\text{ET}}$ over the interparticle distance. **D** Same as in C, but for box-like potential. All graphs: The negative values for small interparticle distances are not real but are a result tracking artifacts, as the tracking procedure are not optimized to discriminate very close objects.

The corresponding plots for the box-like potential are given in Figure 4.49 B and D. Here, the effect is hardly visible until the interparticle distance reaches twice the critical radius of $R_{\text{max}} = 3.9\,\mu\text{m}$ (vertical dashed line). In that case, the laser beams are directly on opposite positions and as the particles are both driven to the center, they are effectively driven towards each other. For shorter distances, $|\mathbf{R}_2 - \mathbf{R}_1| < 2R_{\text{max}}$, even if both laser are switched on, it is likely that the induced drift towards the center only has a little component towards the other particle. Also, most of the time the heating beams are off, *i.e.* neither central nor relative drift is induced whatsoever and the relative motion between the particles is purely determined by Brownian motion and, on short distances, by their interaction potential.

The above analysis shows, that artificial interactions between the particles are only induced by the feedback-controlled laser beams for large interparticle distances. Physical interactions expected on much shorter distances are thus hardly perturbed.

4.3.8 Trapping of Single Macro-Molecules

In the final part of this monograph, it is demonstrated that the trapping by thermophoretic interactions is by no means limited to polystyrene beads. Caused by the complex effects that contribute to the thermophoretic mobility D_T (some major effects have been introduced in Section 2.2) almost all micro and nano-objects, such as particles, polymers, proteins, DNA or ions, are sensitive to temperature gradients. For thermophoretic trapping, the interesting parameter is the Soret coefficient S_T, which needs to be sufficiently large to achieve a stable confinement as discussed in Section 4.3.5. The measurements that are presented in the following are subject to ongoing experiments. Some preliminary results are thus not yet fully understood. However, the presented data gives an outlook on the potential of thermophoretic trapping for the investigation of single or multiple bio-molecules. For demonstration purposes, the upcoming section deals with the thermophoretic trapping of single λ-DNA molecules, which is in its double-stranded form often used as an easy-to-handle model for semi-flexible polymers. The presentation of the results are divided in four parts. First, the center-of-mass (COM) motion of a λ-DNA molecule in the trap is analyzed. Then, the attention switches to the internal motion of the macro-molecule. In a third part, it is shown that with some trade-off single DNA strands can even be trapped in a much simpler experimental configuration, that means without a hole-structure and feedback. In a last part, preliminary results are presented dealing with the influence of the temperature field on the molecule's conformation.

Center-of-Mass Motion For the trapping experiment that is presented with Figure 4.50 a 15 µm-diameter trap structure is used together with a heating power of the focused laser beam of $P_{\text{Heat}} = 3.0\,\text{mW}$. A slow frame rate of 20 Hz is chosen to accumulate fluorescence of the dye-doped DNA molecule. Accordingly, the feedback cycle time is as long as 50 ms.
While being trapped, the molecule undergoes thermally driven conformation fluctuations. Four typical snapshots of the measured two-dimensional projection of the molecule's conformation are shown in Figure 4.50 A. For the purpose of feedback trapping, the camera image is thresholded above the background level and the COM of the bright spot is identified with the molecules position $\mathbf{R}_p$. The laser beam is then controlled according to Equation 4.18. This leads to a stable trapping, where the trapping duration is only limited by the bleaching of the intercalated dye molecules. The COM trajectory is shown in B. In the particular experiment, a trapping duration of longer than 500 s was achieved. Figure 4.50 C gives the position distribution of the COM within the trapping region. An rms displacement of the molecule from the trapping center of $\sigma_{\text{com}} = (0.75 \pm 0.01)\,\mu\text{m}$ is found. Analyzing the step-size distribution yields a diffusion coefficient for a polymer as a whole of $D_{\text{com}} = (0.44 \pm 0.05)\,\mu\text{m}$. The temperature profile that is reconstructed from the position distribution in Figure 4.50 C is shown in D and matches the simulated curve for a Soret coefficient of $S_T = 0.8\,\text{K}^{-1}$. Although using different buffer conditions, the value compares well to the literature.[59]
The average temperature rise of the polymer is about 8 K over ambient temperature. As can be seen from Figure 4.50 the polymer molecule is stablely confined in a temperature well of 6 K depth. With an excess temperature at the heated spot of $\Delta T_{\text{Au}} = 88\,\text{K}$, the polymer explores only very little of

the total depth of the temperature field of about 80 K. The maximum temperature increment that the polymer experiences is thus well below its melting temperature (see Section 2.5.1).
All the analysis that has been presented for polystyrene beads is of course also possible for single molecules. In particular, later experiments could benefit from monitoring the diffusion coefficient and the thermophoretic mobility over time delivering information on temporal changes of the molecule or its surrounding without directly looking at the conformation.

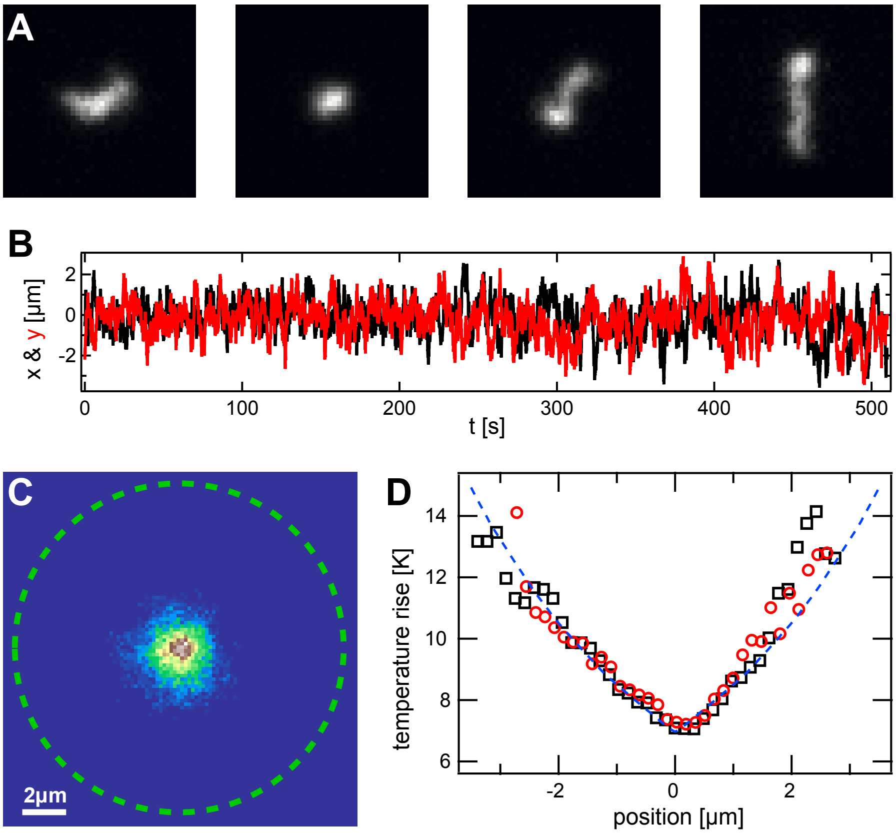

Figure 4.50: **A** Four typical snapshots ($4.6 \times 4.6\,\mu\text{m}^2$) of the trapping of a single λ-DNA molecule in a 15 µm-diameter trap. **B** COM trajectory of the molecule. **C** Positional distribution histogram of the polymer. The green dashed circle indicates the edge of the gold structure. **D** Temperature distribution $\Delta T = -\ln(P/P_0)/S_T$ within the trapping region in x (black) and y direction (red). The experimental data fit the theoretical curve (blue dashed) for $S_T = 0.8\,\text{K}^{-1}$.

A unique feature of the optically controlled thermophoretic trap is the ability to trap a defined number of objects. Figure 4.51 A shows four snapshots of a dataset where two individual DNA molecules are trapped in the same sample. The trapping duration is with about 30 s (see Figure 4.51 B) much shorter which is again attributed to bleaching. In terms of multi-particle trapping, the current version of the setup exhibits a huge disadvantage: in order to generate multiple laser beams, the AOD rapidly scans the single beam to the according positions. By that, depending on the configuration of the laser beams, it often crosses the trapping region leading to additional bleaching. This effect is even worse as the same laser wavelength is used for fluorescence and plasmonic excitation. Eliminating these issues of technical nature will strongly increase the trapping duration to the order of the single particle trapping. This could be interesting to study the interaction of bio-molecules at single molecule concentration.

The confinement to a small region thereby guaranties a high probability of molecular encounters, which would otherwise only be possible with much higher concentrations.

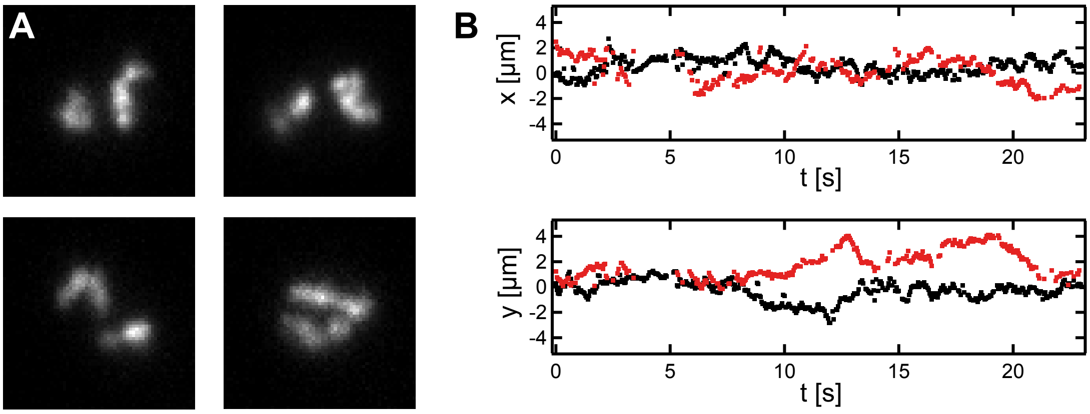

Figure 4.51: **A** Four snapshots of the trapping of two individual λ-DNA molecules ($6.9 \times 6.9\,\mu\text{m}^2$). **B** Center-of-mass trajectories of the two polymers trapped in a 15 µm-diameter trap.

Analysis of the Conformation The homogeneous labeling of the dye molecules along the DNA molecule allows to visualize its conformation as can be seen from the snapshots in Figures 4.50 and 4.51. An analysis of the spatial distribution of the fluorescence thereby yields static properties of the polymer, such as the radius of gyration or the mean squared end-to-end distance, but also dynamic properties describing the internal relaxation.

The analysis of the conformation includes the following preparation. In each recorded frame the polymer is identified and a cropped version is copied to a new dataset. Then, each frame is shifted by the COM of the fluorescence within the particular frame. The background is identified with intensity level in outer corners of the shifted frames and is subtracted accordingly in each frame. Finally, the intensity is normalized to the maximum within each frame to account for the photobleaching over the duration of the measurement. The data set that results from this procedure is denoted with $I(\mathbf{r},t)$ and describes the intensity at the position $\mathbf{r}$ at the time t. Accordingly, $\delta I(\mathbf{r},t) = I(\mathbf{r},t) - \langle I(\mathbf{r},t)\rangle_t$ denotes the intensity fluctuations with respect to the normalized time average $\langle I(\mathbf{r},t)\rangle_t$.

Due to the homogeneous labeling of the dye molecules along the DNA strand, $\langle I(\mathbf{r},t)\rangle_t$ directly represents the molecular density around its COM. Figure 4.52 B shows a line profile through $\langle I(\mathbf{r},t)\rangle_t$ (inset) generated from the dataset of the experiment presented in Figure 4.50. A Gaussian fit (orange) delivers a radius of gyration of $R_\text{g} = (0.37 \pm 0.02)\,\mu\text{m}$, but also shows a broadened density in regions far from the COM. This has been reported before[52] and is interpreted in the ideal polymer chain picture as follows. The probability distribution for distance of each polymer segment to the COM follows a Gaussian. However, the width of the distribution is dependent of the position along the polymer and is broader with increasing distance to the chain center. The resulting molecular density distribution is thus the sum of many different Gaussians of segments along the chain. Following this argumentation, a formula describing the polymer's density distribution has been derived by Adam Cohen in his thesis[170]

$$p(\mathbf{r}) = \frac{3}{2\pi \bar{R}_\text{ee}^2} \int_0^1 \frac{\exp\left(-3r^2/[2\bar{R}_\text{ee}(3\varepsilon^2 - 3\varepsilon + 1)]\right)}{3\varepsilon^2 - 3\varepsilon + 1} \mathrm{d}\varepsilon. \tag{4.33}$$

The relation contains the root mean squared end-to-end distance $\bar{R}_{\mathrm{ee}}$ as the only free parameter. Fitting Equation 4.33 to the measured distribution in Figure 4.52 yields a rms end-to-end distance of $R_{\mathrm{ee}} = (1.05 \pm 0.01)\,\mu\mathrm{m}$. For an ideal chain a ratio of $R_{\mathrm{g}}/\bar{R}_{\mathrm{ee}} = 1/\sqrt{6} \approx 0.41$ is expected (see Section 2.5.2). The same ratio is expected for a worm-like chain with small persistence length as compared to the length of the polymer which is the case for λ-DNA (of order $L_{\mathrm{p}}/L_{\mathrm{c}} \sim 10^{-3}$). The ratio found in the experiment is slightly lower with $R_{\mathrm{g}}/\bar{R}_{\mathrm{ee}} = 0.35 \pm 0.03$. However, the Gaussian fit does not follow the broadened tail, which delivers a lower value of R_{g}. Assuming the polymer to be a worm-like chain, for a common persistence length of dsDNA of $L_{\mathrm{p}} = 50\,\mathrm{nm}$,[183] the contour length of the DNA strand can be calculated from $\bar{R}_{\mathrm{ee}}$ via $L_{\mathrm{c}} = \bar{R}_{\mathrm{ee}}^2/2L_{\mathrm{p}}$. With a contour length of the $L_{\mathrm{c}} = (11.0 \pm 0.2)\,\mu\mathrm{m}$, the trapped molecule is obviously a fragment of about 65% of the nominal total length of 16.5 µm. Alongside in Figure 4.52 C, another molecular density plot of a different dataset is shown yielding a radius of gyration of $R_{\mathrm{g}} = (0.47 \pm 0.03)\,\mu\mathrm{m}$ and an rms end-to-end distance of $R_{\mathrm{ee}} = (1.40 \pm 0.02)\,\mu\mathrm{m}$. From R_{ee} it is concluded on a contour length of $L_{\mathrm{c}} = (19.5 \pm 0.5)\,\mu\mathrm{m}$. This is even longer than the nominal length, however, it is known[184, 185] that the used intercalating dye POPO-3 increases the contour length approximately by the measured amount.

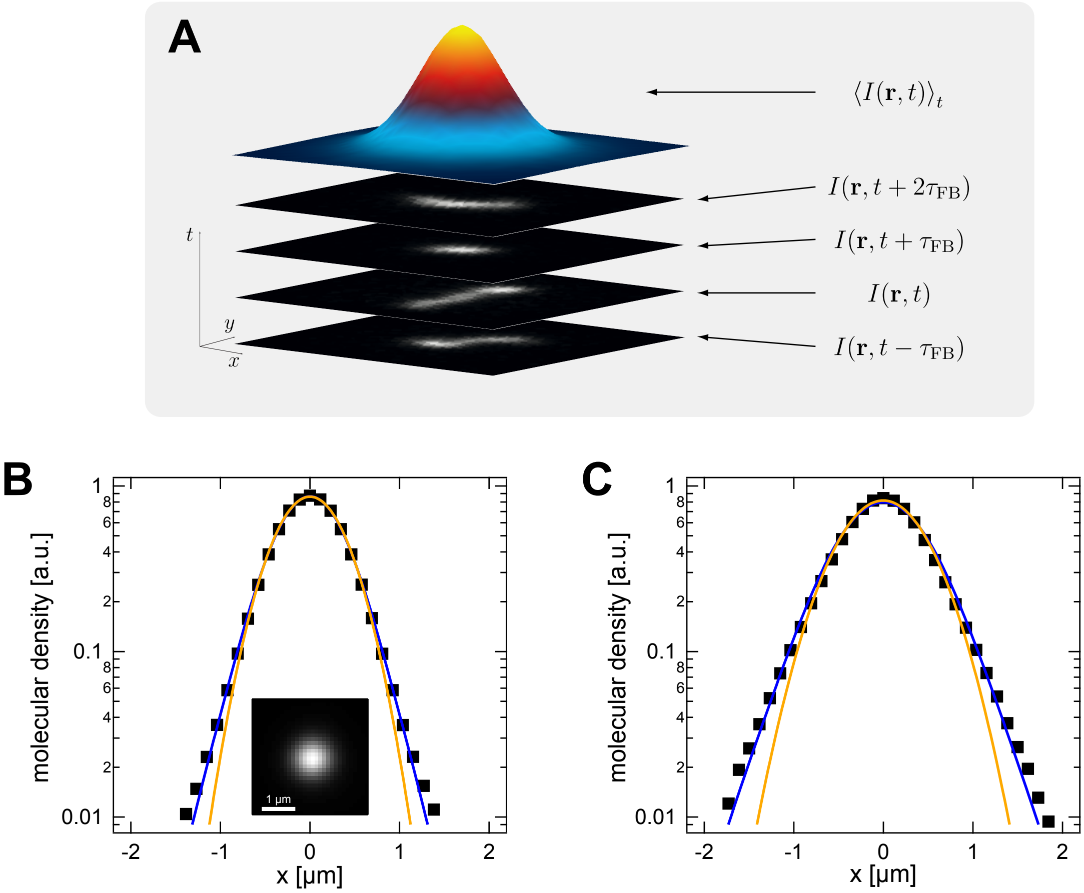

Figure 4.52: **A** The intensity profiles of the polymer in the different frames are accumulated after shifting by the center-of-mass position and normalizing to the maximum intensity. This average intensity distribution can be directly identified with the molecular density of the monomers about the COM. **B** Line profile of the molecular density (see Inset) of a trapped DNA molecule (same dataset used for results of Figure 4.50). A Gaussian fit (orange) yields $R_{\mathrm{g}} = (0.37 \pm 0.02)\,\mu\mathrm{m}$. Fitting Equation 4.33 (blue) gains $R_{\mathrm{ee}} = (1.05 \pm 0.01)\,\mu\mathrm{m}$. **C** Same as B, but for the dataset of another DNA molecule (results of Figure 4.53). Fit results: $R_{\mathrm{g}} = (0.47 \pm 0.03)\,\mu\mathrm{m}$ and $R_{\mathrm{ee}} = (1.40 \pm 0.02)\,\mu\mathrm{m}$.

The second experiment shown here was measured at a higher camera frame rate of 100 Hz in order to approach the internal dynamics of the trapped DNA molecules with a higher temporal resolution. As the polymer chain is labeled continuously along its contour, it is convenient to access the internal dynamics via a correlation of intensity fluctuations

$$C(\mathbf{R},\tau) = \langle \delta I(\mathbf{R},t)\delta I(\mathbf{R},t+\tau)\rangle_t \,. \tag{4.34}$$

The results of the pixel-wise intensity auto-correlation is shown in Figure 4.53 A for a few time lags of 1, 3, 5 and 7 frames. Accounting for the radial symmetry around the COM, Figure 4.53 B gives the radially averaged intensity correlation in dependence on the distance to the COM. A longer decay time or slower relaxation rate of the polymer segments of the radial interval between 0.7 µm to 1.2 µm is already visible by eye. For each distance, the decay is well-fitted with a single exponential function. The extracted decay times are depicted in Figure 4.53 C. The plot reveals a 25% slower relaxation of the segments that are radially about one micron away from the COM. This qualitative characteristic has also been described earlier by Cohen and Moerner,[52] who studied single DNA molecules confined in an ABEL trap. They find the slowest relaxation within the same radial region. Additionally, they see a slow relaxation close to the center of mass. This is seen in the experimental data of Figure 4.53 C as well, however, with large error bars due the low statistics in the center when radially averaging. Interestingly, while the general trend is reproduced, the correlation time in its absolute value is a factor of three slower than measured by Cohen and Moerner. This discrepancy is not yet understood.

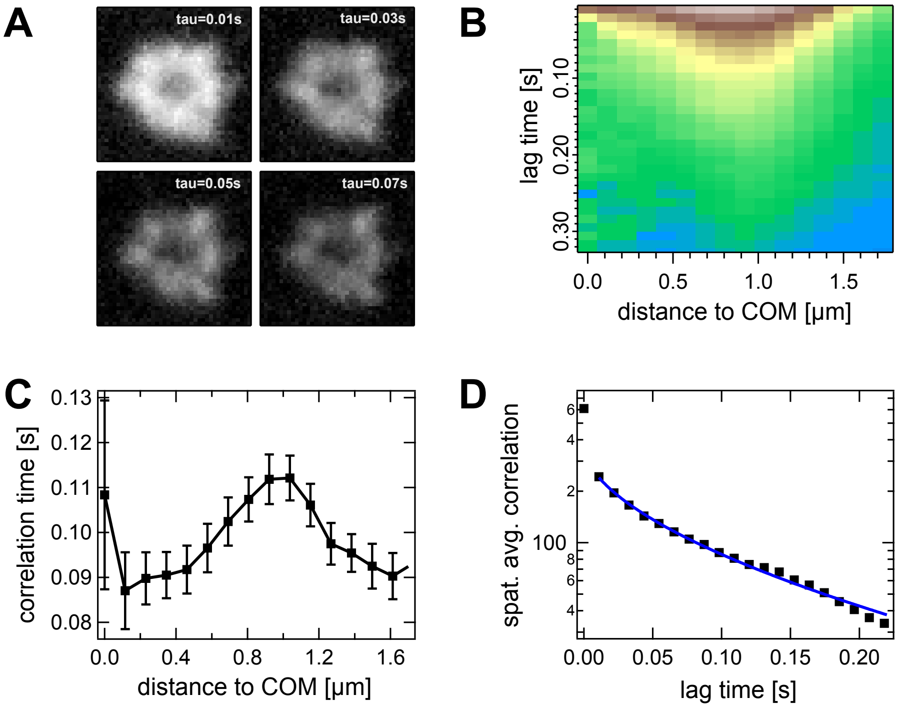

Figure 4.53: **A** Spatial intensity correlation function (Equation 4.34) for four different lag times. **B** Radially averaged intensity correlation in dependence on the distance to the COM. **C** Correlation times extracted from the correlation functions in B via a single exponential for each distance to the COM. **D** Correlation of the spatially accumulated intensity (Equation 4.35). Fit of a stretched exponential function $\sim \exp\left[-(\tau/\tau_0)^\beta\right]$ yielding $\beta = 0.57 \pm 0.03$ and $\tau_0 = (0.052 \pm 0.006)\,\mathrm{s}$.

In addition to the position-dependent correlation function, it is also worthwhile to consider the spatially accumulated correlation function

$$G(\tau) = \sum_{\mathbf{R}} C(\mathbf{R},\tau), \tag{4.35}$$

which in a similar form is of relevance for fluorescence correlation spectroscopy (FCS). Figure 4.53 D presents the accumulated correlation for the experimental data. The curve is fitted with a stretched exponential function $G(\tau) \sim \exp\left[-(\tau/\tau_0)^{\beta}\right]$, yielding a stretching exponent of $\beta = 0.57 \pm 0.03$. When hydrodynamic interactions of the monomers contribute to the polymer dynamics, an exponent of $\beta = 2/3$ is expected from models of dynamic light scattering[92] (Zimm dynamics), whereas an exponent of $\beta = 1/2$ is typically found for the case that hydrodynamic interactions can be neglected (Rouse dynamics). The exponent found in the experiment is in between the latter asymptotic exponents, suggesting that, while typically dsDNA is viewed as a Rouse polymer, hydrodynamic interactions of the segments cannot fully be neglected. Indeed, Shusterman *et al.* showed by FCS measurements on λ-DNA, that hydrodynamic interactions become relevant on time scales longer than 10 ms,[186] which corresponds to the inverse frame rate in the described experiment. Note, that Cohen and Moerner made the same observation in an equivalent experiment on λ-DNA molecules in the ABEL trap.[52]

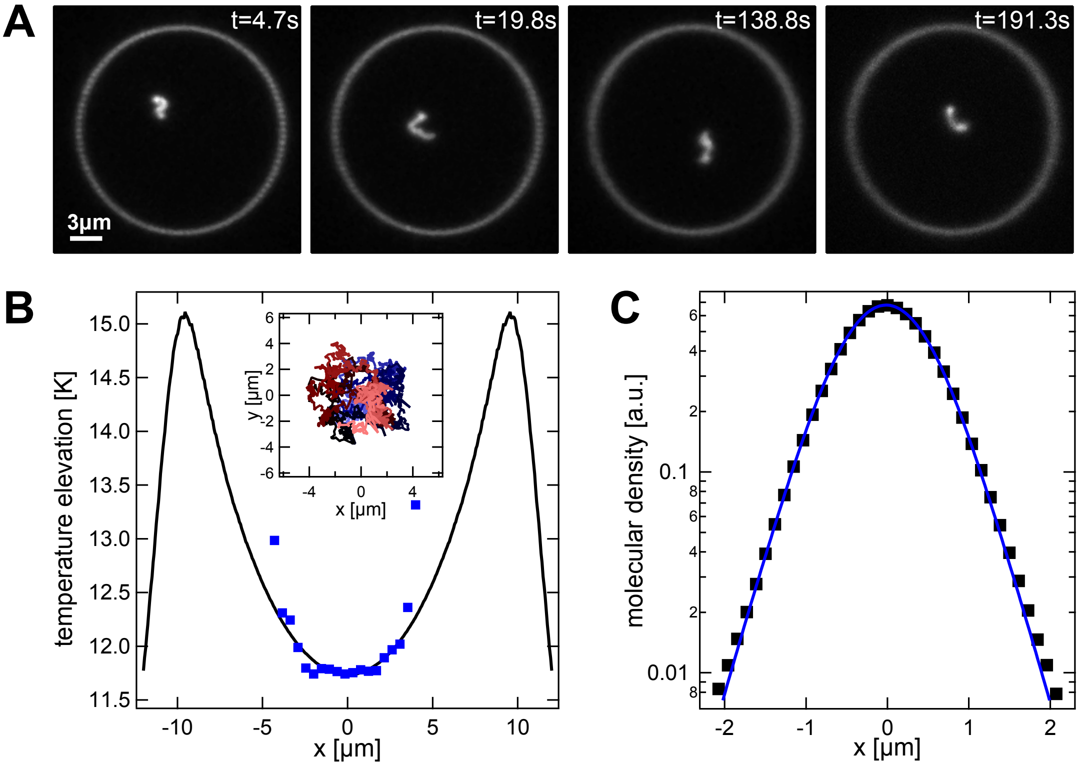

Figure 4.54: **A** Snapshots of the trapping of a single DNA molecule by a quasi-steady heating (see circle resulting from the fluorescence of the gold film) of the plain gold film without a hole structure. **B** Expected temperature profile from simulations (black curve). The reconstructed temperature profile (blue) matches the simulation for $S_\mathrm{T} = 4.2\,\mathrm{K}^{-1}$. Inset: COM trajectory of the DNA molecule within the trapping region. **C** Line profile of the molecular density (see Inset) of a trapped polymer chain. The blue line corresponds to a fit of Equation 4.33.

Trapping by a Quasi-Steady Temperature Profile The large Soret coefficient of the λ-DNA molecule allows for a confinement in a much simpler configuration. Figure 4.54 presents an experiment, where a single polymer chain is trapped via quasi-steady heating of a plain gold film, *i.e.* no special hole structure is present. The laser beam ($P_{\text{heat}} = 3.0\,\text{mW}$) is steered on a circular trace of $9.5\,\mu\text{m}$ radius at a frequency of $f = 100\,\text{Hz}$ as is described in detail in Section 4.2.5. Snapshots of a recorded movie file are shown in Figure 4.54 A. The molecule is trapped in the central region, surrounded by the heating laser beam trace, which is visible by the fluorescence of the gold film. The rms displacement from the center is measured from the trajectory (Inset in B) with $\sigma = (1.66 \pm 0.07)\,\mu\text{m}$. Figure 4.54 B shows the induced temperature profile that is expected from FEM simulations. Note, that the quantitative temperature rise exhibits an upper limit estimation, as the same $\Delta T_{\text{Au}}/P_{\text{heat}} \sim 29\,\text{K}/\text{mW}$ is assumed (see Section 4.3.3), whereas from the measurements in Section 4.3.6 it was suspected that the actual absorption is lower due to the lack of the gold structure. The advantage of the quasi-steady trapping scheme above a plain gold film is its simplicity. The disadvantages compared to the feedback and gold-structure-assisted trapping, however, are also obvious. Instead of an effective depth of the virtual temperature field of about $90\,\text{K}$, here, only about $3\,\text{K}$ is achieved at the same heating laser power and a similar trap size. Nevertheless, the particular trapping event is only limited by bleaching of the dye molecules[a)] . The Soret coefficient of the trapped molecule can be calculated from the position distribution via $S_{\text{T}} = -\ln(P/P_0)/\Delta T$ and is estimated to $S_{\text{T}} = 4.2\,\text{K}^{-1}$. A step-size analysis of the trajectory yields a diffusion coefficient of $D_{\text{COM}} = (0.25 \pm 0.05)\,\mu\text{m}^2/\text{s}$. Figure 4.54 C plots a line profile of the molecular density with respect to the polymer's COM, from which a rms end-to-end distance of $\bar{R}_{\text{ee}} = (1.61 \pm 0.02)\,\mu\text{m}$ is measured. Assuming a maximum contour length of $L_{\text{c}} = 19\,\mu\text{m}$, the persistence length is calculated to $L_{\text{p}} = \bar{R}^2_{\text{ee}}/2L_{\text{c}} = (68 \pm 2)\,\text{nm}$. The parameters extracted from the experiment significantly differ from the parameters presented with Figure 4.50 (much higher S_{T}, lower D, larger R_{g}, longer L_{p}), which was measured at the same day in the very same sample. While no detailed mechanism can be given without further dedicated experiments, the major deviation is possibly connected to the presence the excited metal surface which potentially interacts with the (charged) DNA molecules. The purpose of the presented data, however, is to show the feasibility of trapping a single polymer molecule using a feedback-free heating. The plain gold film used here mimics any absorbing medium that could be in particular the water film itself, heated by an infrared laser beam and creating a temperature profile equivalent to the one shown in Figure 4.54 B. The temperature gradients that are exerted by the quasi-steady heating scheme are much lower as compared to feedback trapping. It is thus not a priori impossible that also the different shape of the temperature field is partially to blame for the deviation in the parameters. The influence of the inhomogeneous temperature gradient field on the polymer's conformation is investigated in the following.

Influence of the Temperature Field on the Conformation In general, the thermophoretic mobility is considered to be independent of the contour length for sufficiently long polymers. That means for a polymer in a homogeneous temperature gradient field, that every monomer feels the same gradient and thus is subjected to the same thermophoretic drift. While the molecule is driven along the temperature gradient, the conformation of the chain as a whole is not altered. Although this argumentation does not fully apply to DNA due to the long-ranged shielding by the charge, the assumption will be used in first approximation for the following considerations. For a spatially localized heat source, the

---

[a)] In fact, only the observation time is limited but not the trapping itself, as no feedback is used.

temperature gradient is strongest close but decays radially with increasing distance to the heat source. Assuming a point heat source, the temperature decays as $\Delta T \sim r^{-1}$. Accordingly, the temperature gradient goes as $\nabla T \sim -r^{-2}$. The focused laser beam of the thermophoretic trap generates a similar temperature and temperature gradient field as can be seen from Figure 4.12 C and D. This particularly means, that the gradient is neither homogeneous over the trapping region nor over the spatial extend of a polymer molecule. It can therefore not anymore be excluded that the conformation of a DNA molecule is influenced while being trapped. Figure 4.55 A shows the relative temperature gradient obtained earlier from simulations plotted in its dependence on the distance to the trapping center for a trap size of 15 µm diameter. A moving average over two times the radius of gyration assumed with $R_\mathrm{g} \approx 0.5\,\mu\mathrm{m}$ has been applied to the curve. The average relative gradient the molecule is exposed to rises for increasing radial distance, that means for decreasing distance to the heat source. While the whole molecule feels that average gradient inducing a thermophoretic drift of the COM, each segment is subject to a local gradient.

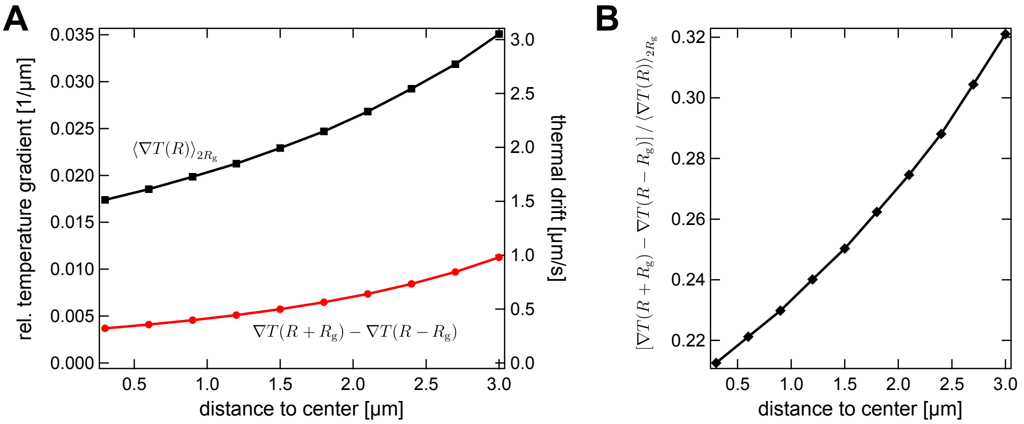

Figure 4.55: **A** Relative temperature gradient averaged over a length of twice the typical radius of gyration of a DNA molecule ($R_\mathrm{g} \approx 0.5\,\mu\mathrm{m}$) vs. the distance from the trap center for a trap size of $d_\mathrm{Trap} = 15\,\mu\mathrm{m}$. Difference in relative temperature gradient over the length of $2R_\mathrm{g}$ for $d_\mathrm{Trap} = 10\,\mu\mathrm{m}$ (red) and $d_\mathrm{Trap} = 15\,\mu\mathrm{m}$ (light red). The right axis shows the corresponding expected average drift velocity of the molecule and relative drift velocity between two segments separated by $2R_\mathrm{g}$ along the temperature field ($D_\mathrm{T} = 1\,\mu\mathrm{m}^2/\mathrm{sK}$, $P_\mathrm{heat} = 3\,\mathrm{mW}$). **B** Ratio of the relative velocity of two segments separated by $2R_\mathrm{g}$ to the average drift velocity of the entire molecule.

As an arbitrary measure, two segments are considered spatially separated by $2R_\mathrm{g} \approx 1.0\,\mu\mathrm{m}$ along the temperature profile, *i.e.* along the radial direction within the trap. Accordingly, the plot also shows the difference in the gradient over the distance of $2R_\mathrm{g}$, which is directly connected to the curvature of the temperature profile. This difference in temperature gradient rises radially away from the trap center as well. In a picture of free and independent segments, this would lead to a relative thermal drift between the two segments. The expected relative movement is shown with the right axis in Figure 4.55 A. For this estimation, a typical thermophoretic mobility of $D_\mathrm{T} = 1\,\mu\mathrm{m}^2/\mathrm{sK}$ and a heating power of $P_\mathrm{heat} = 3\,\mathrm{mW}$ is considered. The COM drift of the molecule close to the trapping center is estimated to about $2\,\mu\mathrm{m}/\mathrm{s}$. Compared to that, the relative motion of the two segments is expected with about $0.5\,\mu\mathrm{m}/\mathrm{s}$. Figure 4.55 B compares the ratio of the difference in the temperature gradient to the average gradient being equivalent to the ratio of the relative motion of the two considered segments to the average induced thermophoretic drift velocity of the whole molecule. The ratio easily exceeds 25%, even for moderate distances of the molecule from the trap center. As the temperature gradient increases with increasing distance from the trap center, segments in far regions are driven faster to the center than segments close to the center. The polymer molecule is therefore expected to show a compression due to the applied temperature field. The latter consideration, however, gives no clue on the magnitude of the compression, but the ratio plotted in Figure 4.55 B suggests that the effect should be reflected in the experimental data.

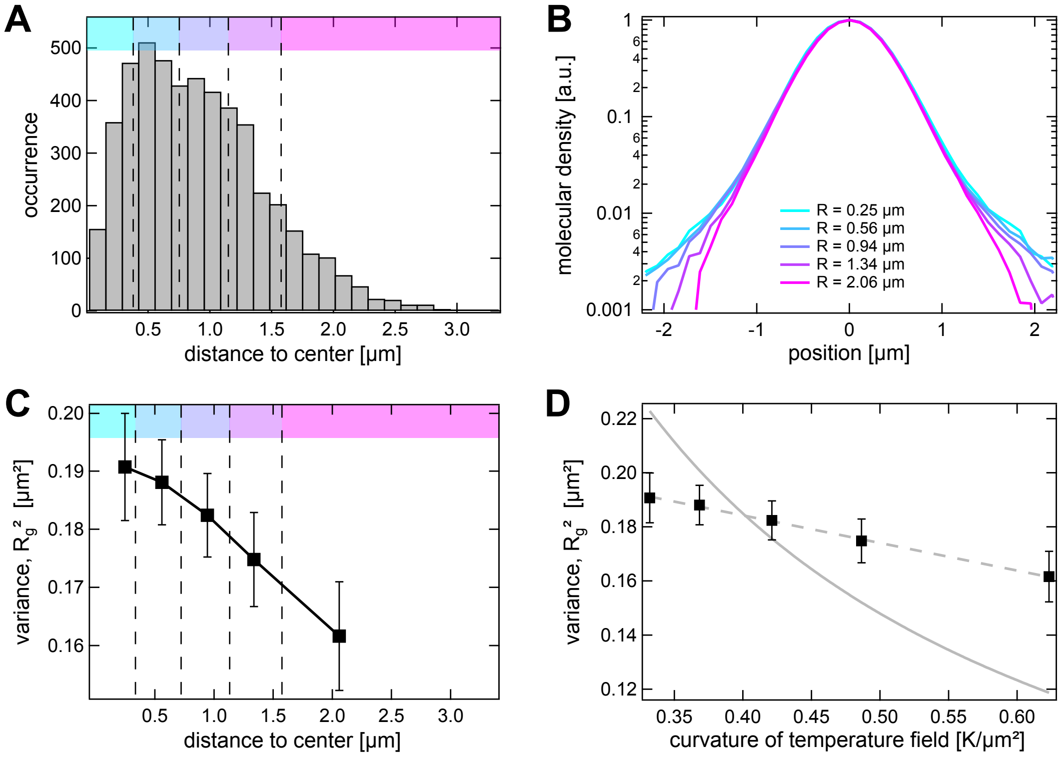

Figure 4.56: **A** COM position distribution of a single λ-DNA molecule confined in a 15 µm diameter trap divided into five concentric region (feedback heating mode at $P_{\text{heat}} = 3.0\,\text{mW}$). **B** Molecular density of the molecule with respect to the COM for the different concentric regions defined in A. **C** Variance (*i.e.* R_g^2) of the distributions in B. **D** Variance of the monomer density in dependence of the curvature of the temperature field in the different spatial regions. The dashed line represents a linear fit. The gray curve represents a one-over-curvature dependence (with arbitrary amplitude).

While being confined in a trap of 15 µm diameter at 3.0 mW heating power, the molecule explores the trapping region up to displacements from the center of about 2.5 µm, which can be seen from the radial position distribution in Figure 4.56 A. As the temperature gradient increases with increasing distance to the trap center, an increasing compression is expected towards the heat source. The position distribution is therefore divided into five concentric regions. For each region, the molecular density of the molecule is calculated separately by accumulating the corresponding cropped molecule images, each shifted by their COM (see Figure 4.52). The resulting molecular density profiles are depicted in Figure 4.56. The width slightly decreases with increasing distance to the trap center. The compression appears to be strongest for the monomers far from the COM. The decreasing width is quantified in Figure 4.56 C plotting the variance of the distributions in B (representing R_g^2) versus the mean distance to the trap center. The local curvature of the temperature profile is calculated from the simulated temperature fields and is compared to the squared radius of gyration gained for the different concentric regions in Figure 4.56 D. Within the regions that are accessible with the experimental data, the curvature of the temperature field almost doubles. A linear relation between the R_g^2 and the curvature of the temperature profile is found with a slope of $(-0.102 \pm 0.006)\,\mu\text{m}^4/\text{K}$. However, the linearity can only represent a local dependence, as the DNA is expected to collapse for infinite curvatures. In Section 4.1.2 it is found that the variance $\sigma^2 = 1/S_T\alpha$ of the position distribution of a single particle in a harmonic temperature field decreases with one over the curvature of the temperature α. This suggests the same one over curvature scaling for the mean squared monomer distribution around the center of mass of the molecule. This dependence represented by the gray curve, however, does not fit the experimental data, which decreases much slower. While a more thorough study is needed to unravel the underlying processes, the preliminary results clearly show that an inhomogeneous temperature gradient in the trapping area affects the conformation and compresses the DNA conformation in the outer regions. This effect is pronounced by using smaller traps where the curvature of the temperature field is stronger.

The possibility of manipulating the conformation of DNA molecules by thermal fields has been already reported by several groups. Jiang and Sano[83] showed that λ-DNA strands that are attached to a surface by one or two ends via biotin-streptavidin interactions are stretched by applying a optically induced thermal gradient. These results show that the monomers are subject to thermophoresis within the polymer and each segments reacts on a local temperature gradient. This leads to internal tension within the DNA molecule. Other experiments confine T4 DNA of 166 kilo base pairs length in nano-channels, which prestretches the molecules.[82] The confined DNA molecule thus becomes a spring to measure equivalent themophoretic forces. Depending on where the heat source is located, the polymer is either further stretched or compressed along the channel direction.[81]

Little is known about the influence of the local temperature field on the conformation of free DNA molecules,[84] that means without attaching the molecule to a surface or a confinement within nano-channels. While compression and self-entanglement dynamics have been investigated by Tang et al. by means of electric fields,[187] the preliminary results presented with Figure 4.56 provide a first example of a compression of a free DNA molecule by thermal fields. Also the height of the water film with about $1\,\mu\text{m}$ is about twice the radius of gyration and confines the molecule much less than a nano-channel. In particular, no prestretching is expected. The thermophoretic trap therefore becomes a promising tool to study non-equilibrium dynamics of bio-molecules. With the usage of a box-like trapping potential (see Section 4.3.4), the induced compression could be directly probed in comparison to the equilibrium conformational dynamics.

Chapter 5

Summary and Outlook

5.1 Summary of the Results

Studying the properties of microscopic systems as small as single molecules is of fundamental importance in particular in bio sciences and soft-matter physics. The investigation of single molecules often reveals processes and functions, that are otherwise hidden in an ensemble average. For this reason, single molecule spectroscopy evolved to a powerful toolbox of optical methods that are nowadays indispensable for biological studies. Without surface tethering, the time scales on which the molecule's properties can be accessed is typically limited by Brownian motion causing the molecule to disappear from the observation volume of, for example, a fluorescence microscope. Well-established techniques such as optical tweezers use optical forces to trap dielectric objects larger than a few hundred nanometer. While these methods are widely used to apply or measure forces in molecular systems, they fail to confine single molecules as the optical gradient force scaling with the polarizability is to weak to compete with Brownian motion. Different techniques based on electric or electromagnetic fields, such as plasmonic tweezers or the ABEL trap, have been developed to overcome this problem. Each exhibits it's strengths and weaknesses depending on the specific application.

A promising and fundamentally different type of interaction is thermophoresis. The term thermophoresis describes the directed motion of a solute along the temperature gradient applied to the solvent. Apart from the fact that directed motion can be induced which allows to actively compensate for Brownian motion, in the context of trapping single biomolecules, thermophoresis becomes interesting for two additional reasons. The strong dependence of the thermophoretic mobility on the molecule and the surrounding properties recently made thermophoresis popular to probe molecular interactions in free solution with the technique of Microscale Thermophoresis. Also, beyond the ability to induce a center of mass drift, thermophoresis is able to apply intra-molecular forces to a macro-molecule if the temperature gradient varies over the extend of the molecule. Moreover, microscopic temperature fields can be easily generated all-optically not requiring an external wiring of electrodes, for example, to produce electric fields. For these reasons, thermophoretic interactions could be of interest to power a micro-fluidic device for single molecule manipulation and analytics.

While being widely used to spatially accumulate particles or molecules typically in combination with advective flows, thermophoresis so far has not been shown to confine single nano-objects. The thesis is dedicated to experimentally explore the feasibility of trapping single particles or molecules by means of local temperature fields. For this purpose, laser heating of a gold nano-structure is used to induce a thermophoretic drift field in an appropriate way to counter act the erratic motion caused by thermal fluctuations. The findings are divided into three parts according to three experimental realizations of the trap, which essentially differ in the way the temperature fields are controlled. Starting from a simple static heating, the technique over the course of the doctoral study developed to a device that allows for an active manipulation of single or multiple nano-objects in solution.

Summary of Section 4.1: Trapping by a Steady Temperature Profile. The sample, on which the experiments are performed, is formed by a water film confined between two glass slides. One slide carries a gold film exhibiting circular holes of a few micron in diameter, which are prepared by micro-sphere lithography. Heating the circumference by means of an expanded cw laser beam leads to a temperature field that exhibits a local minimum in the center. That means, that the resulting inward thermophoretic drift velocity field counter acts the outward diffusive drift due to Brownian motion, which can be used to confine individual particles. This is demonstrated by trapping a single 200 nm polystyrene bead in a gold structure of 5 µm diameter. The dynamical behavior of the particle in the trap is studied by looking at the step size distribution, yielding information about the deterministic thermophoretic drift as well as the Brownian motion, quantified by the diffusion coefficient. By studying the heating power dependence of the diffusion coefficient, a relation between the local temperature rise and the heating laser power is found, which is an essential prerequisite to extract both the thermophoretic mobility as well as the Soret coefficient. The shape of the temperature profile is reconstructed from the position distribution of the particle in the trap. A quantitative comparison to the simulated temperature profile yields the Soret coefficient. The experiments show that the induced thermophoretic drift follows the temperature gradient that is expected from numerical simulations of the temperature profile. Independently from the Soret coefficient, the thermophoretic mobility is calculated from the step size analysis by a comparison of the induced drift with the temperature gradient profile.

The Gaussian position distribution shows that the temperature field in the trap center can be approximated with a parabola (harmonic temperature field). The thermophoretic motion is overall force-free. Nevertheless, the positional distribution of the particle can be compared to a Boltzmann distribution giving rise to an *effective* harmonic trapping potential. The curvature of the temperature field accordingly corresponds to the trapping stiffness and together with the Soret coefficient determines the spatial extend of the particle distribution. Already with this simple experimental realization of the thermophoretic trap, effective trapping potentials of several $k_B T$ can be achieved with an effective trapping stiffness of order fN/µm.

The results show, that a confinement of a single macroscopic particle can be achieved by means of local temperature fields. The employed steady-state heating scheme, however, is inefficient. A general problem is the shallow depth of the local temperature minimum as compared to the high temperature elevation in the center of the trap, which does not contribute to the confinement and is highly undesired for potential biological applications. To decrease the overall heat deposition, different strategies are developed to control the optical heating.

Summary of Section 4.2: Thermophoretic Trapping by Dynamic Temperature Fields. In a second step, the experimental setup is extended with a focused heating laser beam, which can be freely steered within the sample plane. This allows to alter the heating scheme from the simultaneous and steady heating of the entire circumference of the gold structure towards a local heating of only a diffraction-limited spot. By that, a very localized temperature field is generated, which however does not anymore exhibit a confining local temperature minimum. Rather, caused by the thermophoretic repulsion for typically positive Soret coefficients, a steady heating of just a local spot will quickly drive the particle away from the trapping region. Inspired by the Paul trap, which employs rotating electric fields, this problem is solved by steering the laser beam along the rim of the gold structure at a certain rotation frequency in order to achieve a confinement. The dynamic behavior of a trapped particle is studied in detail, particular attention is paid to the influence of this laser rotation frequency. The problem is approached in a frame in which the heating laser beam is still, but the sample rotates about the center of the trap.

Neglecting Brownian motion first yields a deterministic flow field resulting from the advection of the sample within the rotating frame as well as the thermoporetic repulsion from the heat source. Its most important feature is a stable stationary point, where advection and thermophoretic drift compensate. This stable point does not coincide with the center of the trap. Without the erratic Brownian motion, the particle shows a spiral motion around the stable point with a stabilizing inward component, such that the particle approaches the stable point in the long-time limit. Once the stable point in the rotating frame is reached, the particle shows a circular motion in the lab frame about the trap center at the laser rotation frequency. Both, the off-center position as well as the shape of the flow field close to the stationary point are confirmed experimentally by dedicated trapping experiments. It is shown that the stationary point only exists above a minimum frequency that depends on the strength of the thermophoretic drift. This yields a stability condition for the dynamic trapping scheme. In simple terms, the velocity of the heating laser beam needs to exceed the induced thermophoretic drift, which otherwise repels the particle from the trapping region. Adding Brownian motion to the consideration, a balance of the diffusive and thermophoretic drift yields an asymmetric Gaussian position distribution in the rotating frame.

Interestingly, the dynamics of the particle shows an analogy to the Paul trap. The spiraling of the particle in the rotating frame happens at a frequency which differs from the laser rotation frequency. The motion at the two frequencies can be interpreted as macro and micro-motion, that is in a similar fashion seen for ions in a quadrupole trap. In the high-frequency limit, when the velocity of the cycling temperature field is much faster than the induced thermophopretic drift, the stationary point converges to the trap center and the spiraling frequency converges to the laser rotation frequency such that the macro-motion disappears. Also the asymmetry in the position distribution vanishes. Thus, only radial inward components of the flow field survive the back-transformation to the lab frame and the effective temperature field is simply the time-averaged temperature field which exhibits a local minimum in the center. The usage of high frequencies is therefore called quasi-static heating. This means in particular, that no significant decrease in the center temperature elevation is achieved by the new heating scheme.

It is shown, however, that the new heating allows to trap particles even if the hole in the gold structure, that is essential to provide a temperature minimum via steady heating, is omitted. This is equivalent to a direct optical heating of the liquid which is widely applied. Thermophoretic trapping by such a dynamic heating scheme could thus be easily implemented in existing experimental setups that come with steerable heating laser beams.

Summary of Section 4.3: Feedback-Assisted Thermophoretic Trapping. A fundamentally new quality of thermophoretic trapping can be achieved by introducing an active optical feedback control to couple the heating position of the laser beam to the particle's real-time position. In such a way, the gold structure can be heated always at the particular position that is most efficient to drive the particle towards the trap center. A fast switching of the heating laser position is thereby enabled by the fast heat diffusion compared to the Brownian motion of the particle. The feedback leads to a *virtual* temperature profile that differs from the average temperature field. The strong temperature gradients induced by the focused laser beam are thus fully exploited, in contrast to the temperature field generated by the steady or quasi-steady heating scheme, yielding a strong enhancement both in terms of the depth of the trapping potential as well as the stiffness. This in particular solves the major problem with the passively controlled heating schemes, which is the unfavorable temperature elevation in the trapping region. Assuming a trap diameter of 10 µm, the temperature rise reduces from 67% of the maximum temperature at the gold film for the static heating to 14% in the case of a feedback-controlled laser heating.

Modifying the feedback algorithm moreover allows for a versatile manipulation of the trapped particle, such as an active steering of particles within the trapping region. An active shaping of the virtual trapping potential is achieved by altering the feedback rules, *e.g.* by introducing a time-dependent target position. This is demonstrated by the realization of few examples. A particle trapped in a virtual effective double well potential performs a hopping between two spatially separated targets. The target position is thereby coupled to the particle position. The dynamics can be described by a Kramers relation despite of the thermal non-equilibrium and effective potential generated by a dedicated feedback rule. An area target leads to a box-like potential, for which the gold structure is only heated if the nano-object is about to escape. This allows to study a trapped object at ambient temperature in between the heating events. The diffusion coefficient can be gained from the on-off statistics of the heating beam that represents a typical mean first passage time problem.

The limits of the feedback trapping are studied by a thermophoretic modification of the Kramers relation, that describes the escape rate out of the trap considering an instant feedback. The influence on a finite feedback update time as well as a feedback delay is examined experimentally, both broadening the position distribution. An additional broadening appears due non-negligible tangential components of the temperature gradient caused by the Brownian motion within the feedback latency. The effect is thus strongest for slow feedback update rates. The smallest objects that are tested in the feedback trap are 28 nm diameter polystyrene particles with a Soret coefficient of $S_\mathrm{T} = 0.13\,\mathrm{K}^{-1}$, which yield a mean trapping duration of about 15 s.

Enabled by the strong spatial decay of the induced temperature fields, several particles can be addressed by individual heating laser beams, while at the same time the thermophoretic repulsion prohibits outside particles to enter the trapping region. In such a way, a defined number of particles can be held in the trap, which can hardly be realized by well-established trapping techniques such as optical tweezers. A study of the relative motion of two particles shows, that a coupling of the particle dynamics, *i.e.* a repulsion, artificially induced by the feedback control and the two involved heating laser beams is found only for a large spatial separation of the two particles on the order of the trap radius. This thus does not interfere with physical interactions that are expected for much smaller inter-particle distances.

In the last part of the manuscript, the thermophoretic confinement of single macro-molecules is demonstrated, exemplified by the trapping of λ-DNA. As the Soret coefficient is sufficiently high, the trapping duration is limited only by the bleaching of the intercalated dye molecules. An analysis of the center-of-mass motion yields the diffusion and Soret coefficient in the same way as demonstrated for the rigid polystyrene beads. Additionally, the molecule undergoes conformational dynamics, which can be studied over minutes without a disappearance of the molecule from the field of view. An examination of the molecular density around the center-of-mass allows to determine the radius of gyration and the mean-squared end-to-end distance. A correlation analysis of the fluorescence reveals a temporal evolution of the conformation that is in between Rouse and Zimm dynamics being in agreement with earlier studies of other groups. Finally, preliminary experiments show that the spatially varying temperature gradient over the DNA molecule leads to intra-molecular tension and is able to compress the conformation by thermal fields, an effect that has been observed before only on prestretched DNA confined in nano-channels.

5.2 Outlook

The thermophoretic trap is intended as a tool for the investigation of bio-molecular systems. As the method is based on temperature gradients, more fundamental problems of thermal non-equilibrium physics could be addressed as well. The results of this thesis thereby establish a basis for future applications. The following (incomplete) list shall give experiments that are planned with the thermophoretic feedback trap.

- Ongoing experiments extend the preliminary results presented in Section 4.3.8 and address the interaction of a long DNA chain with inhomogeneous temperature fields and gradients. While the effect of different fluctuations along the chain due to varying temperature is expected to be weak, the influence of a variation of the temperature gradients over the chain is much stronger. The shape of the temperature field employed in the thermophoretic trap suggests a compression of the DNA conformation as a stronger thermophoretic drift is exerted to the monomers that are at a higher distance from the trap center. The relaxation dynamics of a compressed chain could be studied by on-off experiments.

- The ability to trap several nano-objects at a time could be exploited to investigate the interaction of a controlled number of polymer chains, that could be also longer T4-DNA. One polymer thereby is expected to act as a random dynamic background potential for the other one. Recent theoretical studies[188, 189] showed that such perturbations for instance affect the persistence length, altering the parameters experimentally accessible, such as the mean end-to-end distance. Also, the additional fluctuating excluded volume could influence the compression and relaxation dynamics. Having a trapping volume of a few ten femtoliters, high nominal concentrations could be achieved even with only two molecules held in the trap.

- The method of thermophoretic trapping could be also of interest to study nucleation, stability and growth of oligomers of amyloid forming proteins. Working in the single oligomer regime, rate constants of decay and aggregation should be directly accessible, which have not been studied before. The growth of a single fluorescently labeled seed oligomer could, for instance, be trapped, while smaller untrapped monomers are free to pass the trapping regions. The evolution of the oligomer could be monitored by its Brownian fluctuation, which are sensitive to the hydrodynamic size. A time-dependent mobility may be detected with the help of a likelihood-based change point analysis methods.[190]

- Besides bio-molecular applications, the thermophophoretic trap may also find attention for the investigation more fundamental questions. Recently, the Landauer principle,[175] which states that erasing information is an irreversible process requiring a minimum amount of work that is $k_\mathrm{B}T\ln 2$ per bit, has been confirmed using a virtual time-dependent potential of an ABEL trap.[191] The key thereby is the ability to measure the work done by a particle in the generated potential. A similar study using the thermophoretic trap could show if Landauer's principle may be extended to also hold for the case that the feedback-generated virtual potential is not the result of a force, but rather due to force-free phoretic motion, in the same way as the Kramers relation seems to hold as shown in Section 4.3.4.

On the other hand, the technical advancement of the proposed trapping technique is by no means completed. The following improvements of hard and software will enhance the planned experiments as well as generally broaden the applicability of the method.

- A separation of heating and fluorescence excitation avoids bleaching when the heating beam traverses the trapping region and reduces fluorescent background. A multi-color detection allows for a distinction of multiple molecules that are stained by different dyes to resolve, for example, spatially overlapping or entangled macro-molecules.
- Advanced feedback rules that also modulate the strength of the heating could address different problems. For instance, artificial interactions induced during multi-particle trapping could be actively corrected. A dedicated algorithm could actively keep unwanted objects away from the trapping region. Also, strategies are thinkable for trapping several objects at different positions in that trap to meet at a well-defined time. Objects of different Soret coefficient could also be trapped by adapting the necessary heating power.
- Modern versions of the ABEL trap use beam-steering-based detection schemes, that are controlled by a field-programmable gate array.[49–51] This allows for a much shorter feedback latency of order 10 µs, which is much faster than a software-based signal processing of CCD camera images. Operating at the limits of shot-noise, these traps are able to trap even single fluorophores. Also, advanced algorithms are used to estimate diffusion coefficient and transport mobilities in real-time. The thermophoretic trap could also profit from a similar detection scheme. Still, the limits in trapping are determined by the maximum amount of heat that can be exposed to the system to generate the temperature gradients. However, the real-time acquisition of the diffusion coefficient and the thermophoretic mobility would strongly benefit from a shorter feedback latency.
- Thermophoresis is driven by quasi-slip flows in the boundary layer along a particle's surface induced by temperature gradients. The same temperature gradients may also induce a flow of the solvent along the surface of the glass slides that are used to confine the film of solvent.[192] These thermoosmotic flows could be of interest to enhance the trapping of objects that exhibit a weak Soret coefficient.
- The current version of the thermophoretic trap only achieves a 2-dimensional confinement. The third dimension is restricted by the thickness of the water film in between two glass slides. A 3D thermophoretic trap using a static heating is hardly possible as no 3-dimensional local temperature minimum can be generated by local heating. Local cooling on the other side by substantial amounts is difficult to realize by optical means. A feedback-based version of a 3D trap, however, could be realized by employing a 3D-steerable infrared laser beam that directly heats a local spot in bulk water. The feasibility in two dimensions is shown in Section 4.3.6 (heating of a plain gold film mimics the heating of a water film). The extended beam waist in z direction (Rayleigh range) could be controlled by beam shaping methods.

Curriculum Vitae

Name: Marco Braun

Date and place of birth: 23.12.1984, Karl-Marx-Stadt
Nationality: German
Marital status: married, one child

Current address: Mühlstr. 12a
04317 Leipzig
Deutschland

Education

Apr. 2011	**-**	**Jun. 2016**	Universität Leipzig, PhD position Institute for Experimental Physics I Molecular Nanophotonics Group, Prof. Dr. F. Cichos
Oct. 2005	**-**	**Mar. 2011**	Universität Leipzig, Field of study: Physics Degree: Diploma
Aug. 2001	**-**	**Jun. 2004**	Secondary School, Technisches Gymnasium Chemnitz Degree: Abitur
Aug. 1995	**-**	**Jun. 2001**	Middle School, Mittelschule Borna
Aug. 1991	**-**	**Jun. 1995**	Elementary School, Grundschule Glösa

Publications

5.3 Journal Publications

The following articles have been published in peer-reviewed journals:

1. **M. Braun**, A. Bregulla, K. Günther, M. Mertig, F. Cichos (2015): *Single Molecules Trapped by Dynamic Inhomogeneous Temperature Fields*, Nano Lett. **15**(8), 5499-5505.
2. **M. Braun**, A. Würger, F. Cichos (2014): *Trapping of Single Nano-objects in Dynamic Temperature Fields*, Phys. Chem. Chem. Phys. **16**, 15207-15213.
3. M. Selmke, A. Heber, **M. Braun**, F. Cichos (2014): *Photothermal Single Particle Microscopy using a Single Laser Beam*, Appl. Phys. Lett. **105**, 013511.
4. **M. Braun**, F. Cichos (2013): *Optically Controlled Thermophoretic Trapping of Single Nano-Objects*, ACS Nano **7**(12), 11200-11208.
5. M. Selmke, **M. Braun**, R. Schachoff, F. Cichos (2013): *Photothermal Signal Distribution Analysis (PhoSDA)*, Phys. Chem. Chem. Phys. **15**, 4250-4257.
6. M. Selmke, R. Schachoff, **M. Braun**, F. Cichos (2013): *Twin-Focus Photothermal Correlation Spectroscopy*, RSC Adv. **3**, 394-400.
7. M. Selmke, **M. Braun**, F. Cichos (2012): *Gaussian Beam Photothermal Single Particle Microscopy*, J. Opt. Soc. Am. A **29**(10).
8. M. Selmke, **M. Braun**, F. Cichos (2012): *Photothermal Single Particle Microscopy: Detection of a Nanolens*, ACS Nano **6**(3), 2741-2749.
9. M. Selmke, **M. Braun**, F. Cichos (2012): *Nano-lens Diffraction around a Single Heated Nano Particle*, Opt. Express **20**(7), 8055-8070.

5.4 Patents

The author is co-holder and co-inventor of the following international patent

1. F. Cichos, M. Selmke, **M. Braun**, R. Schachoff: *Twin-focus photothermal correlation spectroscopy method and device for the characterization of dynamical processes in liquids and biomaterials with the help of absorbing markers*, permalink: `http://patentscope.wipo.int/search/en/WO2013007804`

5.5 Talks

Talks were given at the following symposia and international conferences:

1. DPG spring meeting, Berlin, March 2015.
2. DPG spring meeting, Dresden, March 2014.
3. LOMA Seminar, University of Bordeaux, January 2014.
4. SFG Meeting ‘From Local Constraints to Macroscopic Transport’, Leipzig, December 2013.
5. Diffusion Fundamentals V, Leipzig, August 2013
6. BuildMoNa Symposium, March 2013.
7. European Optical Society: Annular Meeting (EOSAM) 2012, UK, September 2012.
8. DPG Spring Meeting, Berlin, March 2012.
9. 488. WE Heraeus Seminar, Single Molecule Spectroscopy, Chemnitz, July 2011 .

5.6 Poster presentations

Posters have been presented at the following symposia and international conferences:

1. BuildMoNa Symposium, March 2014.
2. Hot Nanostructures Workshop, Leiden, NL, October 2013.
3. Diffusion Fundamentals V, Leipzig, August 2013.
4. DPG Spring Meeting, Regensburg, March 2013.
5. BuildMoNa Symposium, March 2012.
6. Hot Nanoparticles and Nanostructures Symposium, Leipzig, October 2011.
7. Focus On Microscopy (FOM) 2011, Konstanz, April 2011.
8. DPG spring meeting, Dresden, March 2011.

Acknowledgements

At this point, I would like to thank those who helped throughout the development process of this thesis.

I wish above all to thank my supervisor Prof. Dr. Frank Cichos not only for providing a warm-hearted environment in which working was really a pleasure. I am especially grateful for the helpful and stimulating discussions as well as experimental advice, which both were particularly supportive in the early stage of my PhD studies. His distinct scientific curiosity often led to exciting ideas and, from time to time, gave the interpretations of experiments whole new directions and insights.

Further, I am especially indebted to Andreas Bregulla. His impressive ability for handling square-meter-sized LabVIEW code helped a lot with the realization of the feedback-controlled version of the trap. Although being miles away from the groups percolator, sharing the office with him and André Heber was a joy. I'm going to miss the obligatory getaways to the local supermarket.

I would like to thank Prof. Dr. Alois Würger for his theoretical contribution to my work. I deeply appreciate the (often physics unrelated) discussions during his visits in Leipzig as well as my excursion to Bordeaux, where I felt very welcome. Furthermore, I thank Katrin Günther for performing the staining procedure of the DNA molecules, which was a huge help.

I further truly enjoyed the fruitful cooperation with Markus Selmke especially in the beginning of my PhD work. I really appreciated to participate in the development of a theoretical description of photothermal microscopy leading to new perspectives of the technique. I am also very happy to call him a close friend beyond the institute's walls.

In addition, I wish to thank Tobias Thalheim, Markus Selmke and Frank Cichos for carefully proof-reading of the manuscript and by that saving me from the one or another disgrace … hopefully.

You can be rich in many ways beside money. Nevertheless, I am grateful for the financial support of the SFB-Transregio 102 'Polymers under multiple constraints'. I further appreciate the funding by the European Union and the Free State of Saxony in form of a scholarship by the European Social Funds.

A special thank-you deserves the entire Molecular Nanophotonics group for inspirational discussions, breathtaking talks, enjoyable lunch breaks, watery field days and, last but not least, delicious cakes.

I wish to express my honest gratitude to the most important persons in my life, that are my dearest wife Conny, who never gets tired of making me smile, and my beloved son Max, who amazes me every single day.

Finally, I am very much indebted to my parents Kerstin and Steffen, as well as my brother Ronny, for their invaluable support and encouragement throughout the years.

Declaration

I hereby certify that this thesis was written by the author himself and that no means of help were used other than those mentioned in the text. All work and thoughts from other authors and sources have been duly acknowledged and clearly marked as such in the thesis. I especially name Alois Würger, who in cooperation with myself developed the theoretical description presented in Section 4.2.4. I also name Andreas Bregulla, who in cooperation with myself programmed parts of the software used in Section 4.3. Furthermore, Katrin Günther performed the staining of the DNA strands with the dye molecules used in Section 4.3.8.

I hereby name Markus Selmke, Tobias Thalheim and Prof. Frank Cichos as the only persons who assisted the author during the compilation of this thesis by proof-reading and helpful comments.

Apart from the above mentioned individuals, no other person has been involved in the process of the compilation and work on the present thesis. Especially, no attempt has been made to make use of doctoral consulting. No other individuals have received payment of any kind by the author, neither direct nor indirect, for work which is connected with the contents of this thesis.

I further certify that neither this thesis nor any derivative thereof has been submitted or presented to any other examination department for the purpose of achieving a PhD. Neither has it been presented to any other examination office and has not yet been published in its full form.

No earlier attempts to achieve a PhD degree have been made.

I acknowledge the doctoral regulations of the faculty of physics and geosciences (Promotionsordnung der Fakultät für Physik und Geowissenschaften) dated 23rd March 2010 in their full sense.

(Marco Braun)

List of Figures

List of Tables

Bibliography

[1] T. Basché, W. E. Moerner, M. Orrit, and U. P. Wild. *Single-Molecule Optical Detection, Imaging and Spectroscopy*. VCH Verlagsgesellschaft mbH, Weinheim, Germany, 1996.

[2] W. E. Moerner and D. P. Fromm. Methods of single-molecule fluorescence spectroscopy and microscopy. *Review of Scientific Instruments*, 74(8):3597, 2003.

[3] F. Kulzer and M. Orrit. Single-molecule optics. *Annual review of physical chemistry*, 55:585–611, 2004.

[4] M. Orrit, T. Ha, and V. Sandoghdar. Single-molecule optical spectroscopy. *Chemical Society Reviews*, 43(4):973, 2014.

[5] W. E. Moerner. Single-molecule spectroscopy, imaging, and photocontrol: Foundations for super-resolution microscopy (nobel lecture). *Angewandte Chemie International Edition*, 54(28):8067–8093, 2015.

[6] W. E. Moerner and L. Kador. Optical detection and spectroscopy of single molecules in a solid. *Physical Review Letters*, 62(21):2535–2538, 1989.

[7] M. Orrit and J. Bernard. Single pentacene molecules detected by fluorescence excitation in a p -terphenyl crystal. *Physical Review Letters*, 65(21):2716–2719, 1990.

[8] J. R. Lakowicz. *Principles of fluorescence spectroscopy*. Springer Science+Business Media, LLC, Boston, MA, 3. ed edition, 2006.

[9] T. Förster. Zwischenmolekulare energiewanderung und fluoreszenz. *Annalen der Physik*, 437(1-2):55–75, 1948.

[10] L. Stryer. Fluorescence energy transfer as a spectroscopic ruler. *Annual Review of Biochemistry*, 47(1):819–846, 1978.

[11] R. Roy, S. Hohng, and T. Ha. A practical guide to single-molecule fret. *Nature methods*, 5(6):507–516, 2008.

[12] M. Vrljic, S. Y. Nishimura, and W. E. Moerner. Single-molecule tracking. In J. M. Walker and T. J. McIntosh, editors, *Lipid Rafts*, volume 398 of *Methods in Molecular Biology*, pages 193–219. Humana Press, Totowa, NJ, 2007.

[13] K. I. Mortensen, L. S. Churchman, J. A. Spudich, and H. Flyvbjerg. Optimized localization analysis for single-molecule tracking and super-resolution microscopy. *Nature methods*, 7(5):377–381, 2010.

[14] R. M. Dickson, A. B. Cubitt, R. Y. Tsien, and W. E. Moerner. On/off blinking and switching

behaviour of single molecules of green fluorescent protein. *Nature*, 388(6640):355–358, 1997.

[15] E. Betzig, G. H. Patterson, R. Sougrat, O. W. Lindwasser, S. Olenych, J. S. Bonifacino, M. W. Davidson, J. Lippincott-Schwartz, and H. F. Hess. Imaging intracellular fluorescent proteins at nanometer resolution. *Science*, 313(5793):1642–1645, 2006.

[16] S. T. Hess, T. P. Girirajan, and M. D. Mason. Ultra-high resolution imaging by fluorescence photoactivation localization microscopy. *Biophysical Journal*, 91(11):4258–4272, 2006.

[17] M. J. Rust, M. Bates, and X. Zhuang. Sub-diffraction-limit imaging by stochastic optical reconstruction microscopy (storm). *Nature methods*, 3(10):793–796, 2006.

[18] F. P. Schäfer, J. P. Toennies, W. Zinth, R. Rigler, M. Orrit, and T. Basché. *Single Molecule Spectroscopy*, volume 67. Springer Berlin Heidelberg, Berlin, Heidelberg, 2001.

[19] C. Zander, J. ENDERLEIN, and R. A. Keller. *Single Molecule Detection in Solution: Methods and Applications*. Wiley-VCH Verlag GmbH & Co. KGaA, Weinheim, FRG, 2002.

[20] W. E. Moerner. New directions in single-molecule imaging and analysis. *Proceedings of the National Academy of Sciences*, 104(31):12596–12602, 2007.

[21] A. Ashkin. Optical trapping and manipulation of neutral particles using lasers. *Proceedings of the National Academy of Sciences*, 94(10):4853–4860, 1997.

[22] D. G. Grier. A revolution in optical manipulation. *Nature*, 424(6950):810–816, 2003.

[23] J. R. Moffitt, Y. R. Chemla, S. B. Smith, and C. Bustamante. Recent advances in optical tweezers. *Annual Review of Biochemistry*, 77(1):205–228, 2008.

[24] A. Ashkin, J. M. Dziedzic, J. E. Bjorkholm, and S. Chu. Observation of a single-beam gradient force optical trap for dielectric particles. *Optics Letters*, 11(5):288, 1986.

[25] K. C. Neuman and S. M. Block. Optical trapping. *Review of Scientific Instruments*, 75(9):2787, 2004.

[26] K. Berg-Sørensen and H. Flyvbjerg. Power spectrum analysis for optical tweezers. *Review of Scientific Instruments*, 75(3):594, 2004.

[27] A. Noy. *Handbook of molecular force spectroscopy*. Springer, New York, NY, 2008.

[28] K. C. Neuman and A. Nagy. Single-molecule force spectroscopy: optical tweezers, magnetic tweezers and atomic force microscopy. *Nature methods*, 5(6):491–505, 2008.

[29] E. A. Abbondanzieri, W. J. Greenleaf, J. W. Shaevitz, R. Landick, and S. M. Block. Direct observation of base-pair stepping by rna polymerase. *Nature*, 438(7067):460–465, 2005.

[30] Miklos S. Z. Kellermayer, Steven B. Smith, Henk L. Granzier, and Carlos Bustamante. Folding-unfolding transitions in single titin molecules characterized with laser tweezers. *Science*, 276(5315):1112–1116, 1997.

[31] A. E. Cohen and A. P. Fields. The cat that caught the canary: What to do with single-molecule trapping. *ACS Nano*, 5(7):5296–5299, 2011.

[32] M. L. Juan, M. Righini, and R. Quidant. Plasmon nano-optical tweezers. *Nature Photonics*, 5(6):349–356, 2011.

[33] M. Righini, A. S. Zelenina, C. Girard, and R. Quidant. Parallel and selective trapping in a patterned plasmonic landscape. *Nature Physics*, 3(7):477–480, 2007.

[34] M. Righini, G. Volpe, C. Girard, D. Petrov, and R. Quidant. Surface plasmon optical tweezers: Tunable optical manipulation in the femtonewton range. *Physical Review Letters*, 100(18),

2008.

[35] A. N. Grigorenko, N. W. Roberts, M. R. Dickinson, and Y. Zhang. Nanometric optical tweezers based on nanostructured substrates. *Nature Photonics*, 2(6):365–370, 2008.

[36] M. Righini, P. Ghenuche, S. Cherukulappurath, V. Myroshnychenko, García de Abajo, F. J., and R. Quidant. Nano-optical trapping of rayleigh particles and escherichia coli bacteria with resonant optical antennas. *Nano Letters*, 9(10):3387–3391, 2009.

[37] M. L. Juan, R. Gordon, Y. Pang, F. Eftekhari, and R. Quidant. Self-induced back-action optical trapping of dielectric nanoparticles. *Nature Physics*, 5(12):915–919, 2009.

[38] Y. Pang and R. Gordon. Optical trapping of 12 nm dielectric spheres using double-nanoholes in a gold film. *Nano Letters*, 11(9):3763–3767, 2011.

[39] A. Kotnala and R. Gordon. Double nanohole optical tweezers visualize protein p53 suppressing unzipping of single dna-hairpins. *Biomedical Optics Express*, 5(6):1886, 2014.

[40] J. Berthelot, S. S. Aćimović, M. L. Juan, M. P. Kreuzer, J. Renger, and R. Quidant. Three-dimensional manipulation with scanning near-field optical nanotweezers. *Nature Nanotechnology*, 9(4):295–299, 2014.

[41] A. Kotnala, S. Wheaton, and R. Gordon. Playing the notes of dna with light: extremely high frequency nanomechanical oscillations. *Nanoscale*, 7(6):2295–2300, 2015.

[42] R. Hölzel, N. Calander, Z. Chiragwandi, M. Willander, and F. Bier. Trapping single molecules by dielectrophoresis. *Physical Review Letters*, 95(12), 2005.

[43] M. Krishnan, N. Mojarad, P. Kukura, and V. Sandoghdar. Geometry-induced electrostatic trapping of nanometric objects in a fluid. *Nature*, 467(7316):692–695, 2010.

[44] W. Paul. Electromagnetic traps for charged and neutral particles. *Reviews of Modern Physics*, 62(3):531–540, 1990.

[45] W. Guan, S. Joseph, J. H. Park, P. S. Krstic, and M. A. Reed. Paul trapping of charged particles in aqueous solution. *Proceedings of the National Academy of Sciences*, 108(23):9326–9330, 2011.

[46] M. Tanyeri, E. M. Johnson-Chavarria, and C. M. Schroeder. Hydrodynamic trap for single particles and cells. *Applied Physics Letters*, 96(22):224101, 2010.

[47] A. E. Cohen. Control of nanoparticles with arbitrary two-dimensional force fields. *Physical Review Letters*, 94(11), 2005.

[48] A. J. Berglund, K. McHale, and H. Mabuchi. Feedback localization of freely diffusing fluorescent particles near the optical shot-noise limit. *Optics Letters*, 32(2):145, 2007.

[49] A. P. Fields and A. E. Cohen. Electrokinetic trapping at the one nanometer limit. *Proceedings of the National Academy of Sciences*, 108(22):8937–8942, 2011.

[50] Q. Wang and W. E. Moerner. An adaptive anti-brownian electrokinetic trap with real-time information on single-molecule diffusivity and mobility. *ACS Nano*, 5(7):5792–5799, 2011.

[51] Q. Wang and W. E. Moerner. Single-molecule motions enable direct visualization of biomolecular interactions in solution. *Nature methods*, 11(5):555–558, 2014.

[52] A. E. Cohen and W. E. Moerner. Internal mechanical response of a polymer in solution. *Physical Review Letters*, 98(11), 2007.

[53] R. Piazza and A. Parola. Thermophoresis in colloidal suspensions. *Journal of Physics: Con-*

densed Matter, 20(15):153102, 2008.

[54] A. Würger. Thermal non-equilibrium transport in colloids. *Reports on Progress in Physics*, 73(12):126601, 2010.

[55] S. Fayolle, T. Bickel, and A. Würger. Thermophoresis of charged colloidal particles. *Physical Review E*, 77(4), 2008.

[56] A. Würger. Transport in charged colloids driven by thermoelectricity. *Physical Review Letters*, 101(10), 2008.

[57] M. Reichl, M. Herzog, F. Greiss, M. Wolff, and D. Braun. Understanding the similarity in thermophoresis between single- and double-stranded dna or rna. *Physical Review E*, 91(6), 2015.

[58] M. Reichl, M. Herzog, A. Götz, and D. Braun. Why charged molecules move across a temperature gradient: The role of electric fields. *Physical Review Letters*, 112(19), 2014.

[59] S. Duhr and D. Braun. Why molecules move along a temperature gradient. *Proceedings of the National Academy of Sciences*, 103(52):19678–19682, 2006.

[60] M. Braibanti, D. Vigolo, and R. Piazza. Does thermophoretic mobility depend on particle size? *Phys. Rev. Lett.*, 100(10):108303, 2008.

[61] A. Würger. Is soret equilibrium a non-equilibrium effect? *Comptes Rendus Mécanique*, 341(4-5):438–448, 2013.

[62] S. Duhr and D. Braun. Thermophoretic depletion follows boltzmann distribution. *Phys. Rev. Lett.*, 96(16):168301, 2006.

[63] D. Braun and A. Libchaber. Trapping of dna by thermophoretic depletion and convection. *Physical Review Letters*, 89(18), 2002.

[64] S. Duhr, S. Arduini, and D. Braun. Thermophoresis of dna determined by microfluidic fluorescence. *The European Physical Journal E*, 15(3):277–286, 2004.

[65] S. Duhr and D. Braun. Optothermal molecule trapping by opposing fluid flow with thermophoretic drift. *Physical Review Letters*, 97(3), 2006.

[66] S. Iacopini and R. Piazza. Thermophoresis in protein solutions. *Europhysics Letters*, 63(2):247–253, 2003.

[67] S. Iacopini, R. Rusconi, and R. Piazza. The macromolecular tourist: Universal temperature dependence of thermal diffusion in aqueous colloidal suspensions. *The European Physical Journal E*, 19(1):59–67, 2006.

[68] R. Piazza and A. Guarino. Soret effect in interacting micellar solutions. *Physical Review Letters*, 88(20), 2002.

[69] H. Ning, R. Kita, H. Kriegs, J. Luettmer-Strathmann, and S. Wiegand. Thermal diffusion behavior of nonionic surfactants in water. *The Journal of Physical Chemistry B*, 110(22):10746–10756, 2006.

[70] K. J. Zhang, M. E. Briggs, R. W. Gammon, J. V. Sengers, and J. F. Douglas. Thermal and mass diffusion in a semidilute good solvent-polymer solution. *The Journal of Chemical Physics*, 111(5):2270, 1999.

[71] J. Rauch and W. Köhler. Diffusion and thermal diffusion of semidilute to concentrated solutions of polystyrene in toluene in the vicinity of the glass transition. *Physical Review Letters*,

88(18), 2002.

[72] J. Rauch and W. Köhler. On the molar mass dependence of the thermal diffusion coefficient of polymer solutions. *Macromolecules*, 38(9):3571–3573, 2005.

[73] M. Hartung, J. Rauch, and W. Köhler. Thermal diffusion of dilute polymer solutions: The role of solvent viscosity. *The Journal of Chemical Physics*, 125(21):214904, 2006.

[74] S. Wiegand. Thermal diffusion in liquid mixtures and polymer solutions. *Journal of Physics: Condensed Matter*, 16(10):R357–R379, 2004.

[75] C. J. Wienken, P. Baaske, U. Rothbauer, D. Braun, and S. Duhr. Protein-binding assays in biological liquids using microscale thermophoresis. *Nature Communications*, 1(7):100, 2010.

[76] M. Jerabek-Willemsen, C. J. Wienken, D. Braun, P. Baaske, and S. Duhr. Molecular interaction studies using microscale thermophoresis. *Assay and drug development technologies*, 9(4):342–353, 2011.

[77] Seidel, Susanne A. I., C. J. Wienken, S. Geissler, M. Jerabek-Willemsen, S. Duhr, A. Reiter, D. Trauner, D. Braun, and P. Baaske. Label-free microscale thermophoresis discriminates sites and affinity of protein-ligand binding. *Angewandte Chemie International Edition*, 51(42):10656–10659, 2012.

[78] Seidel, Susanne A. I., P. M. Dijkman, W. A. Lea, van den Bogaart, Geert, M. Jerabek-Willemsen, A. Lazic, J. S. Joseph, P. Srinivasan, P. Baaske, A. Simeonov, I. Katritch, F. A. Melo, J. E. Ladbury, G. Schreiber, A. Watts, D. Braun, and S. Duhr. Microscale thermophoresis quantifies biomolecular interactions under previously challenging conditions. *Biophysical Methods for the Study of Protein Interactions*, 59(3):301–315, 2013.

[79] F. Weinert and D. Braun. Observation of slip flow in thermophoresis. *Physical Review Letters*, 101(16), 2008.

[80] C. B. Mast and D. Braun. Thermal trap for dna replication. *Physical Review Letters*, 104(18), 2010.

[81] L. H. Thamdrup, N. B. Larsen, and A. Kristensen. Light-induced local heating for thermophoretic manipulation of dna in polymer micro- and nanochannels. *Nano Letters*, 10(3):826–832, 2010.

[82] J. N. Pedersen, C. J. Lüscher, R. Marie, L. H. Thamdrup, A. Kristensen, and H. Flyvbjerg. Thermophoretic forces on dna measured with a single-molecule spring balance. *Physical Review Letters*, 113(26), 2014.

[83] H.-R. Jiang and M. Sano. Stretching single molecular dna by temperature gradient. *Applied Physics Letters*, 91(15):154104, 2007.

[84] M. Ichikawa, H. Ichikawa, K. Yoshikawa, and Y. Kimura. Extension of a dna molecule by local heating with a laser. *Physical Review Letters*, 99(14), 2007.

[85] G. Baffou and R. Quidant. Thermo-plasmonics: using metallic nanostructures as nano-sources of heat. *Laser & Photonics Reviews*, 7(2):171–187, 2013.

[86] H. Bruus. *Theoretical microfluidics*, volume 18 of *Oxford master series in condensed matter physics*. Oxford University Press, Oxford, 2008.

[87] R. Brown. Xxvii. a brief account of microscopical observations made in the months of june, july and august 1827, on the particles contained in the pollen of plants; and on the general

existence of active molecules in organic and inorganic bodies. *The Philosophical Magazine, or Annals of Chemistry, Mathematics, Astronomy, Natural History and General Science*, 4(21):161–173, 1828.

[88] R. Cont and P. Tankov. *Financial modelling with jump processes*. Chapman & Hall/CRC financial mathematics series. Chapman & Hall/CRC, Boca Raton, Fla, 2004.

[89] I. Karatzas and S. E. Shreve. *Methods of mathematical finance*, volume 39 of *Applications of mathematics*. Springer, New York, 1998.

[90] A. Einstein. Über die von der molekularkinetischen theorie der wärme geforderte bewegung von in ruhenden flüssigkeiten suspendierten teilchen. *Annalen der Physik*, 322(8):549–560, 1905.

[91] Paul Langevin. Sur la théorie du mouvement brownien. *C. R. Acad. Sci. (Paris)*, 146:530–533, 1908.

[92] M. Doi and S. F. Edwards. *The theory of polymer dynamics*, volume 73 of *The international series of monographs on physics*. ClarendonPress, Oxford, 1986.

[93] L. E. Reichl. *A modern course in statistical physics*. Physics textbook. Wiley, Weihheim, 3rd rev. and updated ed edition, 2009.

[94] F. Gittes and C. F. Schmidt. Signals and noise in micromechanical measurements. *Methods in cell biology*, 55:129–156, 1998.

[95] B. Lukić, S. Jeney, Ž. Sviben, A. Kulik, E.-L. Florin, and L. Forró. Motion of a colloidal particle in an optical trap. *Physical Review E*, 76(1), 2007.

[96] F. Schwabl. *Statistical mechanics*. Advanced Texts in Physics. Springer, Berlin and New York, 2nd ed edition, 2006.

[97] D. Magde, W. W. Webb, and E. L. Elson. Fluorescence correlation spectroscopy. iii. uniform translation and laminar flow. *Biopolymers*, 17(2):361–376, 1978.

[98] C. Ludwig. Diffusion zwischen ungleich erwärmten orten gleich zusammengesetzter lösungen. *Sitzungsberichte der Mathematisch-Naturwissenschaftlichen Classe der Kaiserlichen Akademie der Wissenschaften*, 20:539, 1856.

[99] C. Soret. Sur l'état d'équilibre que prend, du point de vue de sa concentration, une dissolution saline primitivement homogène, dont deux parties sont portées à des températures différentes. *Archives de Genève, 3e période, tome II*, page 48, 1879.

[100] S. R. deGroot and P. Mazur. *Non-equilibrium thermodynamics*. Dover Publications, New York, dover ed edition, 1984.

[101] M. Braun and F. Cichos. Optically controlled thermophoretic trapping of single nano-objects. *ACS Nano*, 7(12):11200–11208, 2013.

[102] J. L. Anderson. Colloid transport by interfacial forces. *Annual Review of Fluid Mechanics*, 21(1):61–99, 1989.

[103] H.-R. Jiang, H. Wada, N. Yoshinaga, and M. Sano. Manipulation of colloids by a nonequilibrium depletion force in a temperature gradient. *Physical Review Letters*, 102(20), 2009.

[104] R. D. Astumian. Coupled transport at the nanoscale: The unreasonable effectiveness of equilibrium theory. *Proceedings of the National Academy of Sciences*, 104(1):3–4, 2007.

[105] Dhont, Jan K. G., S. Wiegand, S. Duhr, and D. Braun. Thermodiffusion of charged colloids:

Single-particle diffusion. *Langmuir*, 23(4):1674–1683, 2007.

[106] S. A. Putnam, D. G. Cahill, and Wong, Gerard C. L. Temperature dependence of thermodiffusion in aqueous suspensions of charged nanoparticles. *Langmuir*, 23(18):9221–9228, 2007.

[107] A. Würger. Thermophoresis in colloidal suspensions driven by marangoni forces. *Physical Review Letters*, 98(13), 2007.

[108] D. Stadelmaier and W. Köhler. From small molecules to high polymers: Investigation of the crossover of thermal diffusion in dilute polystyrene solutions. *Macromolecules*, 41(16):6205–6209, 2008.

[109] D. Stadelmaier and W. Köhler. Thermal diffusion of dilute polymer solutions: The role of chain flexibility and the effective segment size. *Macromolecules*, 42(22):9147–9152, 2009.

[110] M. E. Schimpf and J. C. Giddings. Characterization of thermal diffusion in polymer solutions by thermal field-flow fractionation: effects of molecular weight and branching. *Macromolecules*, 20(7):1561–1563, 1987.

[111] F. Brochard and P.-G. d. Gennes. Soret effect of flexible macromolecules. *C. R. Acad. Sci. Paris, Ser. 2*, 293:1025, 1981.

[112] K. I. Morozov and W. Köhler. Thermophoresis of polymers: Nondraining vs draining coil. *Langmuir*, 30(22):6571–6576, 2014.

[113] M. R. Reichl and D. Braun. Thermophoretic manipulation of molecules inside living cells. *Journal of the American Chemical Society*, 136(45):15955–15960, 2014.

[114] P. Reineck, C. J. Wienken, and D. Braun. Thermophoresis of single stranded dna. *ELECTROPHORESIS*, 31(2):279–286, 2010.

[115] Schasfoort, R. B. M and A. J. Tudos. *Handbook of surface plasmon resonance*. Royal Society of Chemistry, Cambridge, 2008.

[116] J. M. Pitarke, V. M. Silkin, E. V. Chulkov, and P. M. Echenique. Theory of surface plasmons and surface-plasmon polaritons. *Reports on Progress in Physics*, 70(1):1–87, 2007.

[117] U. Kreibig and M. Vollmer. *Optical properties of metal clusters*, volume 25 of *Springer series in materials science*. Springer, Berlin and New York, 1995.

[118] E. Kretschmann. The angular dependence and the polarisation of light emitted by surface plasmons on metals due to roughness. *Optics Communications*, 5(5):331–336, 1972.

[119] Y.-Y. Teng and E. A. Stern. Plasma radiation from metal grating surfaces. *Physical Review Letters*, 19(9):511–514, 1967.

[120] E. Kretschmann. Die bestimmung optischer konstanten von metallen durch anregung von oberflächenplasmaschwingungen. *Zeitschrift für Physik*, 241(4):313–324, 1971.

[121] A. Otto. Excitation of nonradiative surface plasma waves in silver by the method of frustrated total reflection. *Zeitschrift für Physik*, 216(4):398–410, 1968.

[122] X. Guo. Surface plasmon resonance based biosensor technique: A review. *Journal of Biophotonics*, 5(7):483–501, 2012.

[123] H. Nguyen, J. Park, S. Kang, and M. Kim. Surface plasmon resonance: A versatile technique for biosensor applications. *Sensors*, 15(5):10481–10510, 2015.

[124] M. Born and E. Wolf. *Principles of optics: Electromagnetic theory of propagation, interference and diffraction of light*. Cambridge University Press, Cambridge and New York, 7th

expanded ed edition, 1999.

[125] O. S. Heavens. *Thin film physics*, volume no. 95 of *Science paperbacks*. Methuen [distributed in the U.S.A. by Halsted Press, a division of John Wiley & Sons, New York], [London], 1973, ©1970.

[126] W. Jacob, A. v. Keudell, and T. Schwarz-Selinger. Infrared analysis of thin films: amorphous, hydrogenated carbon on silicon. *Brazilian Journal of Physics*, 30(3):508–516, 2000.

[127] P. B. Johnson and R. W. Christy. Optical constants of the noble metals. *Physical Review B*, 6(12):4370–4379, 1972.

[128] C. F. Bohren and D. R. Huffman. *Absorption and scattering of light by small particles*. Wiley, New York, 1983.

[129] J. Sinzig and M. Quinten. Scattering and absorption by spherical multilayer particles. *Applied Physics A Solids and Surfaces*, 58(2):157–162, 1994.

[130] P. Zijlstra and M. Orrit. Single metal nanoparticles: optical detection, spectroscopy and applications. *Reports on Progress in Physics*, 74(10):106401, 2011.

[131] C. M. Cobley, J. Chen, E. C. Cho, L. V. Wang, and Y. Xia. Gold nanostructures: a class of multifunctional materials for biomedical applications. *Chemical Society Reviews*, 40(1):44–56, 2011.

[132] M. Hu, J. Chen, Z.-Y. Li, L. Au, G. V. Hartland, X. Li, M. Marquez, and Y. Xia. Gold nanostructures: engineering their plasmonic properties for biomedical applications. *Chemical Society Reviews*, 35(11):1084, 2006.

[133] T. K. Sau and A. L. Rogach. *Complex-shaped metal nanoparticles: Bottom-up syntheses and applications*. Wiley-VCH, Weinheim, 2012.

[134] G. Baffou, C. Girard, and R. Quidant. Mapping heat origin in plasmonic structures. *Physical Review Letters*, 104(13), 2010.

[135] M. H. Aliabadi. *The boundary element method*. Wiley, Chichester, 2002.

[136] B. T. Draine and P. J. Flatau. Discrete-dipole approximation for scattering calculations. *Journal of the Optical Society of America A*, 11(4):1491, 1994.

[137] A. Taflove, S. C. Hagness, and M. Piket-May. Computational electromagnetics: The finite-difference time-domain method. In *The Electrical Engineering Handbook*, pages 629–670. Elsevier, 2005.

[138] V. Myroshnychenko, J. Rodríguez-Fernández, I. Pastoriza-Santos, A. M. Funston, C. Novo, P. Mulvaney, L. M. Liz-Marzán, and García de Abajo, F. Javier. Modelling the optical response of gold nanoparticles. *Chemical Society Reviews*, 37(9):1792, 2008.

[139] J. S. Donner, G. Baffou, D. McCloskey, and R. Quidant. Plasmon-assisted optofluidics. *ACS Nano*, 5(7):5457–5462, 2011.

[140] H. S. Carslaw and J. C. Jaeger. *Conduction of heat in solids*. Clarendon Press and Oxford University Press, Oxford [Oxfordshire] and New York, 2nd ed edition, 1986, ©1959.

[141] G. Baffou and H. Rigneault. Femtosecond-pulsed optical heating of gold nanoparticles. *Physical Review B*, 84(3), 2011.

[142] J. D. Jackson. *Classical electrodynamics*. Wiley, New York, 3rd ed edition, 1999.

[143] G. Baffou, R. Quidant, and C. Girard. Thermoplasmonics modeling: A green's function ap-

proach. *Physical Review B*, 82(16), 2010.

[144] K. Imen, J. Y. Lin, and S. D. Allen. Steady-state temperature profiles in thermally thin substrates induced by arbitrarily shaped laser beams. *JOURNAL OF APPLIED PHYSICS*, 66(2):488, 1989.

[145] M. Selmke. *Photothermal Single Particle Detection in Theory & Experiments*. 2013.

[146] P. Grua, J. P. Morreeuw, H. Bercegol, G. Jonusauskas, and F. Vallée. Electron kinetics and emission for metal nanoparticles exposed to intense laser pulses. *Physical Review B*, 68(3), 2003.

[147] H. Inouye, K. Tanaka, I. Tanahashi, and K. Hirao. Ultrafast dynamics of nonequilibrium electrons in a gold nanoparticle system. *Physical Review B*, 57(18):11334–11340, 1998.

[148] C. Voisin, N. Del Fatti, D. Christofilos, and F. Vallée. Ultrafast electron dynamics and optical nonlinearities in metal nanoparticles. *The Journal of Physical Chemistry B*, 105(12):2264–2280, 2001.

[149] J. D. WATSON and CRICK, F. H. C. Molecular structure of nucleic acids: A structure for deoxyribose nucleic acid. *Nature*, 171(4356):737–738, 1953.

[150] B. Kirby. *Micro- and nanoscale fluid mechanics: Transport in microfluidic devices*. Cambridge University Press, New York, 2010.

[151] F. C. Neidhardt and R. Curtiss. *Escherichia coli and Salmonella: Cellular and molecular biology*. ASM Press, Washington, D.C, 2nd ed edition, 1996.

[152] F. Sanger, A. R. Coulson, G. F. Hong, D. F. Hill, and G. B. Petersen. Nucleotide sequence of bacteriophage lambda dna. *Journal of Molecular Biology*, 162(4):729–773, 1982.

[153] H. Yamakawa. *Modern theory of polymer solutions*. Harper & Row, 1971.

[154] Maarel, Johan R. C. van der. *Introduction to biopolymer physics*. World Scientific, Hackensack, N.J, 2008.

[155] I. Teraoka. *Polymer solutions: An introduction to physical properties*. Wiley, New York, 2002.

[156] S.-M. Yang, S. G. Jang, D.-G. Choi, S. Kim, and H. K. Yu. Nanomachining by colloidal lithography. *Small*, 2(4):458–475, 2006.

[157] H.-R. Jiang, N. Yoshinaga, and M. Sano. Active motion of a janus particle by self-thermophoresis in a defocused laser beam. *Phys. Rev. Lett.*, 105(26):268302, 2010.

[158] A. P. Bregulla, H. Yang, and F. Cichos. Stochastic localization of microswimmers by photon nudging. *ACS Nano*, 8(7):6542–6550, 2014.

[159] F. M. Weinert, C. B. Mast, and D. Braun. Optical fluid and biomolecule transport with thermal fields. *Physical Chemistry Chemical Physics*, 13(21):9918, 2011.

[160] D. Rings, R. Schachoff, M. Selmke, F. Cichos, and K. Kroy. Hot brownian motion. *Physical Review Letters*, 105(9), 2010.

[161] K. D. Kihm, A. Banerjee, C. K. Choi, and T. Takagi. Near-wall hindered brownian diffusion of nanoparticles examined by three-dimensional ratiometric total internal reflection fluorescence microscopy (3-d r-tirfm). *Experiments in Fluids*, 37(6):811–824, 2004.

[162] L. Lobry and N. Ostrowsky. Diffusion of brownian particles trapped between two walls: Theory and dynamic-light-scattering measurements. *Physical Review B*, 53(18):12050–12056, 1996.

[163] A. Rohrbach. Stiffness of optical traps: Quantitative agreement between experiment and electromagnetic theory. *Physical Review Letters*, 95(16), 2005.

[164] R. E. March. Quadrupole ion traps. *Mass Spectrometry Reviews*, 28(6):961–989, 2009.

[165] W. Paul and H. Steinwedel. Ein neues massenspektrometer ohne magnetfeld. *Zeitschrift für Naturforschung A*, 8(7):448–450, 1953.

[166] D. J. Berkeland, J. D. Miller, J. C. Bergquist, W. M. Itano, and D. J. Wineland. Minimization of ion micromotion in a paul trap. *JOURNAL OF APPLIED PHYSICS*, 83(10):5025–5033, 1998.

[167] J. H. Park and P. S. Krstić. Stability of an aqueous quadrupole micro-trap. *Journal of Physics: Condensed Matter*, 24(16):164208, 2012.

[168] M. Braun, A. Würger, and F. Cichos. Trapping of single nano-objects in dynamic temperature fields. *Physical Chemistry Chemical Physics*, 16(29):15207, 2014.

[169] A. E. Cohen and W. E. Moerner. Method for trapping and manipulating nanoscale objects in solution. *Applied Physics Letters*, 86(9):093109, 2005.

[170] A. E. Cohen. *Trapping and manipulating single molecules in solution*. Stanford University, 2006.

[171] Y. Jun and J. Bechhoefer. Virtual potentials for feedback traps. *Physical Review E*, 86(6), 2012.

[172] M. Braun, A. P. Bregulla, K. Günther, M. Mertig, and F. Cichos. Single molecules trapped by dynamic inhomogeneous temperature fields. *Nano Letters*, 15(8):5499–5505, 2015.

[173] J. Schuster, F. Cichos, J. Wrachtrup, and C. v. Borczyskowski. Diffusion of single molecules close to interfaces. *Single Molecules*, 1(4):299–305, 2000.

[174] P. Hänggi. Escape from a metastable state. *Journal of Statistical Physics*, 42(1-2):105–148, 1986.

[175] R. Landauer and J. A. Swanson. Frequency factors in the thermally activated process. *Physical Review*, 121(6):1668–1674, 1961.

[176] R. A. Siegel and R. Langert. A new monte carlo approach to diffusion in constricted porous geometries. *Journal of Colloid and Interface Science*, 109(2):426–440, 1986.

[177] D.-S. Ko, M. Sauer, S. Nord, R. Müller, and J. Wolfrum. Determination of the diffusion coefficient of dye in solution at single molecule level. *Chemical Physics Letters*, 269(1-2):54–58, 1997.

[178] H. A. Kramers. Brownian motion in a field of force and the diffusion model of chemical reactions. *Physica*, 7(4):284–304, 1940.

[179] P. Hänggi, P. Talkner, and M. Borkovec. Reaction-rate theory: fifty years after kramers. *Reviews of Modern Physics*, 62(2):251–341, 1990.

[180] M. D. Armani, S. V. Chaudhary, R. Probst, and B. Shapiro. Using feedback control of microflows to independently steer multiple particles. *Journal of Microelectromechanical Systems*, 15(4):945–956, 2006.

[181] R. Probst, Z. Cummins, C. Ropp, E. Waks, and B. Shapiro. Flow control of small objects on chip: Manipulating live cells, quantum dots, and nanowires. *IEEE Control Systems*, 32(2):26–53, 2012.

[182] S. Chaudhary and B. Shapiro. Arbitrary steering of multiple particles independently in an electro-osmotically driven microfluidic system. *IEEE Transactions on Control Systems Technology*, 14(4):669–680, 2006.

[183] P. J. Hagerman. Flexibility of dna. *Annual Review of Biophysics and Biophysical Chemistry*, 17(1):265–286, 1988.

[184] S. B. Smith, L. Finzi, and C. Bustamante. Direct mechanical measurements of the elasticity of single dna molecules by using magnetic beads. *Science (New York, N.Y.)*, 258(5085):1122–1126, 1992.

[185] A. Sischka, K. Toensing, R. Eckel, S. D. Wilking, N. Sewald, R. Ros, and D. Anselmetti. Molecular mechanisms and kinetics between dna and dna binding ligands. *Biophysical Journal*, 88(1):404–411, 2005.

[186] R. Shusterman, S. Alon, T. Gavrinyov, and O. Krichevsky. Monomer dynamics in double- and single-stranded dna polymers. *Physical Review Letters*, 92(4), 2004.

[187] J. Tang, N. Du, and P. S. Doyle. Compression and self-entanglement of single dna molecules under uniform electric field. *Proceedings of the National Academy of Sciences*, 108(39):16153–16158, 2011.

[188] H.-H. Boltz and J. Kierfeld. Stiff directed lines in random media. *Physical Review E*, 88(1), 2013.

[189] S. Schöbl, S. Sturm, W. Janke, and K. Kroy. Persistence-length renormalization of polymers in a crowded environment of hard disks. *Physical Review Letters*, 113(23), 2014.

[190] D. Montiel, H. Cang, and H. Yang. Quantitative characterization of changes in dynamical behavior for single-particle tracking studies †. *The Journal of Physical Chemistry B*, 110(40):19763–19770, 2006.

[191] Y. Jun, M. Gavrilov, and J. Bechhoefer. High-precision test of landauer's principle in a feedback trap. *Physical Review Letters*, 113(19), 2014.

[192] A. Bregulla, A. Würger, K. Günther, M. Mertig, and F. Cichos. Thermo-osmotic flow in thin films. arXiv:1601.05888 [physics.flu-dyn], 2016.